Universiteit Leiden
The Netherlands

Orion's Dragon and other stories: Feedback by massive stars

Pabst, C.H.M.

Citation
Pabst, C. H. M. (2021, March 18). *Orion's Dragon and other stories: Feedback by massive stars*. Retrieved from https://hdl.handle.net/1887/3147353

Version:	Publisher's Version
License:	Licence agreement concerning inclusion of doctoral thesis in the Institutional Repository of the University of Leiden
Downloaded from:	https://hdl.handle.net/1887/3147353

Note: To cite this publication please use the final published version (if applicable).

Cover Page

Universiteit Leiden

Leiden University Repository

The handle http://hdl.handle.net/1887/3147353 holds various files of this Leiden University dissertation.

Author: Pabst, C.H.M.
Title: Orion's Dragon and other stories: Feedback by massive stars
Issue date: 2021-03-18

Orion's Dragon and Other Stories

Feedback by massive stars

ISBN: 978-94-6419-144-8

An electronic copy of this thesis can be found at https://openaccess.leidenuniv.nl

Cover design: As Orion, the Greek mythological hunter, was passing by the star-forming region of the nebula named in his honor, he beheld, by virtue of his infrared glasses, the funny creature that lived in its midst. The rotated and cropped data cube of the carbon far-infrared emission line came to be called Orion's Dragon. Front cover background image credit: Uwe Kindziorra; dragon drawing credit: Janneke de Jonge. Back cover: [C II] emission in three velocity channels (blue: 4-5 $\mathrm{km\,s^{-1}}$, green: 8-9 $\mathrm{km\,s^{-1}}$, red: 12-13 $\mathrm{km\,s^{-1}}$).

Orion's Dragon and Other Stories

Feedback by massive stars

Proefschrift

ter verkrijging van
de graad van Doctor aan de Universiteit Leiden,
op gezag van Rector Magnificus prof. dr. ir. H. Bijl,
volgens besluit van het College voor Promoties
te verdedigen op donderdag 18 maart 2021
klokke 16.15 uur

door

Cornelia Hilke Manuela Pabst

geboren op 18 september 1989
te Marburg, Duitsland

Promotores:	Prof. dr. A. G. G. M. Tielens	(Universiteit Leiden)
	Dr. J. R. Goicoechea	(Consejo Superior de Investigaciones Científicas)

Promotiecommissie

Voorzitter:	Prof. dr. H. J. A. Röttgering	(Universiteit Leiden)
Secretaris:	Prof. dr. P. P. van der Werf	(Universiteit Leiden)
Overige leden:	Dr. L. D. Anderson	(West Virginia University)
	Dr. M. Gerin	(École Normale Supérieure)
	Prof. dr. C. R. O'Dell	(Vanderbilt University)

Voor iedereen

„Zwei Dinge erfüllen das Gemüt mit immer neuer und zunehmender Bewunderung und Ehrfurcht, je öfter und anhaltender sich das Nachdenken damit beschäftigt: der bestirnte Himmel über mir und das moralische Gesetz in mir.
Beide darf ich nicht als in Dunkelheiten verhüllt oder im Überschwenglichen, außer meinem Gesichtskreise suchen und bloß vermuten; ich sehe sie vor mir und verknüpfe sie unmittelbar mit dem Bewusstsein meiner Existenz.“

– Immanuel Kant („Kritik der praktischen Vernunft“, 1788)

Contents

1 Introduction **1**
1.1 Feedback and the evolution of galaxies . . . 1
1.2 Ionized gas, PDR structures, and forbidden lines . . . 1
1.3 The Orion molecular cloud . . . 4
1.4 SOFIA/upGREAT . . . 5
1.5 Thesis outline . . . 8
1.6 Outlook . . . 9
1.7 Epilogue . . . 11

2 [C II] emission from L1630 in the Orion B molecular cloud **13**
2.1 Introduction . . . 14
2.2 Observations . . . 16
2.2.1 [C II] Observations . . . 16
2.2.2 Dust SED Analysis . . . 17
2.2.3 CO(1-0) Observations . . . 18
2.2.4 Hα Observations . . . 19
2.3 Analysis . . . 19
2.3.1 Kinematics: velocity channel maps . . . 19
2.3.2 Global morphology . . . 19
2.3.3 Kinematics: velocity-resolved line spectra . . . 22
2.3.4 Edge-on PDR models . . . 24
2.3.5 Correlation diagrams . . . 26
2.4 Discussion . . . 29
2.4.1 [C II] Emission from the PDR . . . 29
2.4.2 [C II] Emission from the H II region . . . 30
2.4.3 FIR emission and beam-dilution effects . . . 31
2.4.4 Column densities, gas temperature, and mass . . . 32
2.4.5 Excitation properties from [^{13}C II] . . . 35
2.4.6 Photoelectric heating and energy balance . . . 36
2.4.7 Line cuts . . . 38
2.4.8 Geometry of the L1630 molecular cloud . . . 40
2.4.9 Comparison with models . . . 41
2.4.10 Comparison with OMC1 in the Orion A molecular cloud . . . 43
2.5 Conclusion . . . 44
2.A Calculating [C II] optical depth and excitation temperature . . . 47
2.B Face-on calculation . . . 47

3 Disruption of the Orion molecular core 1 by wind from the massive star θ^1 Orionis C **49**
3.A Methods . . . 56
3.A.1 SOFIA observations . . . 56
3.A.2 Orion . . . 61
3.A.3 Kinematics of the gas . . . 61
3.A.4 Mass estimates of the Veil . . . 64

4 Expanding bubbles in Orion A: [C II] observations of M42, M43, and NGC 1977 69
4.1 Introduction . . . 70
4.2 Observations . . . 73
4.2.1 [C II] observations . . . 73
4.2.2 CO observations . . . 73
4.2.3 Dust maps . . . 73
4.2.4 Hα observations . . . 75
4.3 Analysis . . . 75
4.3.1 Global morphology . . . 75
4.3.2 The expanding Veil shell – M42 . . . 76
4.3.3 M43 . . . 83
4.3.4 NGC 1977 . . . 86
4.4 Discussion . . . 89
4.4.1 The pressure balance . . . 92
4.4.2 Rayleigh-Taylor instability of the Veil shell . . . 95
4.4.3 The structure of M43 . . . 97
4.4.4 The Veil stellar-wind bubble . . . 98
4.4.5 The expanding bubble of θ^2 Ori A . . . 101
4.4.6 The thermal bubbles of M43 and NGC 1977 . . . 102
4.4.7 Stellar wind versus thermal expansion of bubbles . . . 103
4.5 Conclusion . . . 106
4.A SED results . . . 108
4.B The expanding Rim . . . 108
4.C PV diagrams . . . 111

5 [C II] 158 μm line emission from Orion A. I. A template for extragalactic studies? 115
5.1 Introduction . . . 116
5.2 Observations . . . 118
5.2.1 [C II] observations . . . 118
5.2.2 CO(2-1) observations . . . 118
5.2.3 Dust SEDs . . . 118
5.2.4 Ancillary photometric data . . . 119
5.3 Analysis . . . 120
5.3.1 Global morphology of the emission . . . 120
5.3.2 Correlation plots of gas and dust tracers . . . 121
5.4 Discussion . . . 124
5.4.1 Comparison with Orion B . . . 125
5.4.2 The [C II] deficit . . . 126
5.4.3 The photoelectric heating efficiency . . . 131
5.4.4 The origin of [C II] emission . . . 132
5.4.5 Tracers of the star-formation rate . . . 132
5.5 Conclusion . . . 138
5.A Calculation of the ionization parameter γ . . . 140

6 [C II] 158 μm line emission from Orion A. II. PDR physics 141
6.1 Introduction . . . 142
6.2 Observations . . . 144
6.3 Analysis . . . 145
6.3.1 Global morphology and channel maps . . . 145
6.3.2 Definition of regions . . . 148
6.3.3 Edge-on PDR models . . . 149
6.3.4 FIR versus distance . . . 150
6.3.5 [C II] versus 70 μm . . . 152
6.3.6 [C II] versus FIR . . . 154
6.3.7 [C II] versus 8 μm . . . 156
6.3.8 FIR versus 8 μm . . . 158
6.3.9 [C II] versus CO(2-1) . . . 160
6.3.10 Summary of the correlation studies . . . 161
6.4 Discussion . . . 162
6.4.1 Comparison of PDR models with observations . . . 162
6.4.2 The G_0-$p_{\rm th}$ relationship . . . 167
6.4.3 The origin of [C II] emission and CO-dark gas . . . 169
6.4.4 Photoelectric heating efficiency . . . 172
6.5 Conclusion . . . 178
6.A Comparison with Lombardi SED fits . . . 179
6.B Correlation plots from free-β SED fit . . . 181
6.C SED fits to single points . . . 183
6.D Spectral line fits . . . 183
6.D.1 M42 . . . 183
6.D.2 M43 . . . 186
6.D.3 NGC 1977 . . . 186
6.D.4 Spectra behind the Bar . . . 189

Samenvatting 203

Zusammenfassung 213

Publications 223

Curriculum Vitae 225

Acknowledgements 227

1

Introduction

1.1 Feedback and the evolution of galaxies

Since we know that the universe has its origins in the Big Bang, understanding stellar feedback has been one of the key ingredients to understanding the evolution of the universe. Stellar feedback comes in the form of energy input by supernova explosions, stellar radiation, and winds. The exact amount of stellar feedback is crucial for the formation of large-scale structure and galaxies. Computational models describing the evolution of large-scale structure and galaxies, such as EAGLE (Evolution and Assembly of Galaxies and their Environments; Schaye et al. 2015), lean heavily on subgrid physics to be incorporated. These subgrid physics, often parametrized as the star-formation rate (SFR), can be explored in local star-forming regions. However, the star-formation rate is presumed to vary during cosmic lifetime, due to the complex interplay of gravity and stellar feedback with additionally varying elemental abundances, and it is important to understand different physical process involved in the feedback of massive stars on the ISM that control this relationship. While star-formation processes predominantly produce low-mass stars, it is the most massive stars that dominate feedback processes by their strong ultraviolet radiation field, mass-loss winds, and, not least, by their death throes when they go supernova.

Stellar feedback comes in two flavors. Massive stars can disrupt their nascent clouds and thereby prevent further star formation (negative feedback). On the other hand, the compression of clouds under the influence of shock waves induced by stellar winds and radiation can lead to enhanced star formation (positive feedback). The efficiency of both processes is controversial. Some studies imply that the efficiency with which clouds are disrupted is small and that the initial conditions, under which the massive stars formed, are decisive (Dale et al. 2014; Watkins et al. 2019). The model for triggered star-formation (Elmegreen & Lada 1977) was challenged by new models that incorporate a wider range of physical processes (Walch et al. 2015). Also the dominant source of feedback is still heavily debated. While many bubbles surrounding massive stars radiate significant in X-ray emission (Townsley et al. 2014), the tell-tale signature of stellar winds, models imply that stellar radiation, ionizing the gas that expands due to overpressure, is more efficient in driving the expansion of these bubbles (Haid et al. 2018; Geen et al. 2020). This thesis focuses on the region of massive star formation in the Orion molecular cloud as a template for the study of feedback from massive stars on nearby molecular clouds either through radiation creating photoionization and photodissociation flows or through the mechanical energy input by stellar winds.

1.2 Ionized gas, PDR structures, and forbidden lines

It has proven difficult to quantify stellar feedback. Despite the detection of X-rays from the cavities of supernovae remnants and wind-blown bubbles, the mass motions the hot gas induces in the interstellar medium could not be efficiently traced. Velocity-

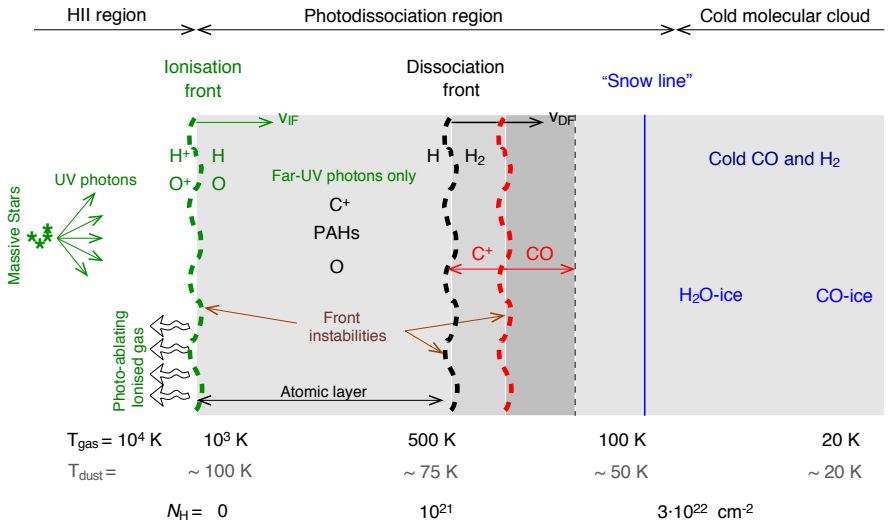

Figure 1.1: Schematic drawing of a photodissociation region (PDR) adjacent to an H II region created by massive stars (Goicoechea et al. 2016).

resolved observations of optical lines from the ionized gas advanced our knowledge of the energy input from massive stars a step further. However, most of the mass in motion is contained in the dense shells of neutral gas that are swept up by the expanding hot and ionized gas (Weaver et al. 1977; Spitzer 1978). Those neutral shells emit strongly at infrared wavelengths, both in continuum emission from UV-heated dust grains, but also in forbidden far-infrared (FIR) lines. Line radiation has the advantage that the dynamics can be traced through the Doppler effect if high-spectral resolution spectrometers are available.

Among the forbidden far-infrared lines is the fine-structure line of ionized carbon, the [C II] $^2P_{3/2}$-$^2P_{1/2}$ line at 158 μm. Together with the [O I] $^3P_1$-$^3P_2$ fine-structure line of atomic oxygen at 63 μm, it is the dominant coolant of neutral gas: The interstellar gas is heated by the photoelectric effect of far-ultraviolet (FUV) photons ($E \simeq$ 6-13.6 eV) on small dust grains and large molecules (polycyclic aromatic hydrocarbons, PAHs) and cools through fine-structure lines of trace elements (Hollenbach & Tielens 1999; Wolfire et al. 1995; Bakes & Tielens 1994). While the ionized gas is heated by photoionization from EUV photons ($E > 13.6$ eV), EUV photons are usually used up in the H II region adjacent to the neutral shells and the neutral gas has the structure of a photodissociation region (PDR). PDRs will be created on the surface of a molecular cloud, where FUV photons impinge on the surface. The schematic structure of such a PDR is shown in Fig. 1.1. The FUV photons are absorbed in the atomic surface layers, where they ionize carbon with an ionization potential of 11.2 eV. Hydrogen atoms combine to hydrogen molecules on dust grains surfaces at the dissociation front. In the deeper layers of a PDR (visual extinction $A_V \gtrsim$ 1-2), carbon will become neutral and eventually form molecules such as CO, the most abundant one after molecular hydrogen. At very low temperatures inside a molecular cloud, molecules freeze out on cold dust grains.

The [C II] line will be the brightest far-infrared line emitted by swept-up shells around massive stars, with moderate gas densities ($n \sim 10^3$-10^4 cm^{-3}) and moderate temperatures ($T \sim$ 100-300 K). As emission lines have a well-defined frequency, it

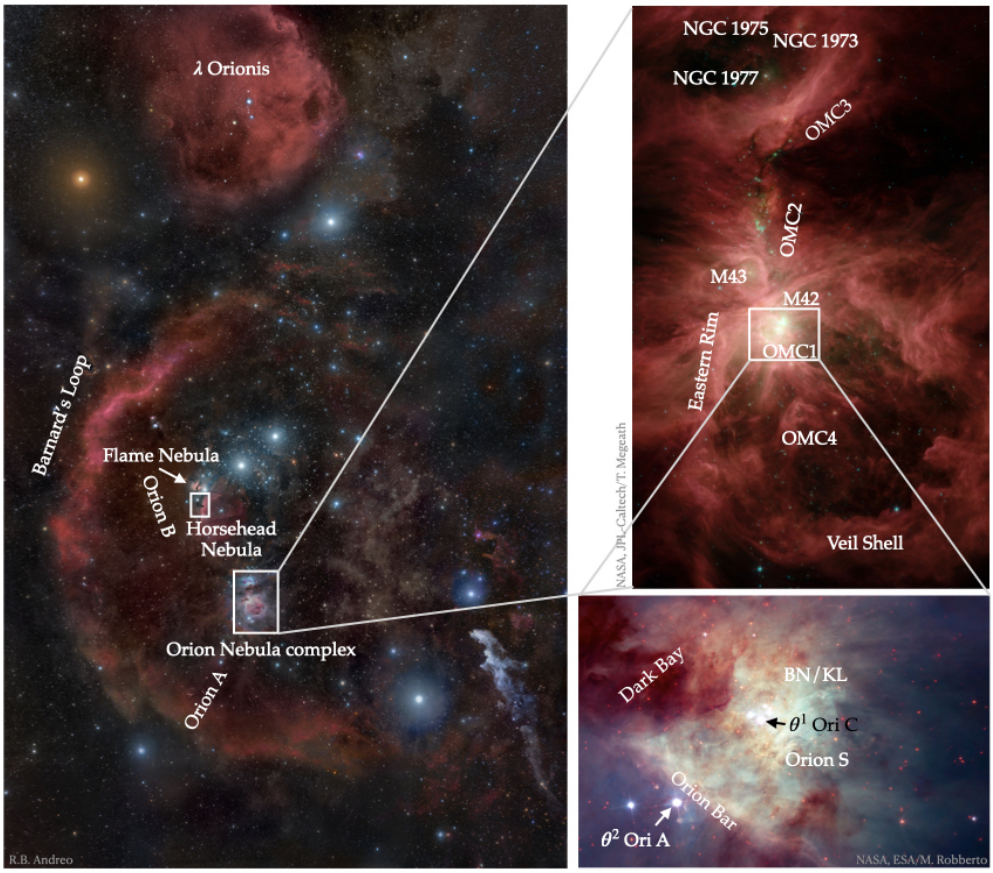

Figure 1.2: Zoom into the constellation of Orion. *Left:* Photograph of the constellation of Orion (image credit: R.B. Andreo). The Horsehead Nebula in the Orion B molecular cloud and the Orion Nebula in the Orion A molecular cloud are visible in this long-time exposure (white rectangles). *Upper right: Spitzer*/IRAC multi-color image of the Orion Nebula complex (image credit: NASA, JPL-Caltech/T. Megeath). Mid-infrared wavelengths reveal dust and large molecules irradiated by star light. *Lower right:* The inner Orion Nebula, with the massive Trapezium stars, as seen by the *Hubble Space Telescope* (image credit: NASA, ESA/M. Robberto). The ionized gas in this regions emits in UV and optical lines. The background PDR and the Orion Bar are mainly visible at infrared and (sub-)millimeter wavelenghts.

is possible to determine gas motions with high accuracy due to the Doppler shift. With the upGREAT instrument onboard SOFIA this has become possible for far-infrared lines such as the [C II] line with sub-km s^{-1} velocity resolution and high spatial resolution (15.9″ at the frequency of the [C II] line). Large-scale mapping of nearby star-forming regions allows to study stellar feedback in more detail than previously possible. In particular, it makes it possible to detect large-scale motion of the gas affected by stellar feedback.

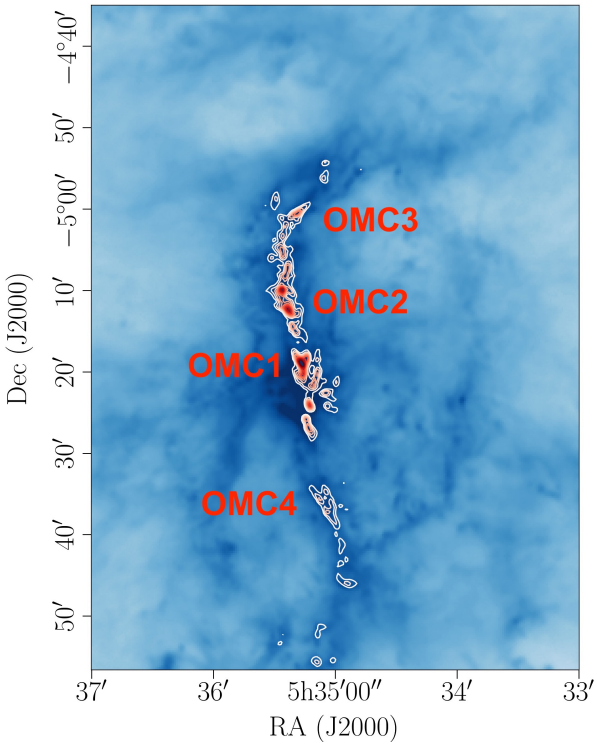

Figure 1.3: *Herschel*/SPIRE 500 μm (blue color scale) and IRAM 30m N_2H^+ (J=1-0) (red contours) emission from the Integral-Shaped Filament. Sub-millimeter emission arises from the cold dust in the extended filament. N_2H^+ emission stems from high-density concentrations along the filament. The positions of the molecular cores OMC1 to 4 are indicated.

1.3 The Orion molecular cloud

The Orion molecular cloud in the constellation of Orion is the nearest site of active massive star formation, with a distance of $\sim$ 400 pc from earth (Menten et al. 2007; Großschedl et al. 2018). The Orion molecular cloud consists of two parts, the Orion A and the Orion B molecular cloud. Figure 1.2 shows an overview of the constellation of Orion, zooming in into the prominent Orion Nebula in Orion A. The Orion Nebula is shaped by the massive stars hosted in its inner regions, the Trapezium stars. Among the Trapezium stars, the O7V star θ^1 Ori C is the most massive with a mass of about 33 solar masses. While originally the denotation Orion Nebula or M42 referred only to the inner bright Huygens Region, an H II region, we know now that the entire shell structure visible at infrared wavelengths is created by feedback from the θ^1 Ori C, whose wind has created a bubble filled with hot, X-rays emitting plasma (Güdel et al. 2008), the Extended Orion Nebula (EON). We subsume the entire structure, including the outward areas of hot and ionized gas, that is affected by feedback from the most massive central stars under the name Orion Nebula. To the north of the Orion Nebula, we find the H II regions of M43, with central B0.5V star NU Ori, and NGC 1973,1975, and 1977. The latter group of reflection nebulae possess as dominant source of radiation the B1V star 42 Orionis in NGC 1977.

The Orion Nebula, M43, and NGC 1977, together the Orion Nebula complex,

are connected by the molecular spine of the Integral-Shaped Filament (ISF), that is readily observed as cold dust at sub-millimeter wavelengths (Johnstone & Bally 1999) and tracers of cold, dense molecular gas such as CO or N_2H^+ rotational lines (Hacar et al. 2017), as shown in Figure 1.3. Along the ISF, we find several star-forming cores, the Orion Molecular Cores (OMC) 1 to 4. The massive Trapezium stars have formed at the surface of the most massive core, OMC1. They are shielded towards the observer by a translucent layer of largely neutral gas, the so-called Orion's Veil (van der Werf & Goss 1989; O'Dell & Yusef-Zadeh 2000; Abel et al. 2004). At the surface of OMC1, the radiation from the Trapezium stars have created an ionized gas region, the Huygens Region. A heavily irradiated PDR (e.g., Goicoechea et al. 2019) separates the ionized gas from the molecular cloud in the background. The Orion Bar is a part of this dense PDR that is curving towards the observer and, hence, is viewed nearly edge-on (e.g., Tielens et al. 1993). Due to its geometry and brightness, it is the most extensively studied PDRs to date. Encircling the constellation of Orion is Barnard's Loop, an expanding shell structure that may have been created by a supernova (Ochsendorf et al. 2015) and is photoionized by massive stars in the Orion OB association (O'Dell et al. 2011). At even larger scales, Barnard's Loop is nested into the Orion-Eridanus superbubble, that is filled with and rejuvenated by dilute gas from stellar feedback events (Ochsendorf et al. 2015).

Another iconic structure in the constellation of Orion is the Horsehead Nebula. Situated at the edge of the L1630 molecular cloud in Orion B, it is illuminated by the O9.5V star σ Ori, that is approaching the cloud and photoevaporating it (Ochsendorf et al. 2014). The Horsehead Nebula and the neighboring edge of L1630 exhibit the layered emission structure of prototypical PDR. As opposed to the Orion A molecular cloud, the star-formation efficiency in Orion B is low (Megeath et al. 2016). Orion B hosts two sites of massive star formation, that have been studied in [C II] emission previously, the Flame Nebula (NGC 2024; Graf et al. 2012) and NGC 2023 (Sandell et al. 2015) close to the Horsehead Nebula. The Horsehead Nebula itself shows weak star-forming potential in its filaments, where only a few young stellar objects (YSOs) can be identified.

1.4 SOFIA/upGREAT

In this thesis, we make use of velocity-resolved [C II] observations to trace stellar feedback in the Horsehead Nebula and the Orion Nebula complex. The observations were obtained with the Stratospheric Observatory for Infrared Astronomy (SOFIA). SOFIA is a heavily modified Boeing 747-SP with a 2.5-meter mirror mounted at the rear (see Fig. 1.4). Flying out of Palmdale, California, or on Southern Deployment out of Christchurch, New Zealand, it is possible to reach altitudes where atmospheric water vapor does not block out infrared radiation completely and it is possible to observe wavelengths from the mid-infrared to the far-infrared (λ = 3-609 μm) with different instruments, that can be exchanged. The heterodyne receiver upGREAT (the upgraded German Receiver for Astronomy at Terahertz Frequencies; Fig. 1.5) allows for observations at far-infrared wavelengths. Heterodyne receivers rely on a signal provided by a local oscillator that is mixed with the telescope signal. The mixed signal can be processed electronically. The Low-Frequency Array (LFA) of upGREAT is tuneable to the frequency of the [C II] line (1.900537 THz) and consists of 2×7 independent pixels in two polarizations. With this, mapping speed is increased by a factor of $\sim$ 20 compared to the single-pixel Heterodyne Instrument for the Far-

Figure 1.4: The Stratospheric Observatory for Infrared Astronomy (SOFIA) in flight (image credit: NASA/Jim Ross).

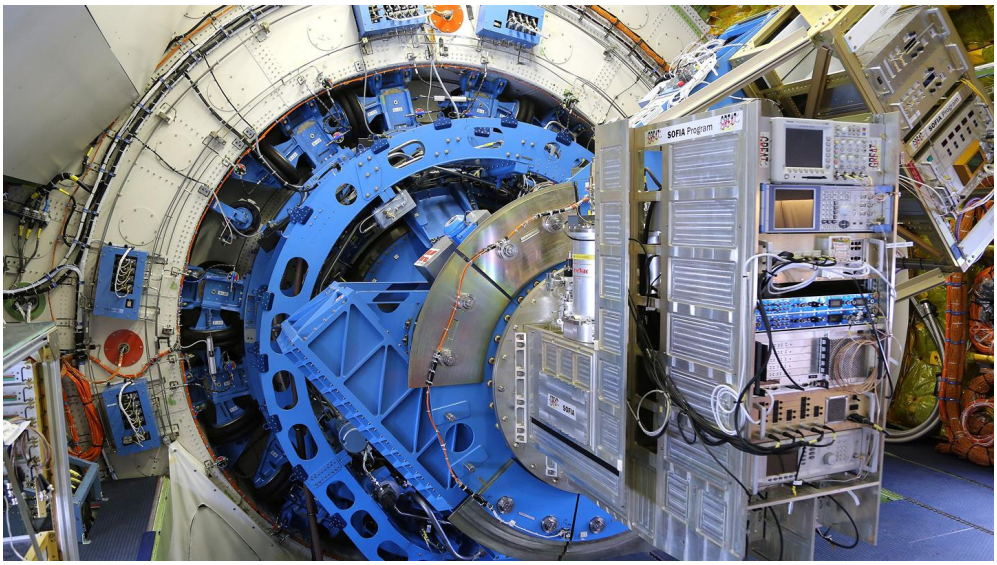

Figure 1.5: The GREAT instrument mounted to SOFIA's mirror backend (image credit: DLR).

Infrared (HIFI) onboard the *Herschel* Space Observatory and large-scale mapping has become feasible.

[C II] observations of the Horsehead Nebula and the adjacent L1630 molecular cloud over an area of $12' \times 17'$ have been obtained in 2015 with SOFIA/ upGREAT

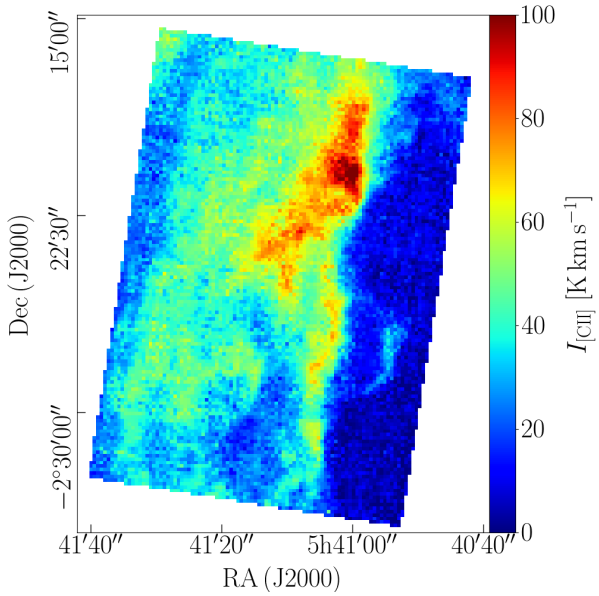

Figure 1.6: [C II] line-integrated emission from L1630 with the Horsehead Nebula in the Orion B molecular cloud.

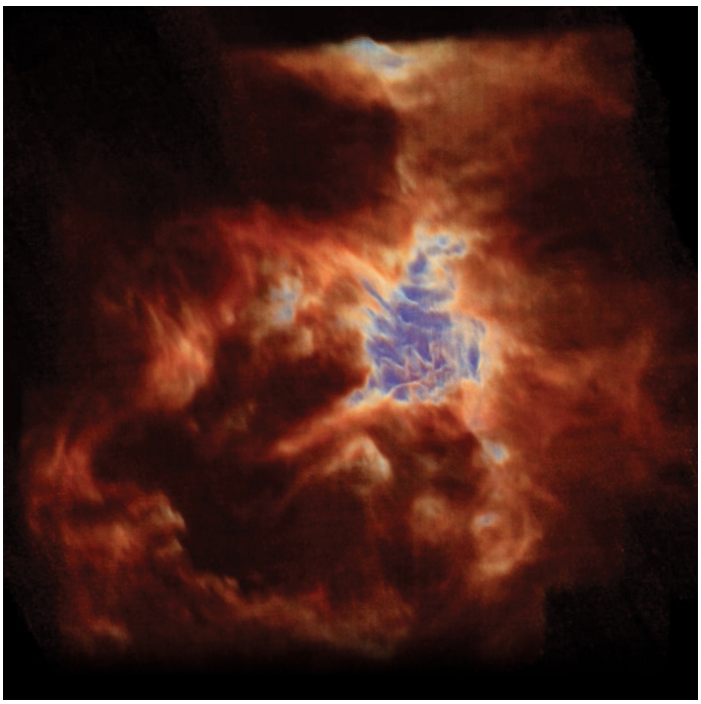

Figure 1.7: A screenshot from the rotating [C II] data cube that is Orion's Dragon, observed by SOFIA/upGREAT (image credit: NASA/SOFIA).

in order to prove the feasibility of large-scale mapping. Figure 1.6 shows the [C II] line-integrated intensity from L1630. The Orion A C^+ Square-Degree survey towards Orion A, carried out in November 2016 and February 2017, proved that even larger areas can be mapped efficiently with SOFIA/upGREAT and lead to the discovery of Orion's Dragon, the nickname of the cropped rotated [C II] data cube of the Orion Nebula complex that is shown in Figure 1.7.

1.5 Thesis outline

Feedback by massive stars is key to understanding the evolution of the interstellar medium of galaxies. In this thesis, I have studied the mechanical and radiative response of molecular clouds on stellar energy input in the Orion molecular cloud, the closest region of massive star formation in our Galaxy.

In Chapter 2 of this thesis, we analyze the velocity-resolved [C II] emission from L1630, comprising the Horsehead Nebula, in the Orion B molecular cloud. We study the characteristics of the PDR gas created by the FUV radiation from the approaching illuminating O9.5V star σ Ori on the surface of this cloud. We compare the SOFIA/upGREAT [C II] emission to *Spitzer*/IRAC 8 μm emission of FUV-irradiated polycyclic aromatic hydrocarbons (PAHs), *Herschel*/PACS and SPIRE FIR continuum emission of warm dust, and IRAM 30m CO(1-0) emission of the molecular gas to determine the origin of [C II] emission.

In Chapter 3, we study the [C II] emission, observed with SOFIA/upGREAT, from the M42 and EON region and demonstrate that the mechanical energy input by the stellar wind from θ^1 Ori C has created a 4 pc diameter bubble that is expanding rapidly with a velocity of $13\,\mathrm{km\,s^{-1}}$.

In Chapter 4, we study the expanding shells of M43 and NGC 1977 created by the respective ionizing stars. The expansion velocity of these bubble is much less than for M42. This reflects the weak stellar winds from these somewhat less massive stars and, in contrast to M42, expansion here is driven by the thermal pressure of the ionized gas.

In Chapter 5 and 6, we analyze the relation between the [C II] emission and other tracers of the radiative interaction of massive stars with their environment. The emphasis is on deriving quantitative relations that can be used to predict the expected [C II] emission from observations of other tracers, and to assess the use of [C II] emission as a SFR indicator. Chapter 5, in particular, discusses the utility of spatially resolved [C II] observations towards the Orion molecular cloud as a template for extragalactic [C II] studies and the so-called [C II] deficit, that is observed towards extragalactic regions of very high FIR luminosity. Chapter 6 explores the detailed spatial relations between tracers of radiative feedback in M42, M43, and NGC 1977 and links this to PDR physics. This in particular makes use of IRAM 30m CO(2-1) line observations, that are part of the Large Program "Dynamic and Radiative Feedback of Massive Stars" (Goicoechea et al. 2020). Furthermore, we investigate the photoelectric heating efficiency as measured by the [C II] cooling efficiency in relation with properties of PAHs.

1.6 Outlook

In this thesis, I have studied the interaction of a single O7V star with its environment, the structure and characteristics of the neutral shell surrounding the bubble it created. This was complemented by a study of an O9.5V star passing by a molecular cloud and a study of the bubbles surrounding two B1/1.5V stars. We expect that feedback processes will be different in regions that differ in the concentration of massive stars and formation history.

Velocity-resolved [C II] mapping of the starburst region 30 Doradus (the Tarantula Nebula) in the Large Magellanic Cloud (LMC), hosting a cluster of massive stars, will shed light on the processes of stellar feedback in a super-starcluster with ~ 1000 OB stars. Large-scale velocity-resolved [C II] mapping of other star-forming regions, such as the sample of the SOFIA C+ Legacy Program FEEDBACK will allow for a more comprehensive study of the forms and effects of stellar feedback in local sources. The FEEDBACK survey observes 11 galactic high-mass star-forming regions in the [C II] 158 μm and the [O I] 63 μm lines. In total, an area of 6700 arcmin^2 will be covered at an angular resolution of 15.9″ in the [C II] line and 6.3″ in the [O I] line. The 11 observed regions differ in their geometry (ridges, filaments, shells, fragmented or not) and their stellar content (ranging from a single late O star to clusters of a few early O stars with several late O stars, with additional B and Wolf-Rayet stars). The survey aims at investigating the morphology and dynamics of the neutral gas, triggered star formation, the energy input into the ISM by massive stars, PDR physics and chemistry assisted by detailed PDR modelling (complemented by other PDR line observations such as the [C I] 609 μm line and mid- and high-J CO lines, observable with the SOFIA and APEX telescopes), and the formation of filaments, pillars, and globules in the vicinity of massive stars (Schneider et al. 2020).

In addition, the [C II] observations will be complemented by observations of low-J CO rotational lines to study transmission of feedback into the molecular counterpart. While the molecular gas in the Orion Nebula is certainly affected by stellar feedback, as evident for instance by the discovery of hydrodynamic instabilities in the CO(2-1)-emitting gas, this has been difficult to quantify on large scales due to the overwhelming amount of data. More comprehensive techniques need to be applied in order to quantify feedback on the molecular gas and its connection to the neutral gas emitting in [C II]. Such techniques have been developed recently, for instance the histrograms of oriented gradients (HOG) (Soler et al. 2019) and the analysis of turbulent modes (Orkisz et al. 2017). Particularly the transmittance of turbulence, into molecular clouds and into the diffuse interstellar medium, is of importance to the understanding of the evolution of the ISM (Federrath & Klessen 2012; Kim et al. 2013). In the context of the Orion Nebula, the hot gas within the cavity will eventually be vented into the surrounding diffuse medium of the Orion-Eridanus superbubble, thus renewing the turbulence of the dilute gas and mass loading the superbubble's interior.

As we have noted earlier, [O I] 63 μm cooling is important to consider in the Orion Nebula complex. Further studies could endeavor to get a better handle on the physical conditions in the shells by observing the [O I] 63 μm and 145 μm cooling lines. The [O I] 63 μm line is optically thick in most contexts, but the [O I] 145 μm can be employed to trace the column of the emitting gas. Besides for the derivation of physical conditions, the [O I] 63 μm intensity is needed to construct a more reliable semi-empirical relation of the gas heating efficiency depending on the physical conditions. As we have seen, [C II] line profiles in the Orion Nebula complex are rich in components, thus high-

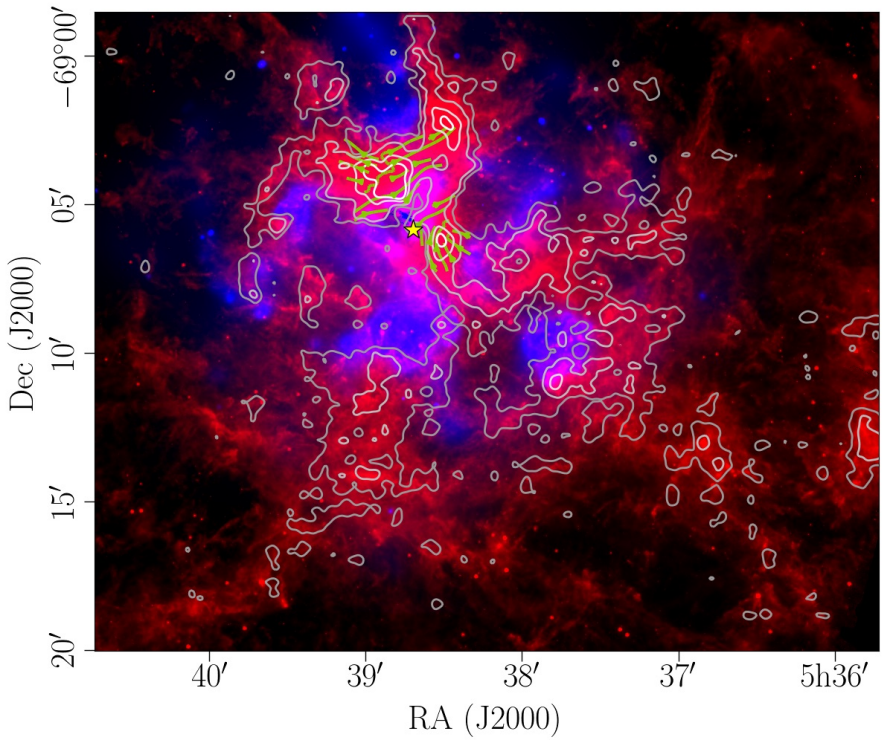

Figure 1.8: [C II] line-integrated intensity towards the starburst region 30 Doradus in the Large Magellanic Cloud (contours, from grey to white: 30, 50, 100, 150 K km s^{-1}) on *Spitzer*/IRAC 8 μm intensity (red) and Chandra X-ray emission (blue). Green streamlines indicate the orientation of the magnetic field lines as measured by SOFIA/HAWC+. The yellow star marks the position of the star cluster R136.

spectral-resolution observations of the [O I] 63 μm and 145 μm lines, as possible with SOFIA/upGREAT, would be required. Also the physical properties and motions of the ionized gas in and adjacent to the shells could be determined using observations of the [NII] FIR lines, for instance the [N II] 205 μm line with SOFIA/4GREAT. Both FIR [O I] line and [N II] line observations could be compared with *Hubble* Space Telescope (HST) optical [O I] 630 nm and [N II] 658 nm observations towards the Orion Nebula to determine the properties of the gas, and hence the amount of stellar feedback and its effect on the geometry of the region, with higher accuracy. The ionized gas could also be traced by hydrogen radio recombination lines (RRLs). Like the [N II] FIR lines, those will be faint towards the cavity of the EON and would require long integration times when observed. Those observations would be possible with the IRAM 30m telescope at Pico Veleta, Spain. The IRAM 30m telescope would be the facility of choice to study molecular line emission from the Orion Nebula in greater detail. While the dense ISF has been studied extensively, the wider molecular background that is affected by the stellar feedback from the massive stars has been less studied. Those studies could reveal important details about the impact of stellar feedback on the natal molecular clouds of massive stars.

One of the least understood aspects of stellar feedback is the role magnetic fields play. Observations of the magnetic field lines, by means of dust polarization measure-

Figure 1.9: Me in front of SOFIA in Palmdale, CA (February 17, 2017).

ments, have become feasible recently with the HAWC+ instrument onboard SOFIA. Magnetic fields build up in compressed gas shells due to flux freezing. The magnetic pressure in the gas counteracts the radiation and gas pressure from the inside of the shell. As such, magnetic fields can inhibit the expansion of shells and thus regulate stellar feedback. SOFIA/HAWC+ observations have been obtained towards the bright filaments close to the stellar cluster R136 in 30 Doradus. In combination with magnetohydrodynamic simulations, combining [C II] line and dust polarization observations will shed light on the magnetic field strength and orientation encountered in such expanding shells. The Davis-Fermi-Chandrasekhar method for determining magnetic field strengths in interstellar gas can then be evaluated numerically. Figure 1.8 shows the [C II] line-integrated intensity towards 30 Doradus and the magnetic field lines from dust polarization on top of the IRAC 8 μm emission and Chandra X-ray emission. The [C II] position-velocity diagrams reveal several expanding bubbles that encircle the hot, X-ray emitting plasma heated by stellar winds and supernovae. Relating the kinetic energies of the shells to the stellar content and the magnetic fields will improve our understanding of the regulation of stellar feedback in a variety of contexts.

1.7 Epilogue

I consider it a great privilege that I was enabled to join not only the flight campaign on observing the [C II] square-degree map, the largest-ever map obtained in [C II] emission, of the Orion Nebula complex, but also the flight series observing the star-forming region 30 Doradus in the Large Magellanic Cloud (LMC). Among my most vivid memories is that of the two faint specks of diffuse starlight that are the Large and the Small Magellanic Cloud, next to the bright band of stars in the Milky Way, seen from the cockpit of SOFIA. But also flying in the crisp morning light above the Sierra Nevada back to Palmdale made an impression. It was amazing, also, what a

sleep-deprived brain is still able to achieve. In summary, I learned a lot, not only about the passion and dedication of those who keep SOFIA running, but of course also a lot about the technical details that are necessary to conduct the precise measurements of far-infrared radiation. And once, when humanity will have been long extinct, and all our knowledge of star-forming processes will be long forgotten, the interstellar horses, dragons, and tarantulas will still shine in all their glory.

2

[C II] emission from L1630 in the Orion B molecular cloud

Abstract

Context: L1630 in the Orion B molecular cloud, which includes the iconic Horsehead Nebula, illuminated by the star system σ Ori, is an example of a photodissociation region (PDR). In PDRs, stellar radiation impinges on the surface of dense material, often a molecular cloud, thereby inducing a complex network of chemical reactions and physical processes.

Aims: Observations toward L1630 allow us to study the interplay between stellar radiation and a molecular cloud under relatively benign conditions, that is, intermediate densities and an intermediate UV radiation field. Contrary to the well-studied Orion Molecular Cloud 1 (OMC1), which hosts much harsher conditions, L1630 has little star formation. Our goal is to relate the [C II] fine-structure line emission to the physical conditions predominant in L1630 and compare it to studies of OMC1.

Methods: The [C II] 158 μm line emission of L1630 around the Horsehead Nebula, an area of $12' \times 17'$, was observed using the upgraded German Receiver for Astronomy at Terahertz Frequencies (upGREAT) onboard the Stratospheric Observatory for Infrared Astronomy (SOFIA).

Results: Of the [C II] emission from the mapped area 95%, 13 $L_\odot$, originates from the molecular cloud; the adjacent H II region contributes only 5%, that is, 1 $L_\odot$. From comparison with other data (CO(1-0) line emission, far-infrared (FIR) continuum studies, emission from polycyclic aromatic hydrocarbons (PAHs)), we infer a gas density of the molecular cloud of $n_{\rm H} \sim 3 \times 10^3\,{\rm cm}^{-3}$, with surface layers, including the Horsehead Nebula, having a density of up to $n_{\rm H} \sim 4 \times 10^4\,{\rm cm}^{-3}$. The temperature of the surface gas is $T \sim 100\,{\rm K}$. The average [C II] cooling efficiency within the molecular cloud is 1.3×10^{-2}. The fraction of the mass of the molecular cloud within the studied area that is traced by [C II] is only 8%. Our PDR models are able to reproduce the FIR-[C II] correlations and also the CO(1-0)-[C II] correlations. Finally, we compare our results on the heating efficiency of the gas with theoretical studies of photoelectric heating by PAHs, clusters of PAHs, and very small grains, and find the heating efficiency to be lower than theoretically predicted, a continuation of the trend set by other observations.

Conclusions: In L1630 only a small fraction of the gas mass is traced by [C II]. Most of the [C II] emission in the mapped area stems from PDR surfaces. The layered edge-on structure of the molecular cloud and limitations in spatial resolution put constraints on our ability to relate different tracers to each other and to the physical conditions. From our study, we conclude that the relation between [C II] emission and physical conditions is likely to be more complicated than often assumed. The theoretical heating efficiency is higher than the one we calculate from the observed [C II] emission in the L1630 molecular cloud.

C. H. M. Pabst, J. R. Goicoechea, D. Teyssier, O. Berné, B. B. Ochsendorf, M. G. Wolfire, R. D. Higgins, D. Riquelme, C. Risacher, J. Pety, F. Le Petit, E. Roueff, E. Bron, A. G. G. M. Tielens

A&A 606, A29 (2017)

2.1 Introduction

One of the main challenges of astronomy and cosmology is to model, and reach an understanding, of the evolution of galaxies and large-scale structure. The star-formation rate (SFR) is a crucial parameter in these models. In order to measure the SFR in distant galaxies, several possible tracers have been and are being studied: ultraviolet (UV) radiation, infrared (IR) radiation, emission from polycyclic aromatic hydrocarbons (PAHs), atomic and molecular lines (e.g., Kennicutt 1998; Kennicutt & Evans 2012). With the advent of the Atacama Large (sub)Millimeter Array (ALMA), it has become popular to use the [C II] 158 μm line as an indicator of the SFR over cosmic history (e.g., Herrera-Camus et al. 2015; Vallini et al. 2015; Pentericci et al. 2016). However, the origin of [C II] emission on a galactic scale is still unclear.

Intuitively, the SFR is expected to depend on the local conditions in the interstellar medium (ISM), the gas and dust that form the environment of stars. The ISM comes in different phases, diffuse gas being the most prevalent. These phases are the cold neutral medium (CNM) with moderate gas densities, $n \sim 30\,\mathrm{cm}^{-3}$, and moderate gas temperatures, $T \sim 100\,\mathrm{K}$, the warm neutral and warm ionized medium (WNM and WIM) with low densities and high temperatures, $n \sim 0.3\,\mathrm{cm}^{-3}$ and $T \sim 8000\,\mathrm{K}$, and the hot ionized medium (HIM) with very low densities and very high temperatures, $n \sim 3 \times 10^{-3}\,\mathrm{cm}^{-3}$ and $T \sim 10^6\,\mathrm{K}$. Most of the gas of the ISM is in the neutral phase. Other ubiquitous components of the ISM are H II regions around massive stars with densities ranging from $n \sim 1\,\mathrm{cm}^{-3}$ to $n \sim 10^5\,\mathrm{cm}^{-3}$ and $T \sim 10^4\,\mathrm{K}$, and molecular clouds with high density and low temperatures, $n \sim 10^3$-$10^8\,\mathrm{cm}^{-3}$ and $T \sim$ 10-30 K (Hollenbach & Tielens 1999). These phases are not isolated from each other, but there is an exchange of matter between them, particularly driven by ionization, winds, and explosions of massive stars. Molecular clouds especially are the birthplaces of new (massive) stars and thereby of vital interest. Meyer et al. (2008) provide a review of star formation in L1630. At the interface between an H II region, ionized by a massive star, and a parental molecular cloud, a photodissociation region (PDR) is formed, where intense stellar UV radiation impinges on the surface of the dense cloud. At the surface of these clouds, the gas is atomic; deeper inside the cloud, the molecular fraction increases. The study of PDRs reveals much about the interplay between stars (including hosts of newly formed stars) and the ISM, thereby yielding valuable insight into the process of star formation (see Hollenbach & Tielens (1999) for a review of PDRs).

The ISM is mainly heated by stellar radiation, specifically by far-ultraviolet (FUV) radiation with energies between 6 and 13.6 eV. The characteristics of the gas cooling allow us to infer the amount and, possibly, the source of the heating. One of the main coolants of the cold neutral medium is the [C II] $^2P_{3/2}$-$^2P_{1/2}$ fine-structure line at $\lambda \simeq 158\,\mu$m, that is, $\Delta E/k_B \simeq 91.2\,\mathrm{K}$. The [C II] line is also one of the brightest lines in PDRs, carrying up to 5% of the total far-infrared (FIR) luminosity, the other 95% mainly stemming from UV irradiated dust. Carbon has an ionization potential of 11.3 eV, hence C^+ traces the transition from H^+ to H and H_2. Another important coolant is the [O I] line at $\lambda \simeq 63\,\mu$m ($\Delta E/k_B \simeq 228\,\mathrm{K}$). The ratio of those two main coolants depends on the temperature and density of the gas. For $T = 100\,\mathrm{K}$, the [O I] cooling efficiency overtakes the [C II] cooling efficiency at $n \simeq 3 \times 10^4\,\mathrm{cm}^{-3}$; at $n = 3 \times 10^3\,\mathrm{cm}^{-3}$, the [O I] contribution to the total cooling is about 5% (cf. Tielens 2010).

The [C II] line has been studied in a variety of environments. Important contribu-

tions may come from diffuse clouds (CNM), dense PDRs, surfaces of molecular clouds, and (low-density) ionized gas including the WIM (Wolfire et al. 1995; Ossenkopf et al. 2013; Gerin et al. 2015, e.g.,)). Langer & Penzias (1990) identify warm CO-dark molecular gas in Galactic diffuse clouds by means of [C II] emission. Jaffe et al. (1994) conducted an earlier study observing the extended [C II] emission from the Orion B molecular cloud (L1630). This study is preceded by a [C II] survey of the Orion Molecular Cloud 1 (OMC1) in Orion A by Stacey et al. (1989). Goicoechea et al. (2015b) present a velocity-resolved [C II] map toward OMC1, observed by the Heterodyne Instrument for the Far-Infrared (HIFI) onboard the *Herschel* satellite in 2012. Velocity-resolved [C II] and [^{13}C II] emission from the star-forming region NGC 2024 in L1630 was observed in 2011 using the GREAT (German Receiver for Astronomy at Terahertz Frequencies) instrument onboard the airborne Stratospheric Observatory for Infrared Astronomy (SOFIA) and analyzed by Graf et al. (2012); the neighboring reflection nebula NGC 2023 was observed in 2013/14 using the same instrument. Sandell et al. (2015) discussed the physical conditions, morphology, and kinematics of that region. A theoretical study on collisional excitation of the [C II] fine-structure transition was performed by Goldsmith et al. (2012). The GOT C^+ survey (Galactic Observations of Terahertz C^+) survey (Pineda et al. 2014), also a Herschel/HIFI study, investigated specifically the relationship between [C II] luminosity and SFR. This study found a good correlation on Galactic scales. This was also established by Stacey et al. (2010) and Herrera-Camus et al. (2015) at low and high redshift.

On December 11, 2015, a part of the Orion B molecular cloud, including the Horsehead Nebula, was observed in [C II] with the upGREAT instrument, the first multi-pixel extension of GREAT, onboard SOFIA, as presented and described in Risacher et al. (2016). The survey was conducted "to demonstrate the unique and important scientific capabilities of SOFIA, and to provide a publicly available high-value SOFIA data set".[1] It allows us to study [C II] emission and its correlations with other astrophysical tracers under moderate conditions (intermediate density and moderate UV-radiation field), as opposed to the high density and intense UV-radiation field in OMC1.

In the present study, we analyze the [C II] emission from a $12' \times 17'$ area of the L1630 molecular cloud in Orion B that is illuminated by the nearby star system, σ Ori. Our distance to the star system is approximately 334 pc, which we also assume to be the distance to the molecular cloud. The projected distance between the star system and the molecular cloud is 3.2 pc (Ochsendorf et al. 2014, and references therein). Part of the mapped area, in which star formation is low, is the well-known Horsehead Nebula. The star-forming regions NGC 2023 and NGC 2024 are adjacent to the mapped area, but not included. We compare the velocity-resolved [C II] SOFIA/upGREAT observations with new CO(1-0) observations of the molecular gas obtained with the 30 m telescope (Pety et al. 2017) at the Institut de Radioastronomie Millimétrique (IRAM), with *Spitzer*/Infrared Array Camera (IRAC) studies of the PAH emission from the PDR surfaces, Hα observations of the ionized gas, and with existing far-infrared continuum studies using *Herschel*/Photoconductor Array Camera and Spectrometer (PACS) and Spectral and Photometric Imaging Receiver (SPIRE) data to determine dust properties and trace the radiation field. This wealth of data allows us to separate emission from the ionized gas, neutral PDR, and molecular cloud, in order to derive global heating efficiencies and their dependence on the local conditions, and to make detailed

[1] `https://www.sofia.usra.edu/science/proposing-and-observing/proposal-calls/sofia-directors-discretionary-time/horsehead-nebula.`

comparisons to PDR models.

This paper is organized as follows. In Section 2, we present the observations. In Section 3, we divide the surveyed area into regions with specific characteristics. Furthermore, we study the kinematics of the gas as revealed by the SOFIA/upGREAT observations of [C II] emission and the correlation of the various data sets with each other. Section 4 contains a discussion of the results obtained in Section 3 and we derive column densities and other gas properties. We conclude with a summary of our results and an outlook for the future in Section 5.

2.2 Observations

2.2.1 [C II] Observations

The [C II] emission in Orion B (L1630) was observed on December 11, 2015 using the upGREAT instrument onboard SOFIA. The region was observed using the upGREAT optimized on-the-fly mapping mode. The region was split into four tiles, each covering an area of $363'' \times 508.2''$. In this mode, the array is rotated 19.1° on the sky and an on-the-fly (OTF) scan is undertaken. By performing a second scan separated by $5.5''$ perpendicular to the scan direction, it is possible to fully sample a region $72.6''$ wide along the scan direction (cf. Risacher et al. 2016, for details). By combining OTF scans in the RA and Dec direction, it is possible to cover the map region with multiple pixels. Each tile was made up of ten x-direction OTF scans and 14 y-direction OTF scans. A spectrum was recorded every $6''$. Scans in the x-direction had an integration time of 0.4 s, while those in the y-direction had an integration time of 0.3 s. Since the y-scan length is longer than the x-scan length, the integration time was reduced. This is due to Allan variance stability time limits of 30 seconds. A reference position at about $12'$ to the west of the map was observed, which was verified to be free of ^{12}CO(2-1) and ^{13}CO(2-1) emission with the James Clerk Maxwell Telescope (JCMT) (G. Sandell, priv. comm.). The reference position was checked to be free of [C II] emission to a 1 K level. A supplementary OFF contamination check was undertaken whereby the reference position was calibrated using the internal HOT reference measurement; these spectra also showed no evidence of OFF emission to a 1 K level. The [C II] map itself, showing no "absorption" features anywhere, confirms that there cannot be notable [C II] emission at the reference position. An OFF measurement is ideally taken after 30 s of ON source integration to avoid drift problems in the calibrated data. For this observing run, each tile was observed twice in the x- and y-directions, resulting in a total integration time per map pixel of 1.4 s. For a spectral resolution of $0.19\,\mathrm{km\,s^{-1}}$, this results in a noise rms in the final data cube of 2 K in the velocity channels free of emission.

The data cube provided by the SOFIA Science Center was processed using the Grenoble Image and Line Data Analysis Software[2]/Continuum and Line Analysis Single-dish Software (GILDAS/CLASS). We subtract a baseline of order one from the spectra. The spectral data were integrated over the velocity range (with respect to the Local Standard of Rest, LSR) $v_{\mathrm{LSR}} = 6\text{-}20\,\mathrm{km\,s^{-1}}$ to obtain the line-integrated intensity, which is shown in Fig. 2.1. Channel maps are shown in Fig. 2.4. The spatial resolution of our final maps is $15.9''$. For comparison with other tracers, we

[2]See `http://www.iram.fr/IRAMFR/GILDAS` for more information about the GILDAS softwares (Pety 2005).

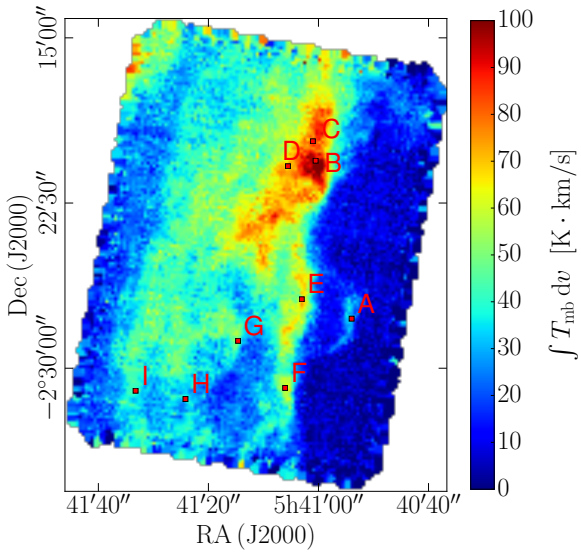

Figure 2.1: [C II] line-integrated intensity; points indicate positions where individual spectra are extracted for illustrative purposes (see Section 2.3.3).

use a Gaussian kernel for convolution. At the rim of the map, the [C II] signal suffers from noise and we ignore an outer rim of 45″ in our analysis.

2.2.2 Dust SED Analysis

In this study we make use of the dust temperature and dust optical depth maps released by Lombardi et al. (2014). Lombardi et al. (2014) fit a spectral energy distribution (SED) to *Herschel*/PACS and SPIRE observations of the Orion molecular cloud complex in the PACS 100 μm and 160 μm, and SPIRE 250 μm, 350 μm, and 500 μm bands. The photometric data, convolved to the SPIRE 500 μm 36″ resolution, are modeled as a modified blackbody,

$$I(\lambda) = B(\lambda, T_\mathrm{d})\, \tau_0 \left(\frac{\lambda_0}{\lambda}\right)^\beta , \tag{2.1}$$

with T_d the effective dust temperature, τ_0 the dust optical depth at the reference wavelength λ_0, and β the grain-emissivity index. Lombardi et al. (2014) use the all-sky β map with 35′ resolution by the Planck collaboration, interpolated to the grid on which the SED is performed; only the effective dust temperature and τ_0 are free parameters in this fit. The β map shows a smooth increase of about 3% from the north-east to the south-west in the area surveyed in [C II], with a mean of 1.56. Lombardi et al. (2014) present their dust optical depth map at $\lambda_0 = 850\,\mu$m, following the Planck standard, but for our analysis we convert τ_{850} to τ_{160} using the β data. We integrate Eq. (6.1) from $\lambda_\mathrm{min} = 20\,\mu$m to $\lambda_\mathrm{max} = 1000\,\mu$m to obtain the far-infrared intensity I_FIR.

We notice that the Horsehead PDR has comparatively low dust temperature in the SED fit, $T_\mathrm{d} \simeq$ 20-22 K. This could be due to beam dilution. In the models of Habart

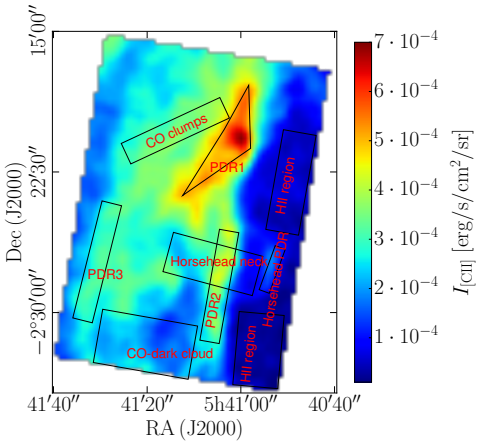

Figure 2.2: [C II] line-integrated intensity convolved to 36″ resolution with selected regions (see Section 2.3.2) indicated.

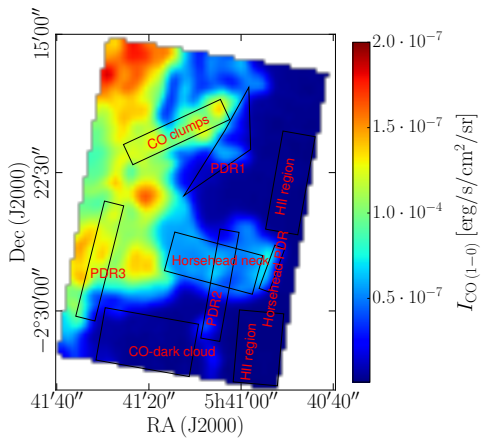

Figure 2.3: CO(1-0) line-integrated intensity convolved to 36″ resolution with selected regions (see Section 2.3.2) indicated.

et al. (2005), the dust temperature is $T_{\rm d} \simeq 30\,{\rm K}$ at the edge, dropping to $T_{\rm d} \simeq 22\,{\rm K}$ for a hydrogen nucleus gas density of $n_{\rm H} = 2 \times 10^4\,{\rm cm}^{-3}$ within 12″, and to $T_{\rm d} \simeq 13.5\,{\rm K}$ for $n_{\rm H} = 2 \times 10^5\,{\rm cm}^{-3}$. Throughout this paper, by "gas density" we mean the hydrogen nucleus gas density: $n_{\rm H} = n_{\rm H\,I} + 2\,n_{\rm H_2}$.

The derived effective dust temperature and dust optical depth can depend significantly on the choice of β: The temperature can be up to 3-4 K lower if $\beta = 2$ instead of $\beta = 1.5$; τ_{160} then increases by a factor of two. The FIR intensity is less sensitive to β: it only decreases by 10% for $\beta = 2$.

Furthermore, we employ *Spitzer*/IRAC observations in the 8 μm band, which is dominated by PAHs but which can be influenced by very small grains. We use a super mosaic image retrieved from the Spitzer Heritage Archive, created October 22, 2012. We also make use of the 850 μm observations from the Submillimetre Common-User Bolometer Array 2 (SCUBA-2) around NGC 2023/2024 first presented by Kirk et al. (2016) as part of the JCMT Gould Belt Survey (GBS). These trace dense regions within the molecular cloud. However, we do not use the map reduced by the GBS group, but we retrieved the data from the Canadian Astronomy Data Centre (CADC) archive, processed on October 1, 2015.

2.2.3 CO(1-0) Observations

In this work we make use of part of the ^{12}CO(1-0) large-scale map at 115.271 GHz obtained by Pety et al. (2017) with the Eight Mixer Receiver (EMIR) 090 at the IRAM 30 m telescope. The fully sampled on-the-fly line maps were taken with a channel spacing of 195 kHz (a velocity resolution of $\sim 0.5\,{\rm km\,s}^{-1}$). CO-emission contamination from the reference position was eliminated by adding dedicated frequency-switched line observations of the reference position itself (see Pety et al. (2017) for details). The median noise levels range from 100 to 180 mK (in the $T_{\rm mb}$ scale) per resolution channel. Here we use the CO(1-0) line-integrated intensity map in the $v_{\rm LSR}$ = 9-16 $\,{\rm km\,s}^{-1}$

range[3], convolved to the 36″ angular resolution of SPIRE 500 μm. The resulting map is shown in Fig. 2.3.

2.2.4 Hα Observations

In this study we use the Hα image of the Horsehead Nebula and its environs in L1630 and the H II region IC 434 taken by the Mosaic 1 wide field imager on Kitt Peak National Observatory (KPNO). For calibration of the KPNO image, we use Hα data of the Horsehead Nebula collected by the Hubble Space Telescope as part of the Hubble Heritage program. We obtained the image from the archive of the National Optical Astronomy Observatory (NOAO), but it was taken as part of the program presented in Reipurth et al. (1998).

The bright star at 05h41′02.70″, −02°18′17.77″ in the Hα image is a foreground star; it is visible in the IRAC 8 μm image, as well. We masked it before convolution, such that it does not show in the convolved images.

2.3 Analysis

2.3.1 Kinematics: velocity channel maps

Perusing the [C II] channel maps from 8.0 km s^{-1} to 16.0 km s^{-1} shown in Fig. 2.4, we recognize several continuous structures in space-velocity. From 10.5-11.5 km s^{-1}, we observe a [C II] front that runs from the south-east to the north-west of the map. From 12.5-14.0 km s^{-1}, a front runs from the north to the south. The Horsehead mane is visible from 10.0-11.5 km s^{-1}. From 12.5-13.0 km s^{-1}, an intermediate [C II] front lights up. Based on the kinematic behavior and assuming that [C II] emission is related to PDR surfaces, we divide the [C II] fronts into four groups: PDR1 in the north-west of the molecular cloud, PDR2 in the south-west, PDR3 in the south-east, and the Horsehead PDR. The intermediate PDR front we do not discuss in detail.

In the luminous north, an almost circular cavity forms in the center of the region of highest intensity. Its boundary lights up in the 14.0 km s^{-1} map. In the 12.5 km s^{-1} and 13.0 km s^{-1} channels, we see bright emission where the rim of the cavity is. This cavity appears quite clearly in the unconvolved IRAC 8 μm image (see Fig. 2.15). Comparison with the 8 μm map reveals a (proto-)star at the northern edge of the bubble. This star is visible in the Hα image as well, but it is not identified as a pre-main-sequence (PMS) object in Mookerjea et al. (2009). Here it is listed as MIR-29, a more evolved star in the vicinity of NGC2023, identified by the Two Micron All Sky Survey (2MASS). In addition to the main emission in the velocity range $v_{\rm LSR}$ = 6-20 km s^{-1}, we see a faint [C II] component at $v_{\rm LSR} \simeq 5$ km s^{-1}, that has also been detected in CO observations by Pety et al. (2017). Due to its faintness, however, we will ignore it in our analysis.

2.3.2 Global morphology

Apart from the four PDR surfaces discussed in Section 2.3.1, we singled out other specific regions that stand out in their morphology in the respective quantities [C II],

[3]The integration range is truncated at $v_{\rm LSR} = 9$ km s^{-1} to avoid contamination from a second CO component at $v_{\rm LSR} \sim 5$ km s^{-1} (cf. Pety et al. 2017).

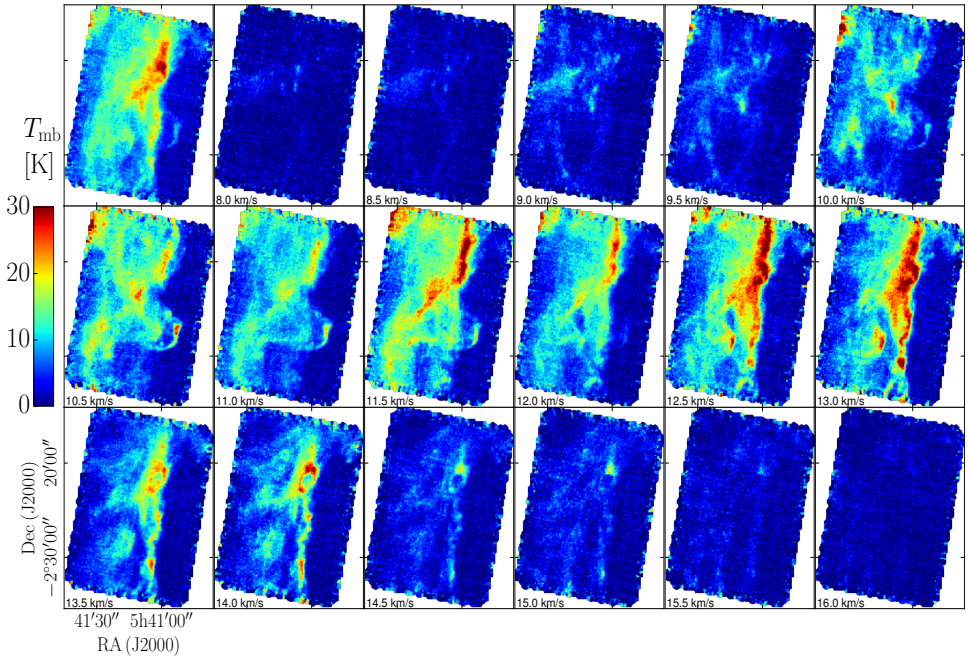

Figure 2.4: [C II] channel maps from $8.0\,\mathrm{km\,s^{-1}}$ to $16.0\,\mathrm{km\,s^{-1}}$ in steps of $\mathrm{d}v = 0.5\,\mathrm{km\,s^{-1}}$ at 15.9″ resolution. The main-beam temperature $T_{\rm mb}$ is averaged over the step size $\mathrm{d}v$. The first panel shows the line-integrated intensity.

CO, and IRAC 8 μm emission (see Fig. 5.2). The 8 μm emission is a tracer of UV-pumped polycyclic aromatic hydrocarbons (PAHs) and therefore of PDR surfaces. Ionized gas is traced by Hα emission and CO traces the molecular hydrogen gas. The regions are indicated in Figs. 2.2 ([C II] map) and 2.3 (CO(1-0) map). We outline the boundary between the H II region IC 434 and the molecular cloud L1630 by the onset of significant [C II] emission at the molecular cloud surface where we also have been guided by the Hα contour of highest emission (see Fig. 2.18).

The four PDR regions, among them the Horsehead PDR[4], are distinct in the IRAC 8 μm map. The Horsehead PDR is not the most luminous part of the region in all maps. The brightest part is region PDR1. We define the neck of the Horsehead Nebula that is traced by the CO(1-0) line; in itself, it has little [C II] emission, but part of it is covered by the [C II]-emitting molecular cloud. Another part of the cloud, where there is little CO emission, we call CO-dark cloud. Deeper inside the molecular cloud, CO emission is high and we define a region of CO cores or clumps. The Horsehead PDR is likely to suffer from beam dilution in all images, since its scale length is found to be less than 10″ (Habart et al. 2005), which is smaller than the beam sizes in question. To the north-east of the map, we recognize the reflection nebula NGC 2023, which has been studied with SOFIA/GREAT in [C II] emission by Sandell et al. (2015). This region will not be discussed here.

Figure 5.2a shows the FIR intensity with [C II] contours in the mapped area. The FIR intensity peaks close to [C II] in the most luminous part (PDR1), but slightly deeper into the cloud. The Horsehead mane is bright in both [C II] and FIR; the

[4]What we call PDR here really is the PDR surface.

Table 2.1: Mean values (standard deviation between brackets) of several quantities in the several regions ($\eta = I_{[\mathrm{C\,II}]}/I_{\mathrm{FIR}}$).

Region	$\bar{\eta}$ [10^{-2}]	$\bar{I}_{[\mathrm{C\,II}]}$ [$\mathrm{erg\,s^{-1}\,cm^{-2}\,sr^{-1}}$]	$\bar{I}_{\mathrm{CO\,(1\text{-}0)}}$ [$\mathrm{erg\,s^{-1}\,cm^{-2}\,sr^{-1}}$]	$\bar{I}_{\mathrm{FIR}}$ [$\mathrm{erg\,s^{-1}\,cm^{-2}\,sr^{-1}}$]	$\bar{\tau}_{160}$ [10^{-3}]
L1630	1.3(0.5)	$2.8(1.6) \times 10^{-4}$	$6.5(4.9) \times 10^{-8}$	$2.5(1.2) \times 10^{-2}$	4.9(6.3)
Horsehead PDR	1.0(0.3)	$1.5(0.3) \times 10^{-4}$	$4.3(1.5) \times 10^{-8}$	$1.5(0.5) \times 10^{-2}$	5.1(2.6)
PDR1	1.1(0.3)	$5.5(0.5) \times 10^{-4}$	$3.2(1.6) \times 10^{-8}$	$5.2(0.9) \times 10^{-2}$	2.2(0.4)
PDR2	2.2(0.4)	$3.5(0.6) \times 10^{-4}$	$3.5(1.9) \times 10^{-8}$	$1.7(0.5) \times 10^{-2}$	2.5(2.0)
PDR3	1.1(0.2)	$2.9(0.2) \times 10^{-4}$	$10(3.0) \times 10^{-8}$	$2.9(0.6) \times 10^{-2}$	6.9(3.7)
CO-dark cloud	1.3(0.1)	$1.9(0.4) \times 10^{-4}$	$0.7(0.4) \times 10^{-8}$	$1.7(0.4) \times 10^{-2}$	0.9(0.2)
CO clumps	1.1(0.1)	$3.5(0.4) \times 10^{-4}$	$11(1.6) \times 10^{-8}$	$3.1(0.6) \times 10^{-2}$	4.5(1.3)
H II region	1.9(0.5)	$0.6(0.3) \times 10^{-4}$	$0.4(0.2) \times 10^{-8}$	$0.3(0.1) \times 10^{-2}$	0.7(0.2)

Notes. Mean values (standard deviation between brackets) of several quantities in the several regions ($\eta = I_{[\mathrm{C\,II}]}/I_{\mathrm{FIR}}$). L1630 is the entire molecular cloud (without H II region) in the mapped area. Face-on values are values calculated from integration along the depth into the cloud from the surface with respect to the incident FUV radiation (see Appendix 2.B).

emission overlaps very well. PDR2 is more pronounced in [C II] emission than in the FIR. PDR3 can only be surmised in I_{FIR}, but it cannot be distinguished very clearly in the integrated [C II] map either.

In Fig. 5.2b, we compare the 8 μm emission with [C II] in contours. The 8 μm emission behaves in a similar way as I_{FIR}, but structures stand out more decidedly. The 8 μm emission, too, peaks slightly deeper into the cloud than [C II]. The bright regions in the Horsehead mane overlap; in both maps it is a thin filament. PDR2 is more pronounced in [C II], but is distinguishable in $I_{8\,\mu\mathrm{m}}$ as well. PDR3 is more distinct in $I_{8\,\mu\mathrm{m}}$.

The CO(1-0) emission in the mapped area does not resemble the pattern of [C II] emission (Fig. 5.2c). In CO, the entire Horsehead and its neck light up with nearly equal intensity while the surroundings remain dark. PDR1 and 2 are not very bright in CO. Interestingly, there is a CO spot in PDR1, right where the cavity is observed in (unconvolved) [C II] and 8 μm emission (see Figs. 2.4 and 2.15, respectively). A "finger" of CO emission, the "CO clumps", points towards PDR1. PDR3 can be inferred as shadow in CO emission, that is, a ridge of low CO emission.

The τ_{160} map (Fig. 5.2d) resembles the CO(1-0) map. The Horsehead and its neck have higher dust optical depth than their surroundings; the material directly behind the mane is a peak in τ_{160}, that overlaps partially with the [C II] peak, but it peaks slightly deeper into the Horsehead. The [C II] peak in PDR1 does not correspond to a peak in dust optical depth, although the onset of the molecular cloud is traced by an increase in τ_{160}. PDR3 corresponds to an optically thin region compared to its environment. The region of highest dust optical depth at the eastern border of the map (not containing NGC 2023) corresponds to a region with little [C II] emission, but high CO emission. The CO "finger" relates to enhanced dust optical depth.

PDR1 and PDR2 border on the H II region, as can be seen from Fig. 5.2e. PDR2 overlaps with a region of significant Hα emission, tracing the ionized gas at the surface of the molecular cloud. The Hα map and the logarithmic [C II] cooling efficiency $I_{[\mathrm{C\,II}]}/I_{\mathrm{FIR}}$ map (Fig. 5.2f) resemble each other. High [C II] over FIR intensity ratios are found near the boundary with high Hα emission. However, $I_{[\mathrm{C\,II}]}/I_{\mathrm{FIR}}$ is a misleading measure in the H II region, since I_{FIR} does not trace the radiation field well here and $I_{[\mathrm{C\,II}]}$ is sufficiently low to be significantly affected by noise. Variations in $I_{[\mathrm{C\,II}]}/I_{\mathrm{FIR}}$

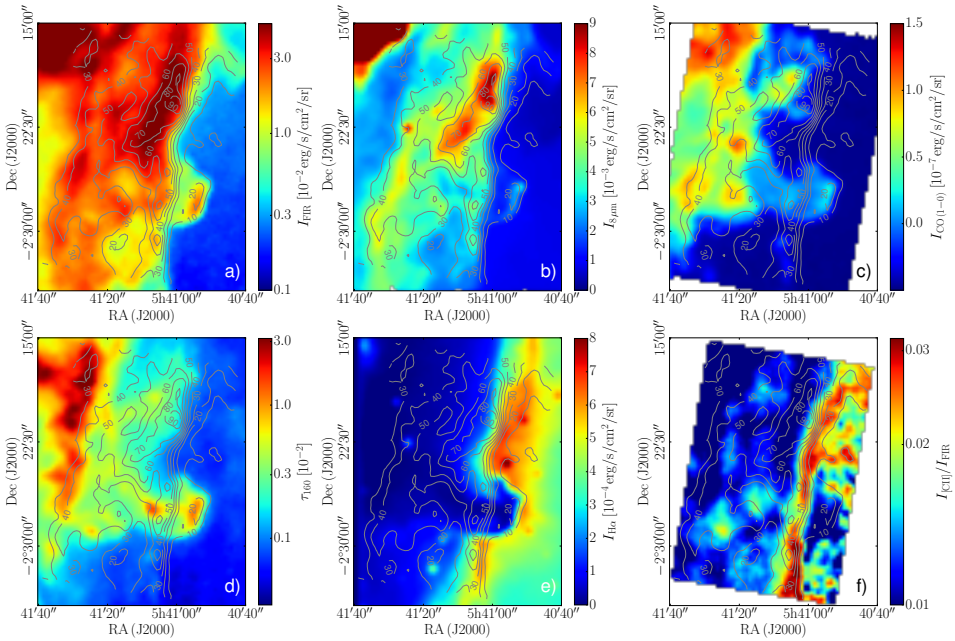

Figure 2.5: Different quantities with [C II] emission in units of K km s^{-1} in contours: $I_{\rm FIR}$ tracing the UV radiation field re-radiated in the FIR by dust particles, $I_{8\,\mu m}$ tracing the UV radiation field by fluorescence of PAHs, $I_{\rm CO\,(1\text{-}0)}$ tracing the molecular gas, τ_{160} tracing the dust column, $I_{\rm H\alpha}$ emitted by ionized gas, and, finally, the ratio $I_{\rm [C\,II]}/I_{\rm FIR}$. All maps are convolved to 36″ spatial resolution and re-gridded to a pixel size of 14″, that of the SPIRE 500 μm map.

across the map span a range from 3×10^{-3} up to 3×10^{-2}. Table 2.1 lists the mean values of the [C II] cooling efficiency $\eta = I_{\rm [C\,II]}/I_{\rm FIR}$, [C II] intensity $I_{\rm [C\,II]}$, CO(1-0) intensity $I_{\rm CO(1\text{-}0)}$, FIR intensity $I_{\rm FIR}$, and dust optical depth τ_{160} for the several regions defined above.

2.3.3 Kinematics: velocity-resolved line spectra

Figure 2.6 displays spectra extracted towards different positions in the map, as indicated in Fig. 2.1. The positions are chosen as representative single points for the different regions we identified earlier. Details on the spectra, that is, peak position, peak temperature, and line width, are given in Table 2.2. Point A represents the Horsehead mane, B lies in the most luminous part of the map, C just north of it, whereas D is displaced to the east; all three represent PDR1. We chose additional points in PDR1, because B might be affected by the bubble structure discussed later. Point E lies in PDR2 behind the Horsehead and F in the southern part of PDR2. Point G is located in the intermediate PDR front which we do not discuss in detail. Point I represents PDR3, whereas H is chosen in the CO-dark cloud, where there is little [C II] emission (and little emission in other tracers).

The spectrum taken towards the Horsehead PDR (point A) shows a narrow line. Opposed to this is the line width of the spectrum extracted towards the most luminous part of the molecular cloud, point B: Here, the line is broadened. It peaks at a slightly

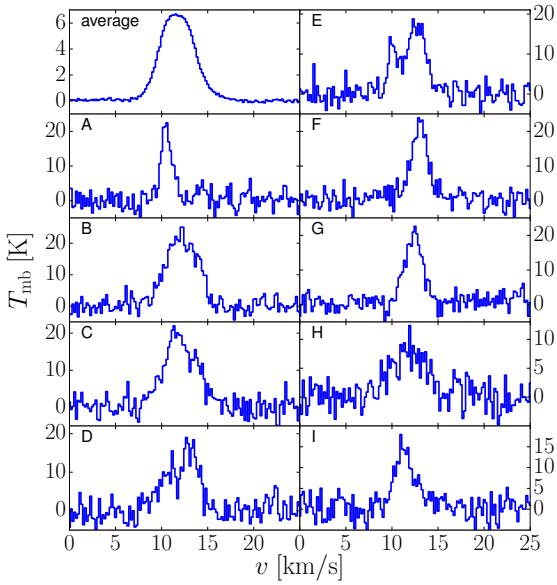

Figure 2.6: Line spectra towards points A–I with average spectrum over the entire map (including H II region) in *the top left panel*. Point A corresponds to the Horsehead PDR, points B to D are located in PDR1, points E and F lie in PDR2, point G represents the intermediate PDR front, point H is located in a region of little [C II] emission, and point I represents PDR3.

higher velocity than the Horsehead PDR. From comparison with the dust optical depth, we conclude that the broadening of the line is not due to a high column density (if dust density and gas density are related). The same holds for point C in PDR1. Here there appears a small side peak at higher velocity, which could also be inferred for point B (as a shoulder). Point D evidently has a spectrum with two peaks. From the distinctly different morphology of the channel maps at the two peak velocities (cf. Fig. 2.4 at $10.5\,\mathrm{km\,s^{-1}}$ and $13.0\,\mathrm{km\,s^{-1}}$), we surmise that the two peaks correspond to two distinct emitting components, rather than to one emission component with foreground absorption. The same goes for point E in PDR2, which also has two peaks. The southern part of PDR2, point F, has only one rather narrow peak. The intermediate PDR, point G, exhibits a strong narrow line, as well. The spectrum taken in the western PDR, point I, shows a somewhat broader line with somewhat lower intensity. At point H, where the intensity is low in all tracers, the [C II] line is also broader.

Strikingly, the peak velocity of point D is shifted towards lower velocity by $1\,\mathrm{km\,s^{-1}}$ with respect to points B and C (all PDR1). However, one component of this spectrum lies at about $11\,\mathrm{km\,s^{-1}}$, which is also the velocity of PDR3 (point I). This is further evidence that PDR3 and a part of PDR1 are spatially connected, as concluded from the channel maps. Point D in PDR1 has a component at about $13\,\mathrm{km\,s^{-1}}$, which is the velocity of PDR2. In B and C (PDR1) this component might be hidden beneath the strong side peak at $14\,\mathrm{km\,s^{-1}}$. The affiliation of the second component at point E in PDR2 is unclear; there might be another layer of gas behind or in front of the main component, or it could originate from the gas of PDR1 and PDR3 at $11\,\mathrm{km\,s^{-1}}$.

Table 2.2: Results from Gaussian fit (points B–E with two components) to individual spectra with a spatial resolution of 15.9″ sampled at 7.55″.

pos.	RA (J2000)	Dec (J2000)	v [km s^{-1}]	$T_{\rm P}$ [K]	FWHM [km s^{-1}]
A	5h40′53″	−2°27′37″	10.5	21.1	1.4
B	5h41′00″	−2°20′27″	12.0	22.5	3.6
			14.2	6.9	1.2
C	5h41′00″	−2°19′34″	11.3	6.1	1.2
			12.2	16.2	4.6
D	5h41′05″	−2°20′42″	10.7	9.5	2.7
			13.2	16.1	1.9
E	5h41′02″	−2°26′44″	10.0	12.4	1.1
			12.6	17.4	2.5
F	5h41′06″	−2°30′46″	13.0	21.9	2.1
G	5h41′14″	−2°28′38″	12.4	20.3	2.3
H	5h41′33″	−2°30′53″	11.8	8.1	4.5
I	5h41′24″	−2°31′16″	11.3	13.9	2.6

Notes. Positions are indicated in Fig. 2.1. Listed are the velocity of the peak, the peak temperature, and the full width at half maximum (FWHM) of the peak. Note to spectrum I: From a Lorentzian fit we obtain $T_{\rm P} = 15.6$ K, which fits the spectrum better by eye; velocity and FWHM are similar.

2.3.4 Edge-on PDR models

We supplement the correlation plots in the following section with model runs that are based on the PDR models of Tielens & Hollenbach (1985), with updates like those found in Wolfire et al. (2010) and Hollenbach et al. (2012). We include the most recent computations on fine-structure excitations of C^+ by collisions with H by Barinovs et al. (2005) and with H_2 by Wiesenfeld & Goldsmith (2014), and adopt a fractional gas-phase carbon abundance of 1.6×10^{-4} (Sofia et al. 2004). The line intensities are calculated for an edge-on case by storing the run of level populations with molecular cloud depth for the excited level of CO and C^+ as calculated in the face-on model. For each line of sight, the intensity is found from integrating eq. (B14) in Tielens & Hollenbach (1985) through the layer of length $z = N_{\rm H}/n_{\rm H}$ with the gas column density $N_{\rm H}$ and the gas density $n_{\rm H}$, where we replace the factor $(2\pi)^{-1}$ for a semi-infinite slab with $(4\pi)^{-1}$. The cooling rate is given by eq. (B1) in Tielens & Hollenbach (1985) in the limit of no background radiation. For the escape probability we take the line-of-sight formulation

$$\beta(\tau) = \frac{1 - e^{-\tau}}{\tau}, \tag{2.2}$$

where τ is the line optical depth calculated as in eq. (B8) in Tielens & Hollenbach (1985).

The FIR continuum intensity in the edge-on case is calculated from the run of dust temperature with depth into the molecular cloud. We find the dust temperature, $T_{\rm d}$, from the prescription given in Hollenbach et al. (1991). We integrate the dust

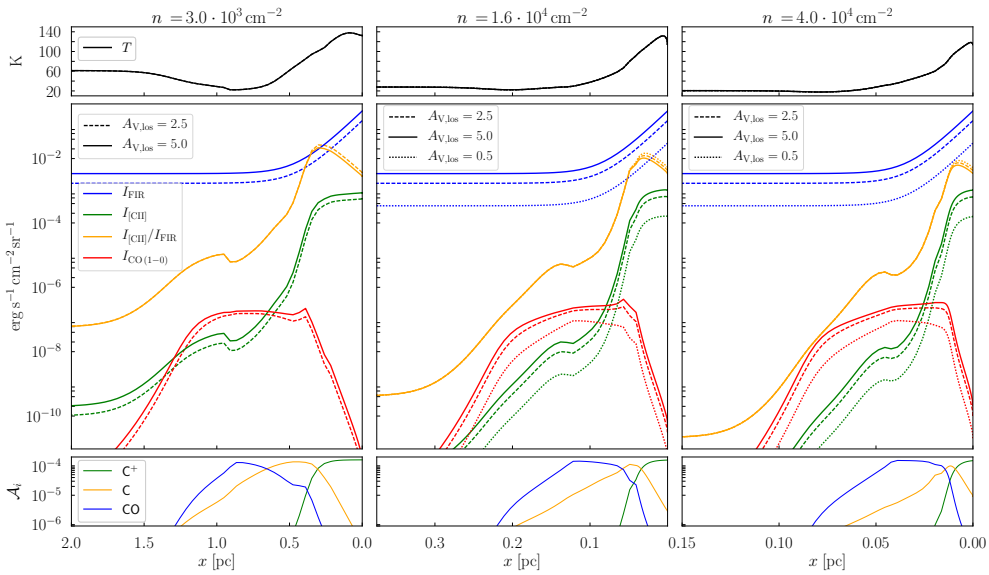

Figure 2.7: Results of our edge-on models described in Section 6.3.3. The panels show the gas temperature T (*upper panels*), I_{FIR}, $I_{[\mathrm{C\,II}]}$, $I_{[\mathrm{C\,II}]}/I_{\mathrm{FIR}}$, and $I_{\mathrm{CO(1\text{-}0)}}$ (*middle panels*) and C^+, C, and CO fractional abundances (lower panel) versus physical scale, for the gas densities $n_{\mathrm{H}} = 3.0 \times 10^3\,\mathrm{cm}^{-3}$, $1.6 \times 10^4\,\mathrm{cm}^{-3}$, $4.0 \times 10^4\,\mathrm{cm}^{-3}$ (*left to right panels*), and $A_{\mathrm{V,los}} = 0.5$, 2.5, and 5.0. We note that the gas temperature does not vary with $A_{\mathrm{V,los}}$.

absorption efficiency, Q_{abs}, through the layer of length z

$$I_{\mathrm{FIR}} = \frac{1}{4\pi} \int 4\pi a^2 \, \frac{n_{\mathrm{d}}}{n_{\mathrm{H}}} Q_{\mathrm{abs}} \, \sigma T_{\mathrm{d}}^4 \, n_{\mathrm{H}} \, \mathrm{d}z, \tag{2.3}$$

where we take the grain size $a = 0.1\,\mu\mathrm{m}$, and $n_{\mathrm{d}}/n_{\mathrm{H}} = 6.36 \times 10^{-12}$, which gives a grain cross section per hydrogen atom of $2.0 \times 10^{-21}\,\mathrm{cm}^2$. For Q_{abs} we use the average silicate and graphite value $Q_{\mathrm{abs}} = 1.0 \times 10^{-6} (a/0.1\,\mu\mathrm{m})(T_{\mathrm{d}}/\mathrm{K})^2$ from Draine (2011).

In Fig. 6.6, we present the results of the models with an incident FUV intensity of $G_0 = 100$ appropriate for σ Ori (Abergel et al. (2003) and references therein) and a Doppler line width of $\Delta v = 1.5\,\mathrm{km\,s}^{-1}$ for different densities on a physical scale. The x-axes share the same range of visual extinction, $A_{\mathrm{V}} = 0.0$-9.3. We computed models for gas densities $n_{\mathrm{H}} = 3.0 \times 10^3\,\mathrm{cm}^{-3}$, $1.6 \times 10^4\,\mathrm{cm}^{-3}$, and $4.0 \times 10^4\,\mathrm{cm}^{-3}$; those densities we estimate from the line cuts in Section 2.4.7 for different parts of the molecular cloud. We integrate along a length $A_{\mathrm{V,los}}$ of the line of sight estimated in Section 2.4.4 for each density, where we assumed $N_{\mathrm{H}} = 2.0 \times 10^{21}\,\mathrm{cm}^{-2} A_{\mathrm{V}}$. $A_{\mathrm{V,los}} =$ 2.5 and 5.0 with $n_{\mathrm{H}} = 3.0 \times 10^3\,\mathrm{cm}^{-3}$ correspond to PDR1 and PDR2, respectively; $A_{\mathrm{V,los}} = 0.5$ and 2.5 with $n_{\mathrm{H}} = 1.6 \times 10^4\,\mathrm{cm}^{-3}$ and $4.0 \times 10^4\,\mathrm{cm}^{-3}$ correspond to potentially dense cloud surfaces in PDR1 and PDR2. The Horsehead PDR should be matched with $A_{\mathrm{V,los}} = 2.5$ or 5.0 with $n_{\mathrm{H}} = 4.0 \times 10^4\,\mathrm{cm}^{-3}$.

The three models substantially show the same result, with a luke-warm surface layer where the gas cools through the [C II] line. The colder gas deeper in the cloud emits mainly through CO. Not surprisingly, the FIR dust emission also peaks at the surface. The line-of-sight depth of the molecular cloud ($A_{\mathrm{V,los}} = 0.5, 2.5,$ or 5.0) only slightly affects the ratios of FIR, [C II]-, and CO-line intensities.

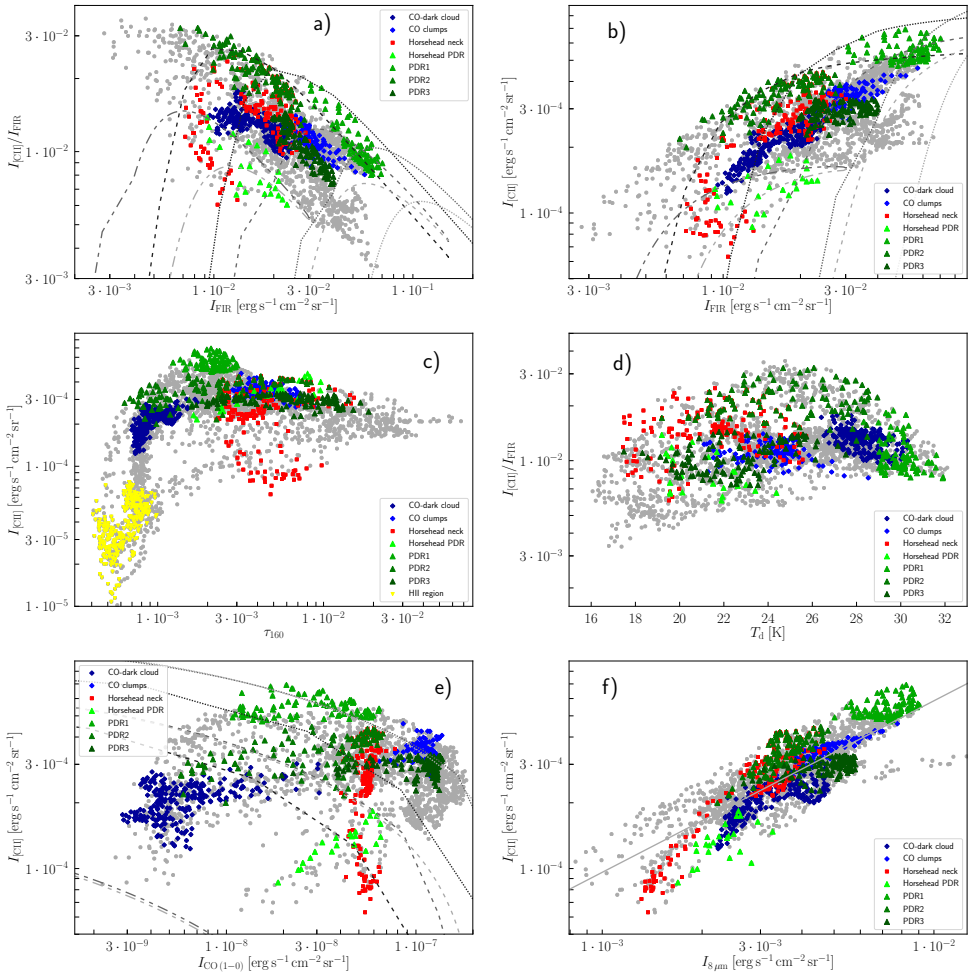

Figure 2.8: Correlation plots extracted from the Orion B maps, convolved to a uniform resolution of 36″ and pixel size of 15″. Dark blue diamonds represent the CO-dark cloud, blue diamonds represent the CO clumps, red squares represent the Horsehead neck, triangles in different shades of green represent the PDRs (bright green is the Horsehead PDR), and yellow triangles represent the H II region. Edge-on model predictions for selected gas densities are plotted as lines. Dashed lines are for $A_{V,los} = 2.5$, with dark gray corresponding to a gas density of $n_H = 3.0 \times 10^3\,cm^{-3}$, medium gray to $n_H = 1.6 \times 10^4\,cm^{-3}$, and light gray to $n_H = 4.0 \times 10^4\,cm^{-3}$; dotted lines are the same but for $A_{V,los} = 5.0$; the medium and light gray dash-dotted lines are for $A_{V,los} = 0.5$, with $n_H = 1.6 \times 10^4\,cm^{-3}$ and $n_H = 4.0 \times 10^4\,cm^{-3}$, respectively. In panel f, the best fit is plotted as a line.

2.3.5 Correlation diagrams

Figure 2.8 shows correlation diagrams between several quantities. The different colors indicate the selected regions assigned in Section 2.3.2 and shown in Figs. 2.1 and 2.3. Gray points represent points that do not lie in either of the defined regions.

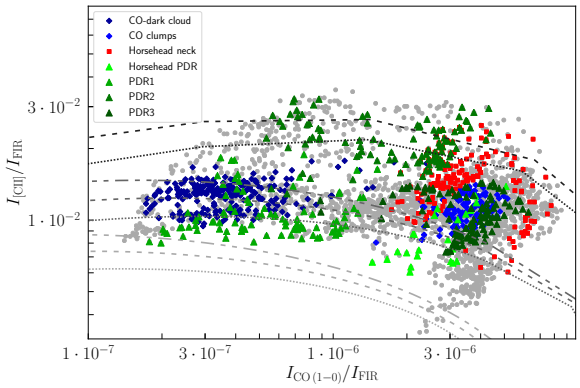

Figure 2.9: Correlation plot of $I_{[\mathrm{C\,II}]}/I_{\mathrm{FIR}}$ versus $I_{\mathrm{CO\,(1\text{-}0)}}/I_{\mathrm{FIR}}$. Edge-on model predictions for selected gas densities are plotted as lines. Dashed lines are for $A_{\mathrm{V,los}} = 2.5$, with dark gray corresponding to a gas density of $n_{\mathrm{H}} = 3.0 \times 10^3\,\mathrm{cm}^{-3}$, medium gray to $n_{\mathrm{H}} = 1.6 \times 10^4\,\mathrm{cm}^{-3}$, and light gray to $n_{\mathrm{H}} = 4.0 \times 10^4\,\mathrm{cm}^{-3}$; dotted lines are the same but for $A_{\mathrm{V,los}} = 5.0$; the medium and light gray dash-dotted lines are for $A_{\mathrm{V,los}} = 0.5$, with $n_{\mathrm{H}} = 1.6 \times 10^4\,\mathrm{cm}^{-3}$ and $n_{\mathrm{H}} = 4.0 \times 10^4\,\mathrm{cm}^{-3}$, respectively.

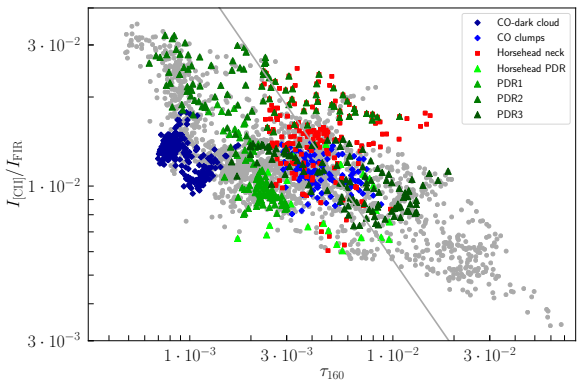

Figure 2.10: Correlation plot of $I_{[\mathrm{C\,II}]}/I_{\mathrm{FIR}}$ versus τ_{160}. The plotted line corresponds to the relation expected from a simple face-on slab model, $C/(1-\exp(-\tau_{160}))$; it is drawn such that it runs through the mean of $I_{[\mathrm{C\,II}]}/I_{\mathrm{FIR}}$ and τ_{160}.

Figure 2.8a shows that the [C II] cooling efficiency $I_{[\mathrm{C\,II}]}/I_{\mathrm{FIR}}$ decreases with increasing I_{FIR}. The different PDRs lie on distinct curves, with similar slopes. Figure 2.8b shows increasing $I_{[\mathrm{C\,II}]}$ with increasing I_{FIR}, but again in distinct branches for the different regions. The relation between $I_{[\mathrm{C\,II}]}$ and $I_{8\,\mu\mathrm{m}}$ resembles that, as can be seen from Fig. 2.8f, but simple fits reveal a tighter relation of $I_{[\mathrm{C\,II}]}$ with $I_{8\,\mu\mathrm{m}}$ than with I_{FIR}. Over-plotted is a least-square fit, $I_{[\mathrm{C\,II}]} \simeq 2.2 \cdot 10^{-2}\,(I_{8\,\mu\mathrm{m}}[\mathrm{erg\,s^{-1}\,cm^{-2}\,sr^{-1}}])^{0.79}$ $\mathrm{erg\,s^{-1}\,cm^{-2}\,sr^{-1}}$ ($\rho = 0.85$).

As Fig. 2.8c shows, $I_{[\mathrm{C\,II}]}$ is roughly constant for higher τ_{160}, that is, in PDR3 and the Horsehead PDR. This might reflect the fact that there is colder, non-PDR material located behind the PDR surfaces. PDR1 and PDR2 at the onset of the molecular cloud, where we do not expect a huge amount of colder material along the line of sight, show a nice correlation: PDR1 lies at twice as high τ_{160} and has twice

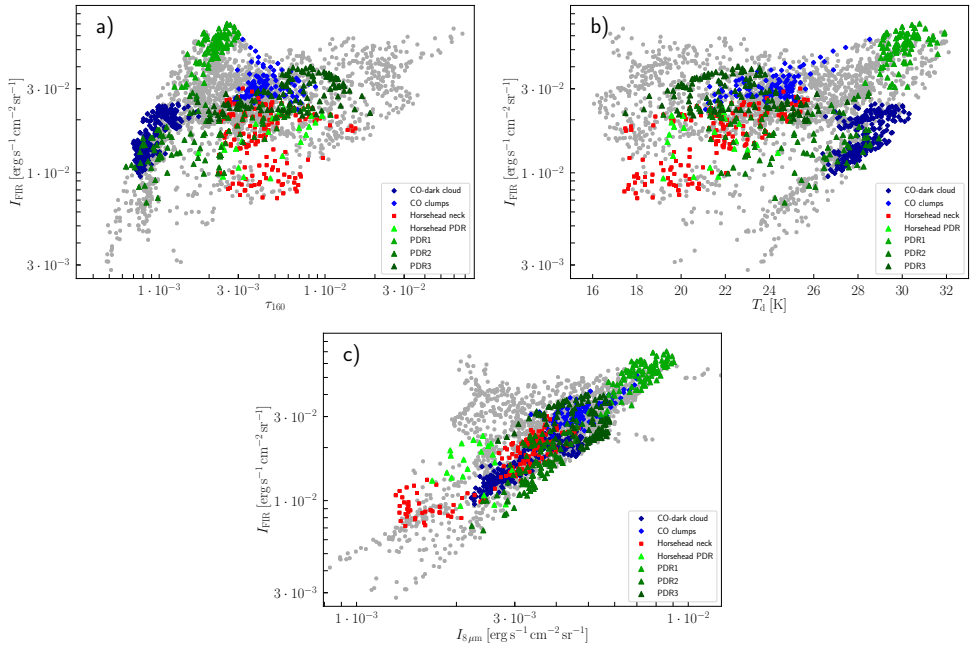

Figure 2.11: Correlation plots of $I_{\rm FIR}$ versus τ_{160}, $T_{\rm d}$, and $I_{8\,\mu m}$, respectively.

as high $I_{[\rm C\,II]}$. For small τ_{160} (i.e., in the H II region and parts of the CO-dark cloud), the data show a steep rising slope. In Fig. 2.8d, there is no obvious relation between $I_{[\rm C\,II]}/I_{\rm FIR}$ and the dust temperature $T_{\rm d}$. Figure 2.8e shows $I_{[\rm C\,II]}$ versus $I_{\rm CO\,(1\text{-}0)}$. Here we notice that the various regions populate distinct areas in the plot. In the diagram of $I_{[\rm C\,II]}/I_{\rm FIR}$ versus $I_{\rm CO(1\text{-}0)}/I_{\rm FIR}$ (Fig. 2.9), we observe no obvious correlation, only the Horsehead PDR exhibits a significant slope.

Figure 2.10 shows that the Horsehead PDR lies at the high end of the τ_{160} distribution. The general trend does not exactly fit a slope of $\simeq -1$, as does OMC1 in a first approximation (from $I_{[\rm C\,II]}/I_{\rm FIR} \simeq C/(1-e^{-\tau_{160}})$, Goicoechea et al. (2015b)), indicating that the emission cannot be modeled by a homogeneous face-on slab of dust with [C II] foreground emission. Of course, dust temperature differences should be taken into account, yet here we assume a constant pre-factor. Moreover, this simple model is derived from a face-on geometry, whereas here we are likely to deal with PDRs viewed edge-on.

FIR intensity increases with increasing τ_{160}, as Fig. 2.11a shows, but temperature differences play a role. The dust is comparatively hotter in PDR1 and PDR2, and in the CO-dark cloud. The FIR intensity scatters a lot when related to $T_{\rm d}$, as can be seen from Fig. 2.11b. Opposed to that, $I_{\rm FIR}$ seems to be well-correlated to $I_{8\,\mu m}$ (Fig. 2.11c).

2.4 Discussion

2.4.1 [C II] Emission from the PDR

The total [C II] luminosity from the mapped area of $\simeq 210$ square arcmin is $L_{\rm total} \simeq 14\,L_\odot$. The luminosity stemming from the molecular cloud is $L_{\rm cloud} \simeq 13\,L_\odot$ and that from the H II region is $L_{\rm H\,II} \simeq 1\,L_\odot$. Thus, about 5% of the total [C II] luminosity of the surveyed area originates from the H II region; 95% stems from the irradiated molecular cloud. This compares to 20% and 80%, respectively, of the area. For comparison, the total FIR luminosity from the mapped area is $L_{\rm FIR} \simeq 1245\,L_\odot$, of which $1210\,L_\odot$ belong to the molecular cloud and $35\,L_\odot$ to the H II regio. However, a small part of the luminosity may be attributed to NGC 2023: $0.2\,L_\odot$ in [C II] and $35\,L_\odot$ in FIR luminosity. Since the $8\,\mu$m intensity as a cloud surface tracer is very well correlated to the [C II] intensity, we may conclude that in the studied region of the Orion molecular cloud complex most of the [C II] emission originates from PDR surfaces. This is in agreement with the distribution of [C II] emission in OMC1: Here, Goicoechea et al. (2015b) find that 85% of the [C II] emission arises from the irradiated surface of the molecular cloud. On Galactic scales, however, Pineda et al. (2014) find that ionized gas contributes about 20% and dense PDRs about 30% to the total [C II] luminosity (the remainder stemming in equal amounts from cold H I gas and CO-dark H_2 gas).

The [C II] line-integrated intensity $I_{\rm [C\,II]}$ ranges from $10^{-5}\,{\rm erg\,s^{-1}\,cm^{-2}\,sr^{-1}}$ in the H II region up to a maximum of $7 \times 10^{-4}\,{\rm erg\,s^{-1}\,cm^{-2}\,sr^{-1}}$ in PDR1, with an average over the mapped area of $\bar{I} = 2.4 \times 10^{-4}\,{\rm erg\,s^{-1}\,cm^{-2}\,sr^{-1}}$. The [C II] cooling efficiency $\eta = I_{\rm [C\,II]}/I_{\rm FIR}$ takes its highest values at the edge of the molecular cloud, bordering on the Hα emitting region. Its peak value is about 3×10^{-2}, ranging down to 3×10^{-3}. The separation of molecular cloud and H II region emission is not trivial, since we think that the surface of the cloud is not straight, but warped. However, [C II] emission from the region exclusively associated with the ionized gas in IC 434 is very weak and has a much wider line profile (cf. Figs. 2.6 and 2.12; see also Section 2.4.2). Hence, we assume that at the edge of the molecular cloud the [C II] and FIR emission from ionized gas is minor compared to emission stemming from the molecular cloud itself.

Considering the average [C II] cooling efficiencies, where beam-dilution and column-length effects should divide out, we note that PDR2 has twice as high [C II] cooling efficiency as the Horsehead PDR and PDR1 have (see Table 2.1). We remark that PDR2 lies in a region where there still is significant Hα emission, indicating a corrugated edge structure. Since the average [C II] emission in the H II region is quite low, we do not expect [C II] emission from the ionized gas to be responsible for the enhanced [C II] cooling efficiency in PDR2. However, $I_{\rm FIR}$ is unexpectedly low in PDR2, which may account for the mismatch in $I_{\rm [C\,II]}/I_{\rm FIR}$.

2.4.2 [C II] Emission from the H II region

From the Hα emission in the studied region, originating from the ionized gas to the west of the molecular cloud, we can estimate the density of the H II region (Ochsendorf et al. 2014). The radiated intensity of the Hα line can be calculated by

$$I_{\mathrm{H}\alpha} = \int_0^d j_{\mathrm{H}\alpha}\,\mathrm{d}z = \int_0^d \frac{4\pi j_{\mathrm{H}\beta}}{n_p n_e}\frac{j_{\mathrm{H}\alpha}}{j_{\mathrm{H}\beta}}\frac{n_p n_e}{4\pi}\,\mathrm{d}z. \tag{2.4}$$

Assuming a gas temperature of $T \simeq 10^4$ K, we use $4\pi j_{\mathrm{H}\beta}/n_p n_e = 8.30\times10^{26}\,\mathrm{erg\,cm^3 s^{-1}}$ and $j_{\mathrm{H}\alpha}/j_{\mathrm{H}\beta} = 2.86$ (Osterbrock 1989). Further, we assume a homogeneous gas distribution along the line of sight, which we take to be $d \sim 1$ pc. Hence, we obtain

$$I_{\mathrm{H}\alpha} \simeq 7.0\times10^{-8}\,n_{\mathrm{e}}^2\,\mathrm{erg\,cm^4\,s^{-1}\,sr^{-1}}, \tag{2.5}$$

where $n_p = n_e$. When a molecular cloud is photoevaporated into a cavity, as the surface of L1630 is, we expect an exponential density profile as a function of distance from the surface. Fitting an exponential to the observed Hα emission along a line cut, we obtain a density law with $n_{e,0} = 95\,\mathrm{cm^{-2}}$ at the ionization front and a scale length of 1.2 pc, which is in good agreement with Ochsendorf et al. (2014). In the surveyed area, the density varies between 60 and 100 $\mathrm{cm^{-3}}$.

Applying again $T \simeq 10^4$ K for the gas temperature to the cooling law of [C II] (eq. (2.36) in Tielens (2010)), we obtain

$$n^2\Lambda \simeq 2.7\times10^{-24}\frac{n_e}{1+\frac{n_{\mathrm{cr}}}{3n_e}}\,\mathrm{erg\,s^{-1}\,cm^{-3}}, \tag{2.6}$$

where we assumed an ionization fraction of $x = 1$ and, hence, consider collisions with electrons only; the critical density scales with T and is, at $T = 10^4$ K, $n_{\mathrm{cr}} \simeq 50\,\mathrm{cm^{-3}}$ (Goldsmith et al. 2012). Neglecting $\frac{n_{\mathrm{cr}}}{3n_e}$ and assuming again $d \sim 1$ pc for the length of the line of sight, the above yields

$$I_{[\mathrm{C\,II}]} \simeq 7\times10^{-5}\left(\frac{n_e}{10^2\,\mathrm{cm^{-2}}}\right)\,\mathrm{erg\,s^{-1}\,cm^{-2}\,sr^{-1}}. \tag{2.7}$$

The observed intensity values lie in the range of 10^{-5}-$10^{-4}\,\mathrm{erg\,s^{-1}\,cm^{-2}\,sr^{-1}}$, which is, given the range of densities, in good agreement with the values derived from Hα emission. However, it is difficult to recognize a declining trend in the [C II] intensity away from the molecular cloud, since the signal is very noisy in the H II region due to the low intensity.

The [C II] spectra extracted from the H II region show a very weak and very broad feature (Fig. 2.12) with a peak main-beam temperature of ~ 1 K and an FWHM of 5-10 $\mathrm{km\,s^{-1}}$, as compared to 10-20 K and 2-4 $\mathrm{km\,s^{-1}}$ for the PDR regions in the molecular cloud. This is distinct from the spectra taken towards the cloud. We cannot distinguish a broad feature in the spectra taken towards the molecular cloud, although there is some Hα emission and we should expect ionized gas in front of the multiple PDR surfaces. Most likely the intensity is simply too low, approximately ten times lower than the intensity towards the H II region, assuming that the H II column in front of the molecular cloud as seen along the line of sight is ~ 0.1 pc, which renders the signal undetectable.

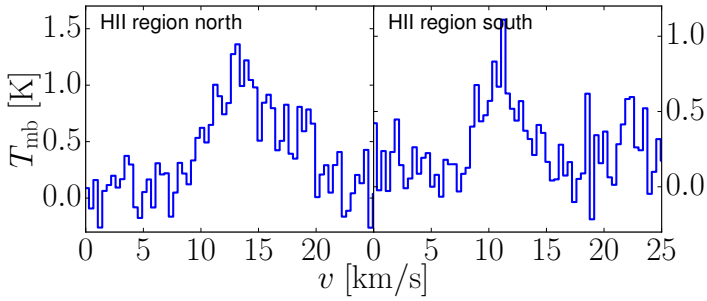

Figure 2.12: [C II] spectra towards the H II region, averaged over 156 (left) and 187 (right) pixels. The left panel represents the H II region north of the Horsehead Nebula, the right panel represents the part south of the Horsehead Nebula. For the northern part, we obtain $T_{\rm P} = 1.0\,{\rm K}$, FWHM $= 8.7\,{\rm km\,s^{-1}}$, and $v_{\rm P} = 14.1\,{\rm km\,s^{-1}}$; for the southern part, a Gaussian fit yields $T_{\rm P} = 0.7\,{\rm K}$, FWHM $= 5.2\,{\rm km\,s^{-1}}$, and $v_{\rm P} = 11.2\,{\rm km\,s^{-1}}$.

2.4.3 FIR emission and beam-dilution effects

We expect that beam dilution affects all maps to some extent when convolved to the SPIRE 500 μm 36″ resolution, since the unconvolved IRAC 8 μm map at 1.98″ resolution reveals features and delicate structures (see Fig. 2.15) that disappear upon convolution. The upGREAT beam has an FWHM of 15.9″, thus beam dilution might be noticeable in [C II] observations towards thin filaments. From the IRAC 8 μm emission, we infer a dilution factor of ~ 2.5 for the Horsehead PDR going from the native resolution of the 8 μm image to 36″ resolution, but only for the narrowest (densest) part of the PDR. The average 8 μm emission is not significantly beam-diluted when convolved to 36″. PDR3 possibly suffers significantly from beam dilution as well, since it shows as a rather sharp filament in 8 μm, where it reaches high peak values (higher than the Horsehead PDR peak values). Values of quantities we observe and compute from that are taken to be beam-averaged values in the respective resolution.

Due to the edge-on geometry of the PDRs in L1630 with respect to the illuminating star system σ Ori (and the low dust optical depth), we expect that $I_{\rm FIR}$ depends on the re-radiating column along the line of sight, which might explain the excess intensity in 8 μm, [C II], and FIR in PDR1 as compared to other PDR surfaces here. The commonly expected value of incident FUV radiation, re-emitted in $I_{\rm FIR}$, is $G_0 \simeq 100$, calculated from properties of σ Ori (Abergel et al. (2003) and references therein). Given the edge-on geometry of the cloud-star complex, the formula by Hollenbach & Tielens (1999),

$$G_0 = \frac{1}{2}\frac{I_{\rm FIR}}{1.3\times10^{-4}\,{\rm erg\,s^{-1}\,cm^{-2}\,sr^{-1}}}, \tag{2.8}$$

cannot be used to infer the intensity of the incident UV radiation. The FIR intensity varies substantially across the mapped area; for a face-on geometry with a single UV-illuminating source, one would expect less divergent values. This realization corroborates the assumption of an edge-on geometry and has been the rationale for building edge-on models with different molecular-cloud depths along the line of sight.

The dust optical depth τ_{160} does not trace the PDR surface column, but the total gas and dust column. The FIR intensity does not increase with increasing τ_{160} for PDR1, PDR2, and PDR3 (in comparison to $\tau_{160} \simeq 2\times10^{-3}$, 1×10^{-3}, 3×10^{-3},

respectively[5]). Especially in the case of PDR3, τ_{160} likely traces not only the PDR but the molecular cloud interior, as well. A fraction of $I_{\rm FIR}$ might stem from deeper, cooler parts of the molecular cloud and not from the PDR surface, although $I_{\rm FIR}$ is biased towards the hot PDR surface, as is τ_{160}. In PDR2, $I_{\rm FIR}$ is lower than we would expect, leading to significantly higher $I_{[\rm C\,II]}/I_{\rm FIR}$ than in PDR1 and PDR3. The dust temperature $T_{\rm d}$ in PDR2 is determined to be considerably lower than in PDR1, although the environments seem similar.

2.4.4 Column densities, gas temperature, and mass

Since we do not detect the [^{13}C II] line in single spectra, we cannot determine the [C II] optical depth by means of it. The noise rms of the spectra is too high to put a significant constraint on $\tau_{[\rm C\,II]}$. In averaged spectra, we can detect the [^{13}C II] F = 2-1 line just above the noise level (see Section 2.4.5). However, knowing the C^+ column density and the intrinsic line width, we can estimate the [C II] optical depth and the excitation temperature (see Appendix 2.A) from single spectra. We compute the C^+ column density of the PDR surface from the dust optical depth, assuming standard dust properties and that all carbon in the PDR surface is singly ionized. Additionally, we expect beam dilution to be insignificant for the [C II] observations. From the native IRAC 8 μm map, we infer a dilution factor of 1.5 when going to 15.9″ resolution, but only towards the thinnest filament in the Horsehead mane. This equally yields a peak temperature of $T_{\rm P} \simeq 20\,$K there, as does the brightest part of the Horsehead PDR.

The gas column density can be computed from the dust optical depth τ_{160}, assuming a theoretical absorption coefficient. This yields

$$N_{\rm H} \simeq \frac{100\,\tau_{160}}{\kappa_{160} m_{\rm H}} \simeq 5 \times 10^{24}\,{\rm cm}^{-2}\,\tau_{160}, \tag{2.9}$$

where we have used a gas-to-dust mass ratio of 100 and assumed $\kappa_{\rm abs} = 2.92 \times 10^5 (\lambda\,[\mu{\rm m}])^{-2}\,{\rm cm}^2/{\rm g}$ (Li & Draine 2001). With the fractional gas-phase carbon abundance [C/H] = 1.6×10^{-4} (Sofia et al. 2004), we can estimate the C^+ column density in the PDR surface from the dust optical depth, under the assumption that all carbon in the line of sight is ionized:

$$N_{\rm C^+} \simeq 8 \times 10^{20}\,{\rm cm}^{-2}\,\tau_{160}. \tag{2.10}$$

Later studies have reported somewhat differing values for [C/H], varying by a factor of two for different sight lines; see e.g. Sofia & Parvathi (2009); Sofia et al. (2011). However, the average is not found to deviate substantially from the earlier value of [C/H] = 1.6×10^{-4}; the general uncertainty seems to be quite large. We discuss the effect of the uncertainty in the column density on the derived gas properties in the following. For PDR1 and PDR2 we have $\tau_{160} \simeq 2 \times 10^{-3}$ and $\tau_{160} \simeq 10^{-3}$, respectively, from the τ_{160} map, where we assume that all the dust actually is in the PDR surface. However, these values for the dust optical depth may be affected by significant uncertainties, up to a factor of two, since τ_{160} depends on the assumed dust properties in the SED fit (see discussion in Section 2.2.2). For PDR3, we suppose that there is a significant amount of cold material located along the line of sight, which renders τ_{160} an inaccurate measure for the depth of the PDR along the line of sight here.

[5]PDR2 partially overlaps with the dense region of the neck of the Horsehead Nebula; hence we take τ_{160} for PDR2 from the region where it does not overlap.

Table 2.3: Results from solving Eq. 2.16.

pos.	RA (J2000)	Dec (J2000)	N_{C^+} [cm^{-2}]	$\tau_{[C\,II]}$	T_{ex} [K]
A	5h40′53″	−2°27′37″	7×10^{17}	2.0	58
B	5h41′00″	−2°20′27″	1.6×10^{18}	1.7	63
F	5h41′06″	−2°30′46″	8×10^{17}	1.4	65

Notes. Position A corresponds to the Horsehead PDR, B is PDR1, F lies in PDR2. The spectrum at point B consists of two components, but here we consider only the main component (the second component is much weaker). Table 2.2 shows the spectral parameters T_P and Δv_{FWHM}.

Inferring the PDR dust optical depth of the Horsehead PDR requires further effort. According to Habart et al. (2005), there is a large density gradient from the surface to the bulk of the Horsehead PDR. In the surface the gas density might be as low as $n_H \sim 10^4\,cm^{-3}$, whereas in the bulk it assumes $n_H \sim 2 \times 10^5\,cm^{-3}$. Abergel et al. (2003) find $n_H \sim 2 \times 10^4\,cm^{-3}$ as a lower limit for the density of the gas directly behind the illuminated filament. The dust optical depth is likely to be beam diluted in the SPIRE 500 μm resolution; the filament has an extent of only 5-10″. Assuming that the maximum $\tau_{160} \simeq 10^{-2}$ occurs in the densest (inner) part of the PDR and that the length along the line of sight remains approximately the same, we conclude that the dust optical depth in the Horsehead PDR surface must be significantly lower than the maximum value, by a factor of approximately ten, due to the decreased density.

From deep integration of the Horsehead PDR with SOFIA/upGREAT, however, we are able to infer a [C II] optical depth of $\tau_{[C\,II]} \simeq 2$ from the brightest [^{13}C II] line, which can be detected in these data (C. Guevara, priv. comm.; paper in prep. C. Guevara, J. Stutzki et al.). According to Eq. 2.16, this translates into a C^+ column density of $N_{C^+} \simeq 7 \times 10^{17}\,cm^{-2}$, that is $\tau_{160} \simeq 10^{-3}$, which is ten times lower than the maximum value in the Horsehead bulk. However, from our models, this [C II] optical depth corresponds to a twice as large C^+ column density of $N_{C^+} \simeq 1.6 \times 10^{18}\,cm^{-2}$, if we assume that all carbon is ionized within our beam, which might not be the case.

We calculate the [C II] optical depth $\tau_{[C\,II]}$ and excitation temperature T_{ex} for PDR1 and PDR2, and T_{ex} for the Horsehead PDR, using the formulas of Appendix 2.A. [6] The results are shown in Table 2.3. In principle, the values we infer for N_{C^+} are upper limits, but the general uncertainty in the C^+ column density is potentially larger than the deviation from the upper limit. The dust optical depth, from which we calculate the C^+ column density, is not well-determined (cf. Section 2.2.2) and the carbon fractional abundance may deviate. If we assume an error margin of the C^+ column density of ±50%, this results in ranges of [C II] optical depth and excitation temperature of $\tau_{[C\,II]} \simeq$ 0.6-2.7 and $T_{ex} \simeq$ 60-90 K, respectively, for PDR1, and $\tau_{[C\,II]} \simeq$ 0.4-2.2 and $T_{ex} \simeq$ 60-100 K, respectively, for PDR2. Certainly, these values are subject to uncertainties in the inferred gas density and the spectral parameters, as well; however, the uncertainty in N_{C^+} seems to be the most significant, leading to considerable deviations, so we will not discuss the influence of the other uncertainties here. In the Horsehead PDR, the precise value of $\tau_{[C\,II]}$ does not overly influence the excitation temperature which we calculate: it is $T_{ex} \simeq 60 \pm 2$ K.

If the density of the gas is known, one can compute the gas temperature from the

[6] We have checked that including raditative excitation by the dust FIR background is insignificant.

excitation temperature:

$$T = \frac{T_{\rm ex}}{1 - \frac{T_{\rm ex}}{91.2\,{\rm K}} \ln(1 + \frac{n_{\rm cr}}{n})}, \tag{2.11}$$

with the critical density $n_{\rm cr} = \beta(\tau_{[{\rm C\,II}]})\frac{A}{\gamma_{\rm ul}}$, where $\beta(\tau_{[{\rm C\,II}]})$ is the [C II] 158 μm photon escape probabilty, $A \simeq 2.3 \times 10^{-6}\,{\rm s}^{-1}$ is the Einstein coefficient for spontaneous radiative de-excitation of C^+, and $\gamma_{\rm ul}$ is the collisional de-excitation rate coefficient, which is $\gamma_{\rm ul} \simeq 7.6 \times 10^{-10}\,{\rm cm}^3\,{\rm s}^{-1}$ for C^+–H collisions (Goldsmith et al. 2012) and $\gamma_{\rm ul} \simeq 5.1 \times 10^{-10}\,{\rm cm}^3\,{\rm s}^{-1}$ for C^+–H_2 collisions (Wiesenfeld & Goldsmith 2014) at gas temperatures of $\simeq 100\,{\rm K}$; n is the collision partner density. At $T \sim 100\,{\rm K}$, $\gamma_{\rm ul}$, and thereby $n_{\rm cr}$ is only weakly dependent on temperature; for C^+–H collisions, $n_{\rm cr} \simeq \beta(\tau_{[{\rm C\,II}]}) \times 3.0 \times 10^3\,{\rm cm}^{-3}$, and for C^+–H_2 collisions, $n_{\rm cr} \simeq \beta(\tau_{[{\rm C\,II}]}) \times 4.5 \times 10^3\,{\rm cm}^{-3}$. At the cloud edge, collisions with H dominate the excitation of C^+, while deeper into the cloud H_2 excitation dominates. We expect that excitation caused by collisions involving both H and H_2 contribute within our beam. Since the points we chose in PDR1 and PDR2 lie close to the surface, we consider collisions with H; in the Horsehead PDR the choice of collision partner does not affect the derived gas temperature significantly due to the higher gas density. We take the photon escape probability to be $\beta(\tau) = (1 - e^{-\tau})/\tau$, as used in our edge-on PDR models. The densities are discussed in Section 2.4.7.

Using $n_{\rm H} \simeq 3 \times 10^3\,{\rm cm}^{-3}$ for PDR1 and PDR2, we obtain $T \simeq 86\,{\rm K}$ and $T \simeq 93\,{\rm K}$, respectively, for C^+–H collisions. In the Horsehead PDR, we compute $T \simeq 60\,{\rm K}$. From models (see Secs. 6.3.3 and 2.4.9) we compute a gas temperature of about $T \simeq$ 100-140 K in the top layers of a PDR (cf. Fig. 6.6). This is in reasonable agreement with the values derived from our observations in PDR1 and PDR2. In the Horsehead PDR, however, the results likely are affected by beam dilution, since the gas temperature drops quickly on the physical scale (within the beam size of 15.9″ of the [C II] observations). Disregarding this, with a low C^+ column density of $N_{\rm C^+} = 1.6 \times 10^{17}\,{\rm cm}^{-2}$ we can match the gas temperature measured by Habart et al. (2011) from H_2 observations, $T \simeq 264\,{\rm K}$; this results in a [C II] optical depth of $\tau_{[{\rm C\,II}]} \simeq 0.1$. We can fit a gas temperature of $T \simeq 120\,{\rm K}$, as predicted by our models for conditions appropriate for the Horsehead PDR, with a column density of $N_{\rm C^+} \simeq 2.0 \times 10^{17}\,{\rm cm}^{-2}$. This would yield a [C II] optical depth of $\tau_{[{\rm C\,II}]} \simeq 0.3$. Both values are significantly lower than what is observed in [^{13}C II].

According to Goldsmith et al. (2012), the [C II] line is effectively optically thin, meaning the peak temperature is linearly proportional to the C^+ column density, if $T_{\rm P} < J(T)/3$, where $J(T)$ is the brightness temperature of the gas. Hence, even though our derived [C II] optical depth for PDR1 and PDR2 is > 1, the line is still effectively optically thin in these regions. It is optically thick in the Horsehead PDR.

From the H column densities, that is, from the dust optical depth, we can estimate the mass of the gas: $M_{\rm gas} = N_{\rm H} m_{\rm H} A$, where A is the surface that is integrated over. The total gas mass of the molecular cloud (not including the H II region IC 434 and the north-eastern corner of gas and dust associated with NGC 2023) in the [C II] mapped area is $M_{\rm gas,total} \simeq 280\,M_\odot$. The Horsehead Nebula and its shadow add $M_{\rm gas} \simeq 33\,M_\odot$ to the total mass, the Horsehead PDR surface contributing $M_{\rm gas} \simeq 3\,M_\odot$. The mass of CO-emitting gas (also computed from $N_{\rm H}$) is $M_{\rm gas} \simeq 250\,M_\odot$. The assumption that CO-emitting gas contributes the bulk of the mass and that [C II] traces PDR surfaces yields a gas mass of PDR surfaces of $M_{\rm gas} \simeq 20\,M_\odot$. Additionally, $\simeq 12\,M_\odot$ are located in gas that emits neither strongly in [C II] nor in CO. The H II region

Table 2.4: Masses within the several regions defined in Section 2.3.2 calculated from the dust optical depth τ_{160} and from the CO (1-0) intensity $I_{\mathrm{CO(1\text{-}0)}}$.

Region	M_{dust} $[M_\odot]$	M_{CO} $[M_\odot]$
entire map	294	200
L1630	283	197
Horsehead PDR	3	1
PDR1	5	3
PDR2	6	4
PDR3	17	13
CO-dark cloud	5	2
CO clumps	12	14
H II region	11	3
CO-emitting gas	251	175

Notes. For the latter we use an X_{CO} of $2 \times 10^{20}\,\mathrm{cm}^{-2}\,(\mathrm{K\,km\,s}^{-1})^{-1}$ (Bolatto et al. 2013, and references therein). "CO-emitting gas" refers to the part of the map with extended CO emission, that is, the deeper layers of L1630.

comprises $M_{\mathrm{gas}} \simeq 10\,M_\odot$ as derived from the dust optical depth; from Hα emission, we estimate $M_{\mathrm{gas}} \simeq 5\,M_\odot$.

Table 2.4 compares the masses computed from the dust optical depth and from CO (1-0) emission, respectively, for the several regions we defined. Since the uncertainties (in the dust optical depth, but also in the conversion factors, especially in the X_{CO} factor (cf. Bolatto et al. 2013)) are substantial, we cannot draw clear-cut conclusions. We note, moreover, that PDR regions might overlap along the line of sight with CO-emitting regions whose emission stems from a different layer of the molecular cloud, as certainly is the case in PDR3. It seems that there is a fair amount of gas mass unaccounted for by CO emission, but within the error margin of 30%, this mass can be between 10 and $100\,M_\odot$. In a larger area mapped in CO, comprising the area mapped in [C II], Pety et al. (2017) find that the CO-traced mass is in fact greater than the dust-traced mass; this especially influences the deeper layers of the Orion B molecular cloud (see Table 4 in Pety et al. 2017), thus these findings might not apply to our study field in L1630. However, they conclude that CO tends to overestimate the gas mass, whereas the dust optical depth underestimates it. In this way, with an area of $\sim 2\,\mathrm{pc}^2$, we find a gas mass surface density of 100-150 $M_\odot\,\mathrm{pc}^{-2}$ in the [C II] mapped area.

2.4.5 Excitation properties from [^{13}C II]

If we average over a large number of spectra in [C II]-bright areas, we are able to identify the [^{13}C II] F = 2-1 line above the 5σ level (see Fig. 2.13); we cannot detect the other two (weaker) [^{13}C II] lines. From the [^{13}C II] F = 2-1 line, we can compute average values of the [C II] optical depth, the excitation temperature, and the C^+ column density. From an average spectrum of the [C II]-bright regions of PDR1 and PDR2 (an area of 50 square arcmin, which is a third of the cloud area and corresponds to 3140 spectra), we obtain $\tau_{[\mathrm{C\,II}]} \simeq 1.5$ (with an uncertainty of 20%). To obtain this result, we used [^{13}C II] line parameters established by Ossenkopf et al. (2013) and the ^{12}C/^{13}C isotopic ratio of 67 for Orion (Langer & Penzias 1990; Milam et al. 2005). This yields a C^+ column density of $N_{\mathrm{C^+}} \simeq 3 \times 10^{17}\,\mathrm{cm}^{-2}$. From an average over

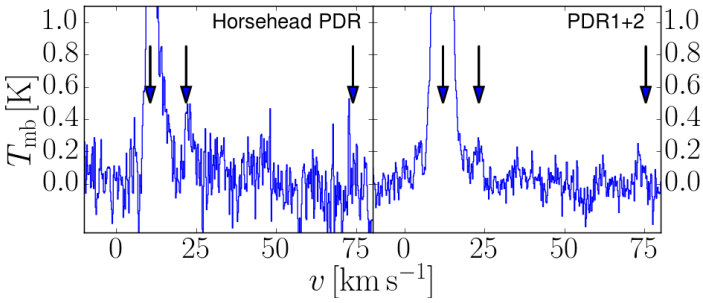

Figure 2.13: [C II] spectra towards the Horsehead PDR and PDR1+2, averaged over 180 (*left*) and 3140 (*right*) pixels. Arrows indicate the positions of the [^{12}C II] line and the [^{13}C II] F = 2-1 and F = 1-1 lines (*from left to right*); the [^{13}C II] F = 1-0 line falls outside the spectral range of our map.

the Horsehead PDR (an area of 3 square arcmin, corresponding to 180 spectra), we obtain $\tau_{[\rm C\,II]} \simeq 5$ (also with 20% uncertainty) and $N_{\rm C^+} \simeq 1 \times 10^{18}\,{\rm cm}^{-2}$. We note that $\tau_{[\rm C\,II]}$ in PDR1 and PDR2 does match the value calculated in Section 2.4.4 from the dust optical depth and single spectra, and $N_{\rm C^+}$ does not, whereas in the Horsehead PDR $\tau_{[\rm C\,II]}$ does not agree, but $N_{\rm C^+}$ does. Excitation temperatures from the averaged spectra are $T_{\rm ex} \simeq 40\,{\rm K}$, which is lower than what we infer from single spectra. Regions with lower-excitation [C II] contribute to the averaged spectra, but we have to include them to obtain a sufficient signal-to-noise ratio. We stress that this spectral averaging over a large area with varying conditions will weigh the emission differently for the [^{12}C II] and [^{13}C II] lines in accordance with the excitation temperatures and optical depths involved. Hence, the averaged spectrum will not be the same as the spectrum of the average. In our analysis, we have elected to rely on the analysis based on the dust column density rather than this somewhat ill-defined average.

2.4.6 Photoelectric heating and energy balance

The most substantial heating source of PDRs is photoelectric heating by PAHs, clusters of PAHs, and very small grains. The photoelectric heating rate is deeply built into PDR models and controls the detailed structure and emission characteristics to a large extent. The heating rate drops with increasing ionization of these species. It can be parametrized by the ionization parameter $\gamma = G_0 T^{0.5}/n_e$, where G_0 is the incident radiation, T is the gas temperature, and n_e is the electron density; the corresponding theoretical curve as derived by Bakes & Tielens (1994) is shown in Fig. 2.14. Okada et al. (2013) confirm in a study of six PDRs, which represent a variety of environments, the dependence of the photoelectric heating rate on PAH ionization and conclude on the dominance of photoelectric heating by PAHs.

The [C II] 158 μm cooling rate increases with gas density and temperature. In the high-density limit ($n_{\rm H} \gg n_{\rm cr}$), it scales with $n_{\rm H}$, whereas for low densities it scales with $n_{\rm H}^2$; the temperature dependence is largely captured in a factor $\exp(-\Delta E/k_B T)$, where ΔE is the energy level spacing.[7] The gas density of the Horsehead PDR, $n_{\rm H} \simeq 4 \times 10^4\,{\rm cm}^{-3}$, lies above the critical density for C$^+$, $n_{\rm cr} = \beta(\tau_{[\rm C\,II]}) \times 3.0 \times 10^3\,{\rm cm}^{-3}$; the densities of PDR1 and PDR2 are close to $n_{\rm cr}$, that is, in the intermediate density

[7] The same is true of other cooling lines, for example, the [O I] 63 μm line, with differing critical densities, however.

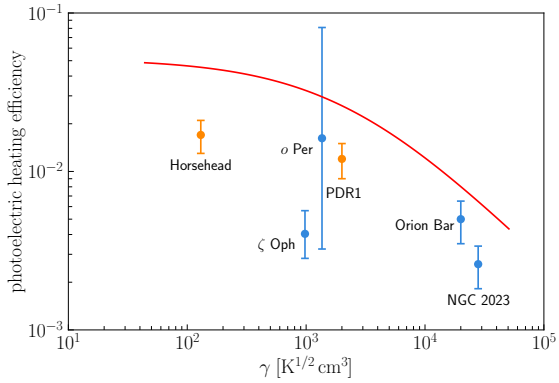

Figure 2.14: Theoretical photoelectric heating efficiency of PAHs, clusters of PAHs, and very small grains is plotted against the ionization parameter $\gamma = G_0 T^{0.5}/n_e$ (Bakes & Tielens 1994). We added the orange data points for the Horsehead PDR and PDR1. Blue data points are for the diffuse-ISM sight lines ζ Oph and o Per, and the PDRs Orion Bar and NGC 2023. Figure adapted from Tielens (2008).

regime. The similar gas temperatures and densities of PDR1 and PDR2, however, do not reflect the difference in the [C II] cooling efficiencies $I_{[\mathrm{C\,II}]}/I_{\mathrm{FIR}}$ calculated in Table 2.1 and visualized in Fig. 2.8a (cf. Section 2.4.3). In the case of the Horsehead PDR, gas cooling through the [O I] 63 μm line becomes important; the [O I] surface brightness is comparable to the surface brightness of the [C II] line (Goicoechea et al. 2009).

We emphasize that we can directly measure the temperature and the density of the emitting gas in the PDR from our observations (see Secs. 2.4.4 and 2.4.7, respectively). Hence, we can test the theory in a rather direct way. Specifically, we assume that all electrons come from C ionization, hence $n_e = 1.6 \times 10^{-4}\, n_{\mathrm{H}}$, where we have adopted the gas-phase abundance of carbon estimated by Sofia et al. (2004). For the Horsehead PDR with $n_{\mathrm{H}} \simeq 4 \times 10^4\,\mathrm{cm}^{-3}$ and $T \simeq 60\,\mathrm{K}$, we compute an ionization parameter of $\gamma \simeq 1 \times 10^2\,\mathrm{K}^{1/2}\,\mathrm{cm}^3$; for PDR1 and PDR2 with $n_{\mathrm{H}} \simeq 3 \times 10^3\,\mathrm{cm}^{-3}$ and $T \simeq 100\,\mathrm{K}$, we obtain $\gamma \simeq 2 \times 10^3\,\mathrm{K}^{1/2}\,\mathrm{cm}^3$. From the cooling lines, that is, assuming that all the heating is converted into [C II] and [O I] emission, we arrive at a heating efficiency of $1.7 \pm 0.4 \times 10^{-2}$ (with $I_{[\mathrm{O\,I}]} \simeq 1.04 \pm 0.14\,\mathrm{erg\,s}^{-1}\,\mathrm{cm}^{-2}\,\mathrm{sr}^{-1}$ from Goicoechea et al. (2009) at similar spatial resolution) for the Horsehead PDR, and $1.1 \pm 0.3 \times 10^{-2}$ for PDR1. From their [O I] study of the Horsehead Nebula, Goicoechea et al. (2009) find a heating efficiency of 1-2 $\times 10^{-2}$, which is consistent with our findings. For PDR2, we calculate an average [C II] cooling efficiency of $2.2 \pm 0.4 \times 10^{-2}$. However, I_{FIR} is unexpectedly low in PDR2, so we wonder whether the mismatch in $I_{[\mathrm{C\,II}]}/I_{\mathrm{FIR}}$ between PDR1 and PDR2 really is due to an erroneous determination of I_{FIR} and is thereby deceptive.

The general behavior of the observationally obtained heating efficiency is indeed very similar to the theoretical curve for photoelectric heating by PAHs, clusters of PAHs, and very small grains, as shown in Fig. 2.14, except that theoretical values seems to be offset to higher efficiency by about a factor of two. Such a shift might reflect a somewhat different abundance of PAHs and related species in the studied regions. We note that these differences between theory and observations can lead to considerable differences in the derived physical conditions. For example, adopting the

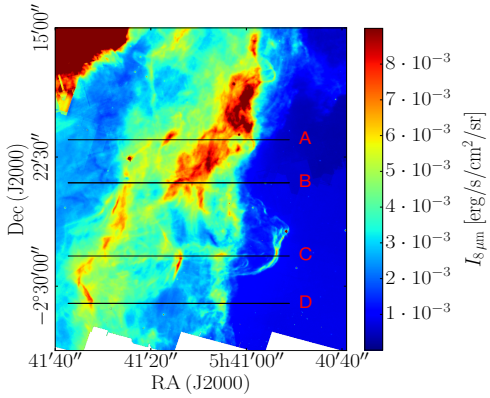

Figure 2.15: IRAC 8 μm image with lines A, B, C, and D indicated.

theoretical relationship and solving the energy balance for the gas density and FUV field appropriate for the Horsehead PDR would result in a derived gas temperature of $T \simeq 100\,\mathrm{K}$, while the temperature as measured from the pure rotational H_2 lines by Habart et al. (2011) is $T \simeq 264\,\mathrm{K}$, and we determine it to be $T \simeq 60\,\mathrm{K}$, which is beam-averaged. For PDR1 and PDR2, the theoretical relationship would imply a temperature of $T \simeq 125\,\mathrm{K}$, while we measure $T \simeq 90\,\mathrm{K}$ from the peak [C II] intensity. From a theoretical perspective, we expect the temperature to decrease with increasing density (cf. Fig. 9.4 in Tielens 2010). This is what we see in [C II] observations. However, from studies by Habart et al. (2011) and Habart et al. (2005), the observational temperature lies in the regime $T \simeq 200\text{-}300\,\mathrm{K}$, albeit in a very narrow surface gas layer. Here, the observational temperature in the Horsehead PDR appears to be higher than the theoretical temperature, despite the heating efficiency being underestimated. This may seem inconsistent; it certainly suggests that we have to be very careful with the assumptions we make. However, the discrepancy may be due to various reasons, not all of them implying inconsistency, that we will not discuss in this paper. Calculating the ionization parameter with either differing observational temperatures or the theoretical temperature does not shift the data points in Fig. 2.14 significantly towards the theoretical curve. Clearly, further validation of the theoretical relationship in a variety of environments is important as photoelectric heating is at the core of all PDR research, including studies on the phase structure of the ISM (Wolfire et al. 1995, 2003; Hollenbach & Tielens 1999). The significance of PAH photoelectric heating is reflected in the tight correlation between PAH and [C II] emission from the PDRs (see Figs. 2.8f and 2.19d). In a future study, we intend to return to this issue of the importance of PAHs to the heating of interstellar gas.

2.4.7 Line cuts

The edge-on nature of the PDR in the Orion B molecular cloud (L1630) is well illustrated by line cuts taken from the surface of the molecular cloud into the bulk (cf. Figs. 2.15 and 2.16). In addition to previously employed tracers (8 μm, Hα, [C II], CO(1-0)), we compare with SCUBA 850μm observations, that trace dense clumps, and compare PACS 160μm data as a measure for I_{FIR}.

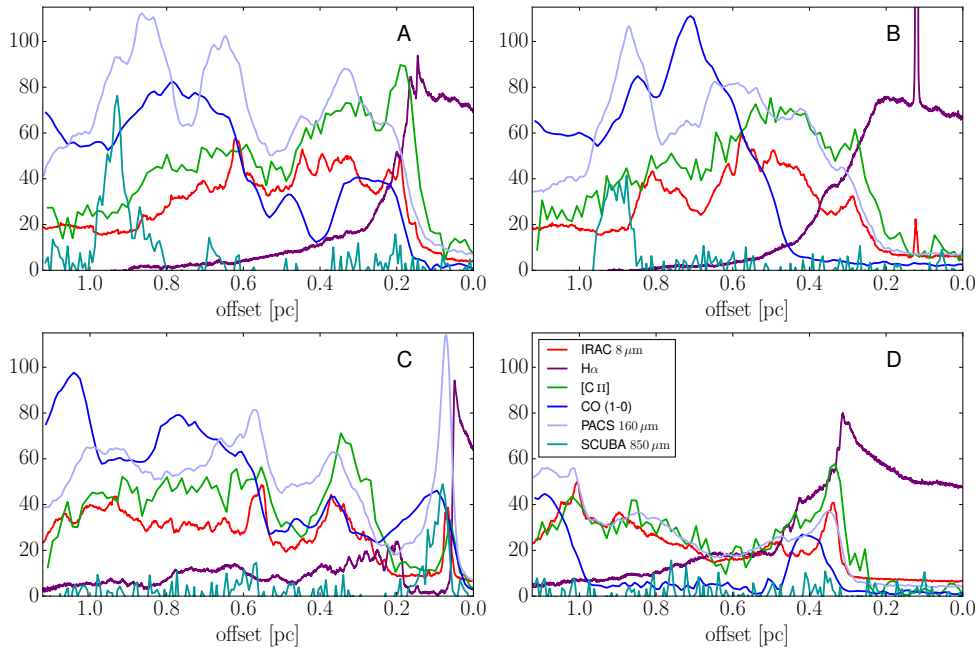

Figure 2.16: IRAC 8 μm (PAH) intensity, Hα intensity, [C II] and CO(1-0) line-integrated intensity, PACS 160 μm intensity, and SCUBA 850 μm intensity plotted in their respective native resolution along lines A, B, C, and D of Fig. 2.15 in their respective original spatial resolution. Multiply plotted values by 1.4×10^{-4}, 2.9×10^{-3}, 7.0×10^{-6}, 1.6×10^{-9}, $3,9\times10^{-5}$, and 2.2×10^{-7}, respectively, for $I_{8\,\mu\mathrm{m}}$, $I_{\mathrm{H}\alpha}$, $I_{[\mathrm{C\,II}]}$, $I_{\mathrm{CO(1\text{-}0)}}$, $I_{160\,\mu\mathrm{m}}$, and $I_{850\,\mu\mathrm{m}}$, respectively, in erg s^{-1} cm^{-2} sr^{-1}.

Along line cut C, the Horsehead PDR is clearly distinguishable; Hα drops immediately and the other four tracers peak, which indicates high density. Assuming A_{V}=2 for the transition from C^+/C to CO and $N_{\mathrm{H}} = 2\times10^{21}\,\mathrm{cm}^{-2}\,A_{\mathrm{V}}$, which is consistent with our models (see Fig. 6.6), we obtain from the physical position of the transition, $d \simeq 0.03$ pc, $n_{\mathrm{H}} \simeq 4\times10^4\,\mathrm{cm}^{-3}$. Since there are no further indications of dense clumps in 850 μm emission, we assume that the rest of the gas located along cut C is relatively diffuse. Having established that, we tentatively assign the CO peak between 0.6 and 0.8 pc to the PDR surface at 0.3 pc. We infer a gas density of $n_{\mathrm{H}} \simeq 3\times10^3\,\mathrm{cm}^{-3}$. Identifying the CO peak at 1.1 pc with the PDR surface at 0.6 pc yields about the same density.

If we perform the same procedure for line cut A, we derive about the same densities, $n_{\mathrm{H}} \simeq 3\times10^3\,\mathrm{cm}^{-3}$. Here, we assign the broad prominent CO feature at 0.8 pc to the broad PDR feature at 0.4 pc. The small CO peak at 0.5 pc possibly relates to the PDR feature at 0.4 pc, hence $n_{\mathrm{H}} \simeq 10^4\,\mathrm{cm}^{-3}$. The broad CO feature between 0.2 and 0.4 pc could originate from a dense surface, located at 0.2 pc.

Line cut B is difficult to interpret. Due to their respective shapes, the PAH peaks around 0.6 pc might correspond to the CO peaks at 0.7 and 0.85 pc, yielding a density of $n_{\mathrm{H}} \simeq 5\times10^3$-$10^4\,\mathrm{cm}^{-3}$. There is no indication of dense clumps in the SCUBA map at this point. The gas at the surface is likely to be relatively diffuse, since there is no distinct CO peak that could be related.

The gas at the surface cut by line D is denser again. Here, we estimate $n_{\mathrm{H}} \simeq$

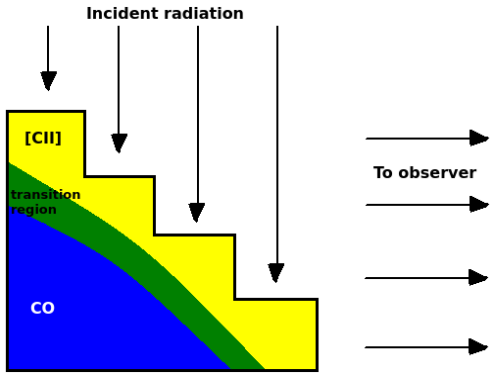

Figure 2.17: Geometry of the L1630 molecular cloud surface.

$3 \times 10^4\,\mathrm{cm}^{-3}$. PDR3 at 1.0 pc might be relatively dense too, since there is CO emission peaking directly behind the PDR front. However, this CO emission could certainly originate from deeper, less dense layers of the molecular cloud, as well. There is no 850 μm peak corresponding to the CO peak, rendering the latter hypothesis more plausible.

There are a number of CO peaks we cannot relate to a specific structure, for example, the one at 0.4 pc in line cut C. This might indicate that there are layers of gas with higher density stacked along the line of sight. Overall, this analysis suffers from numerous uncertainties and unknowns. Nevertheless, the calculated densities seem to be reasonable for a molecular cloud.

2.4.8 Geometry of the L1630 molecular cloud

Our data suggest that the L1630 molecular cloud as we see it consists of stacked layers of PDRs along the line of sight, which are offset against each other. Figure 2.17 shows a schematic illustration, which we inferred from our data, of the edge-on geometry of the studied region of the Orion B molecular cloud. The surface of the molecular cloud is inclined with respect to the incident radiation and the observer, but with steps where strong PDR surfaces can be discerned in the IRAC 8 μm image, for instance. This implies that we generally cannot compare our data with face-on PDRs; in the correlation plots, we need to correlate along line cuts and not along the line of sight. Also, the incident radiation is not easily estimated (see discussion in Section 2.4.3).

The CO emission in the Horsehead neck stems from a different distance along the line of sight than the overlapping [C II] emission. The CO emission stems from the shadow of the Horsehead Nebula, whereas I_{FIR} and $I_{[\mathrm{C\,II}]}$ originate from the surface of the bulk molecular cloud. They are spatially not coincident and are likely to correspond to different densities. Hence, the [C II] and the CO emission from this part cannot be correlated.

We do not see sharp Hα edges along the line cuts, as we would expect for multiple PDR fronts, but only on the primary surface of the molecular cloud. We clearly notice the onset of the bulk cloud behind the Horsehead Nebula in line cut C, and in line cut D there is a distinct shoulder to the primary Hα peak. Apart from that, the Hα emission across the molecular cloud is somewhat diffuse. We do notice coincidence, however, between the Hα emission contours and the PDR surfaces as traced by [C II] emission. In Fig. 2.18, PDR1 and PDR2 are lined-out by contours of high $I_{\mathrm{H}\alpha}$, whereas PDR3

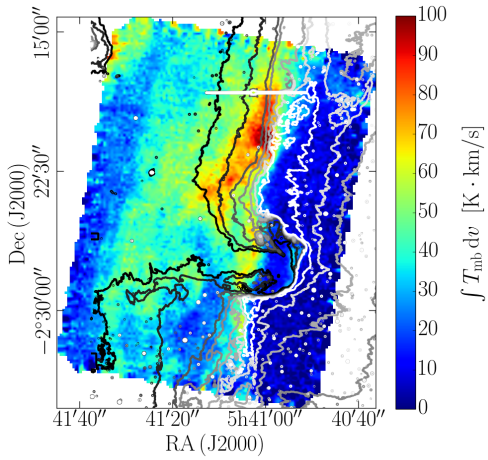

Figure 2.18: Original [C II] image (line-integrated intensity) with Hα emission in contours (slightly smoothed). Contours from black to white: $I_{\mathrm{H}\alpha} = 0.5, 1.0, 2.0, 3.0, 4.0, 5.0, 6.0 \times 10^{-3}\,\mathrm{erg\,s^{-1}\,cm^{-2}\,sr^{-1}}$.

and the intermediate PDR fronts are traced by contours of lower $I_{\mathrm{H}\alpha}$.

From the dust optical depth and the inferred densities, we can estimate the length of the PDR along the line of sight. At the surface of the Horsehead Nebula, $\tau_{160} \simeq 10^{-3}$ together with $n_{\mathrm{H}} \simeq 4 \times 10^4\,\mathrm{cm^{-3}}$ yields an estimate of about $l_{\mathrm{PDR}} \simeq 0.05\,\mathrm{pc}$. In the bulk, however, we would expect something closer to the projected extent, about $\simeq 0.2\,\mathrm{pc}$. Assuming a density of $n_{\mathrm{H}} \simeq 2 \times 10^4\,\mathrm{cm^{-3}}$, Habart et al. (2005) arrive at $l_{\mathrm{PDR}} \simeq 0.5\,\mathrm{pc}$, but comment that this seems implausibly high; they conclude that the density must actually be higher. If we adopt $n_{\mathrm{H}} \sim 2 \times 10^5\,\mathrm{cm^{-3}}$ (Habart et al. 2005) for the bulk and a dust optical depth of $\tau_{160} \simeq 10^{-2}$, we obtain $l_{\mathrm{Horsehead}} \simeq 0.17\,\mathrm{pc}$.

For PDR1 and PDR2, we estimate $l_{\mathrm{PDR1}} \simeq 1\,\mathrm{pc}$ and $l_{\mathrm{PDR2}} \simeq 0.5\,\mathrm{pc}$, respectively. PDR3 yields $l_{\mathrm{PDR3}} \simeq 1.5\,\mathrm{pc}$, but this is most likely not the length of the PDR but of the whole PDR+molecular cloud interior column. From the G_0 values of Section 2.4.3, assuming that $G_0 \propto l_{\mathrm{PDR}}$, we infer that l_{PDR3} lies in between l_{PDR1} and l_{PDR2}.

2.4.9 Comparison with models

As described in Section 6.3.3, we ran PDR models for an edge-on geometry with varying length along the line of sight and varying density (see also Fig. 6.6) at $G_0 = 100$. The respective model relations between tracers are plotted in Figs. 2.8a, b, e, and 2.9: $I_{[\mathrm{C\,II}]}/I_{\mathrm{FIR}}$ versus I_{FIR}, $I_{[\mathrm{C\,II}]}$ versus I_{FIR}, $I_{[\mathrm{C\,II}]}$ versus $I_{\mathrm{CO(1\text{-}0)}}$, and $I_{[\mathrm{C\,II}]}/I_{\mathrm{FIR}}$ versus $I_{\mathrm{CO(1\text{-}0)}}/I_{\mathrm{FIR}}$, respectively.

We have constructed models for selected depths of the molecular cloud along the line of sight $A_{\mathrm{V,los}}$, which we calculated from the gas column density using $N_{\mathrm{H}} = 2.0 \times 10^{21}\,\mathrm{cm^{-2}}\,A_{\mathrm{V}}$, and gas densities n_{H}, that we inferred from τ_{160} in Section 2.4.4 and the line cuts in Section 2.4.7, respectively. For PDR1, we estimated $A_{\mathrm{V,los}} \simeq 5.0$, whereas for PDR2 we got $A_{\mathrm{V,los}} \simeq 2.5$. The Horsehead PDR ranges from $A_{\mathrm{V,los}} \simeq 2.5$ at the edge to $A_{\mathrm{V,los}} \gtrsim 5.0$ deeper in the Horsehead Nebula. For the gas in PDR1 and PDR2, we assume $n_{\mathrm{H}} = 3.0 \times 10^3\,\mathrm{cm^{-3}}$; for the Horsehead PDR we take $n_{\mathrm{H}} = 4.0 \times 10^4\,\mathrm{cm^{-3}}$, but we note that the density increases with depth into the PDR according to a number of studies on that region (cf., e.g., Habart et al. 2005). Further, we ran models for

$n_{\rm H} = 1.6 \times 10^4\,{\rm cm}^{-3}$ to probe a density region that might either be occupied by the Horsehead PDR or by a denser (surface) structure overlaid on PDR1 and PDR2.

Figure 2.8a shows that the model predictions for the Horsehead with $A_{\rm V,los} = 0.5$ and $n_{\rm H} = 1.6 \times 10^4\,{\rm cm}^{-3}$ or $n_{\rm H} = 4.0 \times 10^4\,{\rm cm}^{-3}$ are consistent with the data, whereas we estimated $A_{\rm V,los} = 2.5$. The $A_{\rm V,los} = 2.5$ line with $n_{\rm H} = 4.0 \times 10^4\,{\rm cm}^{-3}$ could fit the data within the extent of beam dilution. The $A_{\rm V,los} = 5.0$ model lines cannot explain the data, even when taking into account beam-dilution effects. Another reason for the discrepancy might be dust depletion in this region decreasing the FIR emission. PDR1 is matched quite well by the curve for $A_{\rm V,los} = 5.0$ and $n_{\rm H} = 3.0 \times 10^3\,{\rm cm}^{-3}$, but the data points lie close to the $A_{\rm V,los} = 2.5$ with $n_{\rm H} = 3.0 \times 10^3\,{\rm cm}^{-3}$ line, as well. The latter also fits PDR2 quite well. The rest of the data points lie between these two curves and the curves for $A_{\rm V,los} = 0.5$. Similar conclusions can be drawn for Fig. 2.8b. The PDR data points are matched by the same model curves as before, with the remaining points lying in between these and the $A_{\rm V,los} = 0.5$ curves.

The comparison of the data with the model predictions for the relation between [C II] and CO(1-0) is less clear-cut. In Fig. 2.8e, PDR1 and PDR2 lie close to the $A_{\rm V,los} = 5.0$ line. However, also the higher density lines agree with the data points in PDR1. The Horsehead points lie close to the $A_{\rm V,los} = 2.5$ lines instead of the $A_{\rm V,los} = 5.0$ or 0.5 lines. This might reflect the fact that $A_{\rm V,los} = 2.5$ in deeper layers of the Horsehead PDR, whereas it might be lower in the [C II] emitting surface layers.

In Fig. 2.9, model lines group according to their respective densities and there is comparatively little variation with $A_{\rm V,los}$. PDR1 lies on the model lines with $n_{\rm H} = 1.6 \times 10^4\,{\rm cm}^{-3}$. This behavior might imply that the density deeper in the cloud in this region is increased. PDR2 lies on the $n_{\rm H} = 3.0 \times 10^3\,{\rm cm}^{-3}$ lines. All the $A_{\rm V,los}$ lines for $n_{\rm H} = 1.6 \times 10^4\,{\rm cm}^{-3}$ run through the Horsehead data points, though some data points lie closer to the model lines for higher or lower density.

The gas temperatures in the top layers of the PDRs are predicted by the models as $T \simeq 130\,{\rm K}$ for PDR1 and PDR2, and $T \simeq 115\,{\rm K}$ for the Horsehead PDR. The latter again is a deviation from the value we infer, $T \simeq 60\,{\rm K}$, and the temperature estimated by Habart et al. (2011), which is $T \simeq 264\,{\rm K}$; it lies close to the value assumed by Goicoechea et al. (2009) for modeling [O I] emission from the Horsehead PDR, $T \simeq 100\,{\rm K}$, and close to the value deduced from equating the photoelectric heating efficiency with the [C II]+[O I] cooling efficiency, $T \simeq 100\,{\rm K}$ (cf. Section 2.4.6). For PDR1 and PDR2, the gas temperatures computed in Section 2.4.4 assuming excitation by C^+–H collisions, $T \simeq 90\,{\rm K}$, are in good enough agreement with the value predicted by the model, especially considering the uncertainties. The derived temperatures would be substantially higher if we considered collisions with H_2 to dominate the excitation of C^+ ($T \simeq$ 160-200 K); the contribution of C^+–H_2 collisions may be reflected in the underestimation of the gas temperature. Other reasons for slight discrepancies may be the uncertainties in gas density, the error margins of the spectral parameters that we used in the analysis, the uncertainty in the C^+ column, and, of course, uncertainties within the models.

In conclusion, we are quite capable of reproducing the observed data with model data within the given uncertainties. Our $A_{\rm V,los}$ and the gas densities can only be estimates, as is the geometry of the molecular cloud that probably has a corrugated surface and density gradients running through it.

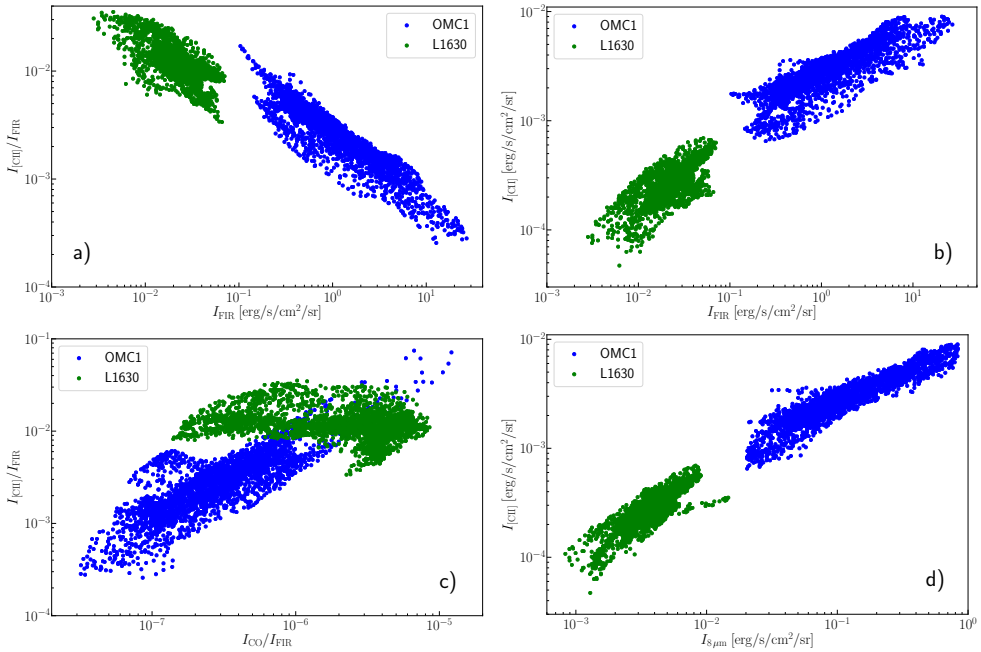

Figure 2.19: Correlation plots for L1630 (Orion B) and OMC1 (Orion A); the OMC1 data are convolved to 25″ resolution, L1630 data to 36″ resolution. CO data are for the CO(1-0) line in L1630 and for the CO(2-1) line, divided by 8 (see Section 2.4.10), in OMC1.

2.4.10 Comparison with OMC1 in the Orion A molecular cloud

One of the aims of the present study is to establish correlations of astrophysical tracers under moderate conditions (intermediate density and moderate UV-radiation field) and to compare those to correlations found under harsher conditions (higher density and strong UV-radiation field). An example of the latter conditions is OMC1 in the Orion A complex. Whereas L1630 has edge-on geometry, OMC1 can be approximated as a face-on PDR with respect to its UV-illuminating sources, the Trapezium cluster. In this section, we compare the correlations found in L1630 to those in OMC1. Data on OMC1 are from Goicoechea et al. (2015b).

The OMC1 data seem to continue the trend found in our L1630 data very well in Fig. 2.19a, b, and d. Both in OMC1 and in L1630, the $8\,\mu$m emission correlates well with $I_{[\mathrm{C\,II}]}$. From a linear fit, we find $I_{[\mathrm{C\,II}]} \simeq 4.9 \times 10^{-2} I_{8\,\mu\mathrm{m}} + 9.0 \times 10^{-5}\,\mathrm{erg\,s^{-1}\,cm^{-2}\,sr^{-1}}$ ($\rho = 0.79$), which is similar to the result of Goicoechea et al. (2015b): $I_{[\mathrm{C\,II}]} \simeq 2.6 \times 10^{-2} I_{8\,\mu\mathrm{m}} + 1.6 \times 10^{-3}\,\mathrm{erg\,s^{-1}\,cm^{-2}\,sr^{-1}}$ ($\rho = 0.91$). However, the slope of Goicoechea et al. (2015b) should be divided by 2.9, since they use a bandwidth of the IRAC $8\,\mu$m band of $1\,\mu$m, whereas it is really $2.9\,\mu$m. Thus, there is some discrepancy, which expresses itself as a flattening of the correlation curve at high $8\,\mu$m and [C II] intensity, comparable to the I_{FIR}-$I_{[\mathrm{C\,II}]}$ dependency (Fig. 2.19a).

In Fig. 2.19c, the $I_{[\mathrm{C\,II}]}/I_{\mathrm{FIR}}$ versus $I_{\mathrm{CO}}/I_{\mathrm{FIR}}$ relation in L1630 and OMC1 is shown. CO-line intensities in L1630 are from the CO(1-0) transition, whereas in OMC1 line intensities are from the CO(2-1) transition; we divide the CO(2-1) intensity in OMC1 by 8, the frequency ratio of the two lines cubed, which for optically thick thermalized CO emission as in OMC1 (cf. Goicoechea et al. 2015b) gives a good

estimate of the CO(1-0) intensity. The data points form two patches with different slopes. Yet, the L1630 data in their entirety seem to show a continuation of the trend set by the OMC1 data. We note that L1630 is characterized by a much higher $I_{[\mathrm{C\,II}]}/I_{\mathrm{FIR}}$ which reflects the decrease of photoelectric heating efficiency with increasing G_0 and the importance of [O I] cooling for high G_0 and high density. The difference in behavior of the $I_{[\mathrm{C\,II}]}/I_{\mathrm{FIR}}$ versus $I_{\mathrm{CO}}/I_{\mathrm{FIR}}$ relation reflects the difference in geometry. As demonstrated in the study of Goicoechea et al. (2015b), OMC1 is well-modeled as a face-on PDR, while L1630 has edge-on geometry (cf. Fig. 2.9).

Goicoechea et al. (2015b) find a decrease of $I_{[\mathrm{C\,II}]}/I_{\mathrm{FIR}}$ with dust temperature, which is notably different from our observation shown in Fig. 2.8d; we find no significant slope. Also, we obtain a less good correlation of I_{FIR} with τ_{160} than do Goicoechea et al. (2015b) for OMC1 (cf. Section 2.3.5, Fig. 2.11a). The figure corresponding to our Fig. 2.10, $I_{[\mathrm{C\,II}]}/I_{\mathrm{FIR}}$ versus τ_{160}, in Goicoechea et al. (2015b), reveals that OMC1 matches a slab of constant foreground [C II] emission, that is, a face-on PDR geometry, much better than the studied region of L1630.

2.5 Conclusion

We have analyzed the velocity-resolved [C II] map towards the Orion B molecular cloud L1630 observed by upGREAT onboard SOFIA. We compared the observations with FIR photometry, IRAM 30 m CO(1-0), IRAC 8 μm, SCUBA 850 μm, and Hα observations.

About 5% of the total [C II] luminosity, 1 $L_\odot$, of the surveyed area stems from the H II region IC 434; the molecular cloud (not including the north-eastern corner with possible contamination from NGC 2023) accounts for 95% , that is, 13 $L_\odot$. The bulk of the [C II] emission originates from PDR surfaces. The total FIR luminosity of the mapped area (without NGC 2023) is 1210 $L_\odot$, of which 1175 $L_\odot$ stem from the molecular cloud and 35 $L_\odot$ from the H II region. This yields an average [C II] cooling efficiency in the molecular cloud within the mapped area of 1%. From the dust optical depth, we derive a total gas mass of $M_{\mathrm{gas}} \simeq 280\,M_\odot$. Most of the gas mass, $M_{\mathrm{gas}} \simeq 250\,M_\odot$, is contained in the CO-emitting molecular cloud. The [C II]-bright gas contributes $M_{\mathrm{gas}} \simeq 20\,M_\odot$, which is only about 8% of the total gas mass in the mapped area. This is in close agreement with the PDR mass fraction traced by [C II] found by Goicoechea et al. (2015b) in OMC1, which also is 8% (within a factor of approximately two). The mass of the H II region accounts for an additional $M_{\mathrm{gas}} \simeq 10\,M_\odot$.

The [C II] cooling efficiency is found to decrease with increasing I_{FIR}, in continuation of the results from OMC1 (Goicoechea et al. 2015b). Its peak value is about 3×10^{-2}, ranging down to 3×10^{-3}. Highest values are obtained at the edge of the molecular cloud towards the H II region. The overall [C II] cooling efficiency of the mapped area, calculated from the total luminosities $L_{[\mathrm{C\,II}]}/L_{\mathrm{FIR}}$, is $\sim 10^{-2}$; this compares to an average single-pixel [C II] cooling efficiency in PDR regions of $1.1 \pm 0.3 \times 10^{-2}$. We note that due to the edge-on geometry of the molecular cloud, I_{FIR} does not trace the incident UV radiation in general, for there may be deeper and colder cloud layers located along the line of sight. The [C II] intensity increases with FIR intensity. [C II] intensity and PAH 8 μm intensity are closely related, reflecting the predominance of gas heating through the photoelectric effect on (clusters of) PAHs and very small grains.

We derive gas densities of the molecular cloud in the range $n_{\mathrm{H}} \simeq 10^3$-$10^4\,\mathrm{cm}^{-3}$,

with the Horsehead PDR having a slightly higher density, $n_{\rm H} \simeq 4 \times 10^4\,{\rm cm}^{-3}$. Dust temperatures lie in the range $T_{\rm d} \simeq$ 18-32 K. From the column densities, we derive an extent of the cloud along the line of sight of $l \simeq$ 0.5-1 pc at the edge of the cloud, and $l \simeq 1.5$ pc at the eastern border of the studied area. The Horsehead Nebula scores low with $l \simeq 0.05$ pc. As discussed, these values are afflicted by significant uncertainties.

We estimated the [C II] optical depth and the excitation temperature towards three representative points in the mapped area. From our analysis we gather that the column density of the Horsehead PDR cannot be straightforwardly calculated from the dust optical depth. By deep observations of the brightest [^{13}C II] line, we can calculate the [C II] optical depth directly, implying [C II] emission to be optically thick: $\tau_{\rm [C\,II]} \simeq 2$. The corresponding (beam-averaged) excitation temperature is $T_{\rm ex} \simeq 60$ K, which is basically equal to the gas temperature. From other studies we observe higher temperatures, which would imply a lower C^+ column density. Also our models for lower C^+ column density match the Horsehead data in the correlation diagrams, as opposed to those for the C^+ column density inferred from [^{13}C II]. Towards PDR1 and PDR2, we obtain [C II] optical depths of $\tau_{\rm [C\,II]} \simeq 1.5$ and excitation temperatures of $T_{\rm ex} \simeq 65$ K, which gives a gas temperature of $T \simeq 90$ K.

The observed [C II] intensity, in combination with the [O I] intensity where appropriate, provides a direct measure of the heating efficiency of the gas. We have compared the observed heating efficiency with models for the photoelectric effect on PAHs, clusters of PAHs, and very small grains by Bakes & Tielens (1994). Theory and observations show a very similar dependence on the ionization parameter γ, albeit that theory seems to be offset to a slightly higher efficiency. This may, for example, reflect a too high abundance of these species in the models, an issue we will revisit in a future study.

We have endeavored to establish the edge-on nature of the Orion B L1630 molecular cloud. The data suggest that there are multiple PDR fronts across the molecular cloud, implying that the cloud surface is warped and not a single edge-on bulk. The edge-on warped geometry makes it difficult to correlate different quantities with each other, since they may relate to offset layers of the molecular cloud and depend on the local inclination of the cloud surface as well as on the length of the emitting column along the line of sight. Our model predictions for edge-on PDRs are capable of replicating the observed correlations between $I_{\rm [C\,II]}$ and $I_{\rm FIR}$; we can also interpret the model correlations between $I_{\rm [C\,II]}$ and $I_{\rm CO(1\text{-}0)}$.

Velocity-resolved line observations are an excellent tool to study gas dynamics and to identify distinct gas components by their different kinematic behavior. The line profile allows inference of the line optical depth, especially when line observations of isotopes (or isotopologues in the case of molecular lines) are available. In the present study, the [C II] line profile yields information on the origin of the emission, narrow in dense PDRs, broad in the H II region. In combination with other tracers, we can form a picture of the physical conditions prevailing in a molecular cloud. Several more tracers could be included to render the picture more comprehensive such as [O I] and H I.

Acknowledgements

JRG and EB thank the ERC for funding support under grant ERC-2013-Syg-610256-NANOCOSMOS, and the Spanish MINECO under grant AYA2012-32032. JP, FLP, ER, and EB acknowledge support from the French program “Physique et Chimie du

Milieu Interstellaire" (PCMI) funded by the Centre National de la Recherche Scientifique (CNRS) and Centre National d'Études Spatiales (CNES). Studies of the ISM at Leiden Observatory are supported through the Spinoza prize of the Dutch Science Foundation, NWO.

2.A Calculating [C II] optical depth and excitation temperature

For optically thick [C II] emission, we can employ the following two equations to get an estimate of the optical depth and the excitation temperature[8]:

$$T_{\mathrm{P}} \approx J(T_{\mathrm{ex}}) = \frac{91.2\,\mathrm{K}}{e^{91.2\,\mathrm{K}/T_{\mathrm{ex}}} - 1} \tag{2.12}$$

$$\tau_{[\mathrm{C\,II}]} = \frac{A\lambda^3}{4\pi b} N_{\mathrm{C}^+} \frac{e^{91.2\,\mathrm{K}/T_{\mathrm{ex}}} - 1}{e^{91.2\,\mathrm{K}/T_{\mathrm{ex}}} + 2} \tag{2.13}$$

$$\approx \frac{A\lambda^3}{4\pi b} N_{\mathrm{C}^+} \frac{91.2\,\mathrm{K}/T_{\mathrm{P}}}{91.2\,\mathrm{K}/T_{\mathrm{P}} + 3}, \tag{2.14}$$

where $A = 2.3 \times 10^{-6}\ \mathrm{s}^{-1}$ and b is the line width with $\tau_{[\mathrm{C\,II}]} b \approx \int \tau_{[\mathrm{C\,II}]} \mathrm{d}v$ (cf. eq. (5) in Gerin et al. 2015). For an optically thin emission, we take into account the dependence of the peak temperature on the optical depth. Here, we assume that $\tilde{f}(\tau) = 1 - e^{-\tau}$ accounts for the increase in the peak temperature with optical depth.[9] Hence, the above becomes

$$T_{\mathrm{P}} \approx J(T_{\mathrm{ex}})(1 - e^{-\tau_{[\mathrm{C\,II}]}}) \tag{2.15}$$

$$\tau_{[\mathrm{C\,II}]} \approx \frac{A\lambda^3}{4\pi b} N_{\mathrm{C}^+} \frac{91.2\,\mathrm{K}(1 - e^{-\tau_{[\mathrm{C\,II}]}})/T_{\mathrm{P}}}{91.2\,\mathrm{K}(1 - e^{-\tau_{[\mathrm{C\,II}]}})/T_{\mathrm{P}} + 3}. \tag{2.16}$$

Equation (2.16) has the form $\tau = g(\tau)$, which can be solved either graphically or by the fix-point method. In order to do so, we need to make some assumptions on b and N_{C^+}. In the following, we assume that opacity broadening is insignificant, that is, the lines are Gaussian such that $b \approx \Delta v_{\mathrm{FWHM}}$. The C^+ column density we take from the dust optical depth.

2.B Face-on calculation

In order to compare our observations with face-on PDRs, we integrate our, presumably edge-on, observations along the depth into the molecular cloud from the surface with respect to the incident FUV radiation. We normalize the measured intensity to the pixel size ($15''$), assuming a line-of-sight length of $l \simeq 1\,\mathrm{pc}$ and an average gas density of $n_{\mathrm{H}} \simeq 3 \times 10^3\,\mathrm{cm}^{-3}$. We further assume that radiation is emitted isotropically and homogeneously along the line of sight. The correlation plots are shown in Fig. 2.20.

[8] Neglecting background IR emission, $T_{bg} \simeq 2.5\,\mathrm{K}$ for $T_{\mathrm{d}} \simeq 25\,\mathrm{K}$.

[9] From Tielens (2010) we get $f(\tau) = \int_0^\tau \beta(\tau')\,\mathrm{d}\tau'$ with eq. (2.44) for β. However, this expression takes into account opacity broadening of the line; the standard radiative transfer solution uses $\tilde{f}(\tau) = 1 - e^{-\tau}$, so we assume this to be the expression describing the increase in peak emission.

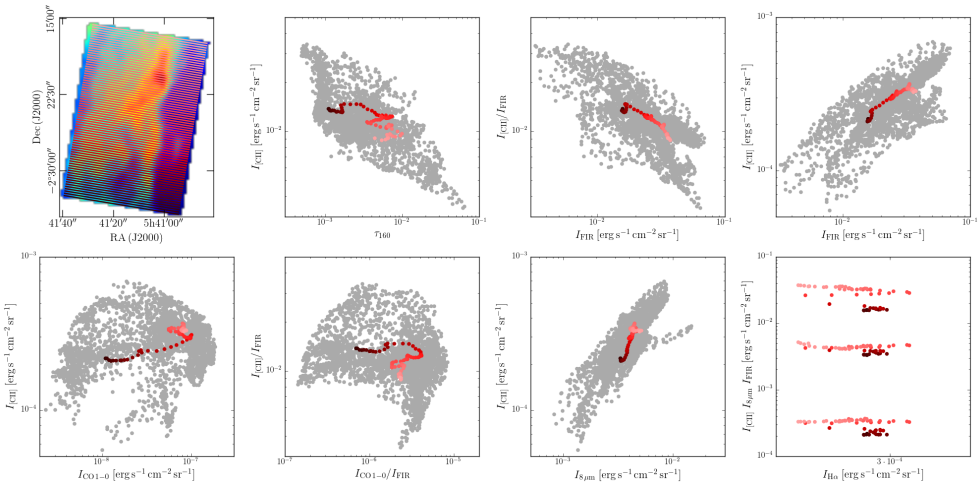

Figure 2.20: Correlation plots. Red dots are the face-on integrated values; gray dots are the original data shown throughout the main text. The first panel shows the lines along which the data are integrated.

3

Disruption of the Orion molecular core 1 by wind from the massive star θ^1 Orionis C

C. Pabst, R. Higgins, J. R. Goicoechea, D. Teyssier, O. Berné, E. Chambers, M. Wolfire, S. T. Suri, R. Guesten, J. Stutzki, U. U. Graf, C. Risacher, A. G. G. M. Tielens

Nature 565, 618 (2019)

Massive stars inject mechanical and radiative energy into the surrounding environment, which stirs it up, heats the gas, produces cloud and intercloud phases in the interstellar medium, and disrupts molecular clouds (the birth sites of new stars; McKee & Ostriker 1977; Kim et al. 2013). Stellar winds, supernova explosions and ionization by ultraviolet photons control the lifetimes of molecular clouds (Williams & McKee 1997; Wareing et al. 2018; Naiman et al. 2018; Peters et al. 2017; Dale et al. 2014). Theoretical studies predict that momentum injection by radiation should dominate that by stellar winds (Haid et al. 2018), but this has been difficult to assess observationally. Velocity-resolved large-scale images in the fine-structure line of ionized carbon ([C II]) provide an observational diagnostic for the radiative energy input and the dynamics of the interstellar medium around massive stars. Here we report observations of a one-square-degree region (about 7 parsecs in diameter) of Orion molecular core 1 – the region nearest to Earth that exhibits massive-star formation – at a resolution of 16 arcseconds (0.03 parsecs) in the [C II] line at 1.9 terahertz (158 micrometres). The results reveal that the stellar wind originating from the massive star θ^1 Orionis C has swept up the surrounding material to create a 'bubble' roughly four parsecs in diameter with a 2,600-solar-mass shell, which is expanding at 13 kilometres per second. This finding demonstrates that the mechanical energy from the stellar wind is converted very efficiently into kinetic energy of the shell and causes more disruption of the Orion molecular core 1 than do photo-ionization and evaporation or future supernova explosions.

We surveyed a one-square-degree region of the Orion molecular cloud, centred on the Trapezium cluster (θ^1 Orionis) and the Orion molecular core 1 (OMC-1) behind it. The survey was conducted in the 1.9-THz (158-μm) [C II] fine-structure line using the 14-pixel, heterodyne, high-spectral-resolution spectrometer upGREAT (Risacher et al. 2016) on board the Stratospheric Observatory For Infrared Astronomy (SOFIA; Methods). In Fig. 3.1 we compare the [C II] integrated intensity map with the mid-infrared and far-infrared maps that result from ultraviolet- pumped fluorescence by polycyclic aromatic hydrocarbon molecules and thermal dust continuum emission, respectively. Each map clearly shows the interaction of the Trapezium cluster with the dense molecular core (centre), the large, wind-blown bubble associated with the Orion Veil (south) and the bubble created by the B stars illuminating the reflection nebulae NGC 1973, NGC 1975, and NGC 1977 (north). Here, we focus on the prominent Veil bubble associated with the stellar wind from θ^1 Ori C. This shell consists of neutral atomic H gas and is very prominent in the [C II] map; however, there is no detectable counterpart in carbon monoxide, H_2 or other molecular tracers because the shell is too tenuous for these species to persist (for example, $H_2/H < 2 \times 10^{-4}$ and $C/C^+ = 10^{-4}$; Welty et al. 2012; Jenkins & Tripp 2011). Likewise, the complex pattern of absorption and emission features and the presence of multiple (foreground) components preclude recognition of the large-scale structure of the shell in 21-cm H I studies (van der Werf et al. 2013). X-ray observations (Güdel et al. 2008) have shown that this bubble is filled with tenuous (about $1\,\mathrm{cm}^{-3}$) hot ($2 \times 10^6\,\mathrm{K}$) gas created by the strong stellar wind (mechanical luminosity $L_w = 8 \times 10^{35}\,\mathrm{erg\,s}^{-1}$; Howarth & Prinja 1989; Stahl et al. 1996) from the most massive star in the region, θ^1 Ori C (Fig. 3.8).

Although each infrared image (Fig. 3.1) traces the morphology of the Veil, only [C II] probes the kinematics, because it can use the Doppler effect to measure gas velocities. The high spectral resolution of upGREAT allows a detailed investigation of the dynamics of the gas, revealing the kinematic signature of an expanding half-shell as, with increasing velocity, it displaces further away from the centre of the projected shell

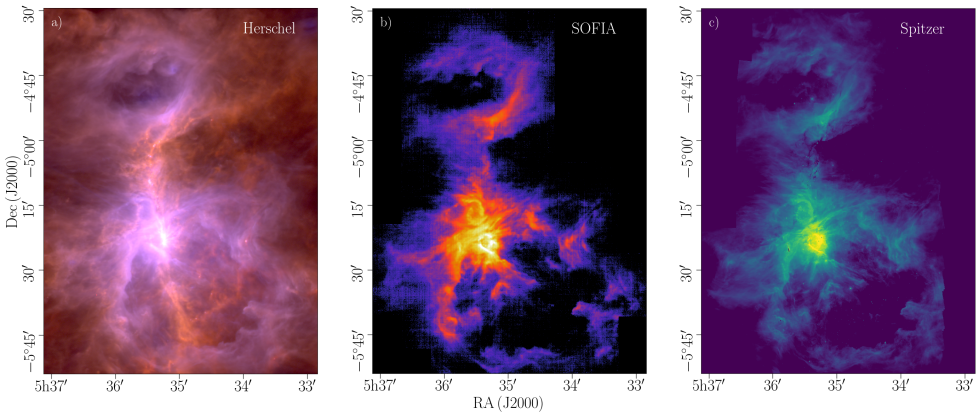

Figure 3.1: Three infrared images of the Orion region of massive star formation. Each of these images shows very similar morphology but in different tracers of the dust and gas in the molecular cloud. a) The dust continuum, observed by the Herschel Space Observatory in far-infrared (blue; using PACS (photodetector array camera and spectrometer)) and sub-millimetre (red; using SPIRE (spectral and photometric imaging receiver)) emission, measures the conversion of far-ultraviolet radiation from massive stars to dust emission in the photodissociation region. b) The integrated 1.9-THz (158-μm) [C II] emission, observed by the upGREAT instrument on board SOFIA, traces the cooling and kinematics of the gas in the photodissociation region. c) The 8-μm polycyclic aromatic hydrocarbon emission, observed by the IRAC instrument on board the Spitzer Space Telescope, outlines the far-ultraviolet-illuminated surfaces of the photodissociation region. A comparison between the three panels does not do justice to the richness of the [C II] data: we can use the roughly 2,200,000 spectra that we obtained to turn this two-dimensional image into a three-dimensional one, enabling a detailed study of the kinematics of the gas.

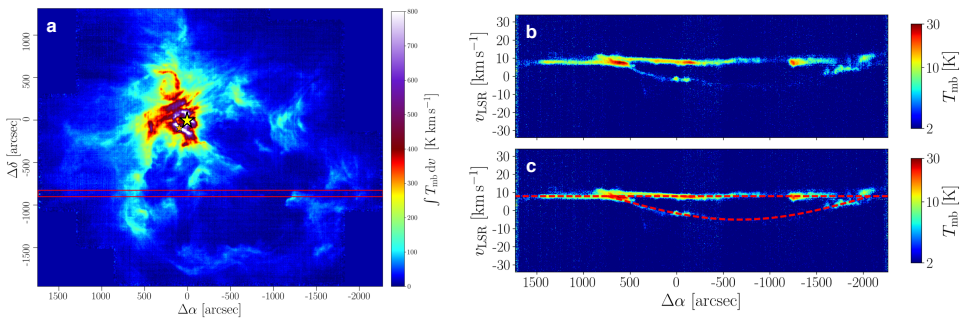

Figure 3.2: Position-velocity diagrams of the [C II] emission along selected cuts across the Veil. a) The Veil bubble in the integrated intensity of the 1.9-THz [C II] emission. The red lines delineate the region over which the spectra were collapsed to produce the east-west cut shown in b and c. The origin (yellow star) corresponds to the position of θ^1 Ori C: right ascension RA(J2000) = 5h 35min 16.46s and declination dec.(J2000) = $-5^\circ\,23'\,22.8''$). The orange star indicates the position of an unrelated star, θ^2 Ori A: RA(J2000) = 5h 35min 22.90s and dec.(J2000) = $-5^\circ\,24'\,57.82''$). b) Position-velocity diagram of the [C II] emission in the east-west cut indicated in a. The velocity shown is measured in the frame of the local standard of rest. Other horizontal and vertical cuts yield similar diagrams (Fig. 3.10). c) A simple model of a spherical half-shell expanding at a constant velocity of 13 km s^{-1} (red dashed lines) is fitted to the data in b. All of the observational position-velocity diagrams are in good agreement with this simple model.

(Fig. 3.9). The kinematic data demonstrate good agreement between the observed velocity structure and a simple model of a half-shell expanding at 13 km s^{-1} towards us while expansion into OMC-1 is stopped by its high density ($n = 10^4$-10^5 cm^{-3}; Fig. 3.2, Fig. 3.10). The small velocity difference (about 1 km s^{-1} towards us) between C^+ and CO emission from the OMC-1 gas represents a slow photo-evaporative flow of atomic gas (H and C^+) into the bubble, where H I s then ionized by extreme-ultraviolet (energy $E > 13.6$ eV) photons from θ^1 Ori C before flowing into the cavity at about 17 km s^{-1} (O'Dell et al. 2017). We determined the mass of gas in the Veil to be between $1,700\,M_\odot$ and $3,400\,M_\odot$, where $M_\odot$ is the mass of the Sun, with a most likely value of $2,600\,M_\odot$ from an analysis of the far-infrared dust emission (Methods). Analysis of the weak [^{13}C II] hyperfine line component that is apparent after averaging over the shell results in a very similar value. This mass estimate is about twice the mass derived from the H I column densities observed along pencil beams towards the Trapezium cluster, which probably reflects known fluctuations in the shell thickness in these directions. The Veil mass that we derive is comparable to the mass of gas in OMC-1 (about $3,000\,M_\odot$; Buckle et al. 2012) and to the mass of the (newly formed) stellar cluster in OMC-1 (about $1,800\,M_\odot$; Hillenbrand 1997), and greatly exceeds the mass of ionized gas ($2\,M_\odot$ in the dense Huygens region and $20\,M_\odot$ in total; Wilson et al. 1997) and the mass of the X-ray-emitting hot plasma ($0.07\,M_\odot$ (Güdel et al. 2008, ; Table 4.8). A schematic of the region is shown in Fig. 3.3.

Adopting a homogeneous cloud and a size of 2 pc, the mass of swept-up material corresponds to an initial H_2 density of 1.4×10^3 cm^{-3}. The radius of the shell is $R_s(t) = [125/(154\pi)]^{1/5}(L_w/\rho_0)^{1/5}t^{3/5}$, where ρ_0 is the initial density and t is time (Weaver et al. 1977), from which we derive an age of 0.2 Myr. This age is in the range of previous (uncertain) estimates of 3×10^4-10^6 yr based on the expansion of the H II region and on the ages of the protoplanetary disks in the Orion nebula and of the stars

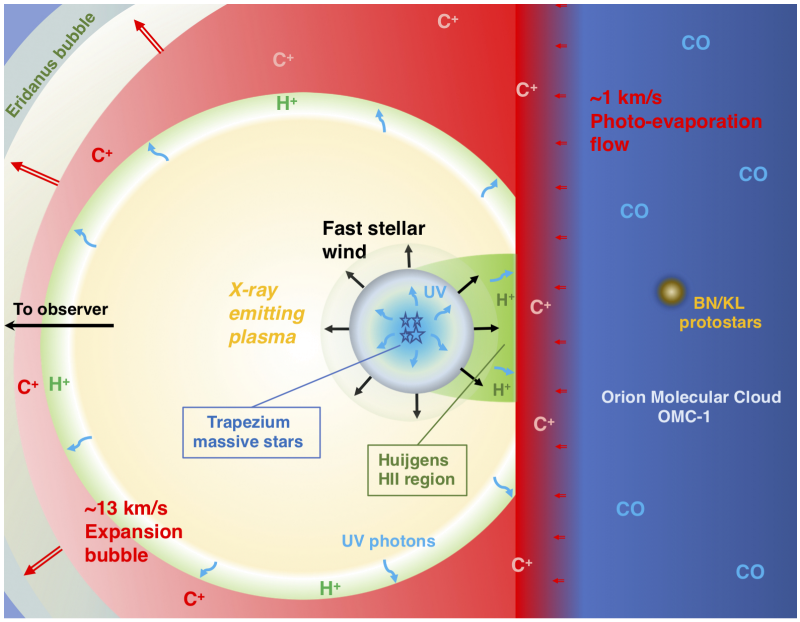

Figure 3.3: Sketch of the structure of the Orion stellar-wind bubble. The stellar wind (black arrows) from the massive star θ^1 Ori C drives a shock into its surroundings which sweeps up the gas. At the same time, this swept-up gas drives another shock (the reverse shock; purple-grey) into the stellar wind, which converts the kinetic motion of the stellar wind into thermal energy, creating a hot (about 2×10^6 K), tenuous (about $1\,\mathrm{cm}^{-3}$), X-ray-emitting plasma (yellow). Adiabatic expansion of this hot gas has swept up the surrounding gas into a slowly expanding ($13\,\mathrm{km\,s}^{-1}$; large red double arrows) 4-pc-diameter half-shell (the Veil bubble; red). The dense Orion molecular core 1 (OMC-1; dark blue) behind the Trapezium cluster (bright blue) stops the bubble expanding in that direction. The BN/KL protostars represent the region of current star formation deep inside OMC-1. Photons with energies of more than 13.6 eV can ionize H to create the dense ionized gas layer (the Huygens region; green) behind the Trapezium cluster, which dominates optical images of the region. This ionized gas expands into the bubble at around $17\,\mathrm{km\,s}^{-1}$ with respect to the background molecular gas. The largely empty interior of the hot gas bubble allows ultraviolet photons (blue wavy arrows) from θ^1 Ori C to travel unimpeded until they interact with the gas and dust in the shell. These photons heat the dust, leading to bright far-infrared continuum emission, and excite large polycyclic aromatic hydrocarbon molecules, producing the 8-μm fluorescence emission (Fig. 3.1a, c). Far-ultraviolet photons will ionize carbon and heat the largely neutral gas in the surface layers of the photodissociation region to about 200 K, causing a gentle ($1\,\mathrm{km\,s}^{-1}$) photo-evaporative flow (small red double arrows). This gas cools through the 1.9-THz [C II] line. On a much larger scale (about 350 pc), the Orion molecular cloud (dark blue) and the Veil bubble (red) are embedded in the Orion-Eridanus superbubble (blue-grey; not to scale).

in the Orion nebula cluster (Hillenbrand 1997; Henney & O'Dell 1999); however, it exceeds the typical dynamical lifetime expected for Trapezium-type multiple systems, 10-50 kyr (Allen et al. 2017). The lifetime of the bubble that we derived (0.2 Myr) and the mass loss rate of θ^1 Ori C imply a total injected stellar mass of $0.08\,M_\odot$, close to the mass of the hot plasma estimated from X-ray observations (Güdel et al. 2008).

We compare the mass, energy and luminosity of the shell to those of other relevant components in Table 4.8. The total kinetic energy of the expanding half-shell is roughly 4×10^{48} erg, comparable to the total mechanical energy delivered by the wind over the age of the bubble (5×10^{48} erg). The total kinetic energy in the ionized gas (6×10^{46} erg) is much less than the kinetic energy of the wind bubble. The X-ray luminosity observed over the age of the bubble is only 3×10^{44} erg and the hot gas expands adiabatically. Assuming that the hot gas fills the cavity, its thermal energy is only around 10^{47} erg (Güdel et al. 2008). Theory predicts that 5/11 of the mechanical energy of the stellar wind will go into heating the hot gas and 6/11 will go into work done on the environment (Weaver et al. 1977). By contrast, we observe that 4/5 of the mechanical energy of the wind has gone into the kinetics of the swept-up shell. This discrepancy may indicate that the bubble is leaking hot gas into the surrounding Orion-Eridanus superbubble (Güdel et al. 2008). However, although detailed inspection of the shell reveals that it is thin in places, the position-velocity diagrams provide no clear kinematic signature of rupture, which would appear as a local, rapid variation in velocity. The radiative luminosity of θ^1 Ori C over 0.2 Myr is 6×10^{51} erg. The kinetic energy of the ionized gas therefore corresponds to an efficiency of 10^{-5} for the coupling of this energy to radial momentum. This efficiency is in good agreement with theoretical studies of this coupling for clouds phases of the interstellar medium (Haid et al. 2018). We note that the radiation pressure ($4 \times 10^4\,\mathrm{cm}^{-3}\,\mathrm{K}$) is well below the thermal pressure of the hot gas ($10^6\,\mathrm{cm}^{-3}\,\mathrm{K}$) and that the Orion nebula cluster (Orion 1d; see Methods section 'Orion' for a detailed description of the region) is very young (less than 1 Myr), so massive stars have not had time to evolve to the supernova stage. Consequently, neither of these processes will have had a role in the creation of the Veil bubble.

The slow shock that propagates into the environment during the expansion will heat swept-up molecular gas to around 3,000 K; this internal energy is quickly radiated away in high-rotational-level emission of CO and rotational H_2 lines. Such low-velocity shocks do not dissociate or ionize molecular gas, or emit in the [C II] line (Flower & Pineau Des Forêts 2010). The total observed luminosity radiated by dust in the swept-up shell is roughly $6 \times 10^4\,L_\odot$, where $L_\odot$ is the luminosity of the Sun, which results in around 1.5×10^{51} erg over the expansion time of the Veil. The luminosity of θ^1 Ori C provides this energy as stellar photons travel unimpeded through the evacuated cavity, illuminating the inner boundary of the bubble. This excavation turns the [C II] line and the far-infrared and mid-infrared tracers into good tracers of the shell (Fig. 3.1). Observations have shown that gas illuminated by strong radiation fields typically emits between 0.5% and 2% of the stellar photon energy in the 1.9-THz [C II] gas cooling line (Hollenbach & Tielens 1999; Pabst et al. 2017). The stellar far-ultraviolet radiation field is coupled to the gas through the photo-electric effect on polycyclic aromatic hydrocarbon molecules and very small grains (Bakes & Tielens 1994). The [C II] emission (luminosity $L_{\mathrm{C}^+} = 200\,L_\odot$) observed for the Orion Veil translates into a photo-electric efficiency of 0.3%, well in line with these studies. Ultraviolet photon energy that does not go into ionization emerges as the polycyclic aromatic hydrocarbon emission features that so prominently outline the shell (Fig. 3.1).

The velocity of the shell that we derived ($13\,\mathrm{km\,s^{-1}}$) exceeds the escape velocities of OMC-1 (about $2\,\mathrm{km\,s^{-1}}$) and the Orion molecular cloud A (about $8\,\mathrm{km\,s^{-1}}$). Eventually, the wind bubble will break open and vent the hot gas and the ionized gas into the surrounding, tenuous Orion-Eridanus superbubble (Methods). The coasting, neutral shell will then dissolve into the hot plasma. Supernovae typically occur every 1 Myr in the Orion OB 1a and 1b sub-associations (see Methods section 'Orion' for details of the sub-associations) and sweep up all the 'loose' material that has been deposited in the superbubble by bubbles such as the Veil bursting and transport it to the wall of the superbubble (Ochsendorf et al. 2015). In essence, mechanical energy from a supernova (about 10^{51} erg) will go into rejuvenation of the hot gas in the superbubble and transportation of the swept-up gas towards its walls; very little will couple to the Orion molecular clouds A and B. Barnard's loop may be the latest episode in this process (Ochsendorf et al. 2015). Estimates of the proper motion of θ^1 Ori C with respect to the molecular cloud range from about $5\,\mathrm{km\,s^{-1}}$ to $15\,\mathrm{km\,s^{-1}}$, with the latest evidence pointing towards the lower value (Kraus et al. 2009). Therefore, θ^1 Ori C will move about 25 pc away from the cloud before it explodes as a supernova. Hence, like the Orion OB 1a and 1b stars, as a supernova θ^1 Ori C will not affect the evolution of its 'birth' core, OMC-1. Three-dimensional hydrodynamic simulations reveal that, from a theoretical perspective, stellar winds are key to the regulation of star formation through their effect on molecular clouds (Gatto et al. 2017). Here we have analysed one specific case of the interaction of a wind from a massive star with its environment; whether our conclusions apply more generally still needs to be assessed. 1.9-THz [C II] observations with SOFIA are ideal for such studies.

Galaxy formation and evolution result from the combined effects of a complicated set of physical processes that affect the baryons in a ΛCDM (Lambda cold dark matter) cosmology dominated by dark matter. In particular, stellar feedback controls the evolution of galaxies (Naab & Ostriker 2017). Stellar winds from O-type massive stars are very effective at disrupting molecular cores and star formation. Because energy input from stellar wind is dominated by the most massive stars in a cluster whereas that from supernovae is dominated by the more numerous B-type stars, the predominance of the disruption caused by stellar winds has a direct effect on cosmological simulations. As our study shows, relevant stellar feedback processes act on much smaller scales (0.2-2 pc) than are resolved by hydrodynamic studies of the evolution of the interstellar medium (more than 2 pc) or cosmological simulations (more than 50 pc; Kim et al. 2013; Wareing et al. 2018; Naiman et al. 2018; Peters et al. 2017; Dale et al. 2014). 1.9-THz [C II] studies on the dynamic interaction of massive stars through stellar winds with nearby molecular clouds can provide validation for theoretical studies.

Acknowledgements

We acknowledge the work during the upGREAT square degree survey of Orion of the USRA and NASA staff of the Armstrong Flight Research Center in Palmdale and of the Ames Research Center in Mountain View, and the Deutsches SOFIA Institut. Research on the interstellar medium at Leiden Observatory is supported through a Spinoza award. We thank the ERC and the Spanish MCIU for funding support under grants ERC-2013-Syg- 610256-NANOCOSMOS and AYA2017-85111-P, respectively.

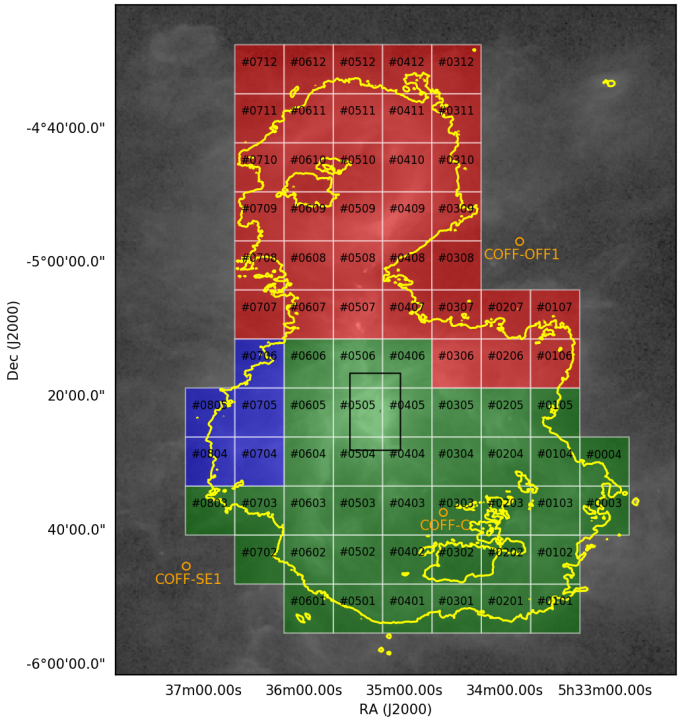

Figure 3.4: Outline of the region mapped in the 1.9-THz [C II] line with upGREAT on SOFIA. The 78 tiles indicated were used to construct the final map. The background image is the 70-μm Herschel/ PACS dust emission. The yellow contours correspond to an approximated far-ultraviolet radiation field of G0 = 50 (in Habing units). The colour of each tile indicates its corresponding OFF position: blue tiles use the COFF-SE1 position, red tiles use COFF-OFF1 and green tiles use COFF-C. Each square tile has a side length of 435.6 arcsec. The black box at the centre indicates the region mapped by the single-pixel Herschel/HIFI instrument in 9h 55min. The total observing time for the SOFIA/upGREAT map was 42 h.

3.A Methods

3.A.1 SOFIA observations

The data presented here were collected using the upGREAT (German Receiver for Astronomy at Terahertz Frequencies) heterodyne receiver on board SOFIA (Welty et al. 2012). SOFIA is an 80/20 joint project between NASA (National Aeronautics and Space Administration) and the DLR (German Aerospace Centre). SOFIA is a modified Boeing 747-SP aircraft with a 2.5-m-diameter telescope mounted in the fuselage aft of the wing (Young et al. 2012). Flying at an altitude of up to 43,000 feet (13 km) provides access to frequencies typically absorbed by the atmosphere. The upGREAT receiver is a heterodyne array receiver with 21 pixels. Two hexagonal arrays each with seven pixels are found in the low-frequency array (LFA), covering a frequency range from 1.81 THz to 2.08 THz. The other seven pixels are found in the high-frequency array (HFA), in a similar hexagonal pattern. The HFA is tuned primarily to the atomic oxygen transition at 4.744 THz. A heterodyne receiver achieves a spectral resolving power of up to $\nu/\Delta\nu = 10^7$ by mixing a locally generated monotone

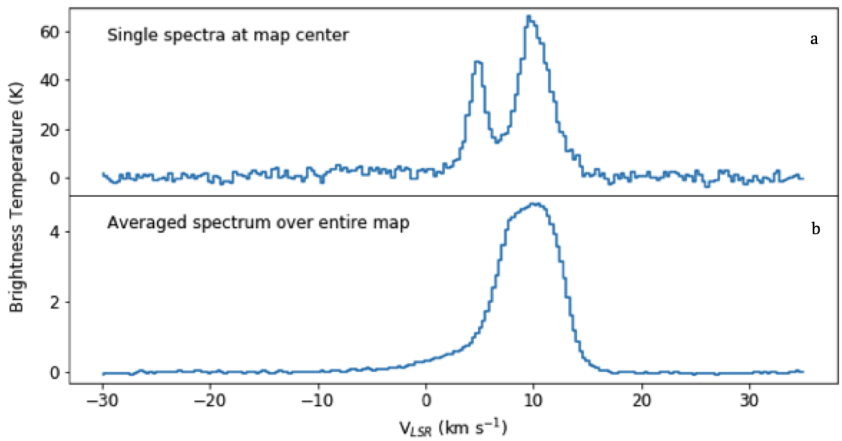

Figure 3.5: Sample 1.9-THz [C II] spectra in our data cube. a) Spectrum obtained at the map centre (RA(J2000) = 5h 35 min 17s; dec.(J2000) = $-5^\circ\,22'\,16.9''$). b) Average spectrum over the entire map.

signal close in frequency to the astronomical signal of interest with the broadband sky signal. The beat tone between the two signals contains the astronomical signal, but at microwave frequencies that can be amplified and sampled using microwave (GHz) electronic components. The original data at a resolution of about $0.04\,\mathrm{km\,s^{-1}}$ was rebinned to $0.2\,\mathrm{km\,s^{-1}}$ to increase the signal-to-noise ratio.

The data was collected using a special array on-the-fly (OTF) mapping mode (Welty et al. 2012). This differs from a classical OTF mode in which a single pixel is traced through the map dimensions and a fully sampled map is generated. In the array OTF observing mode, we use the hexagonal array geometry to generate a fully sampled map. With this approach, each receiver pixel does not cover every map point, but we can map larger regions in the same time as using a classical OTF approach. However, the signal-to-noise ratio is lower and there is some loss of pixel redundancy. The full map region was broken into 78 square tiles of length 435.6 arcsec (Fig. 3.4). Each tile took 22 min to complete. A tile is made up of 84 scan lines separated by 5.2 arcsec. Each tile is covered twice, once in the X and once in the Y direction. Each OTF scan line is made up of 84 dumps of 0.3 s. This returns root-mean-square noise of $T_{\mathrm{mb}} = 1.14$ K per map pixel for a spectral resolution of $0.3\,\mathrm{km\,s^{-1}}$.

The raw data are recorded by a digital spectrometer and come in the form of integer counts per spectrometer channel. These values are converted to antenna temperature using internal hot and cold reference measurements, which establish a scale for the sky measurements. The observation of detected off positions, free from C II emission, is required to remove instrumental artefacts from the data. The next step in the calibration process is to establish the atmospheric transmission and apply it to the astronomical signal. Although SOFIA flies above most of the atmosphere, there are some atmospheric features that need to be considered in the final calibration. The atmospheric emission is determined by fitting an atmospheric model to the off minus internal hot data. The process of atmospheric determination is described in the detail elsewhere (Guan et al. 2012).

Once the atmospheric transmission is applied to each spectrum, a channel map can

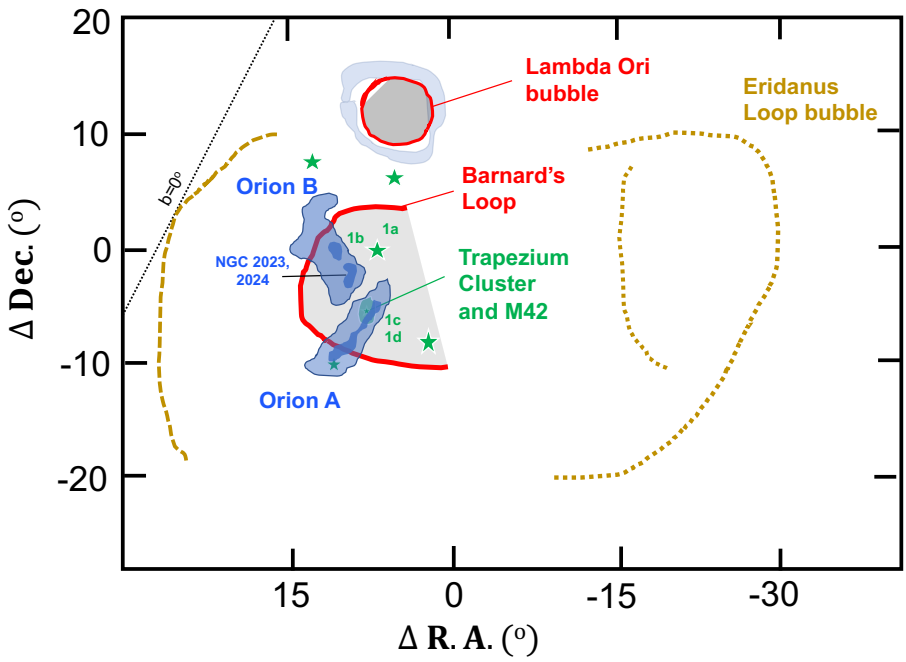

Figure 3.6: Schematic of the large-scale (about 350 pc) structure of Orion. The locations of the massive stars of the Orion constellation are marked with green stars (shoulders and knees; the belt is indicated by a single star; M42 is at the tip of the sword). The two giant molecular clouds A and B are shown in blue, and the prominent H II regions are indicated by the green area, which includes M42 and the Trapezium cluster. Barnard's loop, which is very prominent in Hα, is indicated by the red line. The bubble surrounding λ Ori (grey) is also indicated (red, ionized gas; blue, swept-up molecular shell), as are the boundaries of the superbubble (yellow dashed and dotted lines). Diffuse ionized gas is indicated in grey. The approximate locations of the Orion OB sub-associations – 1a, 1b, 1c and 1d – are marked in green. The dotted line labelled b = 0 indicates the Galactic plane.

be generated. In total 2.2 million spectra were measured. This dataset is converted to a map (Mangum et al. 2007) by defining a map grid; each map pixel is then generated by the distance-weighted sum of all spectra within a given distance of the pixel centre. This begins an iterative process whereby map artefacts are identified and then a correction is applied to the individual spectra and the map is regenerated. The data quality from the upGREAT instrument was exceptional, with 90% of spectra requiring no post-processing. Nominally, problematic spectra could be dropped while still leaving enough for a completely sampled map; however, with the array OTF mapping mode this may not be the case. To recover problematic spectra we developed a spline correction method. The classic approach in heterodyne data processing would be to use a polynomial to remove 'baseline' artefacts from the spectra. However, this can be problematic and is difficult to constrain. We adapted an approach first implemented in the Herschel/HIFI instrument (Kester et al. 2014; Higgins 2011), which used a catalogue of splines generated from data with no astronomical signal. These splines can then be scaled to astronomical data to more effectively remove the baseline. Representative spectra are shown in Fig. 3.5.

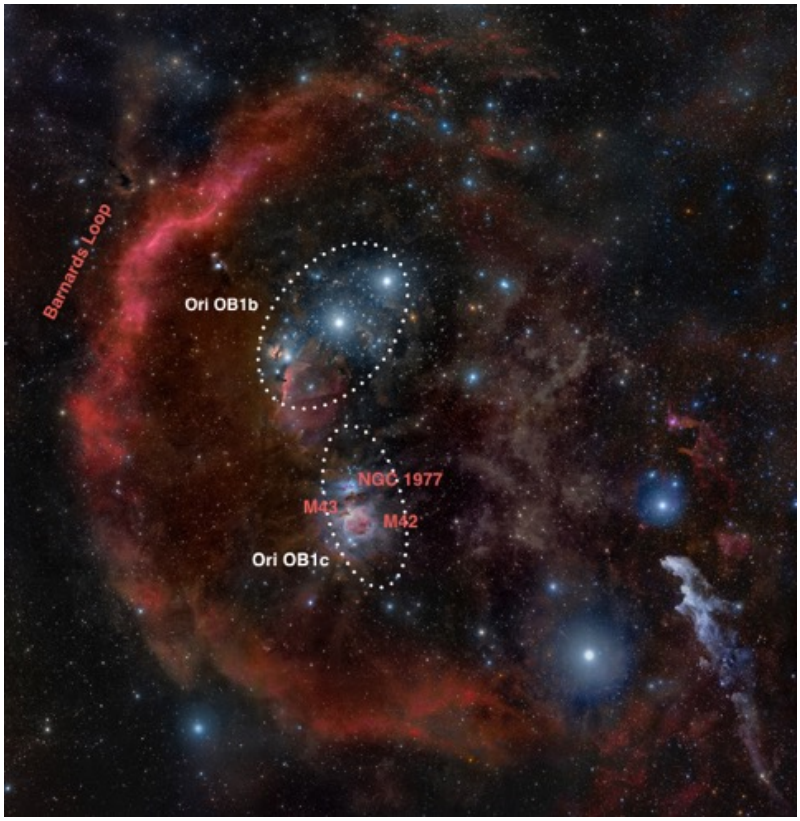

Figure 3.7: Overview of the star-forming region in Orion. The approximate boundaries of the Orion OB associations Ib and Ic are indicated by dashed ellipses. The Orion 1d association is directly associated with the molecular cloud behind the Orion nebula, M42. The reddish glow is due to the Hα line, which originates from recombinations in the ionized gas of Barnard's loop. The belt stars and the knees are obvious. The size of the image is approximately 10^{circ} on the sky.

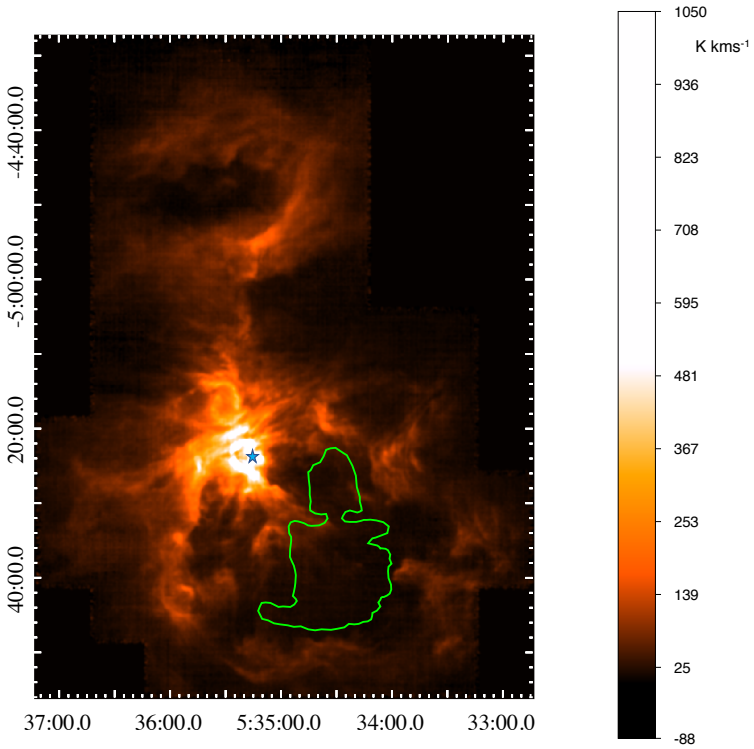

Figure 3.8: Composite infrared and X-ray views of the Orion region of massive star formation. The [C II] integrated intensity map is shown by the colour scale. The X-ray emission (from XMM-Newton) is outlined by a green contour. The hot gas probably entirely fills the bubble, but absorption by the Veil extinguishes the left side. The position of θ^1 Ori C (RA(J2000) = 5h 35min 16.46s, dec.(J2000) = $-5^\circ\,23'\,22.8''$) is indicated by a blue star.

3.A.2 Orion

Orion is the nearest site of massive star formation and has long been used to study the interaction of massive stars with molecular clouds (Elmegreen & Lada 1977; Genzel & Stutzki 1989a). The region contains two molecular clouds, Orion molecular cloud A and B. OMC-1 is one of four cores that have condensed out in the so-called integral-shaped filament that forms the densest part of the Orion molecular cloud A. The distance to the Orion molecular cloud A is known to vary by about 30 pc on a scale of 50 pc (Großschedl et al. 2018), but on the scale of the Orion nebula cluster, the H II region, M42 (the Orion nebula) and the Veil region, the distance is well determined at 414 ± 7 pc (Menten et al. 2007; Zari et al. 2017). This small uncertainty in the distance of OMC-1 does not affect our main results regarding mass or kinetic energy.

The Orion OB associations represent the effects of the ongoing formation of (massive) stars in this region and their interaction with the environment over 10 Myr (Bally 2008). The oldest sub-associations, Orion OB 1a and OB 1b, consist of the stars in the Orion Belt and just north of it (see Figs. 3.6 and 3.7 for an overview of the region). These subgroups have produced several supernovae that have swept up their environment, creating the 350-pc-diameter Orion-Eridanus superbubble. The Orion OB 1c subgroup in the sword is younger (5-8 Myr), and the youngest (less than 1 Myr) stellar subgroup, Orion OB 1d, represents still-active massive star formation associated with the prominent H II regions, M42, M43, and NGC 1977. Part of this subgroup is still embedded in OMC-1.

The Trapezium cluster (θ^1 Ori) is located on the front side of OMC-1. Each of the four stars that make up the Trapezium cluster is a multiple system in itself. θ^1 Ori C is a binary in which the primary has a mass of $34\,M_\odot$ and the companion is only $12\,M_\odot$ (Balega et al. 2015). The spectral type of the primary is O7Vp, with an effective temperature of 39,000 K. θ^1 Ori A and θ^1 Ori D both have much lower mass ($14\,M_\odot$ and $16\,M_\odot$), with spectral type B0.5V. Both are also binary systems with a lower-mass companion (Grellmann et al. 2013). θ^1 Ori B is only $7\,M_\odot$ (Muench et al. 2008). The radiative energy input in the region is dominated by the most massive star, θ^1 Ori C, with the other stars contributing less than 20% of the luminosity of the region. θ^1 Ori C also dominates the ionizing radiation of the cluster (more than 90%). It has a strong stellar wind, with a mass-loss rate of $4 \times 10^{-7}\,M_\odot\,\mathrm{yr}^{-1}$, and a terminal velocity of $2{,}500\,\mathrm{km\,s^{-1}}$, which corresponds to a mechanical luminosity of $L_w = 8 \times 10^{35}\,\mathrm{erg\,s^{-1}}$ (Stahl et al. 1996; O'Dell et al. 2017). Previous estimates (Leitherer 1988) suggest $L_w = 7 \times 10^{35}\,\mathrm{erg\,s^{-1}}$, but this small difference has no influence on our discussion. B0.5 stars have very weak stellar winds and the mechanical energy input by the other Trapezium stars is negligible. The wind from θ^1 Ori C has blown a bubble filled with hot, tenuous gas (density, $n \approx 1\,\mathrm{cm^{-3}}$; temperature, $T \approx 2 \times 10^6$ K; Güdel et al. 2008). This hot gas dominates the diffuse emission at X-ray wavelengths (Fig. 3.8). This bubble is well outlined in the mid-infrared image obtained in the polycyclic aromatic hydrocarbon emission bands and in the far-infrared image of the dust thermal emission (Fig. 3.1). These images trace the interaction of far-ultraviolet (less than 13.6 eV) radiation from θ^1 Ori C with these species in the neutral photodissociation region that separates the hot-bubble gas from the cold material in the molecular cloud.

3.A.3 Kinematics of the gas

Analysis of the individual velocity-channel maps reveals the kinematic signature of an expanding half-shell: with increasing velocity, the shell displaces further away from

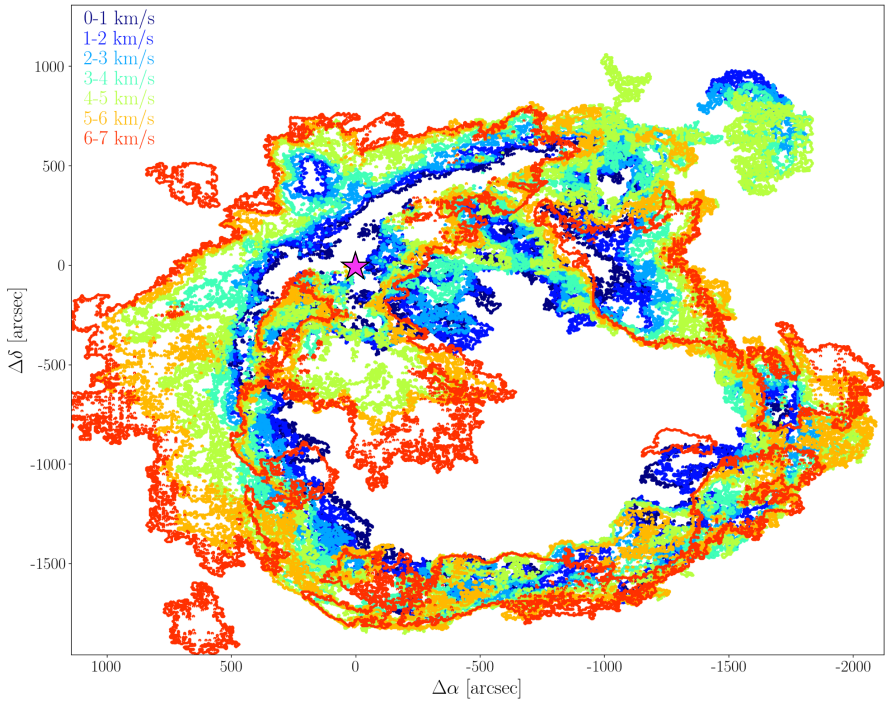

Figure 3.9: Composite figure showing the [C II] emission in different velocity channels. With increasing $v_{\rm LSR}$, the shell is displaced outwards, away from the centre of the bubble. This is the kinematic signature of an expanding half-shell. Each colour outlines the emission boundaries of channels $1\,{\rm km\,s^{-1}}$ wide from $v_{\rm LSR} = 0\,{\rm km\,s^{-1}}$ to $v_{\rm LSR} = 7\,{\rm km\,s^{-1}}$. The origin (magenta star) corresponds to the position of θ^1 Ori C (RA(J2000) = 5h 35min 16.46s, dec.(J2000) $= -5^\circ\,23'\,22.8''$). In the velocity range 4-7 $\,{\rm km\,s^{-1}}$, [C II] emission associated with OMC-4 starts to fill in the interior of the bubble. OMC-4 is a star-forming core near the front of the background molecular cloud and is not part of the Veil bubble.

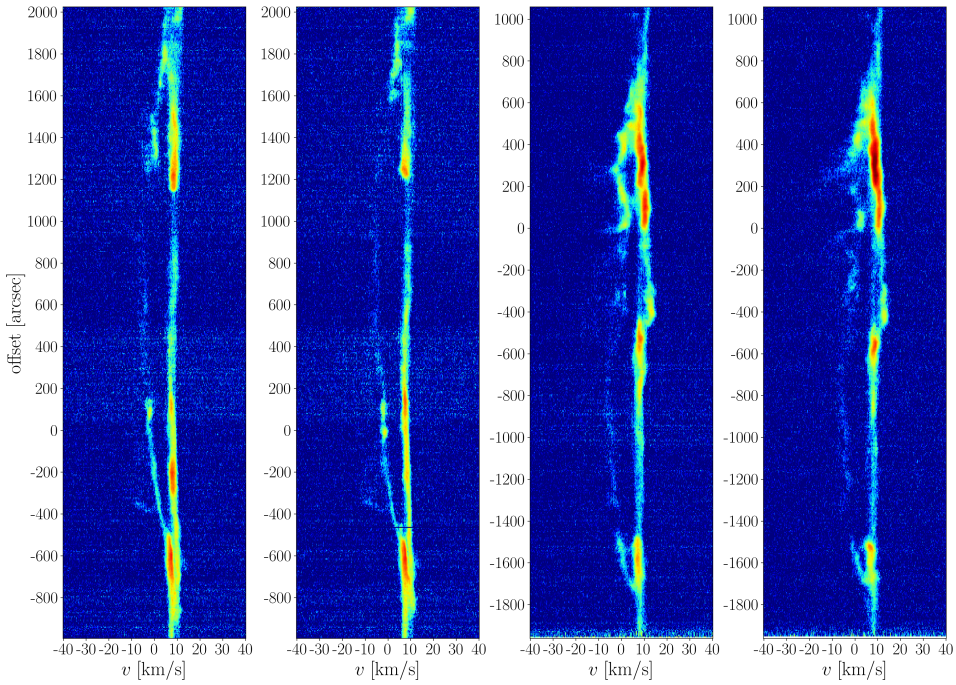

Figure 3.10: Four exemplary position-velocity diagrams of the [C II] emission from selected cuts across the Veil. Each position- velocity diagram exhibits a clear arc structure extending over about $2,500''$, which corresponds to the expanding Veil shell (C.P. et al., manuscript in preparation). The left (right) two panels are cuts along the horizontal (vertical) axis.

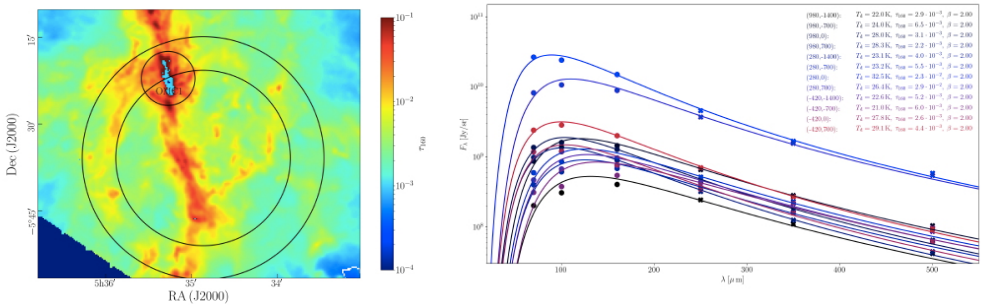

Figure 3.11: Far-infrared dust emission in Orion. Left, optical depth map of the dust emission at 160 μm ($\tau_1 60$), which traces the mass of the shell. The two large circles indicate the extent of the shell used to determine the mass of the limb-brightened shell. The small circle ('OMC1') circumscribes the Huygens region associated with the Trapezium stars. We estimated the mass that is enclosed between the two large circles, excluding the Huygens region. Right, SED of the dust emission observed for different positions in Orion; F_λ is the observed flux. These SEDs are analysed to determine the dust and gas mass. Data and curves represent observed SEDs and model fits for $\beta = 2$, respectively. The legend shows the resulting dust temperature T_d and $\tau_1 60$. These SED fits were analysed for each spatial point and the resulting $\tau_1 60$ values were used to construct the map shown in the left panel.

the centre (Fig. 3.9). We estimate the expansion velocity of the expanding shell of the Orion nebula from position-velocity diagrams. Across the range of the velocity-resolved [C II] map (Fig. 3.2), we build position-velocity diagrams by averaging spectra over cuts that are each 45.5″ wide, along the horizontal and vertical directions (C.P. et al., manuscript in preparation). In Fig. 3.2 we show a representative example of one such diagram; four additional ones are provided in Fig. 3.10. The expanding shell has a clear arc structure that is visible in most of the cuts. From the single position-velocity diagrams that most exhibit this arc, we estimate the expansion velocity by calculating the centroid velocity within the velocity ranges $5\,\mathrm{km\,s^{-1}}$ to $15\,\mathrm{km\,s^{-1}}$ for the [C II] background velocity (at the surface of the molecular cloud) and $-10\,\mathrm{km\,s^{-1}}$ to $5\,\mathrm{km\,s^{-1}}$ for the expanding gas: the difference is the expansion velocity with respect to the background molecular cloud. All [C II] position-velocity diagrams are well described by an expanding-shell model with one central origin and an expansion velocity of $13 \pm 1\,\mathrm{km\,s^{-1}}$ (C.P. et al., manuscript in preparation). Corresponding ^{12}CO(2-1) and ^{13}CO(2-1) position-velocity diagrams46 along the same spatial cut do not show any sign of an expanding shell. This is consistent with the low concentration of molecules in the Veil derived from ultraviolet absorption lines towards the Trapezium stars (Jenkins & Tripp 2011). The position-velocity diagrams reveal that molecular gas is shifted towards slightly higher velocity compared to the [C II] line ($11\,\mathrm{km\,s^{-1}}$ versus $9\,\mathrm{km\,s^{-1}}$).

3.A.4 Mass estimates of the Veil

We estimated the gas mass in the expanding shell from fits to the far-infrared observations of the dust emission using standard dust-to-gas conversion factors (Ochsendorf et al. 2015). We used Herschel far-infrared photometric images in the PACS bands at 70 μm, 100 μm and 160 μm, and the SPIRE bands at 250 μm, 350 μm and 500 μm. We convolved all images to the spatial resolution of the SPIRE 500-μm image (36″). We then fitted the spectral energy distribution (SED) per pixel, using a modified

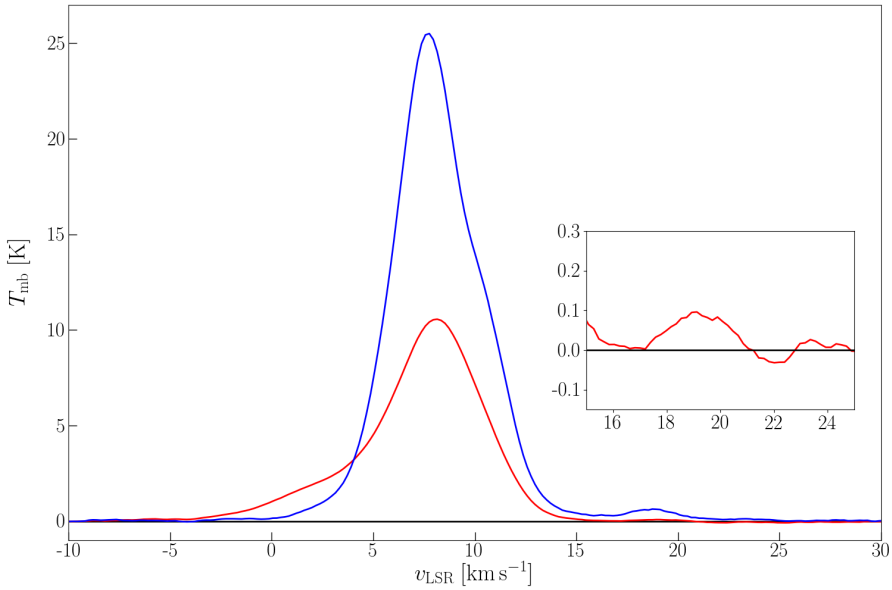

Figure 3.12: Average spectra from the shell. These spectra are dominated by the [C II] line from the main isotope and show the weak hyperfine component of $^{13}C^+$ near $v_{\rm LSR} = 20\,{\rm km\,s^{-1}}$. This line is used to estimate the optical depth of the main isotope line and thus the mass of the emitting gas. The red spectrum corresponds to the area between the two large circles in Fig. 3.11, but excluding Huygens region in the small circle. The blue spectrum is an average over the bright parts in the eastern shell, in the declination range $-5^\circ\,35'$ to $-5^\circ\,45'$. The inset shows a close-up of the (faint) [^{13}C II] line in the average shell spectrum.

Table 3.1: Masses, energetics and luminosities in Orion

Component	Mass	Energy		Luminosity	Ref.
		Thermal	Kinetic		
	$M_\odot$	10^{46} erg	10^{46} erg	$L_\odot$	
OMC-1 molecular gas	3000	0.6	20		1
Veil	2600	3	400		8
Stellar cluster	1800	–	–		2
Ionized gas	20	3	6		3, 4
Huygens Region	2	0.3	2		3, 4
Hot gas	0.07	10	–		5
Stellar wind	–	–	500^a	200^b	6, 7
θ^1 Ori C	–	–	–	2.5×10^5	6
FIR dust emission	–	–	–	6×10^4	8
[C II] 1.9 THz	–	–	–	200	8
X-ray	–	–	–	1.4×10^{-2}	5

Notes. [a] Over the calculated lifetime of the bubble. [b] Mechanical luminosity of the wind. References: (1) Buckle et al. (2012), (2) Hillenbrand (1997), (3) O'Dell et al. (2017), (4) Wilson et al. (1997), (5) Güdel et al. (2008), (6) Howarth & Prinja (1989), (7) Stahl et al. (1996), (8) this study.

blackbody distribution:

$$I(\lambda) = B(\lambda, T)[1 - e^{-\tau(\lambda)}],$$

where $\tau(\lambda) = \tau_{160}(160\,\mu\mathrm{m}/\lambda)^{\beta}$, $B(\lambda, T)$ is the Planck black-body spectrum at temperature T and wavelengthλ, and τ_{160} the optical depth at 160 μm. The optical depth of the dust varies with wavelength; this is parameterized by the grain emissivity index β. Typically, β is in the range 1-2. Here, we have chosen $\beta = 2$, in accordance with the standard dust models for $R_V = 5.5$, which are appropriate for the Orion molecular cloud (C.P. et al., manuscript in preparation). Representative fits to the SEDs and the resulting map of the optical depth of the dust are shown in Fig. 3.11. The expanding shell dominates the dust emission in the region in between the two large circles in Fig. 3.11 (see also Fig. 3.1a). The dust emission in the Huygens region, directly surrounding the Trapezium stars, is dominated by the dense photodissociation region that separates the ionized gas from the molecular core. Because this is not part of the expanding shell, we excluded this region (inside the small circle in Fig. 3.11) from our analysis. Using theoretical extinction coefficients (Weingartner & Draine 2001), we obtain a shell mass of $M = 1,700\,M_{\odot}$. There is considerable uncertainty in the SED fit, associated with the exact choice of β. Choosing $\beta = 1.5$, as suggested by the Planck survey (Lombardi et al. 2014), decreases τ_{160} by about 50%, resulting in a derived mass of $900\,M_{\odot}$ using the same theoretical conversion factor as before. Fig. 3.11 shows SED fits towards single points scattered throughout the Orion nebula. Because these are well fitted using $\beta = 2$, the mass estimate of $1,700\,M_{\odot}$ is appropriate. Finally, we have to make a geometric correction because we included the mass only in the limb-brightened shell. Taking the thickness of the shell as 40% of the radius, we obtain a shell mass of $2,600\,M_{\odot}$. Decreasing the thickness of the shell to 20%, the inferred mass increases to $3,400\,M_{\odot}$. Although there is [C II] emission (almost) everywhere, the Veil shows variations in thickness (see below) and the 'front' surface seems to be thinner than the limb-brightened edge.

The shell mass can also be estimated from the [^{13}C II] lines, which are shifted from the [^{12}C II] line owing to hyperfine splitting. Comparison of the strength of the [^{13}C II] hyperfine lines with the (main-component) [^{12}C II] line provides the [C II] optical depth and the excitation temperature with an adopted ^{12}C/^{13}C abundance ratio. These then yield the C^+ column density and, assuming a C abundance, the H column density and gas mass in the region can be derived. However, the [^{13}C II] line is too weak to be detected in the individual spectra. Only by averaging over a large area are we able to detect the strongest of the three [^{13}C II] components, $F = 2 - 1$ [^{13}C II], with a relative strength of 0.625 of the total [^{13}C II] intensity (Ossenkopf et al. 2013). This line is offset by $11.2\,\mathrm{km\,s^{-1}}$ from the [^{12}C II] line (Ossenkopf et al. 2013). The other two [^{13}C II] components, $F = 1 - 1$ and $F = 1 - 0$, lie at $63.2\,\mathrm{km\,s^{-1}}$ and $-65.2\,\mathrm{km\,s^{-1}}$, respectively, and are too weak to be detected in our data. Fig. 3.12 shows the spectrum averaged over the shell (the area indicated by the two large circles in Fig. 3.11). Again, we have excluded the emission from the dense photodissociation region directly behind the Trapezium (the small circle in Fig. 3.11). We also show the spectrum averaged over the brighter southeastern portion of the shell. These two averages both reveal the presence of the [^{13}C II] hyperfine component. The integrated intensity of the [^{i}C II] line is (Tielens & Hollenbach 1985)

$$I_i = B(T_{\mathrm{ex}})\frac{\delta\nu_{\mathrm{D}}}{c}\nu f(\tau_i),$$

where i indicates the isotope, $T_{\rm ex}$ is the excitation temperature, $\delta\nu_{\rm D}$ is the Doppler velocity width, c is the speed of light and ν is the frequency of the line. The factor $f(\tau_i)$ takes optical depth effects into account:

$$f(\tau_i) = 0.428[E_1(2.34\tau_i) + \ln(2.34\tau_i) + 0.57721],$$

where E_1 is the exponential integral. The [^{13}C II] line is optically thin and so $f(\tau_{13})$ is well approximated by $0.625\tau_{13}$, where the numerical factor takes the hyperfine strength into account. The [^{12}C II] line is optically thick and the logarithmic term will dominate. We relate the optical depth of the two isotopes through the carbon isotopic abundance measured for Orion (^{12}C/^{13}C = 67; Penzias et al. 1972), leaving two equations and two unknowns. We analyse the observed intensity ratio of the two lines averaged over the bright portion of the shell – the best determined portion. This results in $\tau_{12} = 3.5 \pm 1.0$ and an excitation temperature of 44 K. With the observed line width ($5\,{\rm km\,s^{-1}}$), we obtain a ^{12}C$^+$ column density of $3.5 \times 10^{18}\,{\rm cm^{-2}}$. Assuming that all the gas-phase C is ionized – appropriate for a photodissociation region – and a gas phase carbon abundance (Sofia et al. 2004) of 1.6×10^{-4}, extrapolating these values to the full limb-brightened shell yields an inferred hydrogen mass of $1,700 \pm 400\,M_\odot$. Given the large uncertainties involved, this is gratifyingly similar to the estimate from the dust emission. Correcting for geometry, adopting a shell thickness of 40% of the radius, results in a total mass of $2,600\,M_\odot$. This is an upper limit on the total mass because the brightest portion of the [C II] shell might be characterized by a larger-than-average column density. Also, although the derived optical depth is not sensitive to beam dilution, the derived excitation temperature is. If we were to adopt an excitation temperature of 100 K, the inferred mass, corrected for geometric effects, would be only $1,700\,M_\odot$. The mass of the shell can also be estimated from the observed optical extinction towards the ionized gas in the M42 H II region, because this extinction is dominated by the gas in the Veil (O'Dell et al. 1992). From a comparison of the MUSE Hβ map with the radio emission, an average visual extinction of 1.8 mag is derived (O'Dell & Yusef-Zadeh 2000). Using the theoretical extinction law (Weingartner & Draine 2001) for $R_V = 5.5$, this corresponds to an average H column density of $2 \times 10^{21}\,{\rm cm^{-2}}$. This is half the H column density measured directly towards θ^1 Ori C ($N_{\rm H} = 4.8 \times 10^{21}\,{\rm cm^{-2}}$)11. Adopting this latter value, we arrive at a total mass for the shell ($2\pi R^2 N_{\rm H} \mu m_{\rm H}$, with $m_{\rm H}$ the mass of hydrogen, μ the mean molecular weight and R the radius of the shell) of $1,300\,M_\odot$. The observed extinction is very patchy and the optical nebula seems to be located behind a relative thin portion of the Veil (O'Dell et al. 1992). Hence, we consider this a lower limit. As we consider the dust estimate the most direct measurement of the shell mass, we adopt $2,600\,M_\odot$ for the mass of the Veil in our analysis, recognizing that this value is uncertain by a factor of two.

4

Expanding bubbles in Orion A: [C II] observations of M42, M43, and NGC 1977

Abstract

Context: The Orion Molecular Cloud is the nearest massive-star forming region. Massive stars have profound effects on their environment due to their strong radiation fields and stellar winds. Stellar feedback is one of the most crucial cosmological parameters that determine the properties and evolution of the interstellar medium in galaxies.

Aims: We aim to understand the role that feedback by stellar winds and radiation play in the evolution of the interstellar medium. Velocity-resolved observations of the [C II] 158 μm fine-structure line allow us to study the kinematics of UV-illuminated gas. Here, we present a square-degree-sized map of [C II] emission from the Orion Nebula complex at a spatial resolution of $16''$ and high spectral resolution of $0.2\,\mathrm{km\,s^{-1}}$, covering the entire Orion Nebula (M42) plus M43 and the nebulae NGC 1973, 1975, and 1977 to the north. We compare the stellar characteristics of these three regions with the kinematics of the expanding bubbles surrounding them.

Methods: We use [C II] 158 μm line observations over an area of $1.2\,\mathrm{deg}^2$ in the Orion Nebula complex obtained by the upGREAT instrument onboard SOFIA.

Results: The bubble blown by the O7V star θ^1 Ori C in the Orion Nebula expands rapidly, at $13\,\mathrm{km\,s^{-1}}$. Simple analytical models reproduce the characteristics of the hot interior gas and the neutral shell of this wind-blown bubble and give us an estimate of the expansion time of 0.2 Myr. M43 with the B0.5V star NU Ori also exhibits an expanding bubble structure, with an expansion velocity of $6\,\mathrm{km\,s^{-1}}$. Comparison with analytical models for the pressure-driven expansion of H II regions gives an age estimate of 0.02 Myr. The bubble surrounding NGC 1973, 1975, and 1977 with the central B1V star 42 Orionis expands at $1.5\,\mathrm{km\,s^{-1}}$, likely due to the over-pressurized ionized gas as in the case of M43. We derive an age of 0.4 Myr for this structure.

Conclusions: We conclude that the bubble of the Orion Nebula is driven by the mechanical energy input by the strong stellar wind from θ^1 Ori C, while the bubbles associated with M43 and NGC 1977 are caused by the thermal expansion of the gas ionized by their central later-type massive stars.

C. H. M. Pabst, J. R. Goicoechea, D. Teyssier, O. Berné, R. D. Higgins, E. T. Chambers, S. Kabanovic, R. Güsten, J. Stutzki, A. G. G. M. Tielens

A&A 639, A2 (2020)

4.1 Introduction

Stellar feedback, that is injection of energy and momentum from stars, is one of the most important input parameters in cosmological models that simulate and explain the evolution of our universe. Even small variations in this crucial parameter can lead to drastic changes in the results. Too much stellar feedback of early stars disrupts the ambient gas in too early a stage to form more stars and, eventually, planetary systems that allow for the formation of life. Too little feedback fails to prevent the interstellar gas from gravitational collapse to dense, cold clumps. Stellar feedback is often quantified as the star-formation rate (SFR), the rate at which (mostly low-mass) stars are formed. Studies on the interaction of massive stars with their environment generally focus on the effects of supernova explosions injecting mechanical energy into their environment and the radiative interaction leading to the ionization and thermal expansion of the gas. The explosion of a massive star ejects some $10\,M_\odot$ at velocities of some $10,000\,\mathrm{km\,s^{-1}}$, injecting about 10^{51} erg into the surrounding medium. The hot plasma created by the reverse shock drives the expansion of the supernova remnant. The concerted effects of many supernovae in an OB association create superbubbles that expand perpendicular to the plane and may break open, releasing the hot plasma and any entrained colder cloud material into the lower halo (McKee & Ostriker 1977; McCray & Kafatos 1987; Mac Low & McCray 1988; Norman & Ikeuchi 1989; Hopkins et al. 2012).

However, there is evidence that also stellar winds have a profound impact on the interstellar medium (ISM). Observations and models have long attested to the importance of stellar winds from massive stars as sources of mechanical energy that can have profound influence on the direct environment (Castor et al. 1975; Weaver et al. 1977; Wareing et al. 2018; Pabst et al. 2019). These stellar winds drive a strong shock into its surroundings, which sweeps up ambient gas into dense shells. At the same time, the reverse shock stops the stellar wind, creating a hot tenuous plasma. Eventually, the swept up shells break open, venting their hot plasma into the surrounding medium.

Feedback by ionization of the gas surrounding a massive star will also lead to the disruption of molecular clouds (Williams & McKee 1997; Freyer et al. 2006; Dale et al. 2013). Initially, this will be through the more or less spherical expansion driven by the high pressure of the H II region (Spitzer 1978). Once this expanding bubble breaks open into the surrounding low density material, a champagne flow will be set up (Bedijn & Tenorio-Tagle 1981), rapidly removing material from the molecular cloud.

Bubble structures are ubiquitous in the ISM (e.g., Churchwell et al. 2006). Most of these are caused by expanding H II regions (Walch et al. 2013; Ochsendorf et al. 2014). However, due to the clumpy structure of the ISM, and molecular clouds in particular, the expanding shock fronts can be highly irregular. Depending on the morphology of the shock front, that is the formation of a shell and more or less massive clumps, massive star formation can be either triggered or hindered (e.g., Walch et al. 2012).

The relative importance of these three different feedback processes (SNe, stellar winds, thermal expanding H II regions) is controversial. Given the peculiar motion of massive stars, SN explosions may occur at relatively large distances from their natal clouds and therefore have little effect on the cloud as the energy is expended in rejuvenating plasma from previous SN explosions, sweeping up tenuous intercloud material and transporting it to the superbubble walls (McKee & Ostriker 1977; Mac Low & McCray 1988; Norman & Ikeuchi 1989; Ochsendorf et al. 2015). While the mechanical energy output in terms of stellar winds is much less than from SN explosions, they

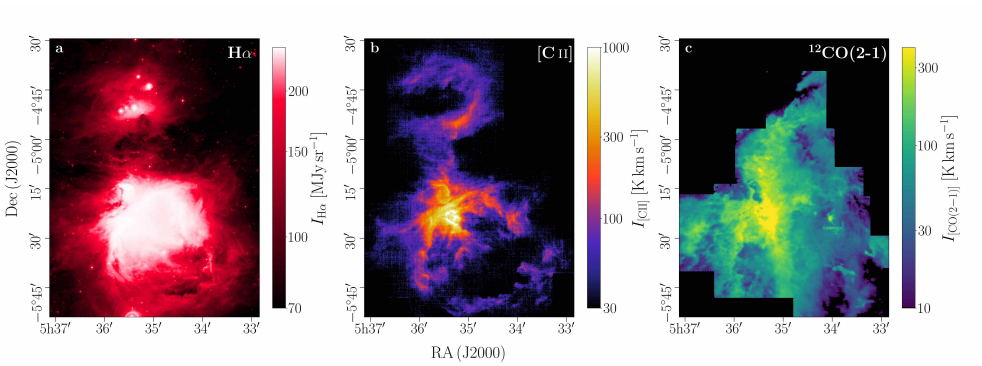

Figure 4.1: Overview of the Orion Nebula (M42), M43, and NGC 1973, 1975, and 1977 in different wavelenghts. Left: DSS2 Hα emission (ESO Archive). Center: [C II] line-integrated emission (Pabst et al. 2019). Right: Line-integrated ^{12}CO(2-1) emission (Berné et al. 2014; Goicoechea et al. 2020). Hα emission stems from the ionized gas ($T \sim 10^4$ K), the [C II] line is emitted by mostly neutral gas ($T \sim 100$ K), whereas CO traces the molecular gas ($T \sim 30$ K). M42 and M43 have a substantial amount of molecular gas in the background, while NGC 1977 seems to be devoid of it (the coverage of the CO map is not sufficient, however, see discussion of the expansion characteristics below). All three regions comprise ionized gas within their neutral limb-brightened shells.

will act directly on the natal cloud.

The Orion molecular cloud is the nearest region of massive star formation and has been studied in a wide range of wavelengths. The dense molecular cloud is arranged in an integral-shaped filament (ISF), which has fragmented into four cores, OMC1, 2, 3, and 4, that are all active sites of star formation. At the front side of the most massive core, OMC1, the massive O7V star θ^1 Ori C has ionized the well-known H II region M42 (NGC 1976), that is known as the Orion Nebula. The Orion Nebula, appearing as the middle "star" in the sword of Orion at a distance of $d \simeq 414$ pc from us (Menten et al. 2007), is one of the most picturesque structures of our universe. The strong stellar wind from this star has created a bubble filled with hot plasma that is rapidly expanding into the lower-density gas located at the front of the core (Güdel et al. 2008; Pabst et al. 2019). In addition, two slightly less massive stars, B0.5V-type NU Ori and B1V-type 42 Orionis, have created their own ionized gas bubbles, M43 and NGC 1977. These stars are not expected to have strong stellar winds and likely the thermal pressure of the ionized gas dominates the expansion of these two regions.

The current picture is as follows[1]: The Trapezium cluster including θ^1 Ori C, the most massive stars in the Orion Nebula complex, is situated at the surface of its natal molecular cloud, the OMC1 region of the Orion A molecular cloud. Presumably, the Trapezium stars live in a valley of the molecular cloud, having swept away the covering cloud layers (see O'Dell et al. (2009) for a detailed discussion of the structure of the inner Orion Nebula). In the immediate environment of the Trapezium stars, the gas is warm and ionized, constituting a dense H II region, the Huygens Region. It is confined towards the back by the dense molecular cloud core and this is exemplified by the prominent ionization front to the south, the Orion Bar, a narrow and very dense struc-

[1]For a 3D journey through the Orion Nebula see `https://www.jpl.nasa.gov/news/news.php?feature=7035&utm_source=iContact&utm_medium=email&utm_campaign=NASAJPL& utm_content =daily20180111-4`.

ture Tielens et al. (1993); Goicoechea et al. (2016). To the west of the Trapezium stars, embedded in the molecular gas of OMC1, one finds two dense cores with violent emission features, strong outflows and shocked molecular gas, that are the sites of active intermediate- and high-mass star formation, the Becklin-Neugebauer/Kleinmann-Low (BN/KL) region and Orion South (S).

Further outward, the gas is still irradiated by the central Trapezium stars, granting us the beautiful images of the Orion Nebula. The outward regions were dubbed the Extended Orion Nebula (EON, Güdel et al. 2008). It is, in fact, a closed circular structure of about 5 pc in diameter surrounding the bright Huygens Region, the latter being offset from its center. In the line of sight near the Trapezium stars in the Huygens Region, Orion's Veil (O'Dell & Yusef-Zadeh 2000) is observed as a layer of (atomic and molecular) foreground gas at 1-3 pc distance from the blister of ionized gas that forms the bright Orion Nebula. H I and optical/UV absorption lines reveal multiple velocity components, some with velocities that link them to the expanding bubble part of the Veil[2] seen across the EON (van der Werf et al. 2013; O'Dell 2018; Abel et al. 2019).

In the vicinity of the Orion Nebula, we find De Mairan's Nebula (NGC 1982 or M43) just to the north of the Huygens Region, and the Running-Man Nebula (NGC 1973, 1975, and 1977) further up north. M43 hosts the central B0.5V star NU Ori and is shielded from ionizing radiation from the Trapezium cluster by the Dark Bay (O'Dell & Harris 2010; Simón-Díaz et al. 2011). NGC 1973, 1975, and 1977 possess as brightest star B1V star 42 Orionis in NGC 1977, which is the main ionizing source of that region (Peterson & Megeath 2008). The structure surrounding NGC 1973, 1975, and 1977 is dominated by the dynamics induced by 42 Orionis, hence, we will denote it by NGC 1977 only in the following.

The hot plasma filling stellar wind bubbles and the ionized gas of H II regions are both largely transparent for far-UV radiation. These non-ionizing photons are instead absorbed in the surrounding neutral gas, creating a warm layer of gas, the photodissociation region (PDR), which cools through atomic fine-structure lines (Hollenbach & Tielens 1999). The [C II] 158 μm fine-structure line of ionized carbon is the dominant far-infrared (FIR) cooling line of warm, intermediate density gas ($T \sim$ 50-300 K, $n \sim 10^3$-10^4 cm^{-3}). It can carry up to 2% of the total FIR emission of the ISM, most of the FIR intensity arising from re-radiation of UV photons by interstellar dust grains. Velocity-resolved line observations provide a unique tool for the study of gas dynamics and kinematics. Velocity-resolved [C II] and [^{13}C II] observations towards the Huygens Region/OMC1, an area of about $7.5' \times 11.5'$, were obtained and analyzed by Goicoechea et al. (2015b). Here, we use a large-scale, $60' \times 80'$, study of velocity-resolved [C II] emission from the Orion Nebula M42, M43 and NGC 1973, 1975 and 1977[3].

This paper is organized as follows. In Section 2, we review the observations that we used in the present study. In Section 3, we discuss the morphology of the shells associated with M42, M43, and NGC 1977 and derive gas masses and expansion velocities. Section 4 contains a discussion of the results presented in Section 3. We compare the observed shell kinematics with analytical models. We conclude with a summary of our results in Section 5.

[2]We refer to Orion's Veil as the Veil in short. We will refer to the large-scale expanding bubble as the Veil shell, being part of the same structure that covers the Huygens Region.

[3]Two movie presentations of the velocity-resolved [C II] data are made available at `http://ism.strw.leidenuniv.nl/research.html#CII`.

4.2 Observations

4.2.1 [C II] observations

Velocity-resolved [C II] line observations towards the Orion Nebula complex, covering M42, M43 and NGC 1973, 1975, and 1977, were obtained during 13 flights in November 2016 and February 2017 using the 14-pixel high-spectral-resolution heterodyne array of the German Receiver for Astronomy at Terahertz Frequencies (upGREAT[4], Risacher et al. (2016)) onboard the Stratospheric Observatory for Infrared Astronomy (SOFIA). We produced a fully-sampled map of a 1.2 square-degree-sized area at a angular resolution of 16″. The full map region was observed in the array on-the-fly (OTF) mode in 78 square tiles, each 435.6″ wide. Each tile consists of 84 scan lines separated by 5.2″, covered once in both x and y direction. Each scan line consists of 84 dumps of 0.3 s, resulting in a root-mean-square noise of $T_{\rm mb} \simeq 1.14\,{\rm K}$ per pixel at a spectral resolution of $0.3\,{\rm km\,s^{-1}}$. The original data at a native spectral resolution of $0.04\,{\rm km\,s^{-1}}$ were rebinned to $0.3\,{\rm km\,s^{-1}}$ channels to increase the signal-to-noise ratio. 90% of the total 2.2 million spectra required no post-processing, while most problematic spectra could be recovered using a spline baselining approach. A catalogue of splines is generated from data containing no astronomical signal. These splines could then be scaled to the astronomical data and more effectively remove the baselines than a polynomial fit. For a detailed description of the observing strategy and data reductions steps see Higgins et al. (in prep.).

4.2.2 CO observations

We also make use of ^{12}CO $J = 2$-1 (230.5 GHz) and ^{13}CO $J = 2$-1 (220.4 GHz) line maps taken with the IRAM 30 m radiotelescope (Pico Veleta, Spain) at a native angular resolution of 10.7″. The central region ($1^\circ \times 0.8^\circ$) around OMC1 was originally mapped in 2008 with the HERA receiver array. Berné et al. (2014) presented the on-the-fly (OTF) mapping and data reduction strategies. In order to cover the same areas mapped by us in the [C II] line, we started to enlarge these CO maps using the new EMIR receiver and FFTS backends. These fully-sampled maps are part of the Large Program "Dynamic and Radiative Feedback of Massive Stars" (see the observing strategy and calibration in Goicoechea et al. 2020).

Goicoechea et al. (2020) provide details on how the old HERA and new EMIR CO maps were merged. Line intensities were converted from antenna temperature ($T_{\rm A}^*$) scale to main-beam temperature ($T_{\rm mb}$) using appropriate beam and forward efficiencies. Finally, and in order to properly compare with the velocity-resolved [C II] maps, we smoothed the CO(2-1) data to an angular resolution of 16″. The typical root-mean-square noise level in the CO(2-1) map is 0.16 K in $0.4\,{\rm km\,s^{-1}}$ velocity resolution channels.

4.2.3 Dust maps

In order to estimate the mass of the [C II]-traced gas in the expanding shells, we make use of FIR photometry obtained by *Herschel*. Lombardi et al. (2014) present a dust spectral energy distribution (SED) fit from *Herschel*/Photoconductor Array Camera

[4] upGREAT is a development by the MPI für Radioastronomie (Principal Investigator: R. Güsten) and KOSMA/Universität zu Köln, in cooperation with the MPI für Sonnensystemforschung and the DLR Institut für Optische Sensorsysteme.

and Spectrometer (PACS, Poglitsch et al. (2010)) and Spectral and Photometric Imaging Receiver (SPIRE, Griffin et al. (2010)) photometric images across a vast region of the Orion molecular cloud. However, they comment that the short-wavelength PACS 70 μm might be optically thick towards the dense molecular cores, hence they exclude it. Since we expect the expanding shell, we are mostly interested in, to mainly consist of optically thin, warm dust, we use the shorter-wavelength bands of PACS at 70 μm, 100 μm, and 160 μm, tracing the warm dust; the longer-wavelength SPIRE bands at 250 μm, 350 μm, and 500 μm, also included in the fit, are dominated by emission from cold (background) dust. We let the dust temperature $T_{\rm d}$ and the dust optical depth τ_{160} be free parameters, and fit SEDs using a modified blackbody for fixed grain emissivity index β:

$$I_\lambda = B(\lambda, T_{\rm d})\, \tau_{160} \left(\frac{160\,\mu{\rm m}}{\lambda}\right)^\beta . \tag{4.1}$$

We convolve and re-grid the PACS and SPIRE maps to the spatial resolution of the SPIRE 500 μm image, that is 36″, at a pixel size of 14″. SED fits to individual pixels are shown in Fig. 4.25. We note that $\beta = 0$ results in the least residual in the PACS bands, but according to Hollenbach et al. (1991), at least $\beta = 1$ should be used. Often (e.g., in Goicoechea et al. (2015b) for OMC1) $\beta = 2$ is adopted. The resulting dust temperature and dust optical depth vary considerably with β. Decreasing β from 2 to 1, decreases the dust optical depth by half, as does decreasing β from 1 to 0. The longer-wavelength SPIRE bands can only be fitted with β = 1-2. Since we use the conversion factors from τ to gas mass of Li & Draine (2001), we revert to $\beta = 2$ as suggested by their models. Lombardi et al. (2014) employ the β map obtained by Planck at 5′ resolution, which amounts to $\beta \simeq 1.6$. We note that τ_{160} is biased towards the warm dust, which is beneficial for our purposes. We could have constrained the SED fits to the three PACS bands, using $\beta = 2$. This leaves the dust temperature and the dust optical depth in the shells mostly unchanged. The only exception is the southern part of the limb-brightened Veil shell, where the dust optical depth turns out to be 30% lower. In addition, the dust optical depth towards the molecular background is reduced by half. From the dust optical depth τ_{160}, we can compute the gas column density:

$$N_{\rm H} \simeq \frac{100\,\tau_{160}}{\kappa_{160} m_{\rm H}} \simeq 6 \times 10^{24}\,{\rm cm}^{-2}\,\tau_{160}, \tag{4.2}$$

where we have used a gas-to-dust mass ratio of 100 and assumed a theoretical absorption coefficient $\kappa_{160} \simeq 10.5\,{\rm cm}^2\,{\rm g}^{-1}$ appropriate for $R_{\rm V} = 5.5$ (Weingartner & Draine 2001).

To estimate the contribution of emission from very small grains (VSGs) in the 70 μm band, we compare the latter with the *Spitzer*/Multiband Imaging Photometer (MIPS) 24 μm image. VSGs in PDRs are stochastically heated and obtain temperatures that are higher than that of larger grains. In the shells of the Orion Veil, M43, and NGC 1977, their contribution is small. In the bubble interiors, however, the emission from hot dust tends to dominate: dust in these H II region becomes very warm due to absorption of ionizing photons and resonantly trapped Lyα photons and radiates predominantly at 24 μm (Salgado et al. 2016). For dust in the PDR, the observed flux at wavelength shorter than 24 μm is due to emission by fluctuating grains and PAH molecules and we defer this analysis to a future study.

4.2.4 Hα observations

We make use of three different Hα observations: the Very Large Telescope (VLT)/ Multi Unit Spectroscopic Explorer (MUSE) image taken of the Huygens Region (Weilbacher et al. 2015), the image taken by the Wide Field Imager (WFI) on the European Southern Observatory (ESO) telescope at La Silla of the surrounding EON (Da Rio et al. 2009), and a ESO/Digitized Sky Survey 2 (DSS-2) image (red band) covering the entire area observed in [C II]. The DSS-2 image is saturated in the inner EON, which is basically the coverage of the WFI image. We use the MUSE image to calibrate the WFI image in units of $\mathrm{MJy\,sr^{-1}}$ with a log fit of the correlation. The units of the MUSE observations are given as $10^{-12}\,\mathrm{erg\,s^{-1}\,cm^{-3}}$, which we convert to $\mathrm{MJy\,sr^{-1}}$ with the central wavelength $\lambda \simeq 656.3\,\mathrm{nm}$ and a pixel size of $0.2''$. We in turn use the thus referenced WFI image to calibrate the DSS-2 image with a fit of the form $y = a(1 - \exp(-bx))$, where x, y are the two intensities scaled by the fit parameters. To calculate the surface brightness from the spectral brightness we use a $\Delta\lambda = 0.85\,\mathrm{Å}$, that is $I = I_\lambda \Delta\lambda = I_\nu \Delta\nu$.

We only use the thus calibrated DSS-2 image in NGC 1977 for quantitative analysis. The Hα surface brightness in the EON is largely due to scattered light from the bright Huygens Region (O'Dell & Harris 2010). Also Hα emission in M43 has to be corrected for a contribution of scattered light from the Huygens Region (Simón-Díaz et al. 2011).

We correct for extinction towards NGC 1977, using $R_\mathrm{V} = 5.5$, suitable for Orion. The reddening is $E(B-V) = 0.08$ (Knyazeva & Kharitonov 1998). For M43, the reddening is $E(B-V) = 0.49$ (Megier et al. 2005). Extinction towards M42 was studied by O'Dell & Yusef-Zadeh (2000), for example, and more recently by Weilbacher et al. (2015).

4.3 Analysis

4.3.1 Global morphology

From the comparison of the three gas tracers in Fig. 4.1, we see that [C II] emission stems from different structures than either Hα, tracing the ionized gas, or ^{12}CO(2-1), tracing the cold molecular gas. In fact, from Fig. 1 in Pabst et al. (2019) we conclude that it stems from the same regions as the warm-dust emission and PAH emission. We can quantify this by correlation plots of the respective tracers (Pabst et al., in prep.). We clearly see bubble-like structures in [C II], that are limb-brightened towards the edges. The southern red circle in Fig. 6.2 indicates the outlines of the bubble of M42. We note that the Trapezium stars, causing the bubble structure, are offset from the bubble center; in fact, they seem to be located at the northern edge of the bubble. We estimate a bubble radius of $r \simeq 2.7\,\mathrm{pc}$. However, when taking into account the offset of the Trapezium stars, the gas at the southern edge of the bubble is some 4 pc from the stars. The geometry of the bubble indicates that there is a significant density gradient from the north, where the Trapezium stars are located, to the south, the ambient gas there being much more dilute.

In M43, the star NU Ori is located at the center of the surrounding bubble. 42 Orionis in NGC 1977 is slightly offset from the respective bubble center (cf. Fig. 6.2). Both bubbles are filled with ionized gas as observed in Hα emission (cf. Fig. 4.1) as well as radio emission (Subrahmanyan et al. 2001). In the main part of this section, we derive the mass, physical conditions and the the expansion velocity of the expanding shells associated with M42, M43, and NGC 1977.

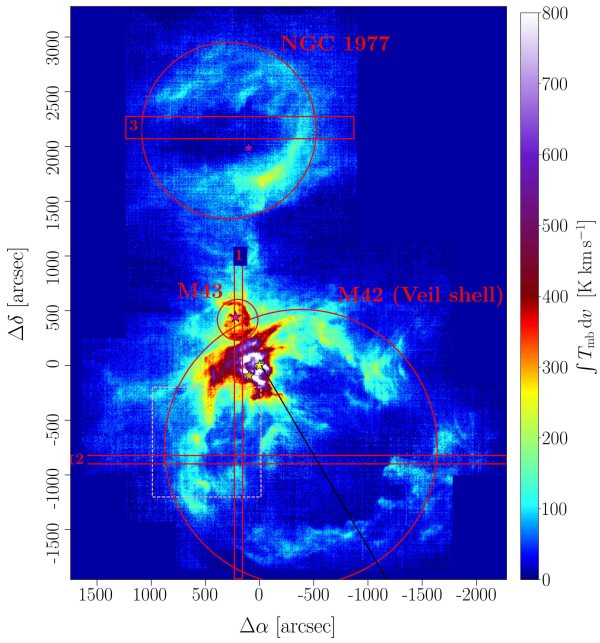

Figure 4.2: [C II] line-integrated intensity from the Orion Nebula (M42), M43, and NGC 1977. The red rectangles 1 and 2 indicate the positions of the pv diagrams shown in Figs. 4.5 (horizontal) and 4.8 (vertical). Rectangle 3 indicates the position of the pv diagram shown in Fig. 4.17. The red circles delineate the approximate extent of the expanding bubbles of gas that are the Veil shell, M43, and NGC 1977, and within which the respective masses and luminosities are computed. The light-red dashed rectangle circumscribes the area of the eastern bright arm shown in Figs. 4.26 and 4.27. The black line indicates the position of the line cut in Fig. 4.4. The stars mark the position of θ^1 Ori C (yellow), θ^2 Ori A (orange), NU Ori (pink), and 42 Orionis (purple). Unless noted otherwise, all coordinate offsets are given with respect to the position of θ^1 Ori C, $(\alpha, \delta) = (5\mathrm{h}35'16.46'', -5°23'22.85'')$.

4.3.2 The expanding Veil shell – M42

Geometry, mass and physical conditions

The prominent shell structure of the Orion Nebula is surprisingly symmetric, although it is offset from the Trapezium cluster. From the pv diagrams (cf. Section 4.3.2 and Appendix 4.C), we estimate its geometric center at $(\Delta\alpha, \Delta\delta) = (-520'', -550'')$ and its radius with $r = 1360'' = 0.38\,\mathrm{deg}$, which corresponds to $r \simeq 2.7\,\mathrm{pc}$ at the distance of the Orion Nebula; the geometric center of the bubble has a projected distance of 1.5 pc from the Trapezium cluster. Hence, the gas in the southern edge of the bubble is about 4 pc away from the Trapezium stars, whereas to the north the bubble outline is more ellipsoid and the gas in the shell is at only 0.5 pc distance.

The limb-brightened shell of the expanding Veil bubble is mainly seen in the velocity range (with respect to the Local Standard of Rest (LSR)) $v_{\mathrm{LSR}} = 5\text{-}8\,\mathrm{km\,s^{-1}}$. The emission from the bubble itself can be found down to $v_{\mathrm{LSR}} \simeq -7\,\mathrm{km\,s^{-1}}$ (cf. Section 4.3.2). The bright main component, that originates from the surface of the background molecular cloud, lies at $v_{\mathrm{LSR}} \simeq 8\,\mathrm{km\,s^{-1}}$; in the bright Huygens Region significant emission extends up to $v_{\mathrm{LSR}} \sim 15\,\mathrm{km\,s^{-1}}$. Here, we also detect the [^{13}C II]

F = 2-1 line in individual pixels, corresponding to gas moving at $v_{\rm LSR} \sim 8\,{\rm km\,s^{-1}}$ (see previous detections of [^{13}C II] lines in Boreiko & Betz (1996); Ossenkopf et al. (2013); Goicoechea et al. (2015b)).

Figure 4.3 shows the average [C II] spectrum towards the Veil shell without OMC1 and the ISF. The [^{13}C II] F = 2-1 line, one of the three [^{13}C II] fine-structure lines, that is shifted by $11.2\,{\rm km\,s^{-1}}$ with respect to the [^{12}C II] line, is marginally detected. We estimate the detection significance over the integrated line from the fit errors at 5σ. From the [^{13}C II] F = 2-1 line, we can compute the [C II] optical depth $\tau_{\rm [C\,II]}$ and the excitation temperature $T_{\rm ex}$:

$$\frac{1-\exp(-\tau_{\rm [C\,II]})}{\tau_{\rm [C\,II]}} \simeq \frac{0.625 T_{\rm P}([^{12}{\rm C\,II}])}{[^{12}{\rm C}/^{13}{\rm C}] T_{\rm P}([^{13}{\rm C\,II}], F = 2\text{-}1)}, \tag{4.3}$$

$$T_{\rm ex} = \frac{91.2\,{\rm K}}{\ln(1 + \frac{91.2\,{\rm K}(1-\exp(-\tau_{\rm [C\,II]}))}{T_{\rm P}([^{12}{\rm C\,II}])+T_{\rm c}})}, \tag{4.4}$$

where [^{12}C/^{13}C] $\sim$ 67 is the isotopic ratio for Orion (Langer & Penzias 1990) and 0.625 is the relative strength of the [^{13}C II] F = 2-1 line (Ossenkopf et al. 2013); $T_{\rm c} = \frac{91.2\,{\rm K}}{\exp(91.2\,{\rm K}/T_{\rm d})-1}$ is the continuum brightness temperature of the dust background (Goicoechea et al. 2015b). In general, $T_{\rm P}([^{12}{\rm C\,II}]) \gg T_{\rm c}$ in the limb-brightened shells. The measured peak temperatures yield $\tau_{\rm [C\,II]} \simeq 0.1$ and $T_{\rm ex} \simeq 144\,{\rm K}$ for the averaged spectrum. We obtain an average C^+ column density of $N_{\rm C^+} \simeq 3 \times 10^{17}\,{\rm cm^{-2}}$. These results have to be interpreted with caution, since we average over a large region with very different conditions (G_0, n) and the signal is likely dominated by the bright eastern Rim of the Veil shell (see Appendix 4.B for a discussion thereof). Also, baseline removal for the [^{13}C II] line is problematic. From the dust optical depth, we estimate a much larger column density towards the Veil shell, $N_{\rm C^+} \gtrsim 10^{18}\,{\rm cm^{-2}}$.

If we assume the [C II] emission from the limb-brightened shell to be (marginally) optical thick, that is $\tau_{\rm [C\,II]} \gtrsim 1$, we can also estimate the excitation temperature from the peak temperature of the [^{12}C II] spectra by eq. 4.4. We obtain excitation temperatures of $T_{\rm ex} \simeq 100\,{\rm K}$ in the Eastern Rim (and similar gas temperatures), and $T_{\rm ex} \simeq 50\,{\rm K}$ in the far edge of the shell. Here, the density presumably is somewhat lower, resulting in a higher gas temperature. The gas (or kinetic) temperature is given by:

$$T_{\rm gas} = \frac{T_{\rm ex}}{1 - \frac{T_{\rm ex}}{91.2\,{\rm K}} \ln(1 + \frac{n_{\rm cr}}{n})}, \tag{4.5}$$

where $n_{\rm cr} \simeq 3 \times 10^3\,{\rm cm^{-3}}$ is the critical density for C^+-H collisions (Goldsmith et al. 2012; Pabst et al. 2017). With the density estimates below, the gas temperature in the southern Veil shell is $T_{\rm gas} \simeq$ 70-125 K.

From the dust SEDs, Pabst et al. (2019) estimate $M \simeq 2600^{+800}_{-900}\,M_\odot$ for the mass of the gas in the Veil shell after accounting for projection effects. This is in good agreement with their mass estimate from the [^{13}C II] line in the brightest parts of the shell. The bright eastern part of the shell, however, might not be representative of the entire limb-brightened shell of the Veil shell. From a line cut through this Eastern Rim (Fig. 4.29), we estimate a density of $n \simeq 9 \times 10^3\,{\rm cm^{-3}}$ from the spatial separation of the peaks in [C II] and CO emission (see Appendix 4.B), assuming an $A_{\rm V}$ of 2 for the C^+/C/CO transition and $N_{\rm H}/A_{\rm V} \simeq 2 \times 10^{21}\,{\rm cm^{-2}}$ (Bohlin et al. 1978). Although continuously connected to the limb-brightened Veil shell in space and velocity, this Eastern Rim might be a carved-out structure in the background molecular cloud, as

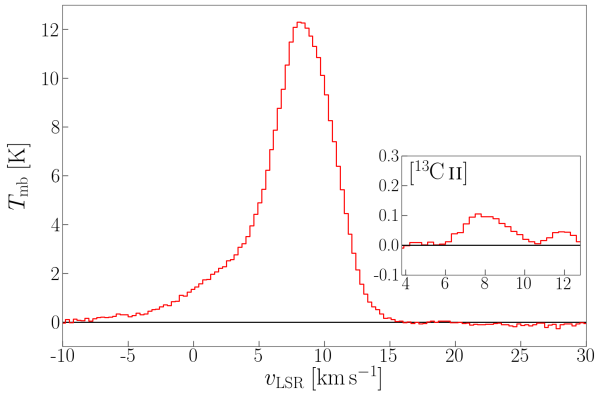

Figure 4.3: Average [C II] spectrum towards the Veil shell without OMC1 and ISF. The inlaid panel shows the residual of the spectrum, in the systemic velocity of the [^{13}C II] F = 2-1 line, after subtracting the [^{12}C II] fit. The [^{12}C II] line can be fitted by two Gaussians with $T_{\rm P} \simeq 11.2 \pm 0.3\,{\rm K}$, $v_{\rm P} \simeq 8.8 \pm 0.1\,{\rm km\,s^{-1}}$, $\Delta v_{\rm FWHM} \simeq 5.0 \pm 0.1\,{\rm km\,s^{-1}}$ and $T_{\rm P} \simeq 2.3 \pm 0.1\,{\rm K}$, $v_{\rm P} \simeq 4.0 \pm 0.4\,{\rm km\,s^{-1}}$, $\Delta v_{\rm FWHM} \simeq 9.3 \pm 0.5\,{\rm km\,s^{-1}}$; the [^{13}C II] F = 2-1 component is fitted by a Gaussian with $T_{\rm P} \simeq 0.11 \pm 0.02\,{\rm K}$, $v_{\rm P} \simeq 8.2 \pm 0.3\,{\rm km\,s^{-1}}$, $\Delta v_{\rm FWHM} \simeq 2.1 \pm 0.6\,{\rm km\,s^{-1}}$. The main line could also be fitted with three Gaussian components, but we compare the respective combined peak temperatures of the [^{12}C II] and [^{13}C II] line for a first-order estimate of the excitation conditions.

has been argued from the presence of foreground scattered light from the Trapezium stars (O'Dell & Goss 2009). We note that the [C II] emission from the expanding shell connected to the Eastern Rim is confined to within the Rim, supporting the view that the Eastern Rim is a static confinement of the expanding bubble.

Morphologically, the Eastern Rim fits well in with the rest of the Veil shell, following its curvature well and forming one, seemingly coherent structure. In contrast, there is no connection to the ISF that spans up the dense core of the Orion molecular cloud in the submillimeter maps (cf. Fig. 4.1). It is then hard to conceive that this part of the nebula is a fortuitous coincidence of the expanding Veil shell encountering a background or foreground molecular cloud structure. On the other hand, the channel maps do not reveal the shift of the shell with increasing velocity in the Eastern Rim that are the signature of an expanding shell in the other parts of the Veil shell (cf. Fig. 4.7). Excluding the area associated directly with the dense PDR around the Trapezium (indicated by the circle in Extended Data Fig. 8 in Pabst et al. (2019)), analysis of the dust SED yields $M \simeq 2600\,M_\odot$ for the mass of the Veil shell. If we also exclude the Eastern Rim, this drops to $M \simeq 1500\,M_\odot$.

From the visual extinction towards the Trapezium cluster, $A_{\rm V} \simeq 1.8$ (O'Dell & Goss 2009), corresponding to a hydrogen column density of $N_{\rm H} \simeq 3.6 \times 10^{21}\,{\rm cm^{-2}}$, the mass of the half-shell can be estimated as $M \simeq 2\pi r^2 N_{\rm H} \mu m_{\rm H}$, where $\mu = 1.4$ is the mean molecular weight. With $r \simeq 2.5\,{\rm pc}$, this gives $M \simeq 1600\,M_\odot$. From H_2 and carbon line observations towards the Trapezium cluster, Abel et al. (2016) estimate a density of $n \simeq 2.5 \times 10^3\,{\rm cm^{-3}}$ and a thickness of the large-scale Veil component B of $d \simeq 0.4\,{\rm pc}$, resulting in a visual extinction of $A_{\rm V} \simeq 1.5$. In a new study of optical emission and absorption lines plus [C II] and H I line observations, Abel et al. (2019) determine $n \simeq 1.6 \times 10^3\,{\rm cm^{-3}}$ for the density in the Veil towards the Trapezium cluster, their Component III(B). However, the central part of the Veil might not be representative

of the entire Veil shell, since the [C II] emission from the Veil in the vicinity of the Trapezium stars is less distinct than in the farther parts of the Veil shell, suggesting somewhat lower column density in the central part. The visual extinction, as seen by MUSE (Weilbacher et al. 2015), varies across the central Orion Nebula and decreases to only $A_{\rm V} \simeq 0.7$ to the west of the Trapezium cluster. Using this value reduces the mass estimate of the Veil shell to $M \sim 600\,M_\odot$.

X-ray observations of the hot plasma within the EON indicate varying extinction due to the foreground Veil shell. Güdel et al. (2008) derive an absorbing hydrogen column density of $N_{\rm H} \simeq 4 \times 10^{20}\,{\rm cm}^{-2}$ towards the northern EON and $N_{\rm H} \leq 10^{20}\,{\rm cm}^{-2}$ towards the southern X-ray emitting region. Assuming again $T_{\rm ex} \simeq 50\,{\rm K}$, these column densities correspond to [C II] peak temperatures of $T_{\rm P} \simeq 2\,{\rm K}$ and $T_{\rm P} \simeq 0.5\,{\rm K}$, respectively, which would be below the noise level of our observations. Yet, we do detect the [C II] Veil shell towards these regions (cf. Figs. 4.30 and 4.31). From the lack of observable X-rays towards the eastern EON and the more prominent [C II] Veil shell in this region, we suspect that the absorbing column of neutral gas is higher in the eastern Veil shell.

With the MUSE estimate for the column density, we can estimate the density and check for consistency with our [C II] observations. With a shell thickness of $d \simeq 0.3\,{\rm pc}$ and a visual extinction of $A_{\rm V} \simeq 0.7$, we estimate a density in the Veil shell of $n \simeq 1.5 \times 10^3\,{\rm cm}^{-3}$. We will use this density estimate in the following, but we note that we consider this a lower limit as the density estimate from a typical dust optical depth, $\tau_{160} \simeq 2 \times 10^{-3}$, in the southern Veil shell and a typical line of sight, $l \simeq r/2$, gives $n \simeq 4 \times 10^3\,{\rm cm}^{-3}$. However, from the lack of detectable wide-spread CO emission from the Veil shell, also in the southern limb-brightened shell, we can set an upper limit for the visual extinction of $A_{\rm V} \sim 2$, equivalent to a gas column of $N_{\rm H} \sim 4 \times 10^{21}\,{\rm cm}^{-2}$ (Goicoechea et al. 2020).

With a shell thickness of $d \simeq 0.3\,{\rm pc}$ and a density of $n \simeq 1.5 \times 10^3\,{\rm cm}^{-3}$, the shell has a radial C^+ column density of $N_{\rm C^+} \simeq 2 \times 10^{17}\,{\rm cm}^{-2}$. Adopting this latter value and an excitation temperature of $T_{\rm ex} = 50\,{\rm K}$, the calculated [C II] optical depth, given by:

$$\tau_{\rm [C\,II]} = \frac{A\lambda^3}{4\pi b} N_{\rm C^+} \frac{\exp\left(\frac{\Delta E}{k_{\rm B} T_{\rm ex}}\right) - 1}{\exp\left(\frac{\Delta E}{k_{\rm B} T_{\rm ex}}\right) + 2}, \tag{4.6}$$

in the shell seen face-on is $\tau_{\rm [C\,II]} \simeq 0.4$, with a line width of $\Delta v_{\rm FWHM} = 2\sqrt{\ln 2}b \simeq 4\,{\rm km\,s}^{-1}$. The expected peak temperature then,

$$T_{\rm P} = \frac{91.2\,{\rm K}(1 - \exp(-\tau_{\rm [C\,II]}))}{\exp\left(\frac{91.2\,{\rm K}}{T_{\rm ex}}\right) - 1}, \tag{4.7}$$

is $T_{\rm P} \simeq 6\,{\rm K}$, which is in reasonably good agreement with the peak temperatures of the narrow expanding components in spectra in Fig. 4.6.

We can also calculate the mass of the [C II]-emitting gas from the luminosity of the shell, $L_{\rm [C\,II]} \simeq 170\,L_\odot$ in the limb-brightened Veil shell, assuming that the line is effectively optically thin. By

$$M = \frac{\mu m_{\rm H}}{\mathcal{A}_{\rm C} A \Delta E} \left(\frac{g_{\rm l}}{g_{\rm u}} \exp\left(\frac{\Delta E}{k_{\rm B} T_{\rm ex}}\right) + 1 \right) L_{\rm [C\,II]}, \tag{4.8}$$

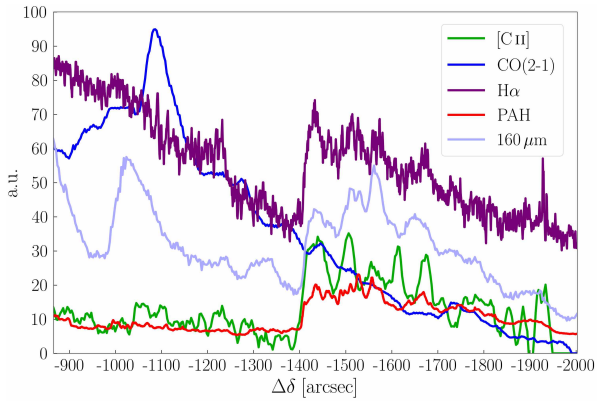

Figure 4.4: Line cut through the southwest of the Veil shell, indicated in Fig. 6.2. The onset of the shell is marked by a steep increase in all tracers, except CO, at $\Delta\delta \simeq -1400''$. With a line angle of 30° with respect to the vertical axis, this is at a distance of 3.25 pc from the Trapezium stars.

where $\mathcal{A}_{\rm C} \simeq 1.6 \times 10^{-4}$ is the carbon gas-phase abundance (Sofia et al. 2004), $A \simeq 2.3 \times 10^{-6}\,{\rm s}^{-1}$ the Einstein coefficient for spontaneous emission, $\Delta E/k_{\rm B} \simeq 91.2\,{\rm K}$ the level separation of the two levels with statistical weights $g_{\rm l} = 2$ and $g_{\rm u} = 4$, we obtain $M \simeq 680\,M_\odot$, assuming an excitation temperature of $T_{\rm ex} = 50\,{\rm K}$. As we expect the line to be (marginally) optically thick in the limb-brightened shell, $\tau_{\rm [C\,II]} \simeq$ 1-2, this value constitutes a lower limit of the shell mass. Correcting with this [C II] optical depth would yield a mass estimate of at least $M \simeq 1100\,M_\odot$. For further analysis we will use the mass estimate from the dust optical depth, where we have subtracted the mass of the Eastern Rim, $M \simeq 1500\,M_\odot$. This mass estimate is robust when considering only the PACS bands in the SED, reducing contamination by cold background gas. We recognize that the column density of the shell is highly variable and is lowest in the foreground shell. This is as expected given the strong pressure gradient from the molecular cloud surface towards us (cf. Section 4.4.1).

We judge that the large-scale arc-structured [C II] line emission mainly stems from the outer dense neutral shell indeed, rather than from the contained ionized gas. Evidence for this is the rather small line width where there is a significant signal, which is comparable to the line width of the main component from the neutral surface layer of the molecular cloud ($\Delta v_{\rm FWHM} \simeq$ 3-4 km s^{-1}, cf. Fig. 4.6). If the [C II] line originated from the hot ($T \sim 10^4\,{\rm K}$) ionized gas, we would expect it to be broader, $\Delta v_{\rm FWHM} \sim 10\,{\rm km\,s^{-1}}$, as observed in the H II region bordering the Horsehead Nebula (Pabst et al. 2017). Where the signal from the expanding shell is weak, we indeed observe such broad lines, hence part of the shell might still be ionized (see Section 4.4.4 for a discussion of the ionization structure of wind-blown bubbles). The limb-brightened shell is also visible in Hα, indicating that the surface is ionized. This is also illustrated by the line cut in Fig. 4.4, where the onset of the shell is marked by a steep increase in all tracers except CO. The relative lack of CO indicates low extinction of FUV photons within the southern shell and gives an upper limit on the density in this part, $n \lesssim 3 \times 10^3{\rm cm}^{-3}$. From the correlation with other (surface) tracers ([C II], 8 μm, 160 μm) along the line cut we conclude that the shell has a corrugated surface structure, as there are multiple emission peaks in these tracers behind the onset of the shell.

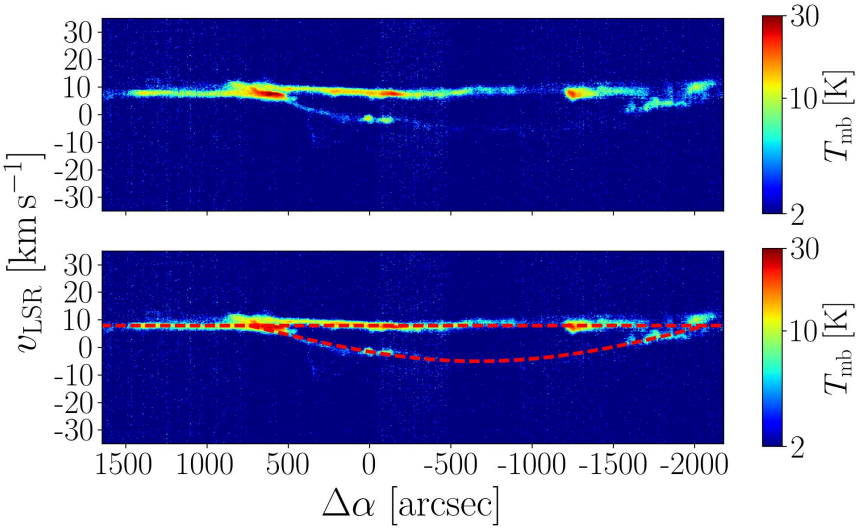

Figure 4.5: [C II] pv diagram along horizontal position cut 2 indicated in Fig. 6.2 ($\Delta\delta = -907''$- $-831''$). The lower panel shows the same cut with the arc structure for an expansion velocity of $13\,\mathrm{km\,s^{-1}}$ on a background velocity of $8\,\mathrm{km\,s^{-1}}$ (red dashed lines).

The broader lines ($\Delta v_{\rm FWHM} > 5\,\mathrm{km\,s^{-1}}$) we observe where the shell arc is barely visible, agree with an estimation of the expected [C II] emission from ionized gas in the shell. Here, we have (Pabst et al. 2017):

$$I_{\rm [C\,II]} \simeq 10\,\mathrm{K\ km\,s^{-1}} \frac{n_e}{10^2\,\mathrm{cm^{-3}}} \frac{l}{1\,\mathrm{pc}}, \tag{4.9}$$

which is, with an electron density of $n_e \sim$ 50-100 $\mathrm{cm^{-3}}$ (O'Dell & Harris 2010) and a line of sight of $l \sim 0.3\,\mathrm{pc}$, what we find in the spectra from the pv diagram in Fig. 4.6. We do not expect much [C II] emission from the inner region of the EON, since the dominant ionization stage of carbon in the vicinity of a O7 star is C^{2+}.

Expansion velocity

Persistent arc structures observed in position-velocity (pv) diagrams are the signature of bubbles that form in the ISM. By the aid of such diagrams one can estimate the expansion velocity of the associated dense shell. The pv diagrams for the Veil shell reveal the presence of a half shell. Figure 4.5 shows one such pv diagram as an example. Other cuts are shown in Appendix 4.C. Pabst et al. (2019) estimate an expansion velocity of $v_{\rm exp} \simeq 13\,\mathrm{km\,s^{-1}}$ for this half shell. This value is consistent with Gaussian fits to single (averaged) spectra taken from the pv diagram where this is possible (Fig. 4.6).

It is important to note that the bubble shell traced by [C II] emission expands in one direction only, which is towards us. Towards the back, the gas is confined by the background molecular cloud hindering rapid expansion. The prominent $8\,\mathrm{km\,s^{-1}}$ emission originates from this dense background gas.

An alternative way to estimate the expansion velocity of the bubble is from channel maps of this region. With increasing $v_{\rm LSR}$, the limb-brightened shell filament of M42 is observed to move outward, away from the Trapezium stars, as can be seen from

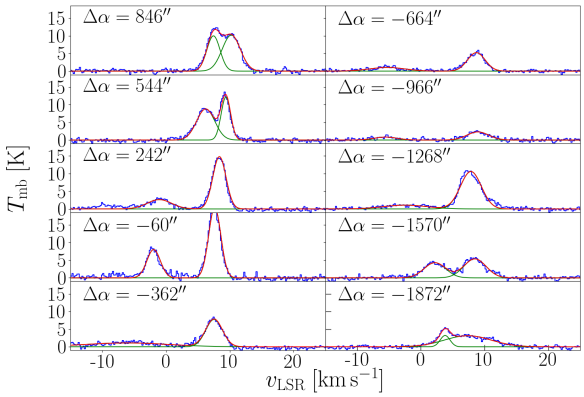

Figure 4.6: [C II] spectra in the Veil shell taken from pv diagram in Fig. 4.5 with Gaussian fits. Spectra at $\Delta\alpha = -362''$ to $\Delta\alpha = -1268''$ are averaged over $151'' \times 75.5''$ in order to improve the signal-to-noise ratio of the faint shell component to be fitted, others are averaged over $75.5'' \times 75.5''$. Coordinate offsets indicate the lower left-hand corner of the rectangle over which the spectra are averaged; $\Delta\delta = -907''$. The fit parameters are given in Table 4.1.

Fig. 4.7. The projected geometry of the filaments in different channels provides an estimate of $v_{\rm exp}$. However, this only works well in the bright eastern arm of the shell, the so-called Rim, which is comparatively narrow (cf. Appendix 4.B, Figs. 4.26 and 4.27). In other parts of the limb-brightened shell, the south and west, the filaments in different velocities do not line up consistently. To the north of the Trapezium stars, we do not see outward expansion at all. From these alternative methods (fitting Gaussians to single spectra, outlines of the limb-brightened shell) we find values agreeing with those computed above from the pv diagram, $v_{\rm exp} \simeq$ 10-15 km s^{-1}. Also the majority of pv diagrams shown in Figs. 4.30 and 4.31 are consistent with an overall expansion velocity of $v_{\rm exp} \simeq 13\,{\rm km\,s^{-1}}$.

Figure 4.8 compares the velocity structures of [C II], ^{12}CO(2-1), ^{13}CO(2-1), and H I along a vertical cut at $\Delta\alpha = 167''$-$242''$. This figure illustrates the complex dynamics in the region of the Orion Nebula and contrasts the various kinematic structures in the different tracers. It gives an impression of the variety of emission structures and the potential synergies between the four data sets. The cut shows arc structures close to the central region (Huygens Region) that coincide with structures detected in H I and discussed in van der Werf et al. (2013). Also, the shell surrounding M43 is distinctly visible (cf. Fig 4.12). We note that to the north the bubble-like arc of the Veil shell is disrupted by apparently violent gas dynamics in that region, even far to the west of the Huygens Region. Closer examination of pv diagrams in this region reveal multiple arcs indicative of bubble structures (see Appendix 4.C for all pv diagrams through the Veil shell). South of OMC1, the observed difference in velocity ($\sim 1\,{\rm km\,s^{-1}}$) between the [C II] background and the molecular cloud as traced by CO is typical for the advection flow through the PDR (Tielens 2010, ch. 12). From our analysis, we conclude that the systematic uncertainty of the mass estimate are of the order of 50%, systematic uncertainties of the estimates of the extent of the shell and of the expansion velocity are about 30%.

Table 4.1: Gaussian fit parameters of spectra in Fig. 4.6.

$\Delta\alpha$	comp.	$T_{\rm P}$ [K]	$v_{\rm P}$ [km s^{-1}]	$\Delta v_{\rm FWHM}$ [km s^{-1}]
846″	1	10.2 ± 0.2	10.2 ± 0.1	3.4 ± 0.2
846″	2	10.0 ± 0.5	7.4 ± 0.1	2.4 ± 0.1
544″	1	12.2 ± 0.2	9.4 ± 0.1	1.7 ± 0.1
544″	2	8.8 ± 0.2	6.2 ± 0.1	3.4 ± 0.1
242″	1	14.8 ± 0.2	8.4 ± 0.1	2.4 ± 0.1
242″	2	2.6 ± 0.2	-1.1 ± 0.1	4.5 ± 0.3
−60″	1	20.0 ± 0.3	7.6 ± 0.1	2.2 ± 0.1
−60″	2	8.0 ± 0.2	-2.0 ± 0.1	2.5 ± 0.1
−362″	1	7.8 ± 0.2	7.5 ± 0.1	3.1 ± 0.1
−362″	2	1.1 ± 0.1	-6.2 ± 0.4	15.4 ± 1.2
−664″	1	5.2 ± 0.1	8.7 ± 0.1	3.3 ± 0.1
−664″	2	1.0 ± 0.1	-5.3 ± 0.3	6.4 ± 0.6
−966″	1	2.3 ± 0.2	8.9 ± 0.1	4.0 ± 0.3
−966″	2	0.8 ± 0.2	-5.5 ± 0.3	4.2 ± 0.7
−1268″	1	10.6 ± 0.2	7.9 ± 0.1	3.9 ± 0.1
−1268″	2	1.1 ± 0.1	-2.5 ± 0.3	8.0 ± 0.8
−1570″	1	5.4 ± 0.2	8.5 ± 0.1	4.1 ± 0.2
−1570″	2	4.3 ± 0.2	2.2 ± 0.1	4.0 ± 0.2
−1872″	1	3.1 ± 0.1	7.4 ± 0.2	8.7 ± 0.3
−1872″	2	3.2 ± 0.2	3.8 ± 0.1	1.8 ± 0.2

Notes. The expanding Veil shell is captured in component 2.

4.3.3 M43

Geometry, mass and physical conditions

The nebula M43 hosts the central star NU Ori, which is located approximately at the geometrical center of the limb-brightened shell. The shell radius is $r \simeq 150'' \simeq 0.3\,\mathrm{pc}$ with a thickness of $\Delta r \simeq 0.05\,\mathrm{pc}$. Fig. 4.9 shows a three-color image of M43. Hα stems from the center of M43, constrained by a thin shell of [C II] and CO in the east and north. To the south lies the massive bulk of OMC1. The H II region of M43 appears as a region of higher dust temperature, the shell is distinctly visible in [C II], IRAC 8 μm emission, FIR emission from warm dust (cf. Fig. 1 in Pabst et al. (2019)), and CO. The limb-brightened shell reveals the structure of a PDR with 8 μm PAH emission, [C II] emission, and 160 μm warm dust emission originating at the inner, illuminated side while the CO emission originate from deeper within the shell (Fig. 4.10). M43 is located just eastwards of the ridge of the molecular ISF, whose illuminated, [C II] emitting outliers form the background against which the half-shell expands.

From our dust SEDs, we derive a mass of $M \simeq 210\,M_\odot$. However, this mass is likely contaminated by the mass of the molecular background, whose surface is visible in [C II] (cf. Fig. 4.8). Using only the PACS bands in the SED, reduces the mass estimate to $M \simeq 110\,M_\odot$. From the [C II] luminosity, $L_{\rm [C\,II]} \simeq 24\,L_\odot$ and assuming $T_{\rm ex} \simeq 90\,\mathrm{K}$ (see below), the mass is estimated to be $M \simeq 55\,M_\odot$.

We note that the limb-brightened shell of M43 consists of two segments. The eastern shell lies closer to the central star and therefore is probably denser. We can

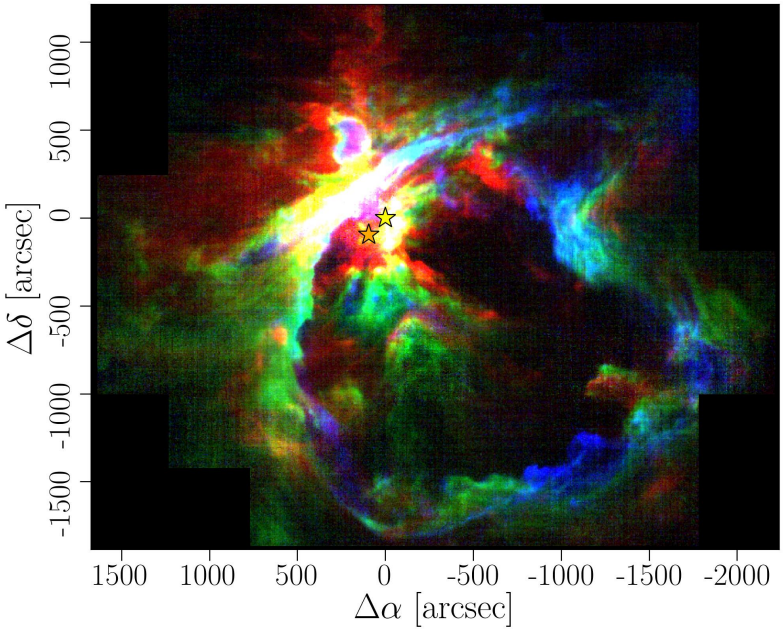

Figure 4.7: Three-color image of velocity channels towards M42 and M43. Blue is the velocity channel $v_{\rm LSR}$ = 4-5 km s^{-1}, green $v_{\rm LSR}$ = 6-7 km s^{-1}, and red $v_{\rm LSR}$ = 9-10 km s^{-1}. With increasing $v_{\rm LSR}$, the limb-brightened Veil shell filament is displaced outward, away from the bubble center. The gas of M43 that is expanding towards us can be observed in the blue channel; the limb-brightened shell of M43 has higher $v_{\rm LSR}$.

derive the density of the shell by the distance between the [C II] and the CO peak in a line cut through that region (Fig. 4.10a), $\Delta d \simeq 20'' \simeq 0.04$ pc between the [C II] peak at $\Delta\alpha \simeq 310''$ and the CO peak at $\Delta\alpha \simeq 330''$. Assuming a typical PDR structure with $\Delta A_{\rm V} \simeq 2$ between the PDR front, traced by [C II], and the CO peak, we arrive at a density of $n \simeq 3 \times 10^4\,{\rm cm}^{-3}$. In the northern shell (Fig. 4.10b) we derive a density of $n \simeq 8 \times 10^3\,{\rm cm}^{-3}$ with $\Delta d \simeq 80'' \simeq 0.16$ pc between the [C II] peak at $\Delta\delta \simeq 560''$ and the CO peak at $\Delta\delta \simeq 640''$. With the shell extent above, that is $V = \frac{2\pi}{3}\left((0.3\,{\rm pc})^3 - (0.25\,{\rm pc})^3\right)$, and the latter density estimate, we compute a mass of the expanding hemisphere of $M \simeq 7\,M_\odot$, which is significantly lower than the mass derived from the dust optical depth and the [C II] luminosity. Given the potential contamination of these mass estimates by background molecular cloud material, we elected to go with the latter estimate for the gas mass.

When averaging over the eastern limb-brightened shell of M43, we detect the [^{13}C II] F = 2-1 line at a 4σ level, as shown in Fig. 4.11. From this[5] we obtain an average $\tau_{\rm [C\,II]} \simeq 2.4^{+1.0}_{-1.4}$ and an excitation temperature of $T_{\rm ex} \simeq 89^{+20}_{-5}$ K. This translates into a C^+ column density of $N_{\rm C^+} \simeq 2.7^{+0.9}_{-1.2} \times 10^{18}\,{\rm cm}^{-2}$ along the line of sight. Assuming that most of the material is located in the limb-brightened shell, we can estimate a density in the shell with the assumed length of the line of sight of $l \sim r/2$. With $r \simeq 0.3$ pc, this gives $n \simeq 3 \times 10^4\,{\rm cm}^{-3}$, which is about the same as the previous estimate from the [C II]-CO peak separation. With this density we compute a gas

[5] We use the peak temperature of the single-component fit, assuming that the [^{13}C II] component corresponds to the combination of the two main components, as suggested by the similar line widths of the single-component fits.

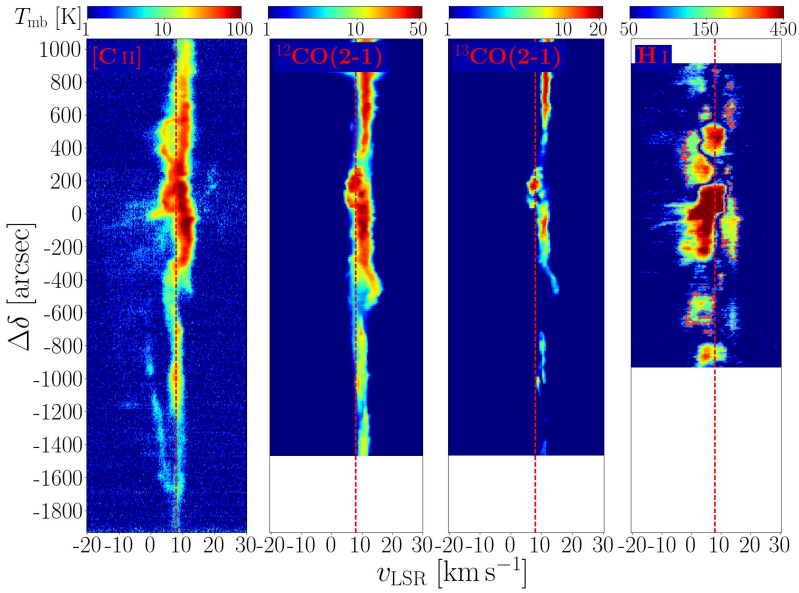

Figure 4.8: PV diagrams along vertical position cut 1 indicated in Fig. 6.2 ($\Delta\alpha$ = 167″-242″) in [C II], ^{12}CO(2-1), ^{13}CO(2-1) (Berné et al. 2014; Goicoechea et al. 2020), and H I (van der Werf et al. 2013).

temperature of $T_{\rm gas} \simeq 90\,$K.

If we assume the [C II] emission from the limb-brightened shell to be (marginally) optical thick, we can estimate the excitation temperature from the [C II] peak temperature. This gives an average of $T_{\rm ex} \simeq 110\,$K, and hence a slightly higher gas temperature than from the [^{13}C II] estimate.

Expansion velocity

The [C II] pv diagram running through M43 clearly exhibits a half shell structure (Fig. 4.12). From the spectra taken towards this region (Fig. 4.12), we measure an expansion velocity of $v_{\rm exp} \simeq 6\,{\rm km\,s^{-1}}$. The bubble only expands towards us, away from the background molecular cloud. We do not see an expanding CO counterpart (cf. Fig. 4.8). The pv diagram is consistent with the radius of the shell of $r \simeq 150'' \simeq 0.3\,$pc and the expansion velocity of $v_{\rm exp} \simeq 6\,{\rm km\,s^{-1}}$, both values are much less than those derived for the Trapezium wind-blown bubble. Also, in Fig. 4.12, we observe [C II] emission from within the shell arc, presumably stemming from the expanding ionized gas.

The eastern shell of M43, that lies closer to the shell center, moves outward at a velocity of about $v_{\rm exp} \simeq 2.5\,{\rm km\,s^{-1}}$ (estimated from channel maps, see above and Appendix 4.B). This corroborates the thesis that this is a denser region compared to other structures in M43. Again, the systematic uncertainty of the mass estimate is of the order of 50%, systematic uncertainties of the estimates of the extent of the shell and of the expansion velocity are about 30%.

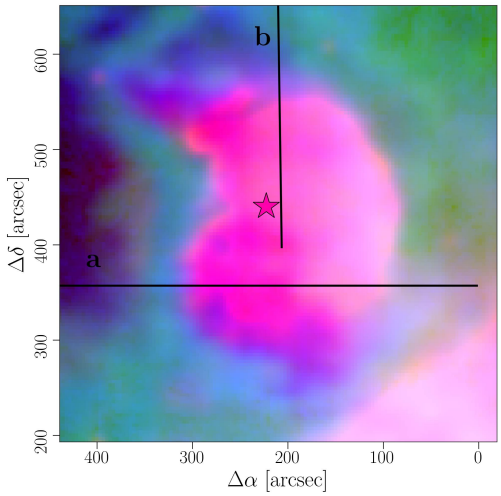

Figure 4.9: Three-color image of M43. Red is Hα emission from the ionized gas, green is line-integrated CO(2-1) emission from molecular gas, and blue is the [C II] line-integrated intensity, tracing the neutral gas. The line cuts in Fig. 4.10 are taken along lines a and b.

Table 4.2: Gaussian fit parameters of spectra in Fig. 4.13.

$\Delta\delta$	comp.	$T_{\rm P}$ [K]	$v_{\rm P}$ [km s^{-1}]	$\Delta v_{\rm FWHM}$ [km s^{-1}]
377″	1	43.1 ± 0.4	10.2 ± 0.1	2.9 ± 0.1
377″	2	26.4 ± 0.3	4.1 ± 0.1	2.1 ± 0.1
377″	3	10.9 ± 0.3	6.3 ± 0.2	8.0 ± 0.1
452″	1	41.6 ± 0.4	10.4 ± 0.1	2.8 ± 0.1
452″	2	10.0 ± 0.3	4.4 ± 0.1	2.0 ± 0.1
452″	3	14.9 ± 0.3	7.2 ± 0.1	8.5 ± 0.1
528″	1	44.7 ± 0.9	10.5 ± 0.1	3.3 ± 0.1
528″	2	14.9 ± 0.4	4.8 ± 0.1	1.8 ± 0.1
528″	3	14.3 ± 0.4	7.3 ± 0.2	6.9 ± 0.2

4.3.4 NGC 1977

Geometry, mass and physical conditions

As for M42 and M43, the shell structure of NGC 1977 is almost spherical, but again it is offset from the central star(s). We estimate its geometric center at $(\Delta\alpha, \Delta\delta) = (195'', 155'')$ (from 42 Orionis, $(\Delta\alpha, \Delta\delta) = (-100.4'', 1984.7'')$ from θ^1 Ori C) and its outer radius with $r = 800'' = 0.22\,\mathrm{deg}$, which corresponds to $r \simeq 1.6\,\mathrm{pc}$, assuming a distance of 414 pc (Menten et al. 2007). Hence, the projected distance of the bubble center from 42 Orionis is 0.5 pc. The thickness of the limb-brightened shell is $\Delta r = 7' \simeq 0.8\,\mathrm{pc}$, somewhat thicker than the shell of M42, but more dilute as well. Figure 4.14 shows a three-color image of NGC 1977. Visible Hα stems from the center of NGC 1977, constituting an H II region, surrounded by a shell of [C II] and constrained by a bulk CO cloud (OMC3) in the southwest.

The limb-brightened shell is seen in [C II] emission in the velocity range $v_{\rm LSR} =$

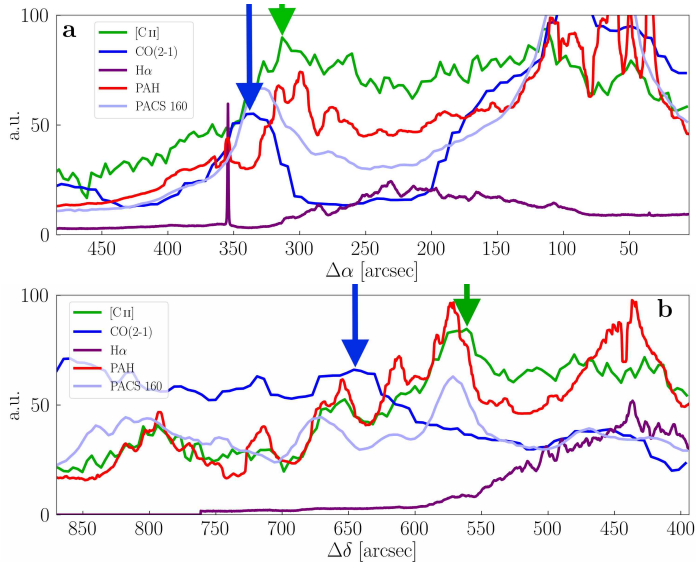

Figure 4.10: Line cuts along lines a and b, indicated in Fig. 4.9. The arrows indicate the peaks in [C II] emission (green) and CO emission (blue) that correspond to the shell.

9-15 km s^{-1}. The brightest [C II] component stems from the molecular core OMC3, which hosts a PDR at its surface towards 42 Orionis. The [C II] emission associated with this PDR is analyzed in detail by Kabanovic et al. (in prep.). With the FUV luminosity given by Kim et al. (2016), we compute an incident FUV intensity of $G_0 \simeq 100$ at the shell surface.

From our τ_{160} map, we estimate the mass of the shell, where we exclude the region of OMC3. We obtain $M \simeq 700\,M_\odot$. With the [C II] luminosity $L_{[\mathrm{C\,II}]} \simeq 140\,L_\odot$, we derive a mass of the [C II]-emitting gas of $M \simeq 540\,M_\odot$ for $T_{\mathrm{ex}} = 50\,\mathrm{K}$, somewhat lower than the mass derived from the dust opacity, but still in good agreement[6].

Figure 4.15 shows the average spectrum towards the [C II]-bright shell of NGC 1977, excluding OMC3. Here, the detection of the [^{13}C II] F = 2-1 line is marginal with $\sigma \simeq 3$. As the [C II] optical depth and excitation temperature are very sensitive to the exact [^{13}C II] peak temperature, it is hard to derive reliable values with the uncertainties at hand (fit uncertainties and baseline ripples). With the results of a Gaussian fit as given in the caption of Fig. 4.15, we obtain $\tau_{[\mathrm{C\,II}]} \simeq 0.7 \pm 0.3$ and $T_{\mathrm{ex}} \simeq 70^{+30}_{-10}\,\mathrm{K}$. The resulting C$^+$column density then is $N_{\mathrm{C^+}} \simeq 6 \pm 2 \times 10^{17}\,\mathrm{cm}^{-2}$. If we assume a column length of $r/2 \simeq 0.5\,\mathrm{pc}$ in the limb-brightened shell, we estimate a density of $n \simeq 2.5 \times 10^3\,\mathrm{cm}^{-3}$. This results in an estimate of the gas temperature of $T_{\mathrm{gas}} \simeq 180\,\mathrm{K}$, which is somewhat higher than expected for the rather moderate radiation field in NGC 1977.

The mean dust optical depth from NGC 1977 (without OMC3) is $\tau_{160} \simeq 2.4 \times 10^{-3}$. From this, with $r/2 \simeq 0.5\,\mathrm{pc}$, we estimate a gas density of $n \simeq 1 \times 10^4\,\mathrm{cm}^{-3}$ in the shell. With the average $T_{\mathrm{ex}} \simeq 70\,\mathrm{K}$ (from the dust optical depth and the peak temperature of the [C II]), this gives $T_{\mathrm{gas}} \simeq 90\,\mathrm{K}$. From the dust optical depth and the [C II] peak temperature, we calculate $\tau_{[\mathrm{C\,II}]} \sim 3$, so [C II] emission is optically thick. This is in disagreement with the result from the [^{13}C II] F = 2-1 line. However, the

[6]The excitation temperature is not well-constrained, see analysis below.

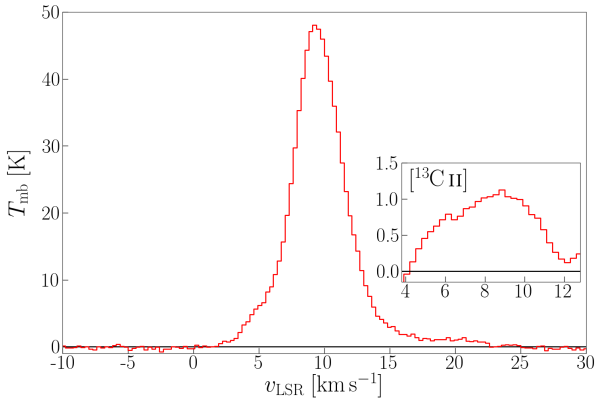

Figure 4.11: Average [C II] spectrum towards the eastern shell of M43. The inlaid panel shows the residual of the spectrum, in the systemic velocity of the [^{13}C II] $F = 2$-1 line, after subtracting the [^{12}C II] fit. The [^{12}C II] line can be fitted by a Gaussian with $T_{\rm P} \simeq 46.2 \pm 0.3\,{\rm K}$, $v_{\rm P} \simeq 9.6 \pm 0.1\,{\rm km\,s^{-1}}$, $\Delta v_{\rm FWHM} \simeq 4.6 \pm 0.1\,{\rm km\,s^{-1}}$; the [^{13}C II] $F = 2$-1 component is fitted by a Gaussian with $T_{\rm P} \simeq 1.1 \pm 0.2\,{\rm K}$, $v_{\rm P} \simeq 8.6 \pm 0.3\,{\rm km\,s^{-1}}$, $\Delta v_{\rm FWHM} \simeq 4.8 \pm 0.8\,{\rm km\,s^{-1}}$. We note that a better fit of the [^{12}C II] line can be obtained by fitting two components with $T_{\rm P} \simeq 30.9 \pm 1.3\,{\rm K}$, $v_{\rm P} \simeq 9.6 \pm 0.1\,{\rm km\,s^{-1}}$, $\Delta v_{\rm FWHM} \simeq 3.3 \pm 0.1\,{\rm km\,s^{-1}}$ and $T_{\rm P} \simeq 17.5 \pm 1.3\,{\rm K}$, $v_{\rm P} \simeq 9.8 \pm 0.1\,{\rm km\,s^{-1}}$, $\Delta v_{\rm FWHM} \simeq 6.8 \pm 0.2\,{\rm km\,s^{-1}}$, but both fits leave significant residuals.

result obtained here seems to be more credible, as it yields a gas temperature that is more in line with a previous [C II] study of the Horsehead Nebula at similar impacting radiation field (Pabst et al. 2017). PDR models predict a surface temperature of $\sim 150\,{\rm K}$ (Kaufman et al. 2006; Pound & Wolfire 2008), but the [C II]-emitting layer is expected to be somewhat cooler.

In the region where the spectrum in Fig. 4.18 is taken, we have an average $\tau_{160} \simeq 8.6 \times 10^{-4}$, corresponding to a hydrogen column density of $N_{\rm H} \simeq 5 \times 10^{21}\,{\rm cm^{-2}}$. From H$\alpha$ emission, we can estimate the electron density in the ionized gas that is contained in the shell. We obtain $n_e \simeq 40\,{\rm cm^{-3}}$. Hence, with a column length of $l \sim 2\,{\rm pc}$ the ionized gas is only a fraction of the total column density. Most of the dust emission within the column stems from the denser expanding shell. With a shell thickness of $d \simeq 0.8\,{\rm pc}$, appropriate for the limb-brightened shell, we estimate a gas density of $n \simeq 2 \times 10^3\,{\rm cm^{-3}}$. From the column density[7] (assuming that all carbon is ionized) and the spectrum we calculate an excitation temperature of $T_{\rm ex} \simeq 37\,{\rm K}$ and a [C II] optical depth of $\tau_{\rm [C\,II]} \simeq 1$. This corresponds to a gas temperature of $T_{\rm gas} \simeq 60\,{\rm K}$, which is somewhat lower than in the limb-brightened shell as calculated above. However, a slight overestimation of the dust optical depth of the expanding material would lead to a significantly increased estimate of the gas temperature.

Towards the center of the H II region, we observe a very broad component in the [C II] spectrum (Fig. 4.16). This component likely stems from the ionized gas. The expected [C II] intensity from ionized gas at a temperature of $T \sim 10^4\,{\rm K}$ with an electron density of $n_e \simeq 40\,{\rm cm^{-3}}$ and a line of sight of $l \simeq 2\,{\rm pc}$ matches the observed intensity very well. We note that the line is broader than what one would expect from thermal broadening alone. The additional broadening might be due to enhanced turbulence and the expansion movement of the gas.

[7] We use half the column density for each of the two [C II] spectral components.

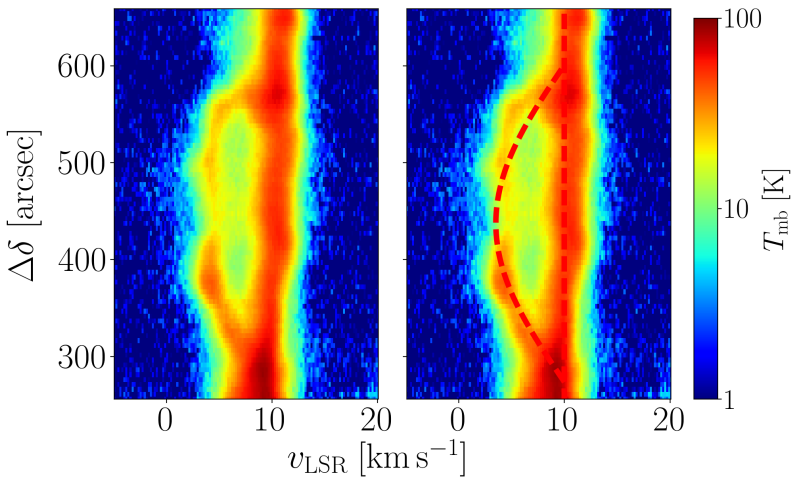

Figure 4.12: [C II] pv diagram along vertical position cut 1 indicated in Fig. 6.2 ($\Delta\alpha$ = 167″-242″), zoomed in to M43 (cf. Fig. 4.8). The right panel shows the same cut with the arc structure for an expansion velocity of 6 km s^{-1} on a background velocity of 8 km s^{-1} (red dashed lines).

Table 4.3: Gaussian fit parameters of spectrum in Fig. 4.16.

comp.	$T_{\rm P}$ [K]	$v_{\rm P}$ [km s^{-1}]	$\Delta v_{\rm FWHM}$ [km s^{-1}]
1	10.3 ± 0.1	11.9 ± 0.1	2.3 ± 0.1
2	1.1 ± 0.1	11.6 ± 0.2	11.6 ± 0.6

Expansion velocity

Figure 4.17 shows a [C II] pv diagram through the center of the bubble associated with NGC 1977. We recognize evidence of expansion but the arc structure is much fainter than in M42 and M43 and disrupted. As opposed to M42 and M43, there is no background molecular cloud constraining the expanding gas: we see the bubble expanding in two directions.

Since the [C II] emission from NGC 1977 is fainter than that of M42, we have opted to determine the expansion velocity from spectra towards this region (Fig. 4.18), resulting in $v_{\rm exp} \simeq 1.3\,{\rm km\,s^{-1}}$. This is consistent with the pv diagram shown in Fig. 4.17, from which we obtain the bubble radius $r \simeq 500'' \simeq 1.0\,{\rm pc}$ with the expansion velocity of $v_{\rm exp} \simeq 1.5\,{\rm km\,s^{-1}}$. As for the Veil shell and M43, the systematic uncertainty of the mass estimate are of the order of 50%, systematic uncertainties of the estimates of the extent of the shell and of the expansion velocity are about 30%.

4.4 Discussion

OMC1, including the Trapezium cluster, is the nearest site of active intermediate- and high-mass star formation (e.g., Hillenbrand (1997); Megeath et al. (2012); Da Rio et al. (2014); Megeath et al. (2016); Großschedl et al. (2019) for discussions of the stellar content). Most of the stars formed and forming are low-mass stars, but also

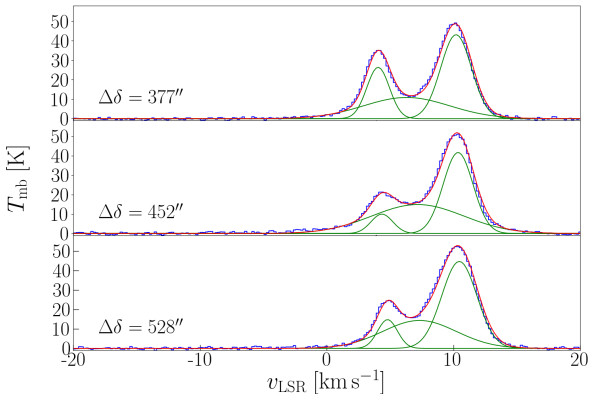

Figure 4.13: [C II] spectra along position cut 1 (cf. Fig. 4.12) in M43 with Gaussian fits. Each spectrum is averaged over $75.5'' \times 25.2''$. The expanding shell has a distinguished emission peak. Additionally to the main component and the shell component, we fit a third, broad, component, that possibly stems from the ionized gas within the shell. Coordinate offsets indicate the lower left-hand corner of the rectangle over which the spectra are averaged; $\Delta\alpha = 242''$. The fit parameters are given in Table 4.2.

Table 4.4: Gaussian fit parameters of spectrum in Fig. 4.18.

comp.	$T_{\rm P}$ [K]	$v_{\rm P}$ [km s^{-1}]	$\Delta v_{\rm FWHM}$ [km s^{-1}]
1	4.0 ± 0.2	10.2 ± 0.1	1.7 ± 0.1
2	4.7 ± 0.2	12.8 ± 0.1	1.8 ± 0.1
3	1.3 ± 0.2	11.3 ± 0.2	9.0 ± 0.7

some high-mass stars, that have profound impact on the characteristics and evolution of their environment. Outside the Huygens Region, a significant massive (triple) star is the O9.5IV star θ^2 Ori A, located just to the southeast of the Orion Bar. The radiation of this star dominates the ionization structure of the gas towards the southeast of the Huygens Region (O'Dell et al. 2017). It also possesses strong winds. The most dominant star in the Orion Nebula is the O7V star θ^1 Ori C, the most massive Trapezium star. It is itself a binary, with possibly a third companion (Lehmann et al. 2010). While its exact peculiar velocity is controversial, the θ^1 Ori C is plowing away from the molecular cloud, the site of its birth, and will have travelled some 25 pc before it explodes as a supernova (O'Dell et al. 2009; Kraus et al. 2009; Pabst et al. 2019).

While the small, 0.5 pc sized Huygens Region has been extensively studied, studies on the much fainter EON are less numerous. O'Dell & Harris (2010) determine the temperature of the ionized gas within the large EON H II region to be $T \sim 8.3 \times 10^3$ K, while electron densities decrease from $n_e \sim 3000\,{\rm cm}^{-3}$ at the Trapezium stars to about $n_e \sim 30\,{\rm cm}^{-3}$ $20'$ away, roughly as d^{-2}, with d the projected distance. Güdel et al. (2008) report that the EON exhibits significant X-ray emission, emanating from hot ($T \sim 2 \times 10^6$ K), dilute ($n_e \sim 0.1$-$0.5\,{\rm cm}^{-3}$) gas. While, in principle, ionization followed by thermal expansion of the H II region can create a bubble of ~ 2 pc size, the hot gas is the tell-tale signature that the stellar wind of massive stars, rather than stellar radiation, is driving the expansion and forming the EON cavity. As Güdel et al. (2008) note, the emission characteristics in conjunction with its structure and young

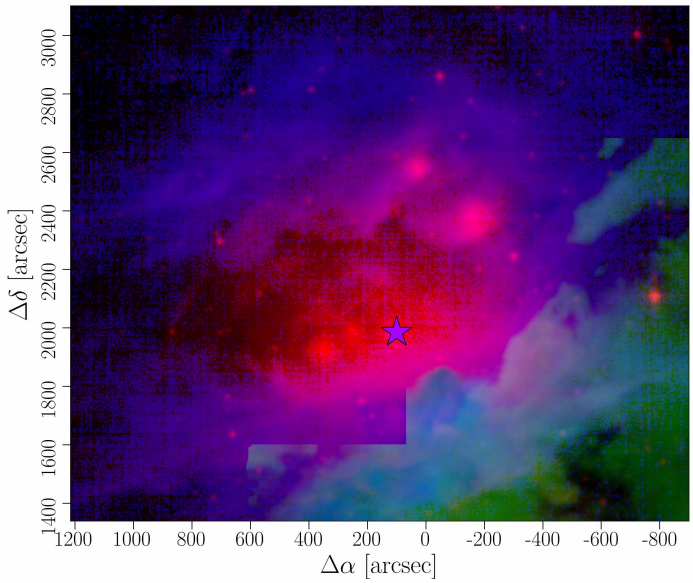

Figure 4.14: Three-color image of NGC 1977. Red is Hα emission from the ionized gas, green is line-integrated CO(2-1) emission from molecular gas (coverage only in OMC3), and blue is the [C II] line-integrated intensity, tracing the neutral gas.

age render it unlikely that the bubble is a supernova remnant. While the observed morphology is in qualitative agreement with simple models for stellar winds from massive stars (Weaver et al. 1977), the observed plasma temperature is lower than expected from refined models and suggests that mass loading of the hot plasma has been important (Arthur 2012).

Recently, the inner shocked wind bubble surrounding θ^1 Ori C has been identified in optical line observations (Abel et al. 2019). This inner shock will heat the gas in the EON that drives the expansion of a larger, outer, shell. These same observations, however, suggest that the thus heated gas is only free to escape through the south-west of the Huygens Region.

The limb-brightened edge of the Veil shell, the dense shell associated with M42, is readily observed edge-on. It is a closed, surprisingly spherically symmetric structure enveloping the inner Huygens Region and the EON (Pabst et al. 2019), and confining the hot X-ray emitting and ionized gas observed by Güdel et al. (2008) and O'Dell & Harris (2010) in the foreground. Likewise, the H II regions of M43 and NGC 1977 are surrounded by rather dense shells. The limb-brightened shell of M43 exhibits a PDR-like layered structure (cf. Fig. 4.10). At the southern edge of the shell surrounding NGC 1977 one encounters OMC3, which also possesses a PDR-like structure, irradiated by 42 Orionis (Kabanovic et al., in prep.).

For our analysis we adopt a distance of 414 ± 7 pc (Menten et al. 2007) towards the Orion Nebula complex, although more recent results suggest somewhat lower values, 388 ± 5 pc (Kounkel et al. 2017), which is in agreement with Gaia DR2 results (Großschedl et al. 2018). In view of other uncertainties in the analysis, we consider this a minor source of uncertainty.

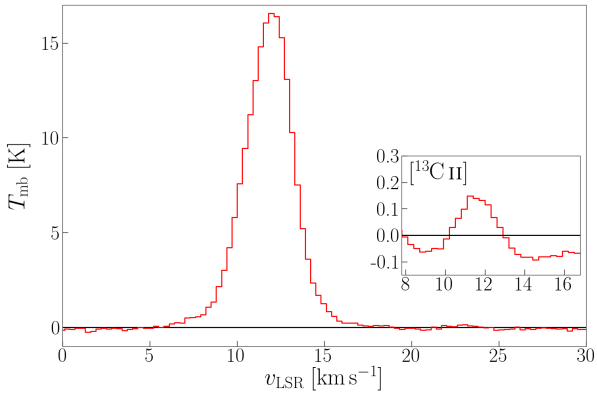

Figure 4.15: Average [C II] spectrum towards [C II]-bright shell of NGC 1977 (without OMC3). The inlaid panel shows the (smoothed) residual of the spectrum, in the systemic velocity of the [^{13}C II] F = 2-1 line, after subtracting the [^{12}C II] fit. The [^{12}C II] component can be approximated by a Gaussian with $T_{\rm P} \simeq 16.5{\pm}0.1$ K, $v_{\rm P} \simeq 12.0{\pm}0.1$ km s^{-1}, $\Delta v_{\rm FWHM} \simeq 3.2 \pm 0.1$ km s^{-1}; the [^{13}C II] F = 2-1 component is fitted by a Gaussian with $T_{\rm P} \simeq 0.21 \pm 0.03$ K, $v_{\rm P} \simeq 11.8 \pm 0.2$ km s^{-1}, $\Delta v_{\rm FWHM} \simeq 2.1 \pm 0.5$ km s^{-1}.

4.4.1 The pressure balance

Table 4.5 summarizes the physical conditions in the H II regions and the limb-brightened PDR shells in M42, M43, and NGC 1977. Table 4.6 summarizes the various pressure terms in the total pressure $p_{\rm tot} = p_{\rm thermal} + p_{\rm magnetic} + p_{\rm turb} + p_{\rm lines} + p_{\rm rad}$ in the PDRs of M42 (Orion Bar and Veil shell), M43, and NGC 1977.

The thermal pressure, $p_{\rm thermal} = nkT$, in the Orion Bar is controversial. Constant-pressure and H II region models of atomic and molecular lines of Pellegrini et al. (2009) and observations of molecular hydrogen by Allers et al. (2005) ($n \simeq 10^5$ cm^{-3}, $T_{\rm gas} \simeq 500$ K) indicate a pressure of $p/k_{\rm B} \simeq 5 \times 10^7$ K cm^{-3}. Observations of [C II] and [O I] emission in the Orion Bar suggest similar values ($n \gtrsim 10^5$ cm^{-3}, $T_{\rm gas} \gtrsim 300$ K) (Bernard-Salas et al. 2012; Goicoechea et al. 2015b). High-J CO observations indicate a higher gas pressure within the Bar, 3×10^8 K cm^{-3} (Joblin et al. 2018). This latter value is in agreement with observations of carbon radio recombination lines (CRRLs) that measure the electron density in the PDR directly ($n \gtrsim$ 4-7$\times 10^5$ cm^{-3}) (Cuadrado et al. 2019). The thermal pressures in the EON portion of M42, M43, and NGC 1977 have been calculated from the parameters given in Table 4.5.

The magnetic field strength in the Orion Bar has been estimated from the far-IR dust polarization using the Davis-Chandrasekhar-Fermi method to be 300 μG (Chuss et al. 2019). This corresponds to a magnetic field pressure, $p_{\rm magnetic} = B^2/8\pi$, of 3×10^7 K cm^{-3}. The magnetic field in the Veil in front of the Huygens Region is measured to be $B_{\rm los} \simeq -50$--75 μG from the H I and OH Zeeman effect (Troland et al. 2016); we compute the magnetic field pressure from the lower value[8]. The turbulent pressure, $p_{\rm turb} = \rho\sigma^2_{\rm turb}$, is calculated from the [C II] line width in the average spectra towards the Veil shell, M43, and NGC 1977 (Figs. 4.3, 4.11, and 4.18) after correction for thermal broadening at a kinetic temperature of $T_{\rm gas} \sim 100$ K (cf. Table 4.5); with a typical line width of $\Delta v_{\rm FWHM} \simeq 4$ km s^{-1} this gives $\sigma_{\rm turb} \simeq 1.7$ km s^{-1}. In the Orion Bar, we use $\sigma_{\rm turb} \simeq 1.5$ km s^{-1} (Goicoechea et al. 2015b).

[8]The magnetic pressure is computed from $B_{\rm tot} = 3B^2_{\rm los}$.

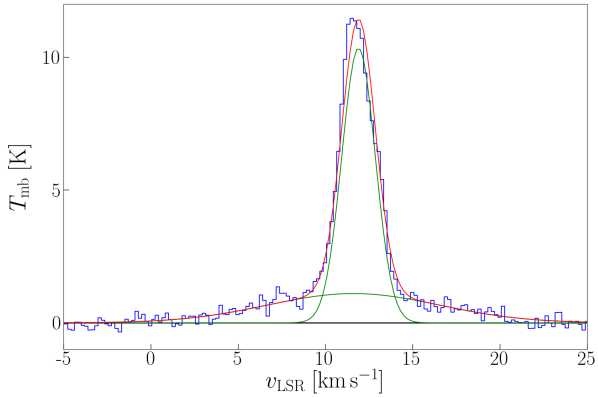

Figure 4.16: [C II] spectrum towards NGC 1977, averaged over circular area with radius 125″ centered at 42 Orionis ($(\Delta\alpha, \Delta\delta) = (-100.4'', 1984.7'')$), with Gaussian fits. The fit parameters are given in Table 4.3.

Table 4.5: Physical conditions of respective H II region and adjacent limb-brightened PDR shell in M42, M43, and NGC 1977.

region		n [cm^{-3}]	$T_{\rm gas}$ [K]	$p_{\rm thermal}/k_{\rm B}$ [cm^{-3} K]	G_0
Orion Bar	H II	5×10^3	8×10^3	8×10^7	
	PDR	6×10^5	500	3×10^8	2×10^4
Veil shell	plasma	0.3	2×10^6	1×10^6	
	H II	50	8×10^3	8×10^5	
	PDR	10^3-10^4	~ 100	1-10 $\times 10^5$	~ 100
M43	H II	500	7.5×10^3	8×10^6	
	PDR	10^4	100	1×10^6	$\sim 2 \times 10^3$
NGC 1977	H II	40	$\sim 10^4$	$\sim 8 \times 10^5$	
	PDR	10^3	90	9×10^4	~ 100

Notes. The plasma in M42 was analyzed by Güdel et al. (2008). Data on the M42 H II region are from O'Dell & Harris (2010), data on the M43 H II region are from Simón-Díaz et al. (2011). We note that the density of the M42 H II region given here is appropriate for the southern EON, as is G_0 in the Veil shell PDR.

The radiation pressure is in principle given by $p_{\rm rad} = L_\star/(4\pi R_S^2 c)$; the luminosities of the central stars are given in Table 4.8. We assume the (projected) distances $R_S \simeq 4\,$pc for the (southern) Veil shell, $R_S \simeq 0.25\,$pc for M43, and $R_S \simeq 1.0\,$pc for NGC 1977. However, for the Orion Bar, a direct measurement of the infrared flux suggests a value that is an order of magnitude lower than the pressure calculated from the stellar luminosity and the projected distance of $R_S \simeq 0.114\,$pc (Pellegrini et al. 2009), an incident radiation field of $G_0 = 2.6 \times 10^4$ (Marconi et al. 1998; Salgado et al. 2016). Hence, we choose to calculate the radiation pressure in the Orion Bar from this latter value. We note that in the other cases the radiation pressure given in Table 4.6 is, thus, an upper limit.

Resonant scattering of Lyα photons constitutes the major contribution to the line pressure term $p_{\rm lines}$. We expect this term to be at most of the order of the radiation pressure and hence negligible in the cases presented here (Krumholz & Matzner 2009).

We consider now the PDR associated with the Orion Bar, which is likely charac-

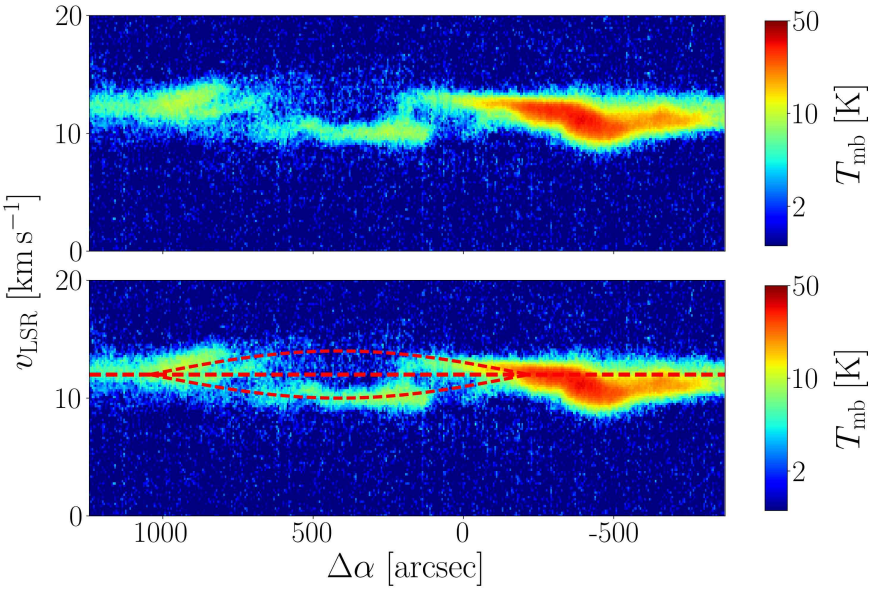

Figure 4.17: [C II] pv diagram of NGC 1977 along position cut 3, indicated in Fig. 6.2 ($\Delta\delta$ = 2085″-2259″). The lower panel shows the same cut with the arc structure for an expansion velocity of $\pm 1.5\,\mathrm{km\,s^{-1}}$ (red dashed lines).

teristic for the dense PDR associated with the OMC1 core. Perusing Tables 4.5 and 4.6, we conclude that the thermal pressure derived from high-J CO lines and CRRLs exceeds the turbulent and magnetic pressure by an order of magnitude. While the [C II] line stems from the surface of the PDR, high-J CO lines and CRRLs stem from deeper within the PDR. Models of photoevaporating PDRs suggest that the pressure increases with depth into the PDR (Bron et al. 2018). The [C II]-emitting PDR surface may be well described by a lower pressure ($5 \times 10^7\,\mathrm{K\,cm^{-3}}$), in which case approximate equipartition holds between the three pressure terms. Their combined pressures of $1 \times 10^8\,\mathrm{K\,cm^{-3}}$ then is balanced by the thermal pressure of the ionized gas, $8 \times 10^7\,\mathrm{K\,cm^{-3}}$, with a contribution from the radiation pressure.

For the PDR in the Veil shell, the thermal, turbulent and magnetic pressure are again in approximate equipartition. In this case, there is approximate pressure equilibrium between the combined pressures in the PDR gas and the combined pressures of the ionized gas and the hot plasma in the EON. Overall, there is a clear pressure gradient from the dense molecular cloud core behind the Trapezium stars to the Veil shell in front. This strong pressure gradient is responsible for the rapid expansion of the stellar wind bubble towards us and sets up the ionized gas flow, which (almost freely) expands away from the ionization front at about $10\,\mathrm{km\,s^{-1}}$ (García-Díaz et al. 2008; O'Dell et al. 2009). During the initial phase, the thermal pressure of the hot gas drives the expansion of the shell and radiation pressure provides only a minor contribution (Silich & Tenorio-Tagle 2013). Radiation pressure takes over once the plasma has cooled through energy conduction and the bubble enters the momentum-driven phase.

Turning now towards the H II regions, M43 and NGC 1977, we note that the sum of the thermal and turbulent pressures in the PDRs of these two regions is well below the thermal pressure of the ionized gas. While, in principle, the pressure could be

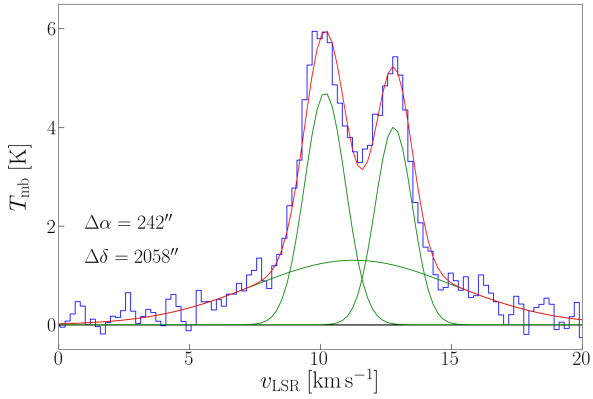

Figure 4.18: [C II] spectrum along pv diagram in NGC 1977 (Fig. 4.17) with Gaussian fits, averaged over $201'' \times 201''$. Coordinate offsets indicate the lower left-hand corner of the square over which the spectrum is averaged. The two narrow components stem from the expanding shell, while the broad component originates in the ionized gas that is contained within the shell. Since the bubble expands in both directions, the peak-velocity difference is twice the expansion velocity, $v_{\rm exp} \simeq 1.3\,{\rm km\,s^{-1}}$. The fit parameters are given in Table 4.4.

Table 4.6: Comparison of pressure terms in PDRs of the Orion Bar, Veil shell, M43, and NGC 1977.

$p/k_{\rm B}$	Orion Bar	Veil shell	M43	NGC 1977
thermal	3×10^8	1-10 $\times 10^5$	1×10^6	9×10^5
magnetic	3×10^7	2×10^6	–	–
turbulence	3×10^7	0.5-3 $\times 10^6$	8×10^5	8×10^4
radiation	1×10^7	1×10^5	3×10^6	8×10^4

Notes. In the Veil shell, higher pressures correspond to the limb-brightened edges, while lower pressures apply to the foreground expanding shell. The radiation pressure is computed from the total luminosity of the central star.

balanced by the magnetic field, we expect equipartition to hold as well. Rather, we take this pressure difference to imply that the overpressure of the ionized gas drives the expansion of these H II regions. We note that radiation pressure is not important for these two nebulae.

4.4.2 Rayleigh-Taylor instability of the Veil shell

Molecular clouds, under the influence of massive stars, can develop hydrodynamical instabilities that compress or fragment the cloud. In our [C II] data as well as in the Hα image, we see evidence that the expanding gas might suffer from Rayleigh-Taylor instability, leading to the formation of elongated structures perpendicular to the expanding surface (cf. Fig. 4.1a and b). These fingers are particularly clear in the EON towards the south of the Veil shell. Figure 4.19 shows this part of the Veil shell with its complex velocity structure. Rayleigh-Taylor instability occurs at the interface of a "heavy" fluid (here the expanding neutral [C II] gas) floating on top of a "light" fluid (here the hot plasma). This instability leads to increased turbulence and mixing of the gas. The presence of magnetic fields may alter the growth behavior

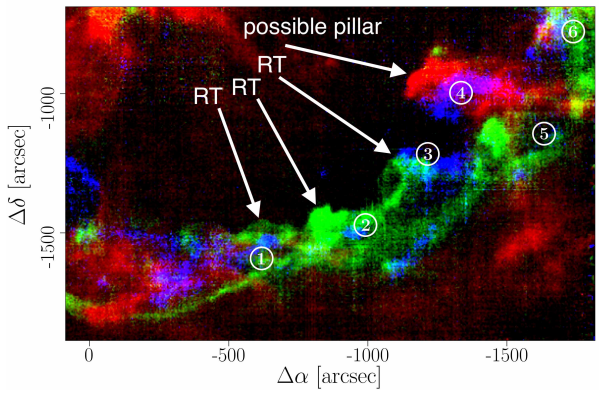

Figure 4.19: Three-color image of [C II] velocity channels of the southern Veil shell. Blue is the velocity channel $v_{\rm LSR}$ = 0-2 km s^{-1}, green $v_{\rm LSR}$ = 4-6 km s^{-1}, and red $v_{\rm LSR}$ = 8-10 km s^{-1}. Arrows indicate structures that resemble fingers formed due to the Rayleigh-Taylor (RT) instability. One of these, labeled "possible pillar", might also be formed by an overdensity encountered by the expanding shell and subsequently sculpted by the strong stellar radiation field, as it also is observed in CO (cf. Fig. 4.1c). The spectra shown in Fig. 4.20 were extracted towards the areas indicated by the numbered circles.

of the characteristic structures, but it is yet under debate whether Rayleigh-Taylor instability will be enhanced or suppressed (Stone & Gardiner 2007; Carlyle & Hillier 2017), the details likely depending crucially on the magnetic field configuration, which is hard to determine observationally.

The scale size of the unstable region after a time t is given by:

$$h = \alpha \mathcal{A} g t^2, \tag{4.10}$$

where g is the (constant) acceleration and the Atwood number $\mathcal{A} = \frac{n_1 - n_2}{n_1 + n_2}$ is a measure of the density contrast across the contact discontinuity (Chevalier et al. 1992; Duffell 2016). In this case, $\mathcal{A} \sim 1$, as the density contrast is large. The parameter α is determined by experiments and numerical simulations to be ~ 0.05. Realizing that the radius of the contact discontinuity is $R_{\rm cd} = \frac{1}{2} g t^2$, experiments and simulations predict that $h/R_{\rm cd} \sim 0.1$, which is in good agreement with the observed structures, that have a typical height of $\sim 100'' \simeq 0.2$ pc in a shell with a radius of ~ 2.5 pc. This lends further support for the interpretation of the observed morphology as the result of the Rayleigh-Taylor instability and for the general interpretation of the dominance of the stellar wind in driving the expansion of the shell.

[C II] observations provide a unique opportunity to probe the injection of turbulence into a molecular cloud through expanding shock waves, as [C II] emission traces the surface layer that transmits the shock wave into the surrounding medium. The morphology and velocity structure of our [C II] observations seem to indicate the importance of Rayleigh-Taylor and Kelvin-Helmholtz instabilities[9] in the transmittance of turbulence into the expanding Veil shell. The simulations of Nakamura et al. (2006) show a similar velocity structure in the synthesized spectra as our observed spectra (Fig. 4.20). With a typical velocity dispersion of 3 km s^{-1}, the energy injected into

[9]Kelvin-Helmholtz instability in the Orion Nebula has been studied by Berné et al. (2010); Berné & Matsumoto (2012). The characteristic "ripples" they detect in the western shell in PAH and CO emission are also present in the [C II] emission from that region.

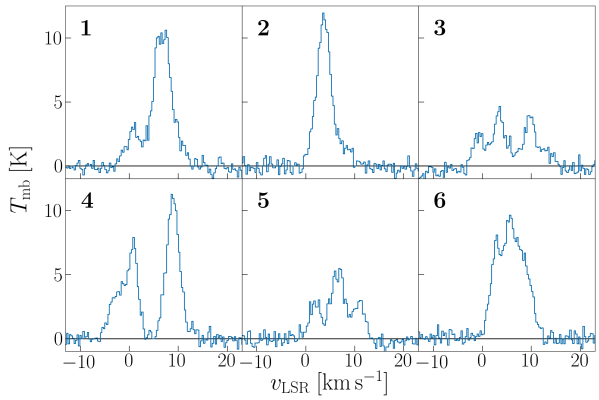

Figure 4.20: [C II] spectra towards southern Veil shell. Each spectrum is averaged over a circle with a radius of 40″ as indicated in Fig. 4.19. We note that each spectrum consists of multiple line components, which is characteristic of thermodynamic instabilities.

the Veil shell by the Rayleigh-Taylor instability can be estimated at $3^2/13^2$ of the kinetic energy of the Veil shell, that is 1.4×10^{47} erg. Such macro-turbulence, associated with cloud destruction, will eventually be converted into micro-turbulence of the cloud medium (Nakamura et al. 2006). Post-processing of such numerical simulations in the [C II] emission and comparison to the data might be very illuminating.

4.4.3 The structure of M43

Both [C II] and H I show three velocity components while CO shows only two (Fig. 4.21 and Table 4.7). We attribute the [C II] high-velocity component (10.7 km s^{-1}) to emission from the background molecular gas associated with OMC1, that we also recognize in CO emission (cf. Fig. 4.8). The 4.7 km s^{-1} [C II] component can be attributed to a half-shell expanding towards us. As this component is also visible in H I absorption against the radio continuum emission from the H II region, this component can be placed firmly in front. We note the difference in line width between the H I and [C II] (3.2 km s^{-1} versus 1.7 km s^{-1}), which we attribute to the importance of thermal broadening for the former. This would imply a temperature of the neutral gas of ~ 150 K.

The 8.3 km s^{-1} [C II] component is more enigmatic. Given its large line width, we are tempted to associated this component with emission from the ionized gas. However, a 8.3 km s^{-1} component is also present in absorption in H I and this would place it in front of the ionized gas. Perhaps, this H I component is really associated with the Veil partially overhanging M43, whereas the [C II] component is clearly confined to the interior of M43 (cf. Fig. 4.12).

Furthermore, we do not see a counterpart to the CO 9.8 km s^{-1} component in [C II] and this gas must be associated with a structure in OMC1. Finally, the very broad, low velocity (1.7 km s^{-1}) H I emission component seems to form a coherent structure with H I emission associated with the Northeast Dark Lane (as can be seen from the comparison of the pv diagrams in Fig. 4.8). This H I component is also seen in dust extinction but there is no counterpart in the [C II] line, in the dust continuum at 70 μm, or in the PAH emission at 8 μm. Hence, this component is not illuminated by either θ^1 Ori C or NU Ori, placing this material firmly in front of the Veil. As

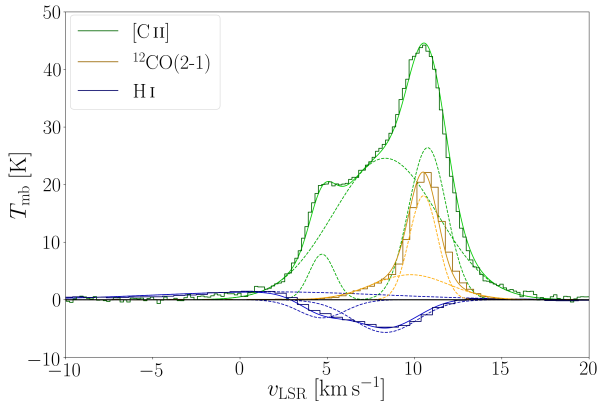

Figure 4.21: [C II] (green), ^{12}CO(2-1) (yellow), and H I (blue) spectra towards the center of M43, averaged over a circle with radius $r \simeq 40''$ and center $(\Delta\alpha, \Delta\delta) = (-226'', 440'')$. Plotted are also the results of Gaussian fits (dashed lines). The fit parameters are given in Table 4.7. The H I spectrum is multiplied by 10^{-2} to fit the scale.

Table 4.7: Gaussian fit parameters of spectra in Fig. 4.21.

line	comp.	$T_{\rm P}$ [K]	$v_{\rm P}$ [km s^{-1}]	$\Delta v_{\rm FWHM}$ [km s^{-1}]
[C II]	1	26.4 ± 0.3	10.7 ± 0.1	2.6 ± 0.1
[C II]	2	24.6 ± 0.2	8.3 ± 0.1	7.0 ± 0.1
[C II]	3	7.9 ± 0.3	4.7 ± 0.1	1.7 ± 0.1
^{12}CO(2-1)	1	18.1 ± 0.1	10.5 ± 0.1	1.9 ± 0.1
^{12}CO(2-1)	2	4.4 ± 0.1	9.8 ± 0.1	5.2 ± 0.1
H I	1	-5.7 ± 0.2	8.3 ± 0.2	4.4 ± 0.3
H I	2	-3.1 ± 0.3	4.7 ± 0.2	3.2 ± 0.3
H I	3	1.4 ± 0.2	1.7 ± 0.6	15.5 ± 0.9

Notes. The H I peak temperatures have to be multiplied by 10^2 to obtain the main-beam temperature.

has been suggested by Troland et al. (2016), this molecular gas very likely has been undisturbed by the star-formation process in OMC1.

In the [C II] line-integrated map (cf. Fig. 4.9), the limb-brightened shell structure of M43 separates into two parts, with a break towards the east. This rupture is reflected in the pv diagram (Fig. 4.12) through the center of M43, exhibiting a gap in the middle of the arc. In pv diagrams along the R.A. axis, this disruption, however, is located in the western part of M43 (cf. Fig. 4.30)

4.4.4 The Veil stellar-wind bubble

Güdel et al. (2008) in their influential paper on the X-ray emission from Orion revealed that the interior of the Veil shell as outlined by the [C II] line, the 8 μm PAH emission, and the 70 μm dust emission is filled with a hot ($T \sim 2{\times}10^6$ K), tenuous ($n \sim 0.5\,{\rm cm}^{-3}$) plasma with a total mass of $\sim 0.07\,M_\odot$. This hot plasma is generated by the reverse shock acting on the fast stellar wind originating from θ^1 Ori C. The observations

reported in this study provide the velocity, radius and mass of the shell swept up by the bubble. Following Güdel et al. (2008), we will use the stellar wind theory of Castor et al. (1975) and Weaver et al. (1977) to analyze these data.

Based on models of Castor et al. (1975) we have obtained the following two time-dependent equations for a thin shell expanding under the influence of stellar winds, under the assumption that the stellar wind is constant; this assumption is valid during most of the lifetime of a star (Haid et al. 2018) and also in the so-called snowplow phase that is discussed by Castor et al. (1975):

$$R_S(t) \simeq 28 \left(\frac{\dot{M}_6 v_{2000}^2}{n_0}\right)^{1/5} \left(\frac{t}{1\,\mathrm{Myr}}\right)^{3/5} \mathrm{pc}, \tag{4.11}$$

$$\dot{R}_S(t) \simeq 16.4 \left(\frac{\dot{M}_6 v_{2000}^2}{n_0}\right)^{1/5} \left(\frac{t}{1\,\mathrm{Myr}}\right)^{-2/5} \mathrm{km\,s^{-1}}, \tag{4.12}$$

where $\dot{M}_6$ is the mass-loss rate in $10^{-6}\,M_\odot\,\mathrm{yr}^{-1}$, v_{2000} is the wind velocity in $2000\,\mathrm{km\,s^{-1}}$, and n_0 is the density of the ambient, uncompressed gas. For θ^1 Ori C, the wind parameters we adopt are $\dot{M}_6 \simeq 0.4$ and $v_{2000} \simeq 1.25$ (Howarth & Prinja 1989; Stahl et al. 1996).

We thus have two equations (R_S, $\dot{R}_S$) and two unknowns (n_0, t). We denote the solution we find for the time between the onset of expansion and the present time by t_0. Re-arranging Eqs. 4.11 and 4.12 gives

$$t_0 \simeq 0.06 \left(\frac{R_S}{1\,\mathrm{pc}}\right) \left(\frac{10\,\mathrm{km\,s^{-1}}}{\dot{R}_S}\right) \mathrm{Myr}, \tag{4.13}$$

$$n_0 \simeq 3.5 \times 10^3\,(\dot{M}_6 v_{2000}^2) \left(\frac{1\,\mathrm{pc}}{R_S}\right)^2 \left(\frac{10\,\mathrm{km\,s^{-1}}}{\dot{R}_S}\right)^3 \mathrm{cm}^{-3}. \tag{4.14}$$

From our observations we estimate the present-day values $R_S(t_0) \simeq 4 \pm 0.5\,\mathrm{pc}$ and $v_{\mathrm{exp}} = \dot{R}_S(t_0) \simeq 13 \pm 2\,\mathrm{km\,s^{-1}}$ at the far (south) side of the expanding shell. With these values, we obtain for the unknowns $n_0 \simeq 5 \pm 2 \times 10^1\,\mathrm{cm}^{-3}$ and $t_0 \simeq 0.2 \pm 0.05\,\mathrm{Myr}$.

With these values, the temperature of the hot plasma inside the bubble and its density are predicted by the model to be $T_{\mathrm{plasma}} \simeq 2.3 \pm 0.2 \times 10^6\,\mathrm{K}$ and $n_{\mathrm{plasma}} \simeq 0.2 \pm 0.05\,\mathrm{cm}^{-3}$ (Castor et al. 1975). This is in excellent agreement with the X-ray observations by Güdel et al. (2008). However, numerical models of Arthur (2012), that take into account saturation of thermal conduction at the shell interface and mass loading by proplyds in the Orion nebula, produce hotter gas with $T_{\mathrm{plasma}} \sim 10^7\,\mathrm{K}$. Yet, the mixing efficiency of the photo-evaporation flow from the proplyds with the stellar wind material is not well constrained and a major source of uncertainties.

In an alternative approach, we fit the five observables (R_S, v_S, M_S, T_{plasma}, n_{plasma}) = ($2.7\,\mathrm{pc}$, $13\,\mathrm{km\,s^{-1}}$, $1500\,M_\odot$, $2 \times 10^6\,\mathrm{K}$, $0.3\,\mathrm{cm}^{-3}$) with the two parameters t_0 and n_0, given the expressions by Castor et al. (1975). From a weighted least-square fit, with relative errors (0.2, 0.2, 0.5, 0.3, 0.5), we find the best fit for $t_0 \simeq 0.24 \pm 0.05\,\mathrm{Myr}$ and $n_0 \simeq 1.7 \pm 0.7 \times 10^2\,\mathrm{cm}^{-3}$. In this fit, only the last three observables are fitted in good agreement; in contrast, the shell radius is predicted to be 3.8 pc and the expansion velocity as $9\,\mathrm{km\,s^{-1}}$. The plasma temperature and density do not depend strongly on t_0 and n_0 (Castor et al. 1975). Adopting a lower gas mass of $600\,M_\odot$ results in a better fit with $t_0 \simeq 0.17 \pm 0.05\,\mathrm{Myr}$ and $n_0 \simeq 1.0 \pm 0.6 \times 10^2\,\mathrm{cm}^{-3}$. In this scheme, however, we rely on the spherical symmetry of the problem, which

is not applicable for the Orion Nebula expanding predominantly along its steepest density gradient. Considering expansion in an ambient medium with a density gradient scaling with R_S^{-2} alters the time-dependent behavior of the bubble kinematics considerably (Ostriker & McKee 1988, sec. VII).

From the morphology of the expansion in the eastern arm of the shell (cf. Appendix 4.B, Figs. 4.26 and 4.27), we obtain with $R_S(t) \simeq 1.75\,\mathrm{pc}$ and $\dot{R}_S(t) \simeq 4.25\,\mathrm{km\,s^{-1}}$ $n_0 \simeq 8 \times 10^3\,\mathrm{cm^{-3}}$ and $t_0 \simeq 0.25\,\mathrm{Myr}$. Here, the ambient gas density is thus much higher.

The derived lifetime of the bubble, $t_0 \simeq 0.2\,\mathrm{Myr}$, indicates that the onset of the gas coupling to the stellar wind is rather recent, but agrees with the presumed ages of the Trapezium cluster and θ^1 Ori C, which is $< 1\,\mathrm{Myr}$ with a median age of the stellar population of 0.3 Myr (Prosser et al. 1994; Hillenbrand 1997). In contrast, Simón-Díaz et al. (2006) give an age of θ^1 Ori C of $2.5 \pm 0.5\,\mathrm{Myr}$, derived from optical spectroscopy of the stars in the Trapezium cluster, which is much longer than the expansion time scale of the Veil bubble. We note, though, that the star has to leave the dense core where it was born before large-scale expansion can set on in a relatively dilute ambient medium. We expect this time to be of the order of 0.1 Myr, considering the peculiar velocity of θ^1 Ori C (Vitrichenko 2002; Stahl et al. 2008; O'Dell et al. 2009). From the absence of evidence for the destruction of nearby proplyds and interaction between the moving foreground layers, O'Dell et al. (2009) estimate the time scale since θ^1 Ori C has moved into lower-density material, starting to ionize the EON, is of a few 10^4 years. This estimate is an order of magnitude younger than the expansion time we find. However, from modelling the disk masses of proplyds close to θ^1 Ori C, Störzer & Hollenbach (1999) find that θ^1 Ori C can be significantly older than 10^5 years if the orbits of the proplyds are radial. Salgado et al. (2016) derive an age of 10^5 years for θ^1 Ori C from the mass of the Orion Bar.

For the density within the shell, the compressed gas, the simple model of Castor et al. (1975) gives

$$n_s = \frac{\mu \dot{R}_S^2}{kT_s}\, n_0. \tag{4.15}$$

If the temperature in the shell is $T_s = 80\,\mathrm{K}$, as assumed by Castor et al. (1975), and $\mu/m_\mathrm{H} = 1.3$, assuming atomic H I gas, the density within the shell becomes $n_s \simeq 200(\dot{R}_S/10\,\mathrm{km\,s^{-1}})^2\, n_0$. In the southern shell, this then yields $n_s \simeq 400\, n_0 \simeq 2 \times 10^4\,\mathrm{cm^{-3}}$. In the eastern bright arm of the shell, we expect a shell density of $n_s \simeq 50\, n_0 \simeq 5 \times 10^5\,\mathrm{cm^{-3}}$: here, the density is much higher but also the shell is much thinner than in the southern part. Both theoretical densities are an order of magnitude higher than what we estimated from observations.

With a mass of the expanding gas shell of $M \simeq 1500\, M_\odot$ and an expansion velocity of $v_\mathrm{exp} \simeq 13\,\mathrm{km\,s^{-1}}$, the kinetic energy in the shell is computed to be $E_\mathrm{kin} \simeq 2.5 \times 10^{48}\,\mathrm{erg}$. Dividing this energy by the expansion time scale provides us with a measure that we can compare to the wind luminosity of the presumed driving star θ^1 Ori C. This yields $\frac{E_\mathrm{kin}}{t_0} \simeq 4 \times 10^{35}\,\mathrm{erg\,s^{-1}}$. Comparing this number with the wind luminosity, $L_w \simeq 8 \times 10^{35}\,\mathrm{erg\,s^{-1}}$, we estimate a wind efficiency of about 50%. Adding the wind of θ^2 Ori A, which is comparable to the stellar wind of θ^1 Ori C, with $L_w \simeq 2 \times 10^{35}\,\mathrm{erg\,s^{-1}}$, reduces the wind efficiency to 40%; the stellar wind parameters of θ^2 Ori A are $\dot{M}_6 \sim 0.08$ and $v_{2000} \sim 1.45$ (Petit et al. 2012). Adding both winds in the above analysis, would increase densities by a factor 1.3, but has no effect on the expansion time.

During the initial stages, the swept up shell will be very thin and the stellar ionizing flux will be able to fully ionize the shell. Once the shell has swept up enough material, the ionization front will become trapped in the shell. The Veil shell has already reached this later stage as evidenced by the morphology of the shell in Hα and [C II] emission (cf. Fig. 4.1) and the narrow line width of the [C II] line. In addition, we note that bright PAH emission (cf. Fig. 1 in Pabst et al. (2019)) mostly originates from the neutral gas in PDRs and is very weak if associated at all with ionized gas. For the ambient densities we estimated above, that is $n_0 \simeq 2\text{-}5 \times 10^1\,\mathrm{cm}^{-3}$, the time when the shell becomes neutral is $t \simeq 0.1\text{-}0.2\,\mathrm{Myr}$ according to the Weaver et al. (1977) model[10]. This is in good agreement with our estimate of the expansion time.

As the [C II] observations reveal, the strong density gradient towards the front of the cloud has produced a rapid expansion of the bubble towards us. We note that the $13\,\mathrm{km\,s}^{-1}$ expansion velocity exceeds the escape velocity from OMC1 ($2\,\mathrm{km\,s}^{-1}$) and eventually the swept-up mass will be lost to the environment. In addition, the bubble will break open, releasing the hot plasma and the expanding ionized gas. Inspection of the pv diagrams (Figs. 4.30 and 4.31) indicates that the Veil shell is quite thin in some directions and break out may be "imminent". Eventually, the shell material, the hot plasma, and the entrained ionized gas will be mixed into the interior of the Orion-Eridanus superbubble. The next supernova that will go off, one of the Orion Belt stars in $\sim 1\,\mathrm{Myr}$, will sweep up this "loose" material and transport it to the walls of the superbubble. The last time this happened, about 1 Myr ago, this created Barnard's loop.

New numerical simulations show that the effects of stellar wind on their surroundings depends strongly on the characteristics of the medium (Haid et al. 2018). Stellar winds dominate if the bubble expands into an ambient warm ionized medium (WIM, $T \sim 10^4\,\mathrm{K}$, $n \sim 0.1\,\mathrm{cm}^{-3}$). If the ambient medium is colder and neutral (CNM, $T \sim 100\,\mathrm{K}$, $n \sim 100\,\mathrm{cm}^{-3}$), ionizing radiation is the dominant driving force. The warm neutral medium (WNM, $T \sim 2 \times 10^3\,\mathrm{K}$, $n \sim 1\,\mathrm{cm}^{-3}$) is an intermediate case. However, these models are not descriptive of the situation of θ^1 Ori C. New studies need to investigate the effects of stellar winds of a star in the outskirts of a molecular cloud, an environment that is rather dilute ($n \sim 10\,\mathrm{cm}^{-3}$) and subject to density gradients. We realize that the Veil shell provides an excellent test case for models of stellar wind expansion into a surrounding medium given the large number of observational constraints, including the mass of the shell, the temperature and density of the shell and of the plasma, the velocities of the shell and the dense ionized gas in the Huygens Region.

4.4.5 The expanding bubble of θ^2 Ori A

van der Werf et al. (2013) discuss the shell structure that seems to surround θ^2 Ori A, their component L, that can be identified in our [C II] data, as well. Figure 4.22 shows the same cut for the [C II] intensity as Fig. 13 of van der Werf et al. (2013) for the H I optical depth. Component L is a rather small arc-like structure, $r \simeq 50'' \simeq 0.1\,\mathrm{pc}$ extending to a LSR velocity of $v_{\mathrm{LSR}} \simeq -3.2\,\mathrm{km\,s}^{-1}$. This would translate into an expansion velocity of $v_{\mathrm{exp}} \simeq 11\,\mathrm{km\,s}^{-1}$. If this was a wind blown bubble, we would obtain from Eqs. 4.13 and 4.14, $t_0 \simeq 0.006\,\mathrm{Myr}$ and $n_0 \simeq 4 \times 10^4\mathrm{cm}^{-3}$. This might be reasonable, considering that the star might only very recently have emerged from the dense material were it was born. It might also be that θ^2 Ori A is the ionizing source

[10] If the density is actually higher, the ionizing radiation gets trapped earlier.

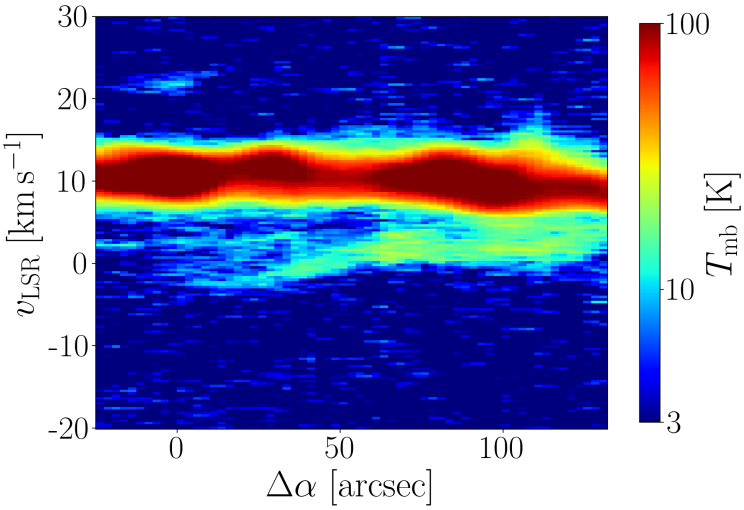

Figure 4.22: PV diagram along position cut shown in Fig. 13 of van der Werf et al. (2013), perpendicular to the Orion Bar through the Huygens Region.

for this structure, but not its cause. Schulz et al. (2006) estimate the stellar age to be $\sim 0.3\,$Myr, similar to θ^1 Ori C, but not much younger.

Also the arc-like structure D of van der Werf et al. (2013) has been discussed as associated with θ^2 Ori A (García-Díaz & Henney 2007), but van der Werf et al. (2013) attribute it to θ^2 Ori B, an early B-type star. However, in the H I cuts component D only appears with a radius of $r \simeq 100''$, while we observe a larger structure, $r \simeq 500'' \simeq 1\,$pc, that has a large negative velocity ($v_{\rm LSR} \simeq -20\,{\rm km\,s^{-1}}$). The latter's geometric center seems to lie more to the southeast, as can be seen in our pv diagrams (cf. 4.30). We do not observe component D in Fig. 4.22, indicating that it is not illuminated by UV radiation and hence a foreground component. Assuming the larger [C II] structure to be the wind-blown bubble of θ^2 Ori A, comparison with models would give $t_0 \simeq 0.002\,$Myr and $n_0 \simeq 3 \times 10^1 {\rm cm}^{-3}$ at the expansion velocity of $v_{\rm exp} \simeq 28\,{\rm km\,s^{-1}}$. Possibly the wind-blown bubble of θ^2 Ori A has been disrupted by the stellar wind of θ^1 Ori C and merged with the second's bubble.

4.4.6 The thermal bubbles of M43 and NGC 1977

The ionizing stars of M43 and NGC 1977 are of spectral types B0.5 and B1, respectively, and such stars have feeble stellar winds that are incapable of driving a bubble into their surroundings. We attribute the bubbles associated with these two nebulae to the thermal expansion of the ionized gas (Spitzer 1978). We will return to the stellar wind aspects later.

Simón-Díaz et al. (2011) conclude that M43 is ionization-bounded. The Strömgren radius of the H II region environing NU Ori with the rate of ionizing photons $\mathbb{N} \simeq 1.5 \times 10^{47}\,{\rm s}^{-1}$ (Simón-Díaz et al. 2011) is $\mathcal{R}_S \simeq 0.2\,{\rm pc}\,(10^3\,{\rm cm}^{-3}/n)^{2/3}$. Assuming the electron density Simón-Díaz et al. (2011) report, derived from optical line ratios, $n_e \simeq 5 \times 10^2\,{\rm cm}^{-3}$, $\mathcal{R}_S \simeq 0.3\,$pc, which is in excellent agreement with the radius we measure.

After the initial phase of rapid ionization, the overpressure of the ionized gas com-

pared to its environment drives the thermal expansion of the H II region (Krumholz & Matzner 2009; Spitzer 1978). For a homogeneous region, the present-time size and velocity of expansion (R_S, $\dot{R}_S$) are related to the expansion time and initial density (t_0, n_0):

$$t_0 \simeq 0.056 \left(\frac{R_S}{1\,\mathrm{pc}}\right) \left(\frac{\dot{R}_S}{c_s}\right)^{4/3} \left(\left(\frac{c_s}{\dot{R}_S}\right)^{7/3} - 1\right) \mathrm{Myr}, \tag{4.16}$$

$$n_0 \simeq 56 \left(\frac{\mathbb{N}}{10^{47}}\right)^{1/2} \left(\frac{c_s}{\dot{R}_S}\right)^{2} \left(\frac{1\,\mathrm{pc}}{R_S}\right)^{3/2} \mathrm{cm}^{-3}, \tag{4.17}$$

where $c_s \simeq 10\,\mathrm{km\,s^{-1}}$ is the sound speed in the ionized gas.

For M43, we obtain with $R_S(t_0) \simeq 0.3 \pm 0.05\,\mathrm{Myr}$ and $v_{\mathrm{exp}} = \dot{R}_S(t_0) \simeq 6 \pm 2\,\mathrm{km\,s^{-1}}$ an expansion time of $t_0 \simeq 0.02 \pm 0.01\,\mathrm{Myr}$ and an initial density of $n_0 \simeq 1.4 \pm 0.7 \times 10^3\,\mathrm{cm^{-3}}$. This implies that the star NU Ori is rather young. The expected main-sequence lifetime of a $\sim 20\,M_\odot$ star like NU Ori is $\sim 10\,\mathrm{Myr}$.

From the Hα emission in NGC 1977, we derive an electron density of $n_e \simeq 35\,\mathrm{cm^{-3}}$ throughout the region, assuming a radius of $r \simeq 1\,\mathrm{pc}$. With the rate of ionizing photons $\mathbb{N} \simeq 1 \times 10^{45}\,\mathrm{s^{-1}}$ (Kim et al. 2016; Diaz-Miller et al. 1998), the Strömgren radius of the H II region surrounding 42 Orionis is $\mathcal{R}_S \simeq 0.3\,\mathrm{pc}$. This is smaller than the size of the shell we observe. However, Hohle et al. (2010) give an effective temperature of $T_{\mathrm{eff}} = 25400\,\mathrm{K}$ for 42 Orionis. Also from its spectral class, B1V, we expect a much higher flux of ionizing photons, $\mathbb{N} \sim 1 \times 10^{47}\,\mathrm{s^{-1}}$ (Sternberg et al. 2003). We can estimate the rate of ionizing photons emitted by 42 Orionis (with minor assistance from other stars) from the Hα emission in the H II region. We have:

$$L(\mathrm{H}\alpha) = \int 4\pi j_{\mathrm{H}\alpha}\,\mathrm{d}V = \int \frac{4\pi j_{\mathrm{H}\alpha}}{n_{\mathrm{p}} n_{\mathrm{e}}} n_{\mathrm{p}} n_{\mathrm{e}}\,\mathrm{d}V, \tag{4.18}$$

$$\mathbb{N} = \int \alpha_{\mathrm{B}} n_{\mathrm{p}} n_{\mathrm{e}}\,\mathrm{d}V. \tag{4.19}$$

With $\frac{4\pi j_{\mathrm{H}\alpha}}{n_{\mathrm{p}} n_{\mathrm{e}}} = 1.24 \times 10^{-25}\,\mathrm{erg\,cm^3\,s^{-1}}$, $j_{\mathrm{H}\alpha}/j_{\mathrm{H}\beta} = 2.85$ (Hummer & Storey 1987), and $\alpha_{\mathrm{B}} = 2.6 \times 10^{-13}\,\mathrm{cm^3\,s^{-1}}$ (Storey & Hummer 1995) we obtain from the Hα luminsity integrated over NGC 1977, $L(\mathrm{H}\alpha) \simeq 45\,L_\odot$, a photon rate of $\mathbb{N} \simeq 1 \times 10^{47}\,\mathrm{s^{-1}}$. With this value, we derive a present-day Strömgren radius of $\mathcal{R}_S \simeq 1.5\,\mathrm{pc}$, which is in good agreement with the observed radius of the shell ($r = 1.0$-$1.6\,\mathrm{pc}$). With the extent of the expanding shell derived from the pv diagram in Fig. 4.17, $R_S(t_0) \simeq 1\,\mathrm{pc} \pm 0.2$, and the expansion velocity $v_{\mathrm{exp}} = \dot{R}_S(t_0) \simeq 1.5 \pm 0.5\,\mathrm{km\,s^{-1}}$ the expansion time is $t_0 \simeq 0.4 \pm 0.2\,\mathrm{Myr}$ and the initial density $n_0 \simeq 2.5 \pm 1.2 \times 10^3\,\mathrm{cm^{-3}}$. This, as well, suggests that 42 Orionis is rather young, compared to its expected lifetime of $\sim 10\,\mathrm{Myr}$.

4.4.7 Stellar wind versus thermal expansion of bubbles

In the previous sections, we analyze the kinematics of the bubbles around M42, M43, and NGC 1977 in terms of stellar-wind driven and thermal-pressure driven expansions, respectively. Here, we compare these two analyses. In Tables 4.8 and 4.9, we summarize our findings for the three regions.

For M42, the momentum and energy in the ionized gas in the champagne-flow model is about two orders of magnitude less than observed for the Veil shell: $22\,M_\odot$ of ionized gas moving at $17\,\mathrm{km\,s^{-1}}$ (O'Dell 2001) versus a (half)shell of $1500\,M_\odot$

Table 4.8: Comparison of stellar parameters with bubble energetics of the three regions.

region	star	stellar type	$T_{\rm eff}$ [K]	$L_\star$ [$L_\odot$]	$L_{\rm w}$ [erg s^{-1}]	$M_{\rm shell}$ [$M_\odot$]	$v_{\rm exp}$ [km s^{-1}]	$E_{\rm kin}$ [erg]	t_0 [Myr]	$E_{\rm kin}/(L_{\rm w}t_0)$
M42	θ^1 Ori C	O7V	3.9×10^4	2.0×10^5	8×10^{35}	1500	13	2.5×10^{48}	0.2	0.5
M43	NU Ori	B0.5V	3.1×10^4	2.6×10^4	$\sim 3 \times 10^{31}$	7	6	3×10^{45}	0.02	50
NGC 1977	42 Ori	B1V	2.5×10^4	1.1×10^4	$\sim 3 \times 10^{31}$	700	1.5	2×10^{46}	0.4	40

Notes. In the last column, we take for t_0 the value derived from the stellar wind models; in case of M43 the lifetime derived from pressure-driven expansion is a third of that value, increasing the ratio $E_{\rm kin}/(L_{\rm w}t_0)$ by a factor of three. Stellar parameters of θ^1 Ori C are from Simón-Díaz et al. (2006), of NU Ori from Simón-Díaz et al. (2011), and of 42 Orionis from Hohle et al. (2010).

Table 4.9: Masses, energetics, and luminosities in the expanding shells of M42 (Veil shell), M43, and NGC 1977.

	M42 (Veil shell)	M43	NGC 1977	reference
$\mathbb{N}_{\rm Lyc}$ [$10^{47}\,{\rm s}^{-1}$]	70	1.5	1	1, 2, 8
$L_{\rm w}$ [$L_\odot$]	400	$\sim 1.5\times10^{-2}$	$\sim 1.5\times10^{-2}$	3, 4
mass of neutral gas [$M_\odot$]	1500	7	700	5, 8
mass of ionized gas [$M_\odot$]	24	0.3	16	6, 8
$E_{\rm kin}$ of neutral gas [10^{46} erg]	250	0.3	2	5, 8
$E_{\rm kin}$ of ionized gas [10^{46} erg]	6	–	–	6, 7
$E_{\rm th}$ of ionized gas [10^{46} erg]	3	0.7	5	5, 8
$E_{\rm th}$ of hot gas [10^{46} erg]	10	–	–	3
$L_{\rm FIR}$ [$L_\odot$]	3.2×10^4	8.5×10^3	1.5×10^4	8
$L_{\rm [C\,II]}$ [$L_\odot$]	170	24	140	8

Notes. There are no X-ray observations of the hot gas in M43 and NGC 1977. References: (1) O'Dell et al. (2017), (2) Simón-Díaz et al. (2011), (3) Güdel et al. (2008), (4) Oskinova et al. (2011), (5) Pabst et al. (2019), (6) Wilson et al. (1997), (7) O'Dell (2001), (8) this work.

expanding at $13\,{\rm km\,s^{-1}}$ (Table 4.9), the neutral Veil shell carrying a total momentum of $2\times10^4\,M_\odot\,{\rm km\,s^{-1}}$. For M43 and NGC 1977, on the other hand, the stellar wind is too feeble to drive the expansion of a large shell and the results are in good agreement with analytical models for the thermal expansion of H II regions. Figures 4.23 and 4.24 summarize this graphically. In this depiction, we have calculated the expected kinetic energy of a stellar wind bubble using the analytical model developed by Weaver et al. (1977),

$$E_{\rm kin} \simeq \frac{6}{11} L_{\rm w} t, \tag{4.20}$$

and the pressure-driven expansion of ionized gas (Spitzer 1978),

$$M_{\rm shell} \simeq \frac{4\pi}{3} R_{S,0}^3 \mu n_0 \left(1+\frac{7t}{4t_s}\right)^{12/7}, \tag{4.21}$$

$$E_{\rm kin} \simeq \frac{1}{2} M_{\rm shell} c_s^2 \left(1+\frac{7t}{4t_s}\right)^{-6/7}, \tag{4.22}$$

where $R_{S,0} = \left(\frac{3\mathbb{N}}{4\pi n_0^2 \alpha_{\rm B}}\right)^{1/3}$ is the initial Strömgren radius and $t_s = R_{S,0}/c_s$. Comparing the predicted shell masses, where we assume that all the swept-up material is in the shell, to the measured masses as shown in Fig. 4.24, we observe that the measured masses of all three shells are slightly above the predictions, by a factor of about two. The mass discrepancy in M42 and NGC 1977 might be due to our choice of β in the SEDs and a contamination from background material that is not expanding. The mass of M43, estimated from the gas density in the shell, is a rather rough estimate as well.

For the Veil shell, the kinetic energy is comparable to the integrated wind luminosity of a wind-blown bubble. In M43 and NGC 1977, the observed kinetic energy of the shells much exceeds the integrated wind luminosity. For M43 and NGC 1977, the kinetics of the shell are in good agreement with the thermal expansion of the H II region, while for M42 this falls short by two orders of magnitude.

From models of O stars and comparison with real O stars (Pauldrach et al. 2001), we obtain an upper limit of $L_w \simeq 1\times10^{34}\,{\rm erg\,s^{-1}}$. In their models of earlier B stars,

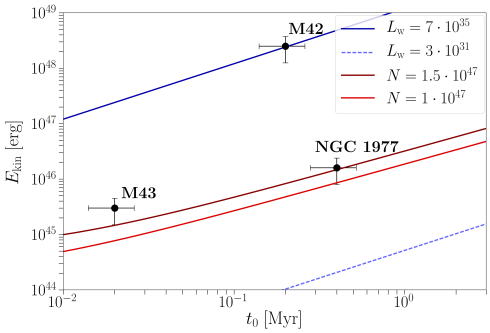

Figure 4.23: Kinetic energy of expanding bubble shells versus expansion time. The lines are the predictions of wind models (blue) and models of pressure-driven expansion (red) with the parameters compiled in Tables 4.8 and 4.9.

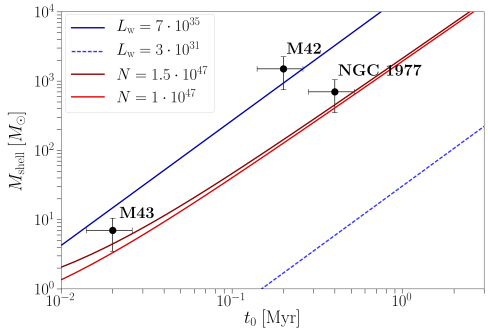

Figure 4.24: Masses of expanding bubble shells versus expansion time. The lines are the predictions of wind models (blue) and models of pressure-driven expansion (red) with the parameters compiled in Tables 4.8 and 4.9.

however, even a B0.5V star has a significant stellar wind with $L_w \simeq 1 \times 10^{33}\,\mathrm{erg\,s^{-1}}$ (Sternberg et al. 2003). Since no X-ray observations are available for M43 and NGC 1977, that might reveal gas shock-heated from stellar winds in the bubble interior as in M42, we cannot judge conclusively on this matter.

4.5 Conclusion

We have observed the [C II] emission from the Orion Nebula M42, M43, and NGC 1973, 1975, and 1977. Velocity-resolved observations of the [C II] fine-structure line provide a unique tool to accurately quantify the kinematics of expanding bubbles in the ISM, in our case the large bubble associated with the Orion Nebula, the Orion Veil, and the bubbles of M43 and NGC 1973, 1975, and 1977. Our extended map of [C II] emission can be further used to disentangle dynamic structures within the same region on larger scales than previously possible. From the consistent arc structures in the pv diagrams and the line profiles, we are able to show that the gas is indeed expanding coherently on large scales as a bubble is blown into the ISM by stellar feedback.

We have compared three regions within the Orion Nebula complex that host different central stars causing the disruption of the molecular cloud cores in which these stars are born. The Orion Nebula M42 hosts the most massive star, an O-type star, which has a strong wind, that drives the expansion of the surrounding medium. M43 and NGC 1977 host less massive stars of early B type with much weaker winds. Still, both are effective in blowing bubbles of significant extent.

Pabst et al. (2019) have demonstrated that the Veil shell is a coherent, half-spherical structure, enclosing the layers of ionized gas observed towards that region. The stellar wind from θ^1 Ori C seems to be very effective in sweeping up its surrounding gas into a large-scale dense shell, leaving the bubble interior filled with dilute, hot X-ray emitting gas. This precise structure, a thin, rather cold shell of swept-up gas enveloping a hot interior medium, is characteristic of wind-blown bubbles. The bubble of the Orion Nebula, though still closed, may be on the brink of entering the bursting phase, thus rejuvenating the medium of the Orion-Eridanus superbubble.

The bubbles associated with M43 and NGC 1977 also exhibit spherical symmetry and possess a rather thin shell. In these two cases, however, the masses and kinetics of these shells are incompatible with an origin in a wind-driven shell. Instead, these shells are due to the pressure-driven expansion of the ionized gas and the observations are in good agreement with simple analytical estimates. All structures we have investigated here are rather young compared to the total lifetime of the driving (massive) stars. As stars in the Orion Nebula cluster will go off as supernovae, these structures will be disrupted as they age.

Acknowledgements

This work is based on observations made with the NASA/DLR Stratospheric Observatory for Infrared Astronomy (SOFIA). SOFIA is jointly operated by the Universities Space Research Association, Inc. (USRA), under NASA contract NNA17BF53C, and the Deutsches SOFIA Institut (DSI) under DLR contract 50 OK 0901 to the University of Stuttgart.

JRG thanks the ERC and the Spanish MCIU for funding support under grants ERC-2013-Syg-610256-NANOCOSMOS and AYA2017-85111-P, respectively. Research on the interstellar medium at Leiden Observatory is supported through a Spinoza award of the Dutch Science Organisation (NWO). We are grateful for the dedicated work during the upGREAT square-degree survey of Orion of the USRA and NASA staff of the Armstrong Flight Research Center in Palmdale and of the Ames Research Center in Mountain View, and the DSI. We thank C. R. O'Dell for commenting on the manuscript and helpful discussions.

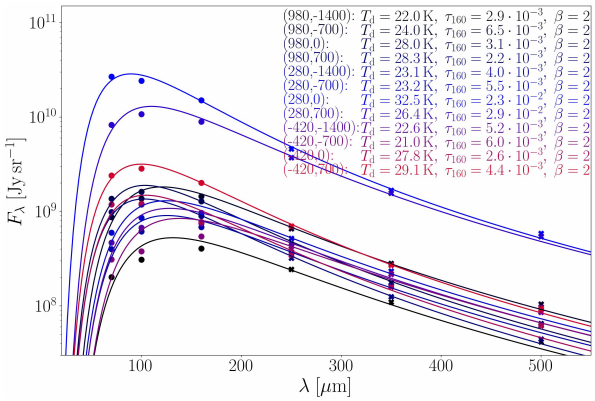

Figure 4.25: SED fits to individual points throughout the Orion Nebula complex. The flux in the PACS bands is plotted as circles; fluxes of the SPIRE bands are plotted as crosses. Numbers in brackets are the R.A. and Dec. offset, respectively, in arc seconds.

4.A SED results

Figure 4.25 shows the results from an SED fit in individual points with the emissivity index $\beta = 2$. The derived dust temperature decreases with increasing β, while the dust optical depth increases significantly. The integrated FIR intensity does not depend strongly on β.

4.B The expanding Rim

We present here our analysis of the kinematics in the eastern bright arm, the so-called Eastern Rim, of the expanding shell. To estimate the three-dimensional expansion velocity, we make use of the following formula:

$$v_{\rm exp} = \frac{v_2 - v_1}{\sqrt{1 - \frac{r_1^2}{r_2^2}}}, \tag{4.23}$$

where $v_2 - v_1$ is the velocity difference of the velocity channels considered; r_1 and r_2 are the respective distances of the emission filament in these two channels. r_2 is the further outward lying filament, for an accurate calculation it must be the outermost. We can write $r_1 = r_2 - \Delta r$, where Δr is the separation between the two channel filaments. If $v_2 > v_1$, the shell is moving toward us and we assign a positive expansion velocity; else it is expanding away from us. Here, we use the [C II] channels at $v_{\rm LSR} = 0\text{-}1\,{\rm km\,s^{-1}}$, $v_{\rm LSR} = 2\text{-}3\,{\rm km\,s^{-1}}$ and $v_{\rm LSR} = 4\text{-}5\,{\rm km\,s^{-1}}$. With $v_2 - v_1 = 2\,{\rm km\,s^{-1}}$, $r_2 \simeq 1.75\,{\rm pc}$ and $\Delta r \simeq 0.2\,{\rm pc}$ (cf Fig. 4.26), we obtain $v_{\rm exp} \simeq 4.25\,{\rm km\,s^{-1}}$. We note that only the distance of the furthest filament (cf. Fig. 4.27) gives an accurate measure of the extent of the expanding shell, which renders the estimate from the three channels used here somewhat inaccurate; however, in higher-velocity channels the displacement between the filamentary structures is not as clear-cut as it is in these channels.

We detect the [^{13}C II] $F = 2\text{-}1$ line in averaged spectra in this region as shown in Fig. 4.28. From the peak temperatures of the [^{12}C II] and [^{13}C II] line (Table 4.10), we compute the [C II] optical depth by Eqs. 4.3 and 4.4. The C^+ column density is given

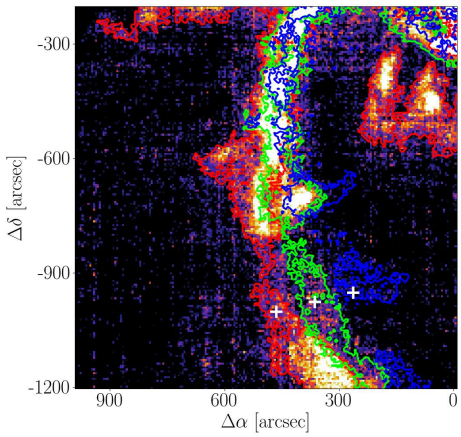

Figure 4.26: Color map of [C II] emission in velocity interval $v_{\rm LSR}$ = 0-5 km s^{-1}, with contours of the channel emission in $v_{\rm LSR}$ = 0-1 km s^{-1}, $v_{\rm LSR}$ = 2-3 km s^{-1}, and $v_{\rm LSR}$ = 4-5 km s^{-1} (blue, green, and red, respectively). From the displacement of the structure of brightest emission in these channels with respect to each other, points marked by the white crosses, we can estimate the expansion velocity to be $v_{\rm exp} \simeq 4.25\,{\rm km\,s^{-1}}$. The projected distance between the crosses is 0.2 pc, and the projected distance from the Trapezium stars of the outermost filament, traced by blue contours, is 1.75 pc.

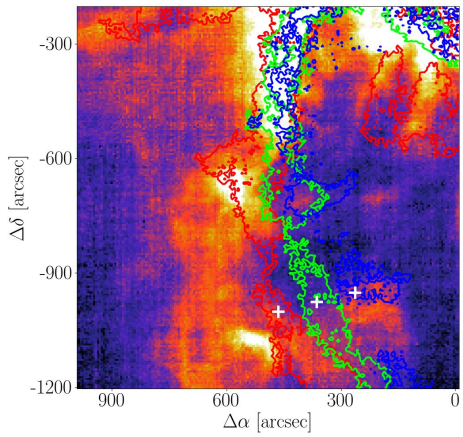

Figure 4.27: Color map of [C II] emission in velocity interval $v_{\rm LSR}$ = 0-15 km s^{-1}, with contours of the channel emission in $v_{\rm LSR}$ = 0-1 km s^{-1}, $v_{\rm LSR}$ = 2-3 km s^{-1}, and $v_{\rm LSR}$ = 4-5 km s^{-1} (blue, green, and red, respectively). The expanding filament grows brighter as it moves outward, probably mainly due to increasing limb-brightening, so the color map is dominated by the most outward filament.

by Eq. 4.6. The analysis yields $\tau_{\rm [C\,II]} \simeq 3$. From the column density, we estimate a gas density of the limb-brightened shell from $n = N_{\rm C^+}/([{\rm C/H}]l)$, where $[{\rm C/H}] \simeq 1.6\times10^{-4}$ (Sofia et al. 2004) and the extent l along the line of sight is $l \simeq r/2 \simeq 1$ pc. This yields $n \simeq 1\times10^4\,{\rm cm^{-3}}$.

Figure 4.29 compares the CO(2-1) emission with the [C II] emission in the expanding Rim, that is observed in the velocity range $v_{\rm LSR}$ = 5-8 km s^{-1}. From the peak separation in line cut 1, $d \simeq 70'' \simeq 0.14$ pc, we derive a density of $n \simeq 9\times10^3\,{\rm cm^{-3}}$ in the Rim. From line cut 2 ($d \simeq 110'' \simeq 0.22$ pc), we derive a density of $n \simeq 6\times10^3\,{\rm cm^{-3}}$ in the south of the bright Rim.

From the dust optical depth, we estimate a mean $\tau_{160} \simeq 4\times10^{-3}$ in the [C II]-bright regions. This translates to a gas column density of $N_{\rm H} \simeq 2\times10^{22}\,{\rm cm^{-2}}$. Assuming that all carbon is ionized, this results in a C^+ column density of $N_{\rm C^+} \simeq 3\times10^{18}\,{\rm cm^{-2}}$, which is a factor of 2 lower than what we estimate from the [C II] spectra. Since τ_{160} strongly depends on the choice of the grain emissivity index β, the agreement might be satisfactory. However, it might be a hint that we overestimate the [C II] optical depth and underestimate the excitation temperature. With these givens the physical temperature of the gas would be $T \simeq 50$ K, which is lower than expected from the PDR models for the [C II]-emitting (surface) layers. At these high opacities opacity broadening of the line might also become significant, which is not what we observe. The fitting procedure is complicated by the presence of multiple components.

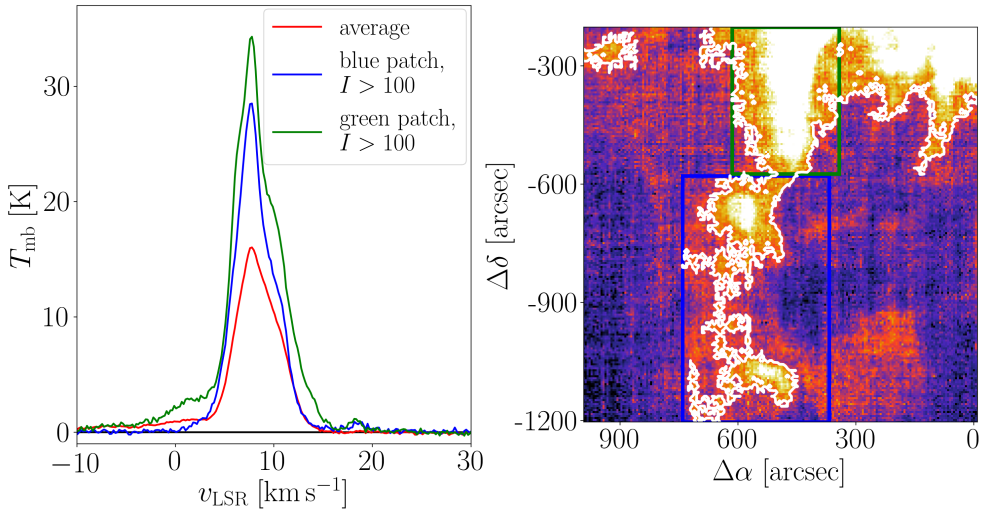

Figure 4.28: Right: [C II] line-integrated intensity in the bright eastern Rim. White contours indicate $I_{\rm [C\,II]} > 100\,{\rm K\,km\,s^{-1}}$. Left: Averaged spectra from this region as indicated. Results of the analysis of the peak temperatures are given in Table 4.10.

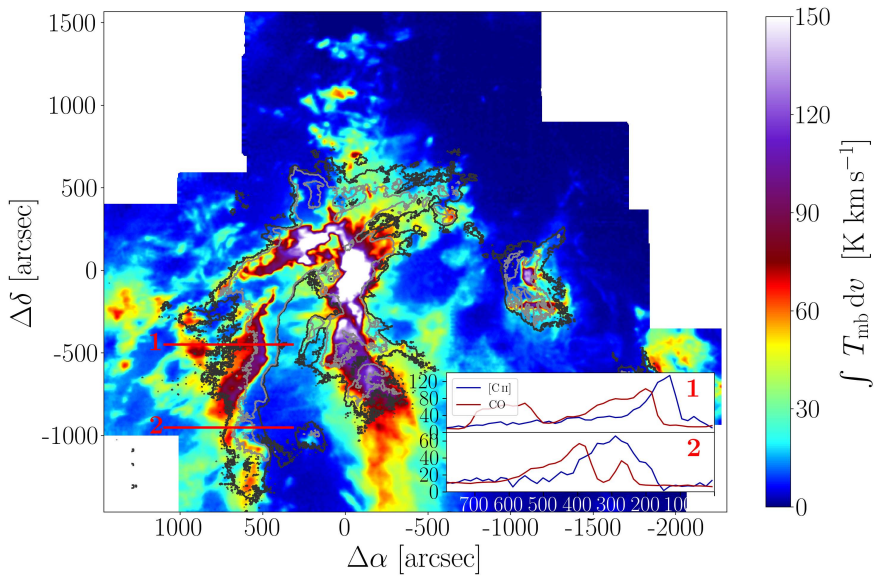

Figure 4.29: ^{12}CO(2-1) emission in velocity interval $v_{\rm LSR}$ = 5-8 km s^{-1} with [C II] emission in same velocity interval in contours (dark grey: 30 K km s^{-1}, light grey: 50 K km s^{-1}). The inlaid panels show the line cuts along the two red lines indicated in the figure.

Table 4.10: Gaussian fit parameters of spectra in Fig. 4.28.

	$T_{\mathrm{P}}([^{12}\mathrm{C\,II}])$ [K]	$T_{\mathrm{P}}([^{13}\mathrm{C\,II}])$ [K]	$\tau_{[\mathrm{C\,II}]}$	T_{ex} [K]	N_{C^+} [cm^{-3}]
green	35	1	2.9	48	5.7×10^{18}
blue	30	1	3.4	44	6.4×10^{18}

The main line can be fitted by two emission components or by one emission and one absorption component. However, the latter would increase the result for $\tau_{[\mathrm{C\,II}]}$ even further. In conclusion, the values obtained here can only be a crude estimate due to the complex emission structure from this region, which might be inadmissibly averaged together in the spectra.

4.C PV diagrams

Figures 4.30 to 4.33 show the pv diagrams resulting from slicing the velocity-resolved [C II] map from the Extended Orion Nebula with M43 and NGC 1977 along the R.A. and Dec. axis, respectively. The coherent arc structure indicative of the expansion of the Veil shell can be seen in almost all pv diagrams. The expanding structure of NGC 1977 is more difficult to recognize.

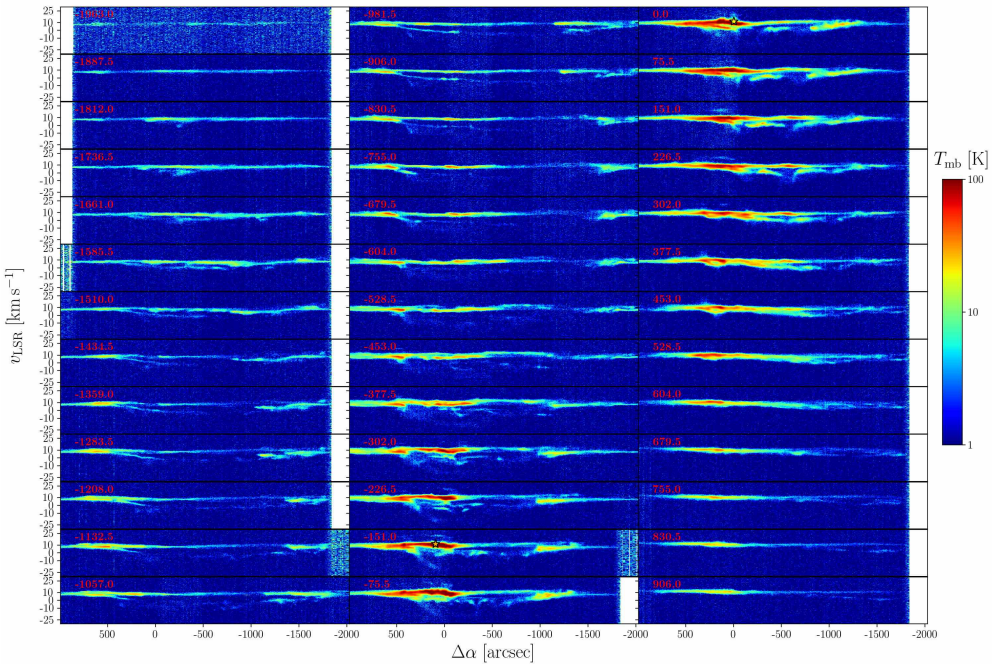

Figure 4.30: [C II] pv diagrams from the Veil shell, sliced along R.A. axis. Red numbers are the respective Dec. offsets in arc seconds.

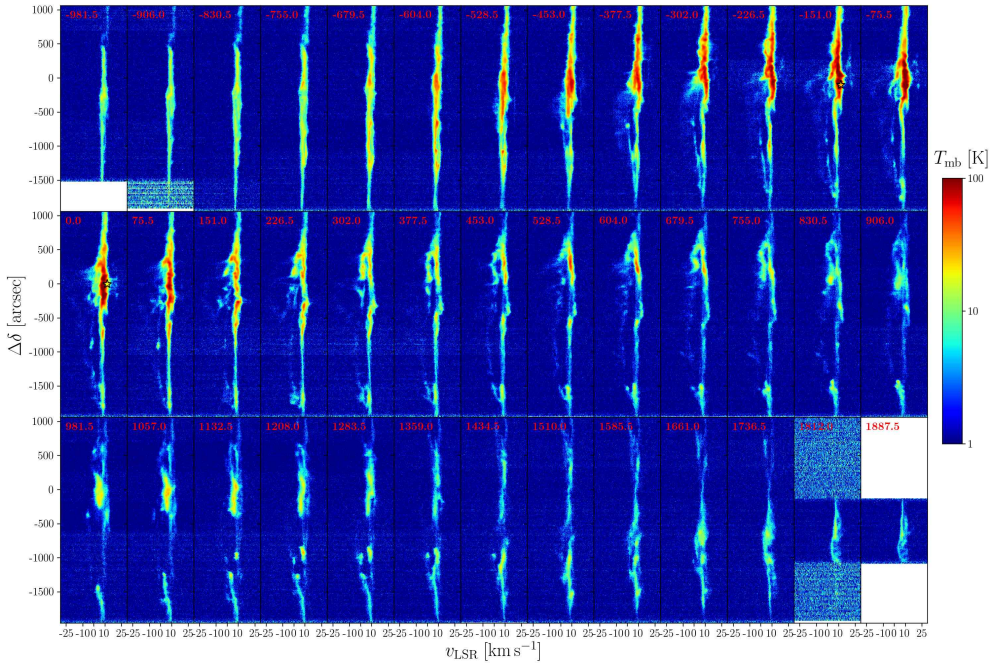

Figure 4.31: [C II] pv diagrams from the Veil shell, sliced along Dec. axis. Red numbers are the respective R.A. offsets in arc seconds.

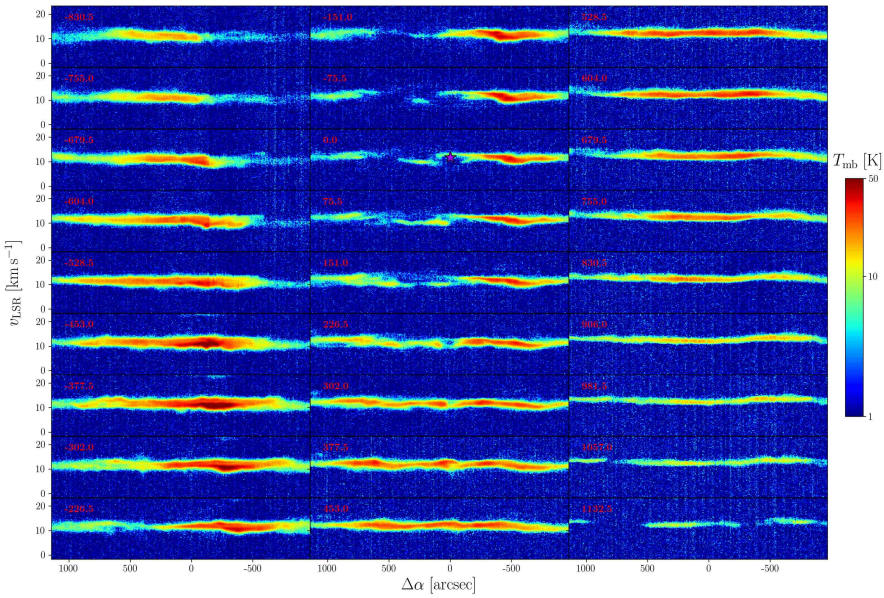

Figure 4.32: [C II] pv diagrams from NGC 1977, sliced along R.A. axis. Red numbers are the respective Dec. offsets in arc seconds. Coordinate offsets are given with respect to the position of 42 Orionis.

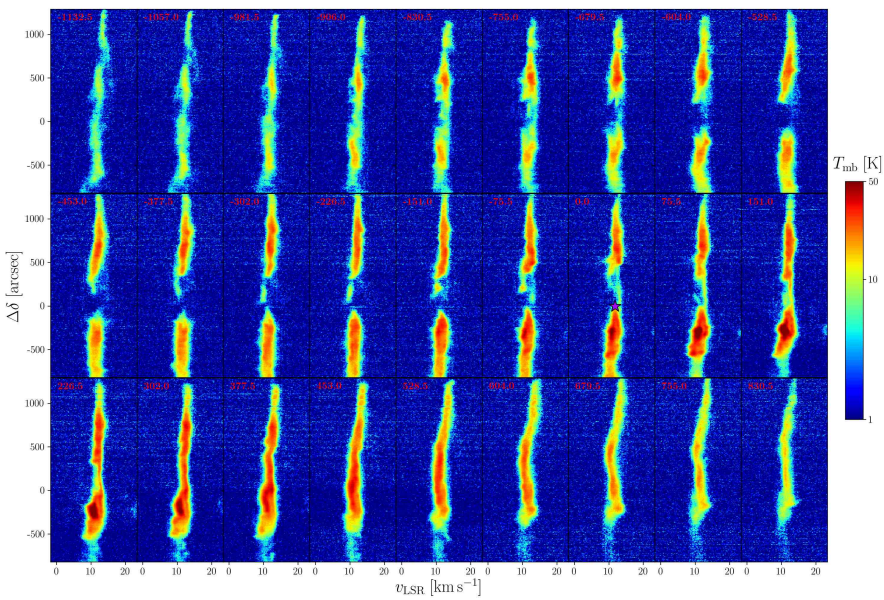

Figure 4.33: [C II] pv diagrams from NGC 1977, sliced along Dec. axis. Red numbers are the respective R.A. offsets in arc seconds. Coordinate offsets are given with respect to the position of 42 Orionis.

5

[C II] 158 μm line emission from Orion A. I. A template for extragalactic studies?

Abstract

Context: The [C II] 158 μm fine-structure line is one of the dominant coolants of the neutral interstellar medium. It is hence one of the brightest far-infrared emission lines and can be observed not only in star-forming regions throughout the Galaxy, but also in the diffuse interstellar medium and in distant galaxies. [C II] line emission has been suggested to be a powerful tracer of star-formation.

Aims: We aim to understand the origin of [C II] emission and its relation to other tracers of interstellar gas and dust. This includes a study of the heating efficiency of interstellar gas as traced by the [C II] line to test models of gas heating.

Methods: We make use of a one-square-degree map of velocity-resolved [C II] line emission towards the Orion Nebula complex, including M43 and NGC 1977. We employ *Herschel* far-infrared photometric images to determine dust properties. Moreover, we compare with Hα emission from the ionized gas, *Spitzer* mid-infrared photometry to trace hot dust and large polycyclic aromatic hydrocarbons (PAHs), and velocity-resolved IRAM 30m CO(2-1) observations of the molecular gas.

Results: The [C II] intensity is tightly correlated with PAH emission in the IRAC 8 μm band and far-infrared emission from warm dust. However, the [C II] intensity depends less than linear on the 8 μm and far-infrared intensity, while 8 μm and far-infrared intensities are approximately linearly correlated. The correlation between [C II] and CO(2-1) does not show a clear trend and is affected by the detailed geometry of the region. We find particularly low [C II]-over-FIR intensity ratios towards large columns of (warm and cold) dust, which suggest the interpretation of the "[C II] deficit" in terms of a "FIR excess". A slight decrease in the FIR line-over-continuum intensity ratio can be attributed to a decreased heating efficiency of the gas. Furthermore, we find that, at the mapped spatial scales, predictions of the star-formation rate from [C II] emission, like most other tracers, underestimate the star-formation rate calculated from YSO counts in the Orion Nebula complex by an order of magnitude.

Conclusions: [C II] emission from the Orion Nebula complex arises dominantly in the cloud surfaces, many viewed in edge-on geometry. Most of the [C II] emission stems from the extended fainter outskirts of the irradiated regions, while the [C II] intensity is deficient with respect to the total far-infrared intensity in the brightest regions. [C II] emission from extended faint cloud surfaces may contribute significantly to the total [C II] emission on galactic scales.

C. H. M. Pabst, A. Hacar, J. R. Goicoechea, D. Teyssier, O. Berné, M. G. Wolfire, R. D. Higgins, E. T. Chambers, S. Kabanovic, R. Güsten, J. Stutzki, C. Kramer, A. G. G. M. Tielens

to be submitted to A&A

5.1 Introduction

The [C II] 158 μm fine-structure line dominates the far-infrared (FIR) spectrum of the Milky Way, carrying up to 1% of the total luminosity (Bennett et al. 1994). Given the small energy separation of the two fine structure-levels ($\Delta E = 91.2\,\mathrm{K}$), low critical density (several $10^3\,\mathrm{cm}^{-3}$ for collisions with hydrogen atoms; e.g., Goldsmith et al. 2012), and the high abundance of carbon, this transition is the dominant cooling line of diffuse atomic gas (Dalgarno & McCray 1972), the so-called cold neutral medium phase of the interstellar medium (ISM). In the surfaces of molecular clouds, the CO molecule is photodissociated and carbon is singly ionized (ionization potential of 11.3 eV) by the interstellar radiation field. This so-called CO-dark (atomic and) molecular gas (Grenier et al. 2005; Wolfire et al. 2010) also radiates substantially in the [C II] line (e.g., Langer et al. 2010). Also in regions of massive star formation, the strong UV field photodissociates molecules, ionizes atoms, and heats the gas. These dense photodissociation regions (PDRs) emit bright atomic fine-structure lines. In particular, the [C II] 158 μm line and the [O I] 63 μm and 145 μm lines (at high gas densities) are the main gas coolants (Hollenbach & Tielens 1999). Finally, the [C II] line can also arise from low-density regions of ionized gas, such as the warm ionized medium (Heiles 1994). Observational studies have demonstrated that each of these ISM components contributes to the [C II] emission of the Milky Way (e.g., Stacey et al. 1991; Shibai et al. 1991; Bennett et al. 1994; Bock et al. 1993; Abdullah & Tielens 2020). In particular, the pencil-beam Herschel/HIFI GOTC+ [C II] survey suggests that much of the observed [C II] emission in our Galaxy emerges from dense PDRs ($\sim 47\%$), with smaller contributions from CO-dark molecular gas ($\sim 28\,\%$), cold atomic gas ($\sim 21\,\%$), and ionized gas ($\sim 4\,\%$; Pineda et al. 2013).

Irrespective of its origin, the [C II] emission is linked to the presence of stellar far-ultraviolet photons (FUV; $E < 13.6\,\mathrm{eV}$). As FUV photons are tied to the presence of massive O and B stars that have short lifetimes, the [C II] 158 μm line is also a star formation rate indicator. Indeed, ISO, Herschel and SOFIA observations have demonstrated the good correlation between the [C II] luminosity and the star-formation rate (SFR) in the Milky Way and in regions of massive star formation in other galaxies (e.g., Kramer et al. 2013; Pineda et al. 2014, 2018; Herrera-Camus et al. 2015, 2018; De Looze et al. 2011). With ALMA and NOEMA, ground-based observations of the [C II] 158 μm line in high redshift galaxies has come into reach and such data is routinely used to infer star formation rates (e.g., Walter et al. 2012; Venemans et al. 2012; Knudsen et al. 2016; Bischetti et al. 2018; Khusanova et al. 2020) based upon validations of this relationship in the nearby Universe (Herrera-Camus et al. 2018; De Looze et al. 2011). However, it is well-understood that the intensity of the [C II] line depends on the local physical conditions (Hollenbach & Tielens 1999). Observationally, the presence of the so-called "[C II]-deficit" – a decreased ratio of [C II] 158 μm luminosity to FIR dust continuum with increasing dust color temperature and also with FIR luminosity – is well established (Malhotra et al. 2001; Díaz-Santos et al. 2013; Magdis et al. 2014; Smith et al. 2017). This deficit is particularly pronounced in (local) ultraluminous infrared galaxies (ULIRGs), very dusty galaxies characterized by vigorous embedded star formation (e.g., Luhman et al. 2003; Abel et al. 2009; Graciá-Carpio et al. 2011). This deficit, however, does not necessarily hold in the early Universe at high redshift (e.g., Stacey et al. 2010; Brisbin et al. 2015; Capak et al. 2015). Some studies have indicated that not only [C II] emission is deficient in some sources, but other FIR cooling lines ([O I], [O III], [N II]), as well (e.g., Graciá-Carpio et al. 2011; Herrera-

Camus et al. 2018). These deficits must be linked to the global ISM properties and star-formation characteristics in these galaxies.

As these FIR cooling lines and FIR dust continuum emission are often the brightest signature from the ISM of distant star-forming galaxies, their luminosities should allow us to determine galaxy-averaged gas physical conditions, SFRs, and ultimately distinguish the dominant star-forming modes and galaxy evolutionary stages (e.g., starbursts, mergers). Before exploiting such a powerful diagnostic tool box of star-formation across cosmic time, it is mandatory to fully understand the origin of the FIR fine-structure line emission, its link with the SFR, and how does it relate to other proxies of the SFR (dust, Hα, PAH, and molecular gas emission). Here we try to answer these questions with square-degree [C II] 158 μm mapping observations of the prototypical star-forming cloud in the disk of the Milky Way, Orion A (Pabst et al. 2019). Our study is relevant in the extragalactic context because, thanks to Herschel and now much more efficiently with SOFIA, we have access to velocity-resolved wide-field (spatial scales of several parsec) maps of the [C II] 158 μm emission over nearby, spatially-resolved regions of massive star formation (Goicoechea et al. 2015b; Pabst et al. 2019, 2020; Schneider et al. 2020). This means that any variation of the surface brightness spatial distribution of these observables can be directly linked to the characteristics of each line-of-sight, its local physical and FUV-illumination conditions, and its SFR surface density. Mapping large spatial scales of star-forming regions in the Milky Way is mandatory to properly compare with the extragalactic emission. As we show here, the [C II]-to-infrared dust intensity ratio over the mapped areas in Orion A varies by about two orders of magnitude, showing the same range of intensity ratios displayed by galaxies hosting very different physical conditions and SFRs (e.g., Stacey et al. 2010). This similarity suggests that Orion A is good local template to understand the origin of the [C II] 158 μm emission and its connection to the SFR in galaxies (see also the discussion by Goicoechea et al. 2015b; Rybak et al. 2020a). In order to expand our study and include regions of low [C II] 158 μm surface brightness into the analysis (i.e. low FUV illumination), and to investigate the role of different environment/stellar content, we also compare with the [C II] emission seen around around the Horsehead Nebula (in Orion B, about 3° north of Orion A; Pabst et al. 2017; Bally et al. 2018) and also with the [C II] emission imaged over the entire nearby spiral galaxy M51 (Pineda et al. 2018), both mapped by SOFIA.

This study is organized into a series of two papers. In this paper (Paper I), we examine the relationship between the [C II] emission and other observational tracers of star formation, as well as the implications for the [C II] deficit, using the square-degree observations of Orion carried out with SOFIA/upGREAT (for details see Pabst et al. 2019, 2020). In a second paper (Paper II), we investigate the correlations in more detail, relate them to small-scale emission features and PDR physics, and compare with detailed PDR models. This paper is organized as follows: In Section 2, we will briefly describe the observations used in this study. Section 3 discusses the global morphology of the [C II] line emission and presents the correlations we find of the [C II] emission with other tracers of gas and dust in the Orion Nebula complex. In Section 4, we discuss the implications of the results of Section 3 and the relation between [C II] emission and the star-formation rate. We summarize our results in Section 5.

5.2 Observations

5.2.1 [C II] observations

We use the same velocity-resolved [C II] line observations as Pabst et al. (2019, 2020). Details of the observing strategy and data reduction are provided by Higgins et al. (in prep.). The [C II] 158 μm line observations towards the Orion Nebula complex, covering M42, M43 and NGC 1973, 1975, and 1977, were obtained during 13 flights in November 2016 and February 2017 using the 14-pixel high-spectral-resolution heterodyne array of the German Receiver for Astronomy at Terahertz Frequencies (upGREAT[1],Risacher et al. (2016)) onboard the Stratospheric Observatory for Infrared Astronomy (SOFIA). We obtained a fully-sampled map of a 1.2 square-degree-sized area at a angular resolution of 16″ using the array on-the-fly (OTF) mode. The resulting root-mean-square noise per pixel at a spectral resolution of 0.3 km s^{-1} resulted in $T_{\rm mb} \simeq 1.14$ K after re-binning the original data with a native spectral resolution of 0.04 km s^{-1}. For the baseline removal, a catalogue of splines was produced from spectra not containing an astronomical signal. and those were scaled to the astronomical data. The repeatability between flights is 7% (Higgins et al., in prep.), and we take this as an estimate of the intensity uncertainty.

5.2.2 CO(2-1) observations

We also make use of ^{12}CO $J = 2$-1 (230.5 GHz) and ^{13}CO $J = 2$-1 (220.4 GHz) line maps taken with the IRAM 30 m radiotelescope (Pico Veleta, Spain). The central region (1° × 0.8°) around OMC1 was originally mapped in 2008 with the HERA receiver array, and the mapping and data reduction strategies were presented by Berné et al. (2014). These CO maps with a native angular resolution of 10.7″ were enlarged using the new EMIR receiver and FFTS backends. The fully-sampled maps are part of the Large Program "Dynamic and Radiative Feedback of Massive Stars". Goicoechea et al. (2020) give details on how the old HERA and new EMIR CO maps were merged and on the conversion from antenna temperature to main-beam temperature. The typical root-mean-square noise in the CO(2-1) map is $T_{\rm mb} \simeq 0.16$ K at a spectral resolution of 0.4 km s^{-1}. The IRAM Large Program is an ongoing survey and we use the data as available in March 2020. Specifically, coverage in NGC 1977 is not complete and the newly observed data will be subject of a future paper.

5.2.3 Dust SEDs

We use the dust SEDs in the Orion Nebula complex described in Pabst et al. (2020). They use the *Herschel*/PACS and SPIRE photometric images of the dust FIR continuum to determine the effective dust temperature and the dust optical depth, and fit a modified blackbody,

$$I_\lambda = B(\lambda, T_{\rm d}) \left[1 - \exp\left(-\tau_{160} \left(\frac{160\,\mu{\rm m}}{\lambda} \right)^\beta \right) \right], \tag{5.1}$$

[1]upGREAT is a development by the MPI für Radioastronomie (Principal Investigator: R. Güsten) and KOSMA/Universität zu Köln, in cooperation with the MPI für Sonnensystemforschung and the DLR Institut für Optische Sensorsysteme.

with dust emissivity index $\beta = 2$ to the three PACS 70 μm, 100 μm, and 160 μm bands, and three SPIRE 250 μm, 350 μm, and 500 μm bands, convolved and re-gridded to the resolution of the SPIRE 500 μm band with 36″ angular resolution and a pixel size of 14″. The brightest regions around the star-forming cores are saturated in the *Herschel* bands and hence excluded from our analysis.

The SED fits are biased towards the warm dust emission, and thus tend to underestimate the dust optical depth where colder dust is mixed in the line of sight. Moreover, the dust optical depth and dust temperature depend crucially on the exact value of β. This is examined in more detail on Paper II. Summarizing, for instance, changing β to 1.5 in the SED fits reduces the dust optical depth by 50%. The integrated FIR intensity is less sensitive: it varies by less than 20%. The general behavior of the correlations identified in this study is not affected. It is worth noting in this context, however, that the flux calibration uncertainty in the PACS bands, that dominate our SED fits, is less than 7% (Balog et al. 2014). We obtain the total FIR intensity by integrating the obtained SEDs in the range 40-500 μm.

The SED fits mainly serve to determine the properties of large dust grains in radiative equilibrium. Stochastically heated UV-irradiated small dust grains might affect our dust SEDs at the shortest FIR wavelenghts. To estimate the contribution of very small grains (VSGs) to the PACS 70 μm band we compute the intensity ratio of this band with the *Spitzer*/Multi-band Imaging Photometer for *Spitzer* (MIPS) 24 μm band. At the moderate temperatures over most of the region, a high 24 μm/70 μm ratio indicates a large contribution by VSGs. Dust inside H II regions is heated by trapped Lyα radiation (Salgado et al. 2016) and thus has a high 24 μm/70 μm ratio. We conclude that the contribution of VSGs is small in the line of sight towards the extended shell of the Orion Nebula. Only in the Veil bubble interior, that is filled with the hot plasma generated by the stellar wind from θ^1 Ori C (Güdel et al. 2008), contribution by VSGs might be significant. We surmise that emission from this region is dominated by dust collisionally heated by hot electrons and cooled through IR emission (Dwek & Arendt 1992). We stress that, examining the optical depth and temperature maps, the FIR emission in these sight lines is dominated by the colder material in the molecular cloud in the background.

5.2.4 Ancillary photometric data

We make use of Hα observations obtained by the Wide Field Imager (WFI) on the European Southern Observatory (ESO) telescope at La Silla (Da Rio et al. 2009) and the ESO/Digitized Sky Survey 2 (DSS-2) red-band image. We use the Hα image obtained with the Very Large Telescope (VLT)/Multi Unit Spectroscopic Explorer (MUSE) towards the Huygens Region (Weilbacher et al. 2015) to calibrate the WFI and DSS-2 images. The DSS-2 image is saturated in the inner EON, but that region is well covered by the WFI image.

Moreover, we employ the *Spitzer*/Infrared Array Camera (IRAC) 8 μm image of the Orion Nebula Complex (described in Megeath et al. 2012) to trace emission from polycyclic aromatic hydrocarbons (PAHs). The 8 μm band contains predominantly emission from ionized PAH species. We apply the surface brightness correction factor, described in the IRAC handbook, of 0.74 to the archival image. This induces a calibration uncertainty of about 10%, according to the IRAC handbook.

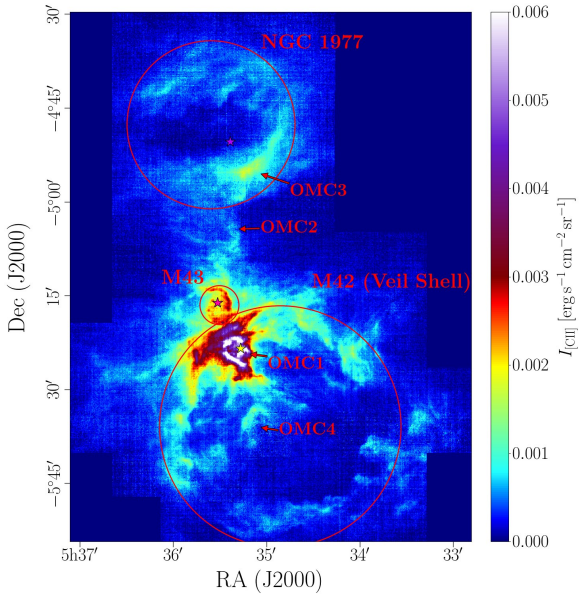

Figure 5.1: [C II] line-integrated intensity ($v_{\rm LSR} = -10\text{-}20\,{\rm km\,s^{-1}}$) from Orion A at its native resolution. The red circles delineate the three distinct shells of M42, M43, and NGC 1977. The stars indicate the most massive stars within each region: θ^1 Ori C (yellow) in M42, NU Ori (pink) in M43, and 42 Orionis (purple) in NGC 1977. Arrows indicate the positions of the four molecular cores OMC1-4 along the Integral-Shaped Filament.

5.3 Analysis

For the analysis, we convolve and re-grid all images to the resolution of the FIR intensity image, that is the poorest resolution with a beam size of 36″ and a pixel size of 14″.

5.3.1 Global morphology of the emission

Figure 6.2 shows the [C II] line-integrated intensity from Orion A. The [C II]-mapped area in Orion A comprises three distinct regions. The most massive stars in the Orion Nebula complex, the Trapezium stars, are found close to the surface of OMC1. Here, they create a heavily irradiated PDR at the surface of the molecular cloud, that radiates bright [C II] emission. Also the Veil Shell, the expanding shell that is created by the stellar wind of the O7V star θ^1 Ori C (the most massive of the Trapezium stars), radiates (limb-brightened) [C II] emission. In M43, we observe a limb-brightened [C II]-emitting shell structure, as well, in addition to the strongly irradiated PDR on the background molecular cloud. The shell surrounding NGC 1973, 1975, and 1977 also emits substantially in the [C II] line, the brightest part, however, being the PDR at the surface of OMC3.

In this paper, we will first focus on the global correlations of the [C II] emission with other star-formation tracers. In Paper II we will study the correlations in more detail by dividing them into several subregions. Figure 5.2 shows the distribution of various gas and dust tracers (FIR, 8 μm, CO(2-1), τ_{160}, Hα intensities, [C II]/FIR ratio) in the Orion Nebula complex with the [C II] line-integrated intensity in contours. While the

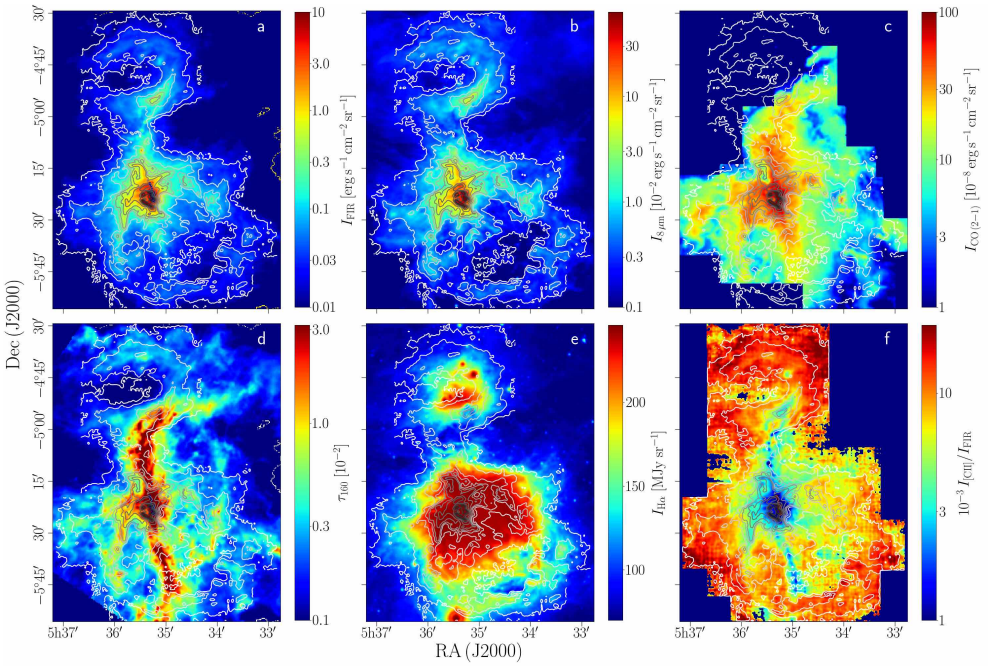

Figure 5.2: Various gas and dust tracers with [C II] line-integrated intensity ($v_{\rm LSR} = -10\text{-}20\,{\rm km\,s^{-1}}$) in contours (from white to black: $1.5, 3.5, 7.0, 10.5, 14.0, 20.0, 30.0, 40.0, 50.0, 60.0 \times 10^{-4}\,{\rm erg\,s^{-1}\,cm^{-2}\,sr^{-1}}$): *a)* FIR intensity, *b)* IRAC 8 μm intensity, *c)* IRAM 30m CO(2-1) intensity, *d)* dust optical depth τ_{160}, *e)* DSS Hα intensity, *f)* [C II]/FIR ratio. All images are convolved to the resolution of the FIR intensity image. Note that the DSS Hα image (panel e) is saturated at $I_{\rm H\alpha} \simeq 250\,{\rm MJy\,sr^{-1}}$.

morphology of the FIR, 8 μm and [C II] emission is very similar, the CO(2-1) intensity and the dust optical depth τ_{160} exhibit a different morphology, tracing the dense gas in the star-forming filament (the Integral-Shaped Filament, ISF). Hα emission traces the ionized gas and is concentrated inside the limb-brightened edges that light up in FIR, 8 μm and [C II] emission. The [C II]/FIR ratio traces the gas heating efficiency and generally increases away from the luminous [C II] sources close to the central stars. Dense filamentary structures, like the ISF, also possess low [C II]/FIR ratios, as the FIR emission is dominated by large columns of cool dust.

5.3.2 Correlation plots of gas and dust tracers

Figure 5.3 shows the point-by-point correlation between the different gas and dust tracers as density plots. Table 5.1 summarizes the power-law fits we find for each correlation, using the ordinary least-squares (OLS) bisector method (Isobe et al. 1990) on the logarithmic scale. We have included all points that lie above the $3\sigma \simeq 8\,{\rm K\,km\,s^{-1}} \simeq 5 \times 10^{-5}\,{\rm erg\,s^{-1}\,cm^{-2}\,sr^{-1}}$ threshold of the [C II] line-integrated intensity (after convolution). We do not apply this threshold to the FIR-8 μm correlation, but we restrict both maps to the coverage of the [C II] map. We subtract an offset of $2 \times 10^{-3}\,{\rm erg\,s^{-1}\,cm^{-2}\,sr^{-1}}$ from the IRAC 8 μm data. However, at low intensities we find 70 μm and FIR emission that does not correspond to [C II] emission. We fit this regime ($I_{70\,\mu{\rm m}} < 5 \times 10^2\,{\rm MJy\,sr^{-1}}$ and $I_{\rm FIR} < 3 \times 10^{-2}\,{\rm erg\,s^{-1}\,cm^{-2}\,sr^{-1}}$, respec-

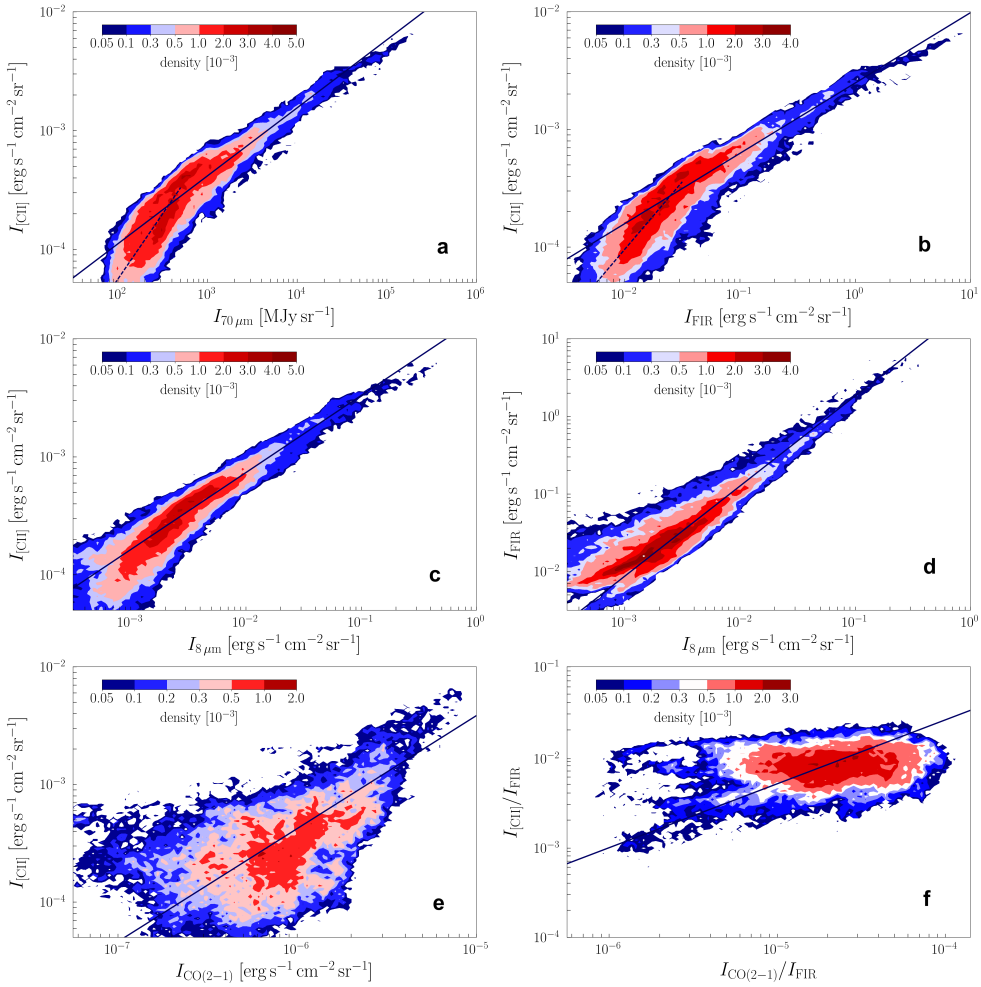

Figure 5.3: Correlations of all map points as point-density plots: *a)* [C II]-70 μm, *b)* [C II]-FIR, *c)* [C II]-8 μm, *d)* FIR-8 μm, *e)* [C II]-CO(2-1), *f)* [C II]/FIR-CO(2-1)/FIR. The regression curve with parameters of Table 5.1 is drawn in the respective panels (solid lines; dashed lines in panels a and b are the regression curves in the low-intensity regime).

Table 5.1: Summary of the point-density correlation plots in Fig. 5.3.

x	y	a	b	ρ	rms [dex]
70 μm	[C II]	0.57 ± 0.31^a	-5.10 ± 1.02	0.90	0.13
FIR	[C II]	0.60 ± 0.28^b	-2.61 ± 0.29^a	0.90	0.12
8 μm	[C II]	0.65 ± 0.30	-1.83 ± 0.64	0.93	0.10
8 μm	FIR	1.16 ± 0.37	1.43 ± 0.77	0.94	0.16
CO(2-1)	[C II]	0.96 ± 0.63	2.39 ± 3.89	0.53	0.37
$\frac{\text{CO(2-1)}}{\text{FIR}}$	$\frac{\text{[C II]}}{\text{FIR}}$	0.71 ± 0.60	1.24 ± 2.85	0.34	0.29

Notes. The regression fitted to the data in a weighted least-square fit is $\log_{10} y = a \log_{10} x + b$. Fit in $I_{[\mathrm{C\,II}]} > 3\sigma \simeq 5 \times 10^{-5}\,\mathrm{erg\,s^{-1}\,cm^{-2}\,sr^{-1}}$, $I_{70\,\mu\mathrm{m}} > 5 \times 10^2\,\mathrm{MJy\,sr^{-1}}$, $I_{8\,\mu\mathrm{m}} > 3 \times 10^{-3}\,\mathrm{erg\,s^{-1}\,cm^{-2}\,sr^{-1}}$, and/or $I_{\mathrm{FIR}} > 3 \times 10^{-2}\,\mathrm{erg\,s^{-1}\,cm^{-2}\,sr^{-1}}$. ρ is the Pearson correlation coefficient, rms is the root-mean-square of the residual of the fit. $^{(a)}$ For $I_{70\,\mu\mathrm{m}} < 5 \times 10^2\,\mathrm{MJy\,sr^{-1}}$ we obtain $a \simeq 1.10 \pm 0.68$ and $b \simeq -6.45 \pm 1.61$. $^{(b)}$ For $I_{\mathrm{FIR}} < 3 \times 10^{-2}\,\mathrm{erg\,s^{-1}\,cm^{-2}\,sr^{-1}}$ we obtain $a \simeq 1.15 \pm 0.76$ and $b \simeq -1.72 \pm 1.37$.

tively) separately. We point out that this low-intensity regime is problematic because of calibration uncertainties in the PACS bands, hence we will refrain from a detailed analysis thereof. The same holds for the IRAC 8 μm map, where we cannot exclude that the offset we subtract has a physical reason. We caution that this has to be taken into account when estimating the [C II] intensity from the IRAC 8 μm intensity at low surface brightness.

The [C II] intensity is tightly correlated with the intensity in the PACS 70 μm band (Fig. 5.3a), the FIR intensity (Fig. 5.3b), and with the intensity in the IRAC 8 μm band (Fig. 5.3c). The FIR intensity is also tightly correlated with the intensity in the IRAC 8 μm band (Fig. 5.3d). The Pearson correlation coefficients (ρ) in panels a to d are about 0.9, while the scatter around the correlations is of the order 0.1-0.2 dex. Most important to note is that the correlation of the [C II] intensity with each of the 70 μm, FIR (in the high-intensity regime), and 8 μm intensity is not linear, but scales with those intensities to a power of less than unity. The FIR-8 μm correlation deviates only slightly from linearity. At low FIR intensity, the [C II] intensity and the 8 μm intensity are largely independent of the FIR intensity.

The [C II]-CO(2-1) correlations are more complex and require a more thorough analysis, which we will return to and follow up in Paper II. The [C II]-low-J CO relationship, either as absolute intensities or normalized to the FIR intensity, is frequently used to infer physical conditions in Galactic and extragalactic star-forming regions (Wolfire et al. 1989; Stacey et al. 1991; Herrmann et al. 1997), which is why we include it here. Collectively, the [C II]-CO(2-1) correlations in Orion A (Figs. 5.3e and f) do not follow a simple power-law trend.

To estimate the FUV radiation field, we discuss briefly the FIR intensity as function of the distance from the massive stars. Figure 6.7 shows the dependence of the FIR intensity on distance from the central star θ^1 Ori C in M42. We find a decline of the FIR intensity in accordance with geometric dilution, that is decreasing with the distance squared. The FIR intensity scales directly with the incident FUV radiation field, given as G_0 in units of the Habing field, typically $G_0 \simeq I_{\mathrm{FIR}}/2/1.3 \times 10^{-4}\,\mathrm{erg\,s^{-1}\,cm^{-2}\,sr^{-1}}$, where the factor 1/2 accounts for the absorption of visible photons by dust (Hollenbach & Tielens 1999). However, geometry and line-of-sight effects are important, most of

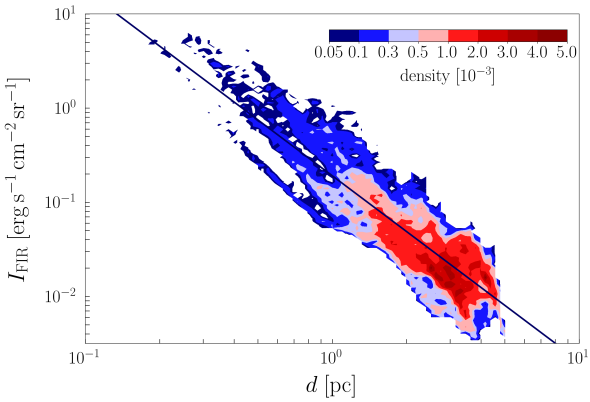

Figure 5.4: FIR intensity in M42 versus (projected) distance from θ^1 Ori C. The solid line is a power-law fit with $I_{\rm FIR} = bd^a$ and $a \simeq -1.97 \pm 0.55$, $b \simeq 10^{-0.72\pm0.24}\,{\rm erg\,s^{-1}\,cm^{-2}\,sr^{-1}}$.

the sight lines being towards limb-brightened cloud edges. The true FUV field may be found by the lower intensities in the correlation of Fig. 6.7, as those correspond to the face-on background cloud and are not affected by limb brightening. This yields $G_0 \simeq 500$ at a distance of 1 pc. Also following the prescription of Meixner et al. (1992), $G_0 \simeq L_{\rm FIR}/(4\pi S)/2/1.3 \times 10^{-4}\,{\rm erg\,s^{-1}\,cm^{-2}\,sr^{-1}}$, where S is the surface that is exposed to the FUV radiation field, we obtain $G_0 \simeq 500$ at a distance of 1 pc from the FIR luminosity of the edge-on eastern shell[2]. From the total FIR luminosity of M42, $1.5 \times 10^5\,L_\odot$ excluding the BN/KL and Orion S region, we estimate $G_0 \simeq 1500$ at a distance of 1 pc. While, in principle, the incident radiation field can be estimated from the stellar luminosity and the (true) distance from the illuminating source, oftentimes only the projected distance is known. In the case of the Orion Nebula, the detailed geometry of the irradiated gas and dust is complex and also the incident angle of the FUV radiation field with respect to the surface normal has to be taken into account (cf. Fig. 13 in O'Dell & Harris 2010). Moreover, the FUV radiation field in the Veil Shell may be attenuated by dust in the H II region and possibly in gas layers between the Trapezium stars and the Veil Shell (cf. van der Werf et al. 2013; Abel et al. 2019).

5.4 Discussion

The Orion A molecular cloud towards the Orion Nebula (NGC 1976 or M42) is the closest site of ongoing massive-star formation, and thus a prefect template to resolve the spatial distribution of the [C II] emission. At a distance of 414 ± 7pc from the earth (Menten et al. 2007), it covers about one square degree on the sky. To the north of the Orion Nebula lies De Mairan's Nebula (NGC 1982 or M43) and the Running-Man Nebula with NGC 1973, 1975, and 1977. The Orion Nebula itself is illuminated by the massive stars in the Trapezium cluster, the dominant star being the O7V star θ^1 Ori C at only ~ 0.3 pc from the molecular cloud. According to the blister model (Zuckerman 1973; Balick et al. 1974), the environing H II region, the so-called Huygens Region, is

[2]We sum over an area of $3' \times 3'$ in the limb-brightened eastern edge, obtaining $L_{\rm FIR} \simeq 1.8 \times 10^3\,L_\odot$. At a distance of 414 pc, $3' \simeq 0.36$ pc. The column exposed to the FUV radiation field has an approximate length of $r/2 \simeq 1.3$ pc, where $r \simeq 2.5$ pc is the radius of the shell structure. Hence, $S \simeq 0.36\,{\rm pc} \times 1.3\,{\rm pc}$.

Table 5.2: Summary of the density correlation plots in Fig. 5.5.

x	y	a	b	ρ	rms [dex]
70 μm	[C II]	0.50 ± 0.13	-4.85 ± 0.39	0.93	0.11
FIR	[C II]	0.56 ± 0.15	-2.65 ± 0.20	0.94	0.11
8 μm	[C II]	0.70 ± 0.18	-1.79 ± 0.40	0.95	0.10
8 μm	FIR	1.19 ± 0.17	1.39 ± 0.43	0.93	0.20

Notes. The regression fitted to the data is $\log_{10} y = a \log_{10} x + b$. Fit in $I_{[\mathrm{C\,II}]} > 3\sigma$ of the Orion B data. ρ is the Pearson correlation coefficient, rms is the root-mean-square of the residual of the fit.

located in front of the background Orion A molecular cloud. This very central part of the cloud includes the Orion Molecular Core 1 (OMC1) that hosts the embedded massive-star forming clumps Orion BN/KL and Orion S (e.g., Genzel & Stutzki 1989b). OMC1 also hosts the famous Orion Bar, a FUV-illuminated edge of the molecular cloud, and an archetypical example of a strongly irradiated PDR ($G_0 \simeq 10^4$) that has been subject of many detailed studies (e.g., Tielens et al. 1993; Goicoechea et al. 2016). The H II regions of M43 and NGC 1977 are ionized by the B0.5V star NU Ori and the B1V star 42 Ori, respectively. All these regions are subject to ongoing dynamical evolution. M42 is surrounded by a stellar-wind driven shell expanding at $13\,\mathrm{km\,s^{-1}}$ (Pabst et al. 2019), filled with a photo-ionized medium (O'Dell & Harris 2010) and an X-ray emitting hot plasma (Güdel et al. 2008). Both M43 and NGC 1973, 1975, and 1977 are surrounded by shells that expand under the influence of the contained over-pressurized ionized gas (Pabst et al. 2020).

5.4.1 Comparison with Orion B

An early spatial correlation study of the central OMC1/Huygens region ($\sim 85\,\mathrm{arcmin}^2$) was carried out by Goicoechea et al. (2015b) using Herschel/HIFI. This region is very bright in the FIR and shows very low [C II]/FIR intensity ratios (approaching 10^{-4}) reminiscent of the "[C II] deficit" seen in local ULIRGs. These authors concluded that the low luminosity ratios in this particular region are produced by the very large column density of warm dust throughout the star-forming core. Here, we expand this correlation study to much larger spatial scales, encompassing a much wider range of physical conditions, dust column densities, and FUV radiation illumination. In order to include regions of very low [C II] surface brightness into the analysis, and to study the role of different environment/stellar-illumination conditions, we also incorporate the [C II] emission mapped by SOFIA around the Horsehead Nebula and adjacent IC 434 H II region (located in Orion B, about 3° north of Orion A; Pabst et al. 2017; Bally et al. 2018). This region in Orion B is illuminated by the multiple star system σ Ori, dominated by a massive star of spectral type O9.5V and located $\sim 3\,\mathrm{pc}$ (in projection) from the Horsehead, producing $G_0 \simeq 100$ at the surface of the molecular cloud (e.g., Abergel et al. 2003).

Figure 5.5 compares the correlations of the [C II] intensity with the 70 μm, FIR, and 8 μm intensity, and the FIR-8 μm correlation in Orion A and B. For Orion A, we plot the data in M42 only (with $I_{[\mathrm{C\,II}]} > 2 \times 10^{-4}\,\mathrm{erg\,s^{-1}\,cm^{-2}\,sr^{-1}}$). Data of Orion B are taken from Pabst et al. (2017) and plotted for $I_{[\mathrm{C\,II}]} > 3\sigma \simeq 6 \times 10^{-5}\,\mathrm{erg\,s^{-1}\,cm^{-2}\,sr^{-1}}$. The correlations we find from the combined data sets, summarized in Table 5.2, are

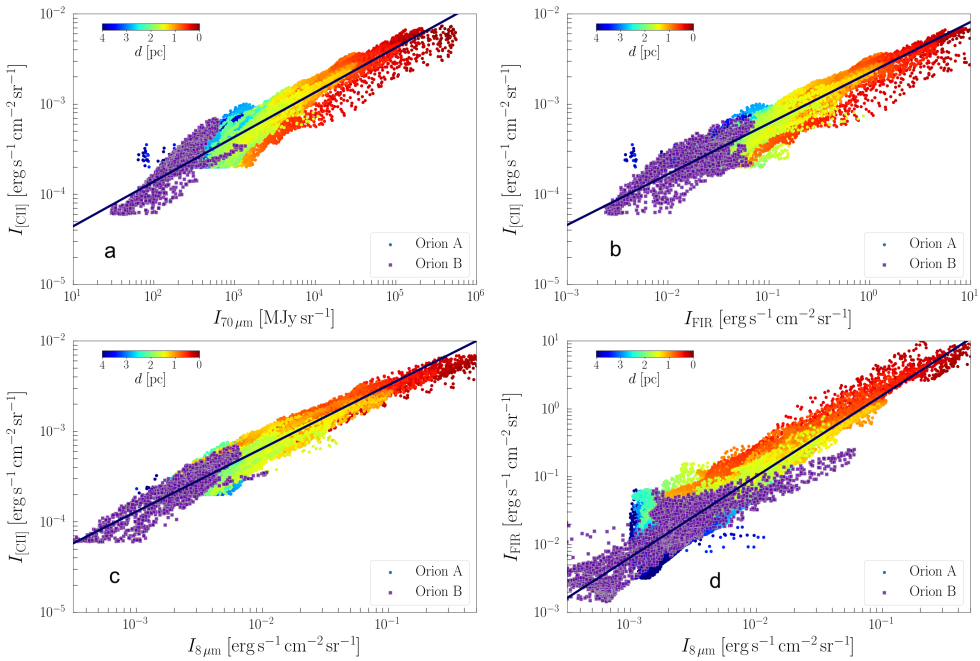

Figure 5.5: Comparison of the correlations in Orion A and B: *a)* [C II]-70 μm, *b)* [C II]-FIR, *c)* [C II]-8 μm, *d)* FIR-8 μm. The color scale in Orion A indicates the distance from θ^1 Ori C.

very similar to those found from the Orion A data only (cf. Table 5.1). The Orion A data form a perfect continuation of the earlier study of [C II] emission in Orion B, allowing us to extend the correlations over more than two orders of magnitude in [C II] intensity.

While Orion A is a region shaped by the stellar feedback from the locally formed massive stars, L1630 in Orion B is shaped by a chance encounter of a massive star with a molecular cloud. The O9.5V star σ Ori in Orion B is approaching the cloud and photoevaporating the gas from its surface (Ochsendorf et al. 2014). On the other hand, the shell structures that emit most of the [C II] luminosities in Orion A are created by the stars in their respective centers. Regardless of the formation history of the emitting gas structures, the [C II] intensity is determined by PDR physics, as the tight correlations with the FIR and 8 μm intensity, respectively, reveal.

5.4.2 The [C II] deficit

Multiple studies of galaxies report that the [C II]/FIR ratio drops with increasing FIR luminosity and increasing FIR color temperature (e.g., Malhotra et al. 2001; Luhman et al. 2003). This is referred to as "[C II] deficit". Usually, other FIR lines are affected, as well (e.g., Herrera-Camus et al. 2018). For the [C II] 158 μm line, in particular, emission may be suppressed and cooling could come out in, for example, the [O I] 63 μm line (critical density of several 10^5 cm^{-3}) in dense PDRs, the photoelectric heating rate depends non-linearly on the incident FUV radiation field as small dust grains and PAHs get charged at high radiation field, the relative contribution from different components of the ISM to the [C II] emission varies, and/or the FIR continuum emission has a large contribution from non-PDR dust. The [C II] deficit has been

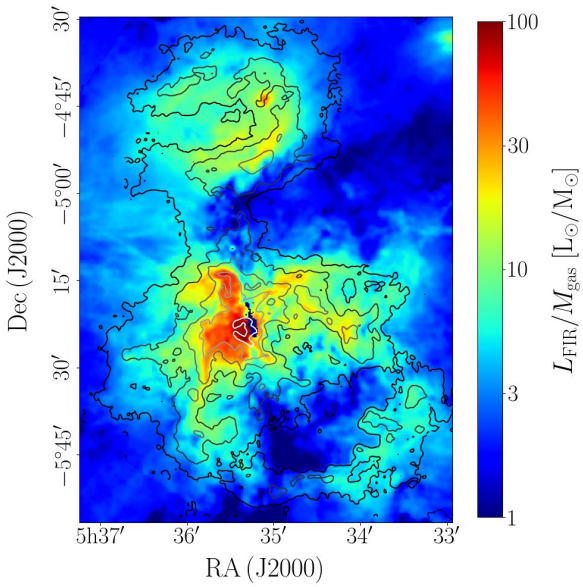

Figure 5.6: Spatial distribution of $L_{\rm FIR}/M_{\rm gas}$ in Orion A with [C II] line-integrated intensity in contours (from black to white: $2, 5, 10, 20, 50 \times 10^{-4}\,{\rm erg\,s^{-1}\,cm^{-2}\,sr^{-1}}$).

attributed to the importance of [O I] cooling at high UV fields and densities as well as the importance of heating sources of dust other than stellar radiation in (U)LIRGs (e.g., AGN activity Malhotra et al. 2001; Luhman et al. 2003; Croxall et al. 2012; Pineda et al. 2018; Rybak et al. 2020b). In more distant high-mass star-forming regions and in distant galaxies, some of the low [C II]/FIR ratios may be explained by [C II] absorption by foreground diffuse gas, for example diffuse clouds in the spiral arms (Gerin et al. 2015). Nearby, well-resolved regions of massive star formation provide an ideal opportunity to study some of these effects in detail as any "deficit" can be linked to the characteristics of the source and the local physical conditions. The large-scale [C II] map of the Orion Nebula complex allows us to address some of the issues that may influence the [C II]/FIR ratio.

Figure 1 in Herrera-Camus et al. (2018) illustrates the [C II] deficit in a local sample of archetypical galaxies. The authors note that the threshold value in FIR surface luminosity, above which the [C II]/FIR ratio decreases, marks galaxies with $L_{\rm FIR}/M_{\rm gas} \gtrsim 50\,L_\odot/M_\odot$. Values of $L_{\rm FIR}/M_{\rm gas} \simeq$ 50-80 $L_\odot\,M_\odot^{-1}$ have been suggested to characterize galaxies with enhanced star formation (e.g., Genzel et al. 2010). In the Orion Nebula complex, high values of $L_{\rm FIR}/M_{\rm gas}$ (computed from the dust SEDs and using standard dust properties of Weingartner & Draine (2001)) are found towards OMC1 and close to the central stars of M43 and NGC 1977 (see Fig. 5.6). In fact, we can express the ratio as

$$\frac{L_{\rm FIR}}{M_{\rm gas}} \simeq 4\pi \times 4 \times 10^{-2} \int_{40\,\mu{\rm m}}^{500\,\mu{\rm m}} B(\lambda, T_{\rm d}) \left(\frac{160\,\mu{\rm m}}{\lambda}\right)^{\beta} {\rm d}\lambda\, \frac{L_\odot}{M_\odot}, \tag{5.2}$$

with $L_{\rm FIR} = 4\pi A \tau_{160} \int_{40\,\mu{\rm m}}^{500\,\mu{\rm m}} B(\lambda, T_{\rm d})(160\,\mu{\rm m}/\lambda)^{\beta}\,{\rm d}\lambda$ (in the optically thin limit) and

$M_{\rm gas} = 6\times10^{24}\,{\rm cm}^{-2}\mu m_{\rm H} A\tau_{160}$, where A is the surface area, $\mu = 1.4$ the mean atomic weight, and $B(\lambda, T_{\rm d})\left(\frac{160\,\mu{\rm m}}{\lambda}\right)^{\beta}$ is the modified blackbody function (cf. Eq. 6.1). In a second step, we approximated the integral over FIR wavelengths by the infinite integral $\int_0^\infty B(\lambda, T_{\rm d})(160\,\mu{\rm m}/\lambda)^{\beta}\,{\rm d}\lambda \simeq 4.17\times10^{-8}\,{\rm erg\,s^{-1}\,cm^{-2}\,sr^{-1}\,K^{-6}}\,T_{\rm d}^6$ for $\beta = 2$, and obtain

$$\frac{L_{\rm FIR}}{M_{\rm gas}} \simeq 2\times10^{-2}\left(\frac{T_{\rm d}}{10\,{\rm K}}\right)^6 \frac{L_\odot}{M_\odot}. \tag{5.3}$$

This is accurate for optically thin dust FIR emission and $10\,{\rm K} \lesssim T_{\rm d} \lesssim 35\,{\rm K}$. For $T_{\rm d} = 40\,{\rm K}$, the finite integral is overestimated by 10%, and by 25% for $T_{\rm d} = 50\,{\rm K}$. Below $T_{\rm d} = 10\,{\rm K}$, the dust blackbody emission rapidly shifts towards millimeter wavelengths and the infinite integral is not a good approximation for the FIR emission either[3].

Expressed in this way, the ratio $L_{\rm FIR}/M_{\rm gas}$ is independent of the gas column and depends solely on the *effective* dust temperature. Naturally, the effective dust temperature in Orion A is highest towards the ionized gas, that is close to the central heating source. We show a map of the dust temperature in Paper II. In our SED fits, the molecular ridge with the BN/KL region and Orion S is excluded (for detailed SED fitting of this region, see Chuss et al. 2019). $L_{\rm FIR}/M_{\rm gas}$ assumes peak values of $80\,L_\odot\,M_\odot^{-1}$ in M42, $60\,L_\odot\,M_\odot^{-1}$ in M43, and $20\,L_\odot\,M_\odot^{-1}$ in NGC 1977 (with the exception of $40\,L_\odot\,M_\odot^{-1}$ towards NGC 1973). These highest values are concentrated in the H II regions of M43 and NGC 1977, like in OMC1. From SED fits of Chuss et al. (2019), we learn that exceedingly high values, $L_{\rm FIR}/M_{\rm gas} \sim 10^3\,L_\odot\,M_\odot^{-1}$, are found in a small region around the BN/KL core with $T_{\rm d} \simeq 95\,{\rm K}$. The global $L_{\rm FIR}/M_{\rm gas}$ ratio for M42 amounts to $14\,L_\odot\,M_\odot^{-1}$, while in M43 it is $26\,L_\odot\,M_\odot^{-1}$, and $7\,L_\odot\,M_\odot^{-1}$ in NGC 1977. Thus, globally, the Orion Nebula is characterized by rather low $L_{\rm FIR}/M_{\rm gas}$ and probably not representative of environments that dominate the FIR emission in ULIRGs, that may comprise large amounts of embedded star-forming cores like BN/KL. As we will discuss below, those embedded sources show a FIR excess in the continuum emission compared to the line emission.

In conclusion, in particular dense H II regions (like the Huygens Region and M43) exhibit high $L_{\rm FIR}/M_{\rm gas}$ ratios in their centers. $L_{\rm FIR}/M_{\rm gas}$ is expected to be proportional to the H II ionization parameter $U = Q(H)/4\pi R^2/c/n_e$ (Abel et al. 2009). Indeed, U is similar in M43 and NGC 1977 ($U \simeq 10^{-3}$), but higher in the Huygens Region ($U \simeq 10^{-2}$). The $L_{\rm FIR}/M_{\rm gas}$ ratio in Orion is dominated by the FIR emission from the dust column of the limb-brightened edges and the background molecular cloud (in M42 and M43) or the enveloping expanding shell (in NGC 1977) and does not trace the ionized gas directly. Yet, the properties of a PDR are closely related to the properties of the central H II region (Young Owl et al. 2002; Abel et al. 2005; Seo et al. 2019).

We now turn to discuss the [C II] line deficit in spatially resolved samples, Orion A and M51. Figure 2 of Pineda et al. (2018) shows the [C II]/TIR versus TIR correlation and the [C II]/TIR versus $70\,\mu{\rm m}/160\,\mu{\rm m}$ correlation in the spiral galaxy M51. Following Pineda et al. (2018), we compute the total infrared (TIR, integrated between 3 and $1000\,\mu$m; Croxall et al. 2012) intensity by

$$I_{\rm TIR} = 0.95\nu I_{\nu,8\,\mu{\rm m}} + 1.15\nu I_{\nu,24\,\mu{\rm m}} + \nu I_{\nu,70\,\mu{\rm m}} + \nu I_{\nu,160\,\mu{\rm m}}. \tag{5.4}$$

[3]If the FIR intensity includes the wavelength range 500-1000 μm, the infinite integral is accurate down to $T_{\rm d} \sim 5\,{\rm K}$.

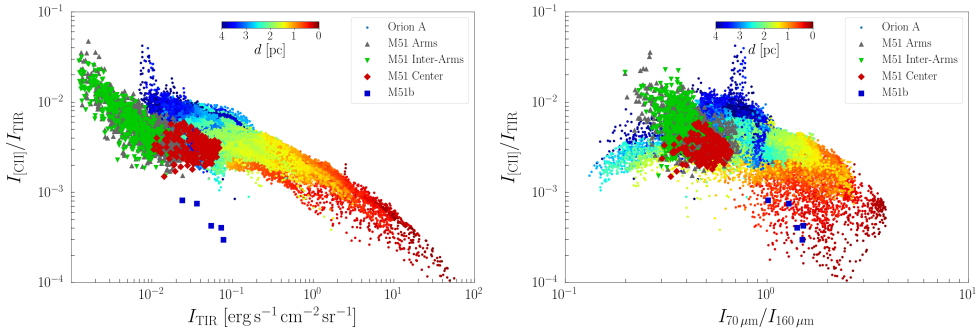

Figure 5.7: *Left*: [C II]/TIR intensity ratio versus TIR intensity in M51 and the Orion Nebula with M43. *Right*: [C II]/TIR intensity ratio versus PACS 70 μm over 160 μm intensity ratio in M51 and the Orion Nebula with M43. Fig. 1 in Pineda et al. (2018) shows the mask used to divide the M51 map into the four separate regions displayed here. Colors in Orion indicate distance from Trapezium stars as before (see colorbar).

Since the MIPS 24 μm image is saturated towards OMC1, we approximate $I_{\nu,24\,\mu m} \simeq 0.1 I_{\nu,70\,\mu m}$, which is valid for most of the bright, edge-on structures in the Orion Nebula (see Paper II). With this, we find $I_{TIR}/I_{FIR} \simeq 2$ towards the Orion Nebula. As extragalactic observations of regions of massive star formation are generally beam diluted, it is better to compare the relation between the [C II]/FIR and the 70 μm-160 μm color temperature. This latter ratio is a measure for the dust temperature. We show both correlations in Fig. 5.7, where for Orion we plot only points associated with M42 and M43. Points in NGC 1977 follow the same trend, but cover only the low-TIR end of the correlation. The trend of Pineda et al. (2018) is very similar to the trend observed in the Orion Nebula complex. The M51 relationship is slightly offset from the Orion data to lower 70 μm/160 μm ratios and/or lower [C II]/FIR. We ascribe this to a contribution of diffuse neutral HI clouds in the interstellar medium of M51 which is characterized by cooler dust.

In Orion, the [C II]/FIR ratio drops particularly for regions that are close to the illuminating star. These are regions with $G_0 > 10^4$ and $n > 4\times10^4$ cm^{-3}. For these regions cooling by [O I] 63 μm is known to be important with $I_{[O\,I]\,63\mu m}/I_{[C\,II]\,158\mu m} \simeq$ 5-10 (Herrmann et al. 1997). Following Luhman et al. (2003) and Croxall et al. (2012), we attribute the drop in the [C II]/FIR relation with increasing FIR or 70 μm/160 μm color temperature to a shift of the gas cooling to [O I] 63 μm line. Implicitly, this assumes that the heating efficiency does not depend strongly on the physical conditions in the emitting region. Variations in the heating efficiency are generally ascribed to variations in the ionization balance, which is controlled by the PDR ionization parameter $\gamma = G_0 T^{1/2}/n$ (cf. Section 6.4.4; Bakes & Tielens 1994). The observed relation between G_0 and the thermal pressure $p_{th} = nk_B T$ (see Paper II) translates this into a very weak dependence of the ionization parameter on physical conditions. We note that the [C II] optical depth of the bright [C II]-emitting structures in Orion A is usually of the order $\tau_{[C\,II]} \simeq$ 1-3, both in the edge-on shells and in the very bright core OMC1 (see Paper II; Goicoechea et al. 2015b), which may affect the correlations slightly, but we deem the effect too small to correct for the [C II] deficit. When estimating star-formation rates of galaxies, however, the [C II] optical depth has to be taken into account, as Okada et al. (2019) point out.

Besides close to the central heating sources, where [O I] cooling is dominant, low

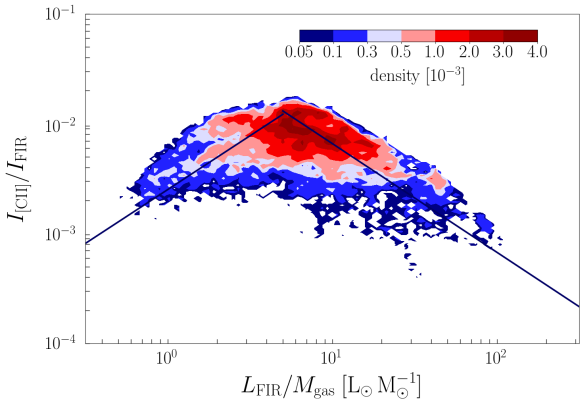

Figure 5.8: [C II]/FIR intensity ratio versus $L_{\rm FIR}/M_{\rm gas}$ ratio. Fit for $L_{\rm FIR}/M_{\rm gas} > 5$: $\log_{10} I_{[\rm C\,II]}/I_{\rm FIR} \simeq -0.99 \pm 0.86 \log_{10} L_{\rm FIR}/M_{\rm gas} - 1.19 \pm 0.87$, $rms \simeq 0.21$ dex, $\rho \simeq -0.65$; fit for $L_{\rm FIR}/M_{\rm gas} < 5$: $\log_{10} I_{[\rm C\,II]}/I_{\rm FIR} \simeq 0.98 \pm 0.62 \log_{10} L_{\rm FIR}/M_{\rm gas} - 2.60 \pm 0.27$, $rms \simeq 0.20$ dex, $\rho \simeq 0.53$.

[C II]/FIR ratios ($I_{[\rm C\,II]}/I_{\rm FIR} \simeq 2 \times 10^{-3}$) are found along the dense spine of the ISF (cf. Fig. 5.2f). Considering the low temperature of these structures, we do not expect [O I] emission to contribute significantly. Rather, we interpret these ratios as a "FIR excess" from cold dust in the dense molecular gas. Particularly deficient [C II]/FIR ratios ($I_{[\rm C\,II]}/I_{\rm FIR} \simeq 2 \times 10^{-4}$) are also found towards the active star-forming cores in the BN/KL region and Orion S (FIR intensity from Goicoechea et al. 2015a). Here, [O I] cooling is dominant ($I_{[\rm O\,I]\,63\mu m}/I_{[\rm C\,II]\,158\mu m} \simeq 20$ Herrmann et al. 1997), but in addition to excitation by FUV radiation at the surface, the [O I] lines have a contribution from shocked gas in the interior (Goicoechea et al. 2015a). Also the FIR emission stems from the inner layers of embedded star formation. As opposed to the FIR excess from cold dust in the ISF, this FIR excess is produced by warm molecular gas in the star-forming cores. The heavily irradiated PDR on the surface of the molecular core east of the Trapezium stars, devoid of star-forming activity, shows less deficient FIR line ratios, $(I_{[\rm O\,I]} + I_{[\rm C\,II]})/I_{\rm FIR} \simeq$ 5-10 $\times 10^{-3}$. Large columns of warm dust, such as in BN/KL and Orion S, lead automatically to high $L_{\rm FIR}/M_{\rm gas}$ ratios, as we have shown by Eq. 5.2, whereas the effective dust temperature will be lower for an irradiated surface with a large column of cooler (not internally heated) material behind it. Fig. 5.8 shows that the [C II]/FIR ratio in Orion A decreases with increasing $L_{\rm FIR}/M_{\rm gas}$ ratio for $L_{\rm FIR}/M_{\rm gas} \gtrsim 5$. At lower $L_{\rm FIR}/M_{\rm gas}$ ratios, however, the [C II]/FIR ratio tends to increase with increasing $L_{\rm FIR}/M_{\rm gas}$.

In Section 5.3.2, we have shown that the [C II] luminosity depends less than linear on the FIR luminosity per pixel. While the regions we study have different stellar content, the [C II]-FIR correlation is very similar in all of the regions. Moreover, we note that the [C II]/FIR versus FIR in the L1630 region (Pabst et al. 2017) is a good continuation of the correlation in the central OMC1 (Goicoechea et al. 2015b). Yet, L1630 represents the chance encounter of an O star with a molecular cloud (Ochsendorf et al. 2014) rather than emission from a region of active massive star formation. This provides further support for an interpretation of the [C II]/FIR relation in terms of the physical conditions rather than the star-formation history of the region. On the other hand, we have argued that particularly low FIR line-to-continuum ratios are found towards regions of large columns of (warm and cold) dust, which suggests the

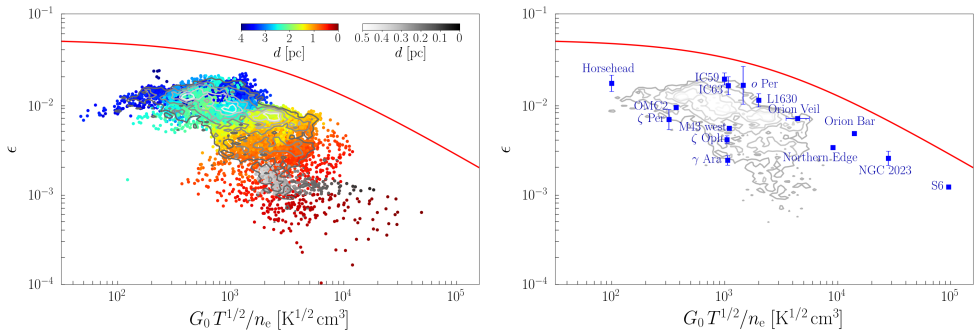

Figure 5.9: *Left:* The photoelectric heating efficiency, equated as cooling efficiency [C II]/FIR, throughout the Orion Nebula as function of the ionization parameter $\gamma = G_0 T^{1/2}/n_e$. Color scales indicate the distance from θ^1 Ori C. Contours indicate the density levels above which 90, 70, 50, 30 and 10% (from light to dark grey) of the points lie. The red curve is the theoretical prediction of Eq. 43 by Bakes & Tielens (1994). *Right:* The photoelectric heating efficiency ϵ in PDRs and diffuse sight lines, equated as the cooling efficiency by [C II] and [O I] cooling, overlaid on contours from the left-hand panel. Data for the diffuse ISM are taken from Gry et al. (1992) and van Dishoeck & Black (1986), data of NGC 2023 are from Hollenbach & Tielens (1999), data for the Horsehead and L1630 are from Pabst et al. (2017), data for IC 59 and IC 63 are from Andrews et al. (2018), data for the Orion Bar, S6, M43 west, and OMC2 are from Herrmann et al. (1997), and data for the Orion Veil are from Salas et al. (2019).

interpretation of the FIR line "deficit" in terms of a "FIR excess".

5.4.3 The photoelectric heating efficiency

The heating mechanism of the interstellar gas is of great importance for the understanding of the properties of the ISM. The UV-illuminated gas is dominantly heated by the photoelectric effect acting on small grains and PAHs (Bakes & Tielens 1994; Wolfire et al. 1995). The efficiency of this process is a crucial parameter in models of the ISM. Assuming equilibrium of heating and cooling processes, we can estimate the photoelectric heating efficiency by the cooling efficiency of the gas. At intermediate temperatures and densities the cooling is dominated by cooling through the [C II] line. At higher temperatures and densities, like those in the Huygens Region, the [O I] 63 μm line becomes important (Hollenbach & Tielens 1999). However, in the shell surrounding the Extended Orion Nebula, gas cooling is most likely dominated by [C II], as the temperatures and densities are rather moderate. In M43, [O I] 63 μm emission will be important, in NGC 1977 only in the densest part of the shell abutting OMC3 (Herrmann et al. 1997; Young Owl et al. 2002).

Theoretically, the photoelectric heating efficiency depends on the ionization parameter $\gamma = G_0 T_{\rm gas}^{1/2}/n_e$ (Bakes & Tielens 1994, Eq. 43). We equate the heating efficiency in our sample with the [C II] cooling efficiency $I_{\rm [C\,II]}/I_{\rm FIR}$, which is accurate for most points in our data set. In Appendix 5.A, we estimate γ in each pixel of the map. The correlations between the photoelectric heating efficiency ϵ and the ionization parameter γ in the Orion Nebula is shown in Fig. 6.21. Points in NGC 1977 overlap and are not shown. The data reveal a similar trend with a decreased efficiency with increased ionization parameter as the theoretical predictions of Bakes & Tielens (1994). The offset between the two might reflect a somewhat lower abundance of PAHs and VSGs

in Orion than assumed by Bakes & Tielens (1994). Closer to the central source, [O I] cooling dominates. Adding the [O I] 63 μm intensity to the [C II] intensity, shifts the heating/cooling efficiency to $\epsilon \simeq 7 \times 10^{-3}$ (outside of BN/KL) and corrects for the steep decline in the [C II]-TIR plot (with $I_{[\mathrm{O\,I}]}/I_{[\mathrm{C\,II}]} \simeq 6$ in OMC1). Nevertheless, the heating efficiency seems to slightly decline with radiation field, from $\sim 10^{-2}$ in the distant shell to 5×10^{-3} in the very center. While the [C II] deficit (and other FIR line deficits) observed on galactic scales might reflect different physical processes (XDRs, AGN activity), the [C II] deficit in the Orion Nebula reflects PDR physics with [O I] cooling correcting for the majority of the [C II] deficit and a slightly decreased heating efficiency at higher radiation field causing the slight decline.

5.4.4 The origin of [C II] emission

Table 6.6 gives the luminosities and masses of M42, M43, and NGC 1977, total and for the respective brightest region and the extended shell structure. Paper II discusses the origin of the [C II] emission in greater detail.

Most of the [C II] emission stems from the limb-brightened shell edges in M42, M43, and NGC 1977 (30-50%), but a significant contribution also comes from the more diffuse emission (25-45%), that is faint emission from extended surfaces. Even though the regions close to the central stars are very bright, their area is small and the contribution to the total [C II] emission minor (10-20%) compared to the large shells. For FIR emission, 20-30% stem from the shells, 20-30% from the regions close to the central stars of M43 and NGC 1977, but 45% from OMC1 in M42, and 10-20% from diffuse emission.

In Galactic samples, Pineda et al. (2013) note that most of the [C II] emission arises in moderately FUV-illuminated regions ($G_0 \simeq$ 2-50 in Habing units), that is large faint surfaces rather than small extreme regions. Our observations towards the Orion Nebula are reminiscent of this, the bright inner OMC1 region being a minor contributor to the total [C II] luminosity. The [C II] observations towards L1630, comprising the Horsehead Nebula, predominantly highlight the PDR surfaces illuminated by σ Ori, where 95% of the total [C II] emission in the mapped area arise. Yet, regions that are bright in [C II] trace only 8% of the gas mass, while 85% of the mass is associated with strong CO emission (Pabst et al. 2017). In the Orion Nebula complex, we find that 70% of the [C II] emission arises in bright PDR surfaces with $G_0 \gtrsim 100$. The [C II]-emitting regions contain 64% of the gas mass (traced by dust). A portion of that gas mass, about 30-50%, is likely associated with the molecular background rather than the PDR surface. Hence, bright [C II] emission, that traces the $\mathrm{H/H_2}$ transition in a PDR, traces about 30% of the total gas mass in the Orion Nebula complex.

We conclude that [C II] emission from PDRs with $G_0 \gtrsim 100$ is the main origin of [C II] emission from the Orion Nebula complex, with about 70%. The [C II] emission from ionized gas is a minor contributor, less than 5% in M42 and NGC 1977, but 15% in M43. From the remainder, we estimate that less irradiated gas that is not captured in bright PDR surfaces, contributes with about 20% within the mapped area. These percentages elucidate the importance of observations towards fainter extended regions, for those can carry a significant amount of [C II] luminosity (Abdullah & Tielens 2020).

5.4.5 Tracers of the star-formation rate

Observations with COBE revealed that the [C II] line is the brightest emission line in the far-IR spectrum of the Milky Way (Bennett et al. 1994). As this line originates

Table 5.3: Luminosities and masses of M42, M43, and NGC 1977.

Region		A [pc^2]	$L_{\rm FIR}$ [L$_\odot$]	$L_{\rm [C\,II]}$ [L$_\odot$]	$L_{\rm [C\,II]}/L_{\rm FIR}$	$M_{\rm gas}$ [a] [M$_\odot$]	$L_{\rm CO(2\text{-}1)}$ [b] [L$_\odot$]	$M_{\rm CO}$ [c] [M$_\odot$]	$L_{24\mu\rm m}$ [d] [L$_\odot$]	$L_{\rm H\alpha}$ [e] [L$_\odot$]
M42	all	45	1.8×10^5 [f]	510	2.8×10^{-3}	10000	1.1	8800	4700	3500
	OMC1	0.4	8.2×10^4 [f]	53	6.5×10^{-4}	640	8.9×10^{-2}	720	–	1500
	shell	10.0	5.2×10^4	209	4.0×10^{-3}	3000	3.2×10^{-1}	2500	2000	850
M43	all	0.74	1.4×10^4	38	2.7×10^{-3}	530	3.0×10^{-2}	240	740	190
	background, H II	0.13	3.1×10^3	8.9 [f]	2.8×10^{-3}	53	4.6×10^{-3}	37	100	99
	shell	0.31	8.2×10^3	19	2.3×10^{-3}	250	1.4×10^{-2}	110	410	63
NGC 1977	all	17	1.8×10^4	160	8.9×10^{-3}	2600	1.2×10^{-1}	950	1000	63
	OMC3	2.6	5.8×10^3	34	5.9×10^{-3}	1200	8.9×10^{-2}	720	190	8.6
	shell	6.2	5.4×10^3	69	1.3×10^{-2}	670	1.6×10^{-2}	130	100	7.9

Notes. [a] Gas mass derived from dust mass, using $N_H \simeq 6 \times 10^{24}\,\mathrm{cm}^{-2}\,\tau_{160}$ (Weingartner & Draine 2001). [b] The CO(2-1) map does not cover the entire NGC 1977 region (cf. Fig. 5.2). [c] Molecular gas mass from CO(2-1) intensity, using $X(\mathrm{CO}) \simeq 2 \times 10^{20}\,\mathrm{cm}^{-2}\,(\mathrm{K\,km\,s}^{-1})^{-1}$ (Bolatto et al. 2013). [d] The MIPS 24 μm image is saturated towards the Huygens/OMC1 region. [e] The Hα surface brightness in the EON is largely due to scattered light from the bright Huygens Region (O'Dell & Harris 2010). Also Hα emission in M43 has to be corrected for a contribution of scattered light from the Huygens Region (Simón-Díaz et al. 2011). [f] BN/KL and Orion S contribute with $L_{\rm FIR} \simeq 3 \times 10^4\,L_\odot$.

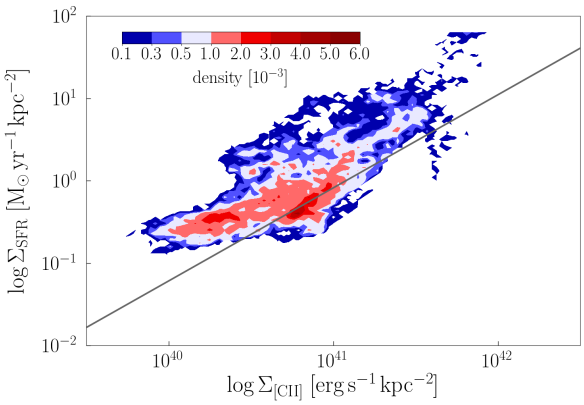

Figure 5.10: SFR surface density, estimated from Hα and 24 μm emission (Calzetti et al. 2007) versus the [C II] luminosity per unit area in Orion A as point-density plot. The grey line indicates the relation calibrated by Herrera-Camus et al. (2015) from a sample of local galaxies.

Table 5.4: Star-formation rates from different tracers

Tracer	SFR($M_\odot\,{\rm yr}^{-1}$)	Reference
FIR	$4.5 \times 10^{-44}\, L({\rm FIR})({\rm erg\,s^{-1}})$	Kennicutt (1998)
Hα, 24 μm	$5.3 \times 10^{-42}\, (L({\rm H}\alpha)_{\rm obs} + 0.0031\, L(24\,\mu{\rm m}))({\rm erg\,s^{-1}})$	Calzetti et al. (2007)
24 μm	$1.27 \times 10^{-38}\, [L(24\,\mu{\rm m})({\rm erg\,s^{-1}})]^{0.8850}$	Calzetti et al. (2007)
Hα, TIR	$5.5 \times 10^{-42}\, [L({\rm H}\alpha)_{\rm obs} + 0.0024\, L({\rm TIR})]({\rm erg\,s^{-1}})$	Kennicutt et al. (2009)
[C II](1)	$5.0 \times 10^{-37}\, [L([{\rm C\,II}])({\rm erg\,s^{-1}})]^{0.89}$	Pineda et al. (2014)
[C II](2)	$2.286 \times 10^{-43}\, [L([{\rm C\,II}])({\rm erg\,s^{-1}})]^{1.034}$	Herrera-Camus et al. (2015)
dense gas	$1.5 \times 10^{-8}\, M_{\rm dense}(M_\odot)$	Lada et al. (2012)

from gas illuminated by FUV photons emitted by OB stars, it was quickly recognized that this line might provide an excellent probe of the star formation rate in distant galaxies. Indeed, one of the main drivers of the design of ALMA was the requirement to be able to detect this line in Milky Way type galaxies at redshifts of $z \sim 3$. Since then, various Herschel-based studies have calibrated the [C II] line as a star-formation rate indicator. We discuss the relations compiled in Table 5.4 in the context of our observations towards the Orion Nebula complex[4]. Table 5.5 summarizes the values we calculate with these formulae for the star-formation rate from observations, both total and divided into the three regions M42, M43 and NGC 1977.

Perusing Table 5.5, we conclude that the different tracers of star-formation predict significantly different values at our mapped spatial scales. Specifically, the two SFR estimates from the [C II] luminosity differ from each other by an order of magnitude. Overall, the relation derived by Herrera-Camus et al. (2015) predicts lower values than

[4]Since these are empirical relations, we do not correct for [C II] optical depth.

Table 5.5: Star-formation rates in $M_\odot\,\mathrm{yr}^{-1}$ in M42, M43 and NGC 1977 predicted by several tracers using the correlations presented in Table 5.4.

Region	FIR	Hα, 24 μm	24 μm	Hα, TIR^a	[C II](1)	[C II](2)	dense gas^b	YSOs
all	3.0×10^{-5}	7.7×10^{-5}	1.6×10^{-5}	1.0×10^{-4}	1.3×10^{-4}	1.1×10^{-6}	1.5×10^{-4}	7.5×10^{-4}
M42	2.4×10^{-5}	7.1×10^{-5}	1.2×10^{-5}	9.2×10^{-5}	9.9×10^{-5}	7.6×10^{-6}	1.3×10^{-4}	5.5×10^{-4}
M43	2.4×10^{-6}	3.9×10^{-6}	2.3×10^{-6}	5.4×10^{-6}	9.9×10^{-6}	5.2×10^{-7}	3.6×10^{-6}	–
NGC 1977	3.1×10^{-6}	1.3×10^{-6}	3.0×10^{-6}	3.1×10^{-6}	3.5×10^{-5}	2.3×10^{-6}	1.4×10^{-5}	1.5×10^{-4}

Notes. $^{(a)}$ Total infrared luminosity approximated by twice the far-infrared luminosity. $^{(b)}$ Dense gas taken as CO-traced mass.

expected from other traces such as FIR, Hα and 24 μm emission. Only in NGC 1977, the relation by Pineda et al. (2014) overpredicts the SFR compared to the other traces (besides CO-traced mass).

In general, our correlations show that the [C II] intensity depends not linearly on the FIR intensity, but by a power law: it increases less steeply than the FIR intensity (Section 5.4.1). This reflects the decreased heating efficiency at higher radiation field (Section 6.4.4). This means that the galactic relations of FIR and [C II] emission are compatible with each other only within a limited range of conditions. The predictive power of the [C II] line in galactic context depends on the dominant source of [C II] line emission. A study by Abdullah & Tielens (2020) of the Orion-Eridanus environment on $\sim$ 400 pc scale suggests that [C II] emission arises mostly from extended, moderately irradiated cloud surfaces.

We note that the different measures for the star-formation rate trace different evolutionary stages in the star-formation process. While the dense mass mainly traces the sites of potential future star formation, Hα traces visible sites of already existing massive stars, that are ionizing their environment. The FIR luminosity also includes contributions from the embedded phase of massive star formation which is missed by Hα and 24 μm. For galactic sources, this phase is rather short and gets averaged out in the beam, but that is not always the case in extragalactic settings (e.g., ULIRGs with vigorous embedded star formation). Moreover, locally the 24 μm intensity, tracing the warmer shell interiors, is not correlated with the [C II], FIR and 8 μm intensities, that trace the somewhat cooler gas in PDR surfaces. Locally, also the ionized gas emitting in Hα fills the space interior to the shells.

We compare the gas-derived SFR with an actual count of the YSOs in the Orion Nebula cluster (ONC). Megeath et al. (2016) report 3001 YSOs in the ONC (after sample incompleteness correction). Adopting an average mass of 0.5 $M_\odot$ and an average duration of the protostellar/disk phase of 2 Myr (Evans et al. 2009), gives an SFR of $7.5 \times 10^{-4}\,M_\odot\,\mathrm{yr}^{-1}$. Da Rio et al. (2014) estimate a total mass of the ONC of 1000 $M_\odot$. Using the age of the cluster of 2 Myr, this yields a SFR of $5 \times 10^{-4}\,M_\odot\,\mathrm{yr}^{-1}$. Not surprisingly, as we are zooming in on a region of active star formation, these values are significantly higher than suggested by extragalactic correlations. This is illustrated by comparing with the upper-left panel of Figure 2 in Pineda et al. (2018), the SFR-[C II] correlation per unit surface. The Orion Nebula complex[5] lies off the upper right end of the correlation, with $\log \Sigma_{[\mathrm{C\,II}]}[\mathrm{erg\,s^{-1}\,kpc^{-2}}] \simeq 40.7$ and $\log \Sigma_{\mathrm{SFR}}[\mathrm{M_\odot\,yr^{-1}\,kpc^{-2}}] \simeq 0.9$-1.7 from star and YSO counts or $\log \Sigma_{\mathrm{SFR}} \simeq 0.1$ from Hα and 24 μm emission (cf. Table 5.5). We note, however, that a pixel-by-pixel comparison of the SFR predicted by Hα and 24 μm emission (according to Calzetti et al. 2007) and the [C II] emission in the Orion Nebula, as shown in Fig. 5.10, exhibits a similar spread as the SFR-[C II] correlation of Pineda et al. (2018) (here, $\rho \simeq 0.78$ and $rms \simeq 0.45$ dex), despite the fact that the emission tracers possess different morphologies. In the Orion Nebula, the Hα and 24 μm emission are strong in the (ionized) shell interior, whereas [C II] emission is arising predominantly from the shell's PDR surfaces.

Zooming in into separate regions, we discuss the distribution of the YSOs, as catalogued by Megeath et al. (2012), in relation with [C II] emission in somewhat more detail. Fig. 5.11 shows the distributions of YSOs across the [C II]-mapped area. We have counted the YSOs per 14″ pixel and convolved the resulting surface density to a beam of 2′. At our spatial resolution, the [C II] intensity is not correlated with the

[5]The total [C II] luminosity from the Orion Nebula complex is 750 $L_\odot$ from an area of 62 pc^2.

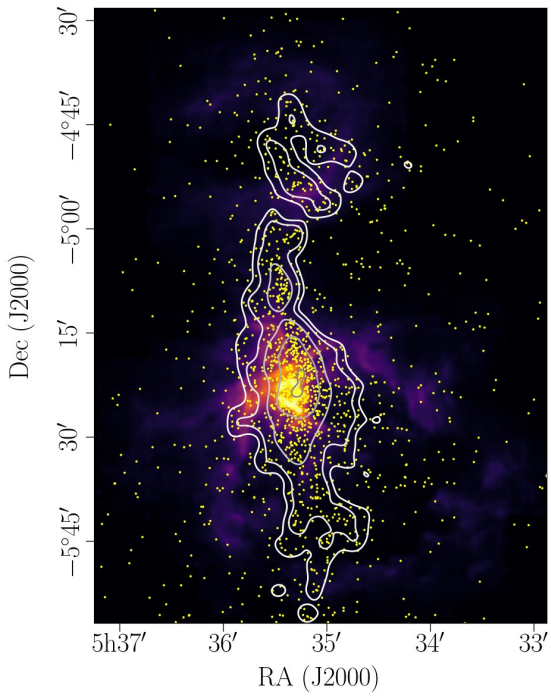

Figure 5.11: [C II] line-integrated intensity with YSO surface density in contours (from white to grey: $20, 30, 60, 120, 200\,M_\odot\,\mathrm{pc}^{-2}$). Yellow stars mark the positions of the dusty YSOs (Megeath et al. 2012).

YSO surface density locally, which also means a lack of evidence for triggered star formation in this early stage of evolution of the expanding shells in the Orion Nebula complex (see also Goicoechea et al. 2020). Strikingly, while OMC2 does not exhibit bright [C II] emission, we find many YSOs (about 120 within $1.6\,\mathrm{pc}^2$) located in the line of sight towards OMC2, concentrated along the ISF. Towards NGC 1977, we find about 300 YSOs across $17\,\mathrm{pc}^2$. The majority of YSOs is located in front of M42 and M43, about 1100 YSOs distributed over $42\,\mathrm{pc}^2$. Here, the YSO surface density is $26\,M_\odot\,\mathrm{pc}^{-2}$, where we have used an average mass of $0.5\,M_\odot$ and corrected for sample incompleteness by a factor of 2, following Megeath et al. (2016). The YSO surface density is slightly lower in NGC 1977, $18\,M_\odot\,\mathrm{pc}^{-2}$, but highest of the three regions in OMC2 with $75\,M_\odot\,\mathrm{pc}^{-2}$. Generally, high YSO surface density is found along the ISF, concentrating in the molecular cores OMC1–4. The maximum surface density is found towards OMC1. Thus, the SFR is highest in M42 and M43, together $6\times10^{-4}\,M_\odot\,\mathrm{yr}^{-1}$. NGC 1977 and OMC2 count with $2\times10^{-4}\,M_\odot\,\mathrm{yr}^{-1}$ and $6\times10^{-5}\,M_\odot\,\mathrm{yr}^{-1}$, respectively. We note that the removal of some 40% of the mass from the OMC1 core by the stellar wind of θ^1 Ori C will decrease the gravitational binding of the ONC cluster. We expect that it will take some 10^5 years for the stars to respond.

From COBE observations, Abdullah & Tielens (2020) derive a [C II] flux of $6.9\times10^{-7}\,\mathrm{erg\,s^{-1}\,cm^{-2}}$ from a region encompassing the Orion Nebula and NGC 1977. This corresponds to $3.7\times10^3\,L_\odot$. Hence, the SFR relations of Pineda et al. (2014) and Herrera-Camus et al. (2015) predict $6\times10^{-4}\,M_\odot\,\mathrm{yr}^{-1}$ and $6\times10^{-5}\,M_\odot\,\mathrm{yr}^{-1}$, respectively. Taking into account the contribution of molecular cloud surfaces exposed to

only moderate radiation fields, averaged in the beam of COBE, thus increases the SFR derived from extragalactic correlations. Locally, the SFR can be much higher (like in the Orion Nebula), but on galactic scales larger structures may contribute significantly, as we noted that a large portion of the [C II] luminosity from the Orion Nebula complex stems from rather extended, low-intensity regions (cf. Section 4.4).

5.5 Conclusion

Using a square-degree sized map of the [C II] 158 μm line towards the Orion Nebula complex, including M43 and NGC 1977, obtained with SOFIA/upGREAT, and comparing with *Herschel*/PACS and SPIRE FIR photometry, *Spitzer*/IRAC 8 μm emission and velocity-resolved IRAM 30m CO(2-1) observations, we have obtained the following results:

1. Our comparison of the [C II] line emission with FIR emission from FUV-heated dust and PAH emission in the 8 μm band reveal tight correlations with correlation coefficients of $\rho \gtrsim 0.9$. The [C II] line-integrated intensity depends less than linear on the PACS 70 μm intensity, FIR (40-500 μm) intensity, and IRAC 8 μm intensity. In particular, we find that the [C II] intensity scales with the 70 μm, FIR intensity, and the 8 μm intensity to the power of ~ 0.6 each. The FIR and PAH 8 μm intensities are approximately linearly correlated, the IRAC 8 μm band carrying about 10% of the FIR emission.

2. The less-than-linear dependence of the [C II] intensity on the FIR intensity implies a decreasing [C II]/FIR ratio with increasing FIR intensity. This is reminiscent of the "[C II] deficit" in ULIRGs, that has also been observed towards extragalactic sources like M51. However, including [O I] cooling corrects for most of the deficit in the Orion Nebula complex. The remaining slight deficit can be attributed to a reduced heating efficiency in the heavily irradiated PDR surfaces close to the central stars. Some sight lines host large columns of (warm and cold) dust that produce a "FIR excess", leading to particularly low [C II]/FIR intensity ratios.

3. Most of the [C II] luminosity of the Orion Nebula complex, 33% of the total 750 $L_\odot$, arises in the large, moderately illuminated shells surrounding the Orion Nebula, M43, and NGC 1977. Only 10% of the [C II] luminosity in M42, 53 $L_\odot$, stem from the brightest region, OMC1. A large amount of [C II] luminosity, 35%, stems from extended faint surfaces.

4. The scaling relations invoked to estimate the star-formation rate on galactic scales and in high-redshift galaxies do not apply to our local sample of [C II]-emitting sources. In the Orion Nebula complex, the [C II] line is dominantly excited by FUV radiation from the most massive stars. Smaller sources contribute to small-scale [C II]-emitting structures, but minor to the large-scale shells surrounding the massive stars. However, even the total [C II] emission from the mapped area is short of predicting the YSO content within the field of view. We surmise that [C II] emission from extended [C II]-faint structures contribute significantly to [C II] emission on galactic scales. In our sample, [C II] emission is dominated by larger, comparatively faint structures, rather than the bright dense cores.

Studies of the relations of [C II] emission to other tracers of gas and dust help to reveal "the local truth" about the origins of the [C II] line emission. Further investigations have to show whether the same correlations between those gas and dust tracers hold in different environments, for instance, the starburst region 30 Doradus (with also lower metallicity) and other sources shaped by stellar feedback. Taking into account the geometry of the sources is crucial in understanding the details of the correlations.

Acknowledgements

This work is based on observations made with the NASA/DLR Stratospheric Observatory for Infrared Astronomy (SOFIA). SOFIA is jointly operated by the Universities Space Research Association, Inc. (USRA), under NASA contract NNA17BF53C, and the Deutsches SOFIA Institut (DSI) under DLR contract 50 OK 0901 to the University of Stuttgart. This project has received funding from the European Research Council (ERC) under the European Union's Horizon 2020 research and innovation programme (grant agreement No. 851435). JRG thanks the Spanish MCIU for funding support under grant AYA2017-85111-P. Research on the interstellar medium at Leiden Observatory is supported through a Spinoza award of the Dutch Science Organisation (NWO). We thank S. T. Megeath for helpful advice on the *Spitzer*/IRAC data. This work made use of the TOPCAT software (Taylor 2005).

5.A Calculation of the ionization parameter γ

We use the ionization parameter $\gamma = G_0 T_{\rm gas}^{1/2}/n_{\rm e}$ in Section 6.4.4 to semi-empirically determine the heating curve of the interstellar gas. Here, we elaborate the procedure by which we estimate γ throughout the [C II] map.

To obtain the kinetic temperature of the gas we use the peak temperature $T_{\rm P}$ of the [C II] line:

$$T_{\rm gas} = \frac{T_{\rm ex}}{1 - T_{\rm ex}/91.2\,{\rm K}\log(1 + n_{\rm cr}/n)} \tag{5.5}$$

where the critical density depends on the [C II] optical depth $\tau_{[{\rm C\,II}]}$, $n_{\rm cr} = n_{\rm cr,0}\beta(\tau_{[{\rm C\,II}]})$, and $n_{\rm cr,0} = 2.7 \times 10^3\,{\rm cm}^{-3}$. The function $\beta(\tau)$ can be approximated as $(1 - \exp\tau)/\tau$. For simplicity, we fix $\tau_{[{\rm C\,II}]} = 2$, as is consistent with the [^{13}C II] line analysis where possible (see Paper II). We note that the gas temperature is only weakly dependent on the exact value of $\tau_{[{\rm C\,II}]}$. We estimate the excitation temperature $T_{\rm ex}$ assuming optically thick emission:

$$T_{\rm ex} = \frac{91.2\,{\rm K}}{\log(91.2\,{\rm K}/(T_{\rm P} + J(T_{\rm d})) + 1)}. \tag{5.6}$$

We approximate the gas density by the gas column density estimated from the dust opacity, assuming a line of sight of $\sim r/2 \simeq 1.4\,{\rm pc}$, i.e. $n \sim 6 \times 10^{24}\,{\rm cm}^{-2}\tau_{160}/1.4\,{\rm pc}$ in the Veil shell; in the OMC1 region, we take $n \sim 10^5\,{\rm cm}^{-2}$, in accordance with studies of the Orion Bar (Pellegrini et al. 2009; Bernard-Salas et al. 2012; Goicoechea et al. 2015b). We assume that all electrons stem from carbon ionization and that carbon is fully ionized. For the radiation field in the Orion Nebula, we assume $G_0 \simeq 500(1\,{\rm pc}/(d + 0.1\,{\rm pc})^2$, as obtained from the FIR-d relation in Section 5.3.2. We note that for points close to θ^1 Ori C, the estimate of the radiation field using the projected distance is not accurate and we add the vertical offset of 0.1 pc.

6

[C II] 158 μm line emission from Orion A. II. PDR physics

Abstract

Context: The [C II] 158 μm fine-structure line is the dominant cooling line of moderate-density photodissociation regions (PDR) illuminated by moderately bright far-ultraviolet radiation fields. This makes this line a prime diagnostic for extended regions illuminated by massive stars.

Aims: We aim to understand the origin of [C II] emission and its relation to other tracers of gas and dust in PDRs. One focus is a study of the heating efficiency of interstellar gas as traced by the [C II] line to test models of the photo-electric heating of neutral gas by polycyclic aromatic hydrocarbon molecules and very small grains.

Methods: We make use of a one-square-degree map of velocity-resolved [C II] line emission towards the Orion Nebula complex, and split this out into the individual spatial components, the expanding Veil Shell, the surface of OMC4, and the PDRs associated with the compact H II region of M43 and the reflection nebulae NGC 1973, 1975, and 1977. We employ *Herschel* far-infrared photometric images to determine dust properties. Moreover, we compare with *Spitzer* mid-infrared photometry to trace hot dust and large molecules, and velocity-resolved IRAM 30m CO(2-1) observations of the molecular gas.

Results: The [C II] intensity is tightly correlated with PAH emission in the IRAC 8 μm band and far-infrared emission from warm dust, with small variations between the four studied subregions (Veil Shell, OMC4, M43, and NGC 1977). The correlation between [C II] and CO(2-1) is very different in the four subregions and is very sensitive to the detailed geometry of the respective regions. Constant-density PDR models are able to reproduce the observed [C II], CO(2-1), and FIR intensities. The physical conditions in the Veil Shell of the Orion Nebula reveal a constant $p_{\rm th}/G_0$ ratio. We observe strong variations in the photoelectric heating efficiency in the Veil Shell behind the Orion Bar and these variations are seemingly not related to the spectral properties of the PAHs.

Conclusions: [C II] emission from the Orion Nebula complex stems mainly from moderately illuminated PDR surfaces. The correlations of the different tracers show small variations that are not yet understood, but the global correlations can be used to estimate the expected [C II] intensity of future observations.

C. H. M. Pabst, A. Hacar, J. R. Goicoechea, D. Teyssier, O. Berné, M. G. Wolfire, R. D. Higgins, E. T. Chambers, S. Kabanovic, R. Güsten, J. Stutzki, C. Kramer, A. G. G. M. Tielens

to be submitted to A&A

6.1 Introduction

The [C II] 158 μm fine-structure line is the dominant cooling line of neutral atomic gas at moderate densities ($n_{\rm H} \lesssim 10^4\,{\rm cm}^{-3}$) and temperatures ($T_{\rm k} \lesssim 300\,{\rm K}$; Dalgarno & McCray 1972). This includes diffuse clouds in the general interstellar medium (ISM) of galaxies as well as regions illuminated by nearby, newly formed, massive stars (Hollenbach & Tielens 1999). In these regions carbon atoms are rapidly ionized by penetrating far-UV photons (FUV; $E < 13.6\,{\rm eV}$) and molecules such as CO are quickly photodissociated. Hence, most of the gaseous carbon is in the form of C^+ ions. The ground state of C^+ has two fine structure levels separated by $\Delta E/k_{\rm B} = 91.2\,{\rm K}$. This transition has a critical density of (2-6) $\times\, 10^3\,{\rm cm}^{-3}$ for collisions with atomic or molecular hydrogen. Since the upper fine-structure level $^2P_{3/2}$ is easy to excite collisionally, and the interstellar carbon abundance is high, the [C II] 158 μm line dominates the cooling of the neutral ISM.

Extreme UV radiation (EUV; $E > 13.6\,{\rm eV}$) from massive stars ionize hydrogen atoms and create an H II region in their environment. This ionized gas is separated from the surrounding nascent molecular cloud by a photodissociation region (PDR) where penetrating FUV photons dissociate molecules and ionize low ionization potential atoms. These FUV photons ultimately heat the PDR gas to temperatures of 200-1000 K. The neutral gas (i.e., hydrogen in neutral form) couples to the FUV photon field through the photo-electric effect on large polycyclic aromatic hydrocarbon molecule (PAHs) and very small grains (VSGs; Bakes & Tielens 1994). This same process heats the gas in diffuse interstellar clouds (Wolfire et al. 1995). Dense PDRs in star-forming regions are bright in the far-IR atomic cooling lines, e.g. the [C II] 158 μm line at moderate densities and warmish temperatures (Tielens & Hollenbach 1985; Hollenbach et al. 1991), as well as the PAH emission features (Tielens 2008, and references therein), fluorescent ro-vibrational lines (e.g., Sellgren 1986; Field et al. 1998; Kaplan et al. 2017), pure rotational H_2 lines (e.g., Sheffer & Wolfire 2013; Habart et al. 2011; Allers et al. 2005), warm dust (e.g., Berné et al. 2007; Arab et al. 2012), and a plethora of molecular radicals and reactive ions (e.g., Pety et al. 2005; Fuente et al. 2003; Nagy et al. 2013; Goicoechea et al. 2017). Their high surface brightness and compact size make dense PDRs very appropriate targets for observational studies on the interaction of massive stars with their interstellar environment. This allows detailed studies of the physics and chemistry relevant to radiative feedback by massive stars. In particular, observations of the dominant atomic fine structure lines, through the energy balance, provide a direct probe of the heating processes of interstellar neutral atomic gas (e.g., Tielens 2008; Okada et al. 2013; Pabst et al. 2017; Salas et al. 2019).

The [C II] 158 μm line is the brightest far-IR line in the spectrum of the Milky Way and, in general, of star-forming galaxies, typically radiating about 0.3% of the IR dust continuum emission (e.g., Crawford et al. 1985; Bennett et al. 1994; Malhotra et al. 2001; Luhman et al. 2003; Stacey et al. 2010; Díaz-Santos et al. 2013). As ionization of carbon requires FUV photons with energies in excess of 11.2 eV, and such photons are only emitted by short-lived massive stars, the [C II] emission line is also considered a tracer of the star formation rate (SFR; e.g., Pineda et al. 2014; De Looze et al. 2011; Herrera-Camus et al. 2015, 2018). With ALMA and NOEMA, the use of the [C II] line as a SFR tracer has now been extended to the high redshift universe (e.g., Walter et al. 2012; Venemans et al. 2012; Knudsen et al. 2016; Bischetti et al. 2018; Khusanova et al. 2020). The use of the [C II] 158 μm line as a SFR indicator requires a reliable conversion

factor and extensive observational studies have focused on determining this factor through detailed studies of the [C II] line in samples of nearby star forming galaxies (e.g., Malhotra et al. 2001; Herrera-Camus et al. 2015, 2018; Chevance et al. 2016; Pineda et al. 2018). These observational studies have revealed a so-called C^+-deficit issue: the [C II]/FIR luminosity ratio is systematically lower in regions characterized by warm dust, possibly due to the onset of other cooling processes of neutral dense gas (e.g., the [O I] 63 μm line), changes in the coupling between the neutral atomic gas and the FUV photons, or the presence of energy sources other than FUV photons (e.g., AGNs or deeply embedded star formation; Luhman et al. 2003; Abel et al. 2009; Graciá-Carpio et al. 2011). Besides this observational validation of the use of the [C II] line as a SFR indicator, we also need to develop a deep understanding of the underlying physics involved in the heating and cooling of neutral atomic gas if we want to confidently extrapolate the local results over cosmological relevant timescales.

The recent rapid development of receiver technology has allowed the construction of multi-element heterodyne arrays at far-IR frequencies. In particular, the upGREAT instrument has been specifically designed to map the [C II] 158 μm line (Risacher et al. 2016). This sensitive instrument coupled with the nimble telescope of the Stratospheric Observatory For Infrared Astronomy (SOFIA) allows for the first time wide-field [C II] observations of regions of massive star formation at sub-km s^{-1} spectral resolution (Pabst et al. 2017; Bally et al. 2018). The C+SQUAD SOFIA Large Program has surveyed one square degree of the molecular cloud cores in Orion in the [C II] 158 μm line to probe the radiative and mechanical energy feedback of massive stars with their environment. The results revealed the presence of a ~ 2 pc radius massive ($\sim 1500\,M_\odot$) shell of neutral atomic gas expanding at 13 km s^{-1} (Pabst et al. 2019). The rapid expansion of this bubble is driven by the hot plasma generated by the stellar wind from the O6.5 star θ^1 Ori C (Güdel et al. 2008) as envisioned by Weaver et al. (1977). The data also revealed bubbles of neutral gas expanding at a slower pace around the B1 stars powering the H II regions M43 and NGC 1977 (Pabst et al. 2020). In this case, expansion is driven by the overpressure of the ionized gas, a so-called Spitzer expansion. While these studies focused on the kinematics of the region and the mechanical feedback by massive stars, this data also allows an in depth study of the radiative interaction of massive stars with neutral atomic gas on unprecedented spatial scales.

In Paper I, we used the C+SQUAD results to study the global characteristics of the [C II] emission in Orion as a template to understand the use of the [C II] emission as a SFR indicator and to investigate the [C II] deficit. In this paper, we separate the surveyed region in its spatial components, compare the observations with specific PDR models, and examine the radiative interaction of the powering stars with their environment in detail. This paper is organized as follows: In Section 2, we will summarize the observations used in this study. Section 3 discusses the global morphology of the [C II] line emission and presents the correlations we find of the [C II] emission with other tracers of gas and dust in the Orion Nebula (M42), M43, and NGC 1977, separately. In Section 4, we compare the observations to PDR models, discuss the implications thereof, and examine the heating efficiency of the [C II]-emitting gas. We summarize our results in Section 5.

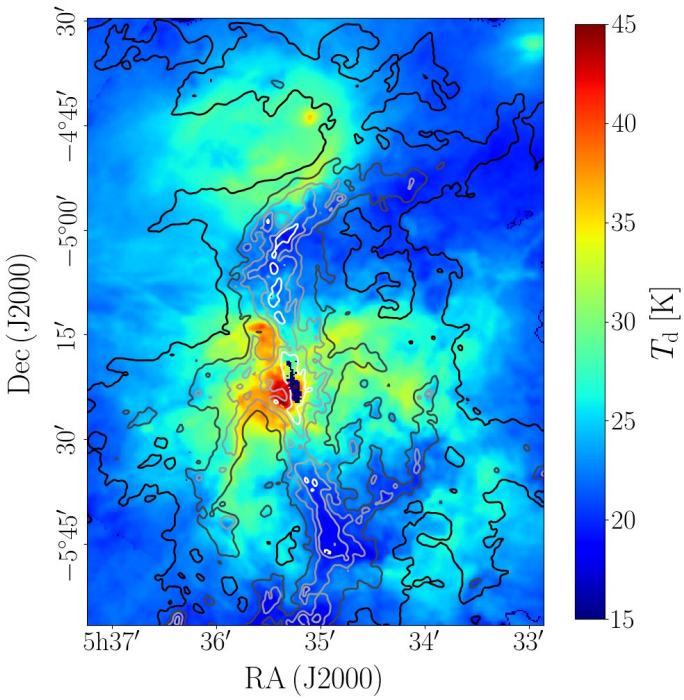

Figure 6.1: Dust temperature (color scale) and optical depth at 160 μm (contours, from black to white: 3×10^{-3}, 5×10^{-3}, 1×10^{-2}, 3×10^{-2}, 5×10^{-2}) from SED fit ($\beta = 2$).

6.2 Observations

We make use of velocity-resolved [C II] line observations towards Orion A, obtained by upGREAT onboard SOFIA, IRAM 30m velocity-resolved ^{12}CO $J = 2$-1 (230.5 GHz) and ^{13}CO $J = 2$-1 (220.4 GHz) line observations (see Berné et al. 2014; Goicoechea et al. 2020), *Herschel* dust continuum photometry, and *Spitzer* observations in the Infrared Array Camera (IRAC) 8 μm band. The observations are described in Paper I. We convolve all images to the same angular resolution of 36″ with a pixel size of 14″. In the analysis of the [C II] data we include only points above the 3σ threshold, that is $I_{[\mathrm{C\,II}]} > 5 \times 10^{-5}\,\mathrm{erg\,s^{-1}\,cm^{-2}\,sr^{-1}}$.

From the dust continuum photometry, we determine the dust effective temperature and the dust optical depth by fitting a modified blackbody with dust emissivity index $\beta = 2$,

$$I_\lambda = B(\lambda, T_\mathrm{d}) \left[1 - \exp\left(-\tau_{160} \left(\frac{160\,\mu\mathrm{m}}{\lambda}\right)^\beta\right)\right], \tag{6.1}$$

to the PACS 70 μm, 100 μm, and 160 μm bands, and the SPIRE 250 μm, 350 μm, and 500 μm bands (cf. Paper I and Pabst et al. (2019) for details). Where the coverage of the PACS 100 μm band is not sufficient, we complete the SED output maps with an SED fit of the remaining five PACS and SPIRE bands, which we use for illustrative purposes only. The dust temperature in the five-band fit is slightly higher than in the six-band fit (by about 0.3-0.5 K), and the dust optical depth is somewhat lower, but negligibly so. The differences are largest in the low-intensity regions. The brightest

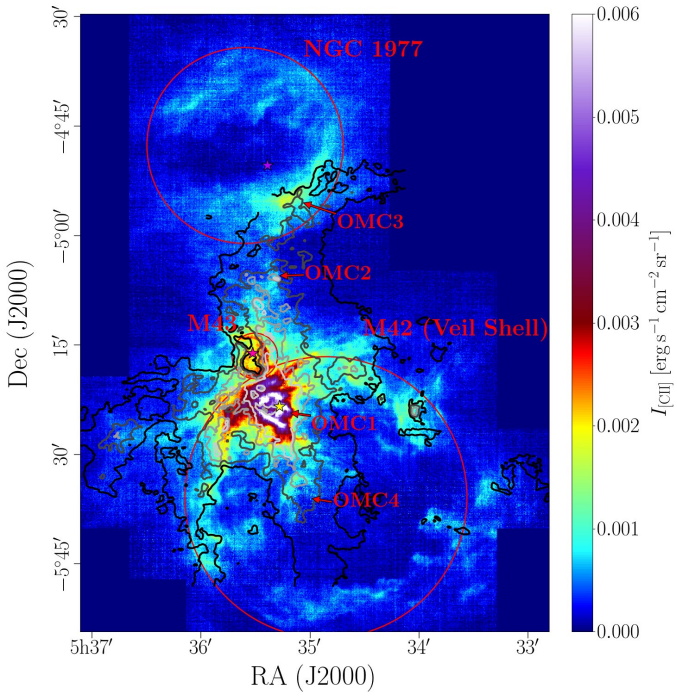

Figure 6.2: [C II] line-integrated intensity ($v_{\mathrm{LSR}} = -10\text{-}20\,\mathrm{km\,s^{-1}}$) from Orion A at its native resolution with CO(2-1) line-integrated intensity ($v_{\mathrm{LSR}} = -10\text{-}20\,\mathrm{km\,s^{-1}}$, coverage not complete, cf. Paper I) in contours (from black to light grey: $1, 2, 3, 4 \times 10^{-6}\,\mathrm{erg\,s^{-1}\,cm^{-2}\,sr^{-1}}$). The red circles delineate the three distinct shells of M42, M43, and NGC 1977. The stars indicate the most massive stars within each region: θ^1 Ori C (yellow) in M42, NU Ori (pink) in M43, and 42 Orionis (purple) in NGC 1977. Arrows indicate the positions of the four molecular cores OMC1-4 along the Integral-Shaped Filament.

regions in the BN/KL region and Orion S, the star-forming cores close to the massive Trapezium stars, are saturated in the *Herschel* images and hence excluded from our analysis.

Figure 6.1 shows the dust temperature and dust optical depth resulting from the SED fits ($\beta = 2$). The dust optical depth and dust temperature depend sensitively on the exact value of β. In Appendix 6.A and 6.B we compare the SED fits used here with the SED fits of Lombardi et al. (2014), who employ $\beta \simeq 1.6$, and to SED fits, where we let β be a free parameter. The general behavior of the correlations identified in this study is not affected.

6.3 Analysis

6.3.1 Global morphology and channel maps

Figure 6.2 shows the line-integrated [C II] intensity from the Orion Nebula complex in the Orion A molecular cloud. The mapped area comprises three distinct regions: M42, M43, and NGC 1977. The most massive stars in the Orion Nebula complex, the Trapezium stars, are found close to the surface of OMC1. The heavily irradiated

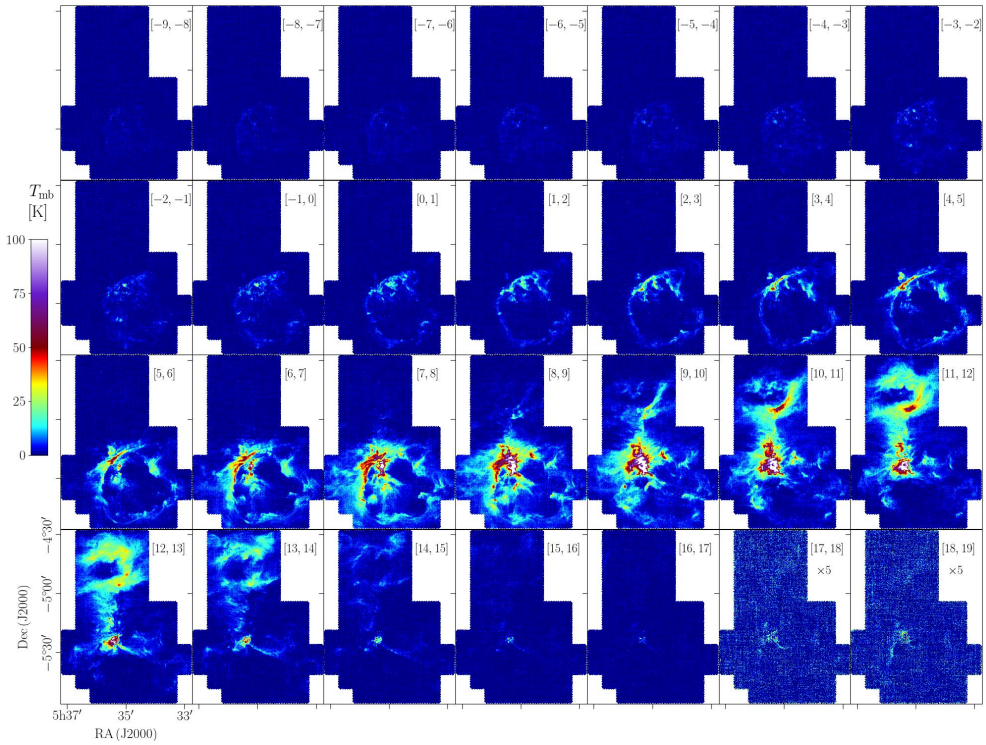

Figure 6.3: [C II] intensity per 1 km s^{-1} channel in the range $v_{\rm LSR}$ = −9 - 19 km s^{-1}. The intensities in the last two channels ($v_{\rm LSR}$ = 17-19 km s^{-1}) contain [^{13}C II] F = 2-1 emission and are are multiplied by 5.

PDR at the surface of the molecular cloud radiates bright [C II] emission. Also the Veil Shell, the expanding shell that is created by the stellar wind of the O7V star θ^1 Ori C (the most massive of the Trapezium stars), is readily observed in [C II] emission. The H II region of M43 is encircled by a [C II]-emitting shell, as well. In the background of the B0.5V star NU Ori, M43 is bounded by the molecular cloud with a [C II]-emitting PDR at its surface. The shell surrounding the H II regions NGC 1973, 1975, and 1977 also emits substantially in the [C II] line. The brightest part associated with NGC 1977 and irradiated by the B1V star 42 Orionis, however, is the PDR at the surface of the molecular core OMC3. The three shells associated with M42, M43, and NGC 1977 are subject to ongoing dynamical evolution due to over-pressurized hot plasma (M42) and ionized gas (M43 and NGC 1977) created by the central stars (Pabst et al. 2019, 2020).

Figure 6.3 shows the [C II] intensity of the Orion Nebula complex per 1 km s^{-1} channel in the range $v_{\rm LSR}$ = −9-19 km s^{-1}. Channel maps of velocity-resolved observations allow to disentangle spatially distinct structures within the line of sight and thus to obtain insight into the global morphology of a region. We can distinguish several components: For $v_{\rm LSR} < -2$ km s^{-1}, we observe [C II] emission that fills the space within the shell filaments of the Orion Nebula. This emission is associated with the expanding Veil Shell, that is moving towards us (Pabst et al. 2019). The edge-on shell filaments form a coherent structure and are most distinctly visible in the velocity range $v_{\rm LSR}$ = 0-9 km s^{-1}. In the $v_{\rm LSR}$ = 8-12 km s^{-1} range, the bright OMC1/Huygens

Region reveals its structure, studied in detail by Goicoechea et al. (2015b). M43 also becomes apparent in this velocity range. In $v_{\rm LSR}$ = 12-15 km s^{-1}, a structure that seems to be an extension of the Orion Bar becomes visible, that was also noted in optical observations (Henney et al. 2007). Emission contributed by the [^{13}C II] F = 2-1 hyperfine component[1] can be discerned in the last two channels, $v_{\rm LSR}$ = 17-19 km s^{-1}, towards the brightest part of the map, that is OMC1 and the bright eastern arm of the Veil Shell, the Eastern Rim. The northern part of the map with NGC 1973, 1975, and 1977, is visible in the range $v_{\rm LSR}$ = 10-14 km s^{-1}, offset by $\sim$ 2 km s^{-1} from the emission peak of the OMC1 region. Many small-scale structures also possess distinct dynamic morphology, that can be observed in the channel maps, but this is outside the scope of this study.

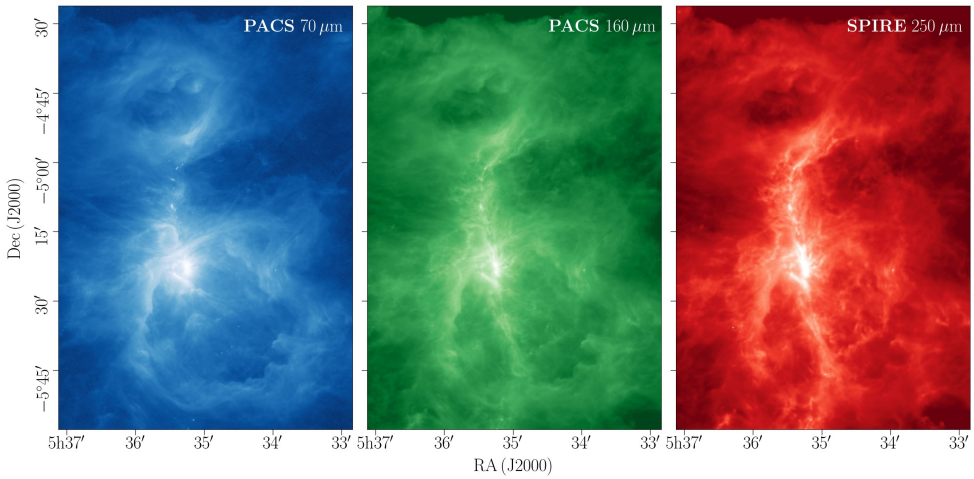

Figure 6.4: PACS 70 μm, PACS 160 μm and SPIRE 250 μm bands in their respective native resolutions.

Figure 6.4 shows the PACS 70 μm, PACS 160 μm and SPIRE 250 μm photometric images. We observe that colder structures become more prominent in wavelengths longwards of 160 μm. At sub-millimeter wavelengths, the dust emission is dominated by the the so-called integral-shaped filament (ISF, Johnstone & Bally 1999). The ISF is a cold and dense structure that runs through the entire Orion Nebula complex and has fragmented into molecular cores, OMC1, 2, 3, and 4, that are sites of active star formation.

On large scales ($\sim$ 25 pc) along the Orion molecular cloud, a global north-south velocity gradient was determined from observations of the molecular gas (Bally et al. 1987). In the region observed in [C II], we cannot distinguish a significant global velocity gradient. Rather, the velocity gradient is dominated by the separation of structures that move at distinct velocities, the M42 Veil Shell in the south and the northern bubble of NGC 1977. The local velocity gradient between OMC1 and OMC3

[1]The [^{13}C II] line splits into three hyperfine components (the frequency of the [^{12}C II] line is 1900.537 GHz and Δv is given with respect to this frequency):

component	ν [GHz]	Δv [km s^{-1}]	rel. intensity
F = 1-0	1900.950	-65.2	0.250
F = 2-1	1900.466	+11.2	0.625
F = 1-1	1900.136	+63.3	0.125

is also observed in molecular observations of Hacar et al. (2017). This abrupt velocity change, as noted by Bally et al. (1987), is larger than the global velocity gradient ($\sim 0.5\,\mathrm{km\,s^{-1}\,pc^{-1}}$) from molecular observations would suggest.

In Paper I, we have discussed the global correlations. In this paper, we will study the correlations in more detail by dividing them into the subregions described in Section 6.3.2. Figure 3 of Paper I shows the correlation plots disregarding individual (sub)regions, including all areas that fall outside of the later-defined regions, as point-density plots. Table 1 of Paper I summarizes the power-law fits we find for each correlation, using the ordinary least-squares (OLS) bisector method (Isobe et al. 1990).

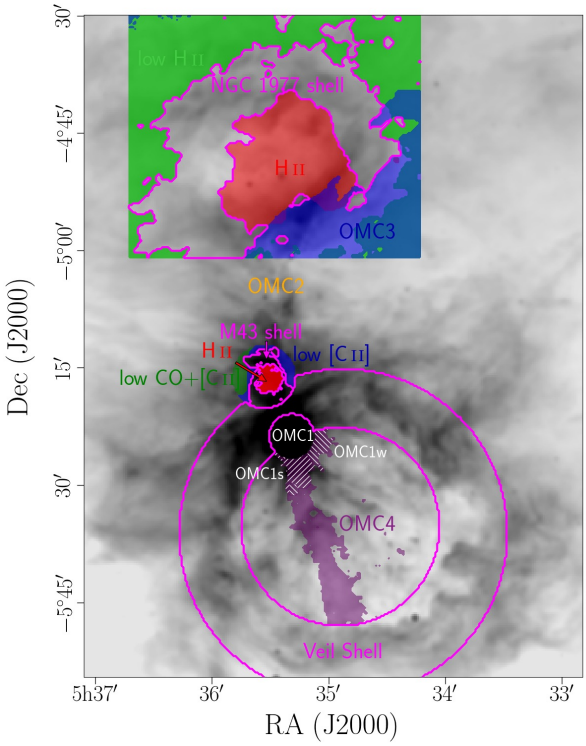

Figure 6.5: Regions in correlations plots discussed in Sections 6.3.4 to 6.3.9 on IRAC 8 μm emission convolved to an angular resolution of 36″.

6.3.2 Definition of regions

Because some of the spread in the correlation plots may stem from differences in the characteristics of the sources and their individual components, we have subdivided the survey area into four regions, that are further subdivided by their emission components. Figure 6.5 gives an overview of the regions we define in order to study the correlations in the following plot in greater detail. We have divided the Orion Nebula into two regions, the region that is viewed edge on, which comprises the Eastern Rim, the edge-on Veil Shell and the rim separating M42 from M43, and the region that presumably has face-on geometry, that is the surface of the ISF in the region of OMC4. We have defined the latter as regions situated inside the Veil Shell with $\tau_{160} > 8 \times 10^{-3}$, which includes areas close to OMC1 (purple hatched areas in Fig.

6.5). Those latter areas are defined by $I_{\rm FIR} > 2 \times 10^{-1}\,{\rm erg\,s^{-1}\,cm^{-2}\,sr^{-1}}$ and are divided into two subregions, OMC1s in the south and OMC1w in the west of OMC1, according to their behavior in the [C II]-FIR correlation (Fig. 6.9). Points in OMC1s lie above the regression curve computed from all OMC4 points, points in OMC1w lie below this average regression curve. We encircle the points in OMC1w with black circles. In the panels showing the OMC4 correlation, we include the points lying inside the OMC1 region in grey scale.

We have divided M43 into four subregions: The interior H II region with the molecular background and foreground expanding shell ($I_{\rm H\alpha} > 4 \times 10^3\,{\rm MJy\,sr^{-1}}$), the bright rim around it, that is the shell, a region where [C II] emission is faint ($I_{\rm [C\,II]} < 1.4 \times 10^{-3}\,{\rm erg\,s^{-1}\,cm^{-2}\,sr^{-1}}$) but CO(2-1) emission is still bright ($I_{\rm CO(2\text{-}1)} > 1.5 \times 10^{-6}\,{\rm erg\,s^{-1}\,cm^{-2}\,sr^{-1}}$), and a region where both [C II] and CO(2-1) emission are faint.

NGC 1977 is divided into four subregions, as well: The H II region with the expanding shell ($I_{\rm H\alpha} > 150\,{\rm MJy\,sr^{-1}}$), the shell surrounding it, the region of OMC3, defined by $\tau_{160} > 6 \times 10^{-3}$ and $I_{\rm CO(2\text{-}1)}/I_{\rm FIR} > 3 \times 10^{-5}$, and the outward areas with faint Hα emission ($I_{\rm H\alpha} < 90\,{\rm MJy\,sr^{-1}}$).

6.3.3 Edge-on PDR models

We complement the correlations of the [C II] emission with gas and dust tracers in the following with new PDR model runs that are based on the models of Tielens & Hollenbach (1985) with updates of Wolfire et al. (2010) and Hollenbach et al. (2012). Pabst et al. (2017) describe the procedure by which the emission from an edge-on PDR of a given line-of-sight depth ($A_{\rm V,los}$) is computed from the output of a 1D face-on PDR model. Compared to those earlier models, we have updated the collisional excitation rates and chemical rates in the models. In particular, we adopt the [O I] collisional rates with H and H_2 from (Lique et al. 2018, (and F. Lique priv. comm.)). Updates to chemical rates are noted in Neufeld & Wolfire (2016). More recently, we updated the photorates to those from Heays et al. (2017) and adopted the exponential integral formalism for the depth dependence due to dust. Additional changes to the chemical rates include oxygen chemistry rates from Kovalenko et al. (2018) and Tran et al. (2018), and carbon chemistry rates from Dagdigian (2019). In order to compute synthetic line emission intensities we assume a Doppler line width of $\Delta v = 1.5\,{\rm km\,s^{-1}}$.

In Fig. 6.6, we present the results of the constant-density PDR models for incident FUV intensities of $G_0 = 100, 500,$ and 1000, appropriate for selected regions in the Orion Nebula, on a physical scale. The x-axes share the same range of visual extinction, $A_{\rm V}$ = 0-10 mag. We computed models for several FUV intensities, gas densities, and line-of-sight visual extinctions $A_{\rm V,los}$ appropriate for different regions in the Orion Nebula, M43 and NGC 1977 (cf. Section 6.4.1). The three models in Fig. 6.6 qualitatively produce similar results: A warm surface gas layer cools through the [C II] and [O I] lines. The FIR dust emission also peaks at the surface. The colder gas deeper in the cloud emits mainly in low-J CO lines. Deep in the cloud, CO and water molecules freeze out, while cosmic ray ionization enhances the abundance of atomic carbon. The line-of-sight depth of the cloud slightly affects the ratios of FIR, [C II]-, and CO-line intensities. The [O I] 145 μm intensity is significantly increased compared to face-on models, while [O I] 63 μm is optically thick in both geometries. For higher radiation field and density, the contribution of the [O I] lines to the cooling overtakes that of the [C II] line.

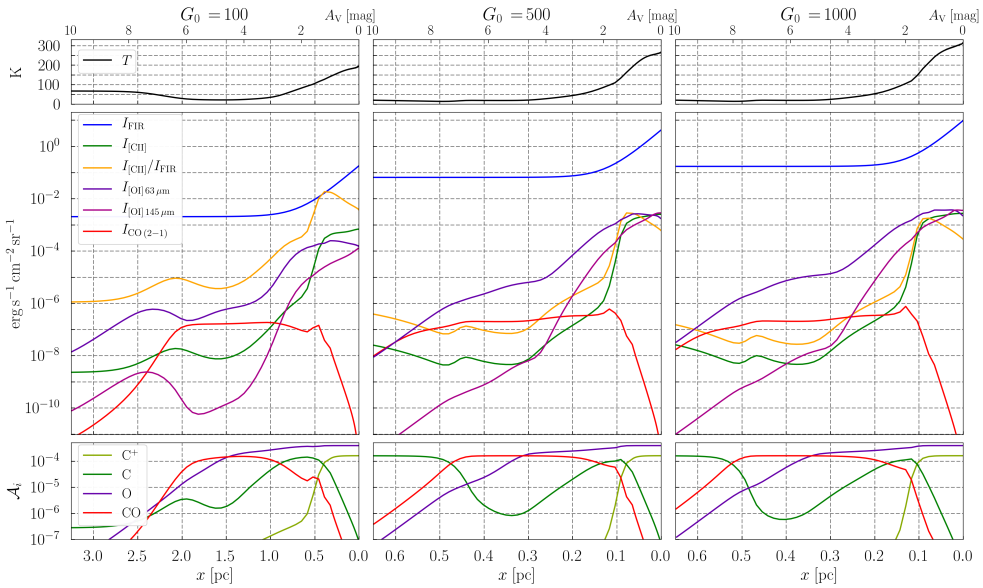

Figure 6.6: Results of our edge-on models described in Section 6.3.3 for incident FUV intensities of $G_0 = 100,\ 500,$ and 1000 on physical scale, illuminated from the right. The panels show the gas temperature T (upper panels), $I_{\rm FIR}$, $I_{\rm [C\,II]}$, $I_{\rm [C\,II]}/I_{\rm FIR,}$, $I_{\rm [O\,I]\,63\,\mu m}$, $I_{\rm [O\,I]\,145\,\mu m}$, and $I_{\rm CO\,(2\text{-}1)}$ (middle panels) and C^+, C, O, and CO fractional abundances (lower panels) versus physical scale. The gas densities are $n_{\rm H} = 2.0\times10^3\,{\rm cm}^{-3},\ 1.0\times10^4\,{\rm cm}^{-3},\ 1.0\times10^4\,{\rm cm}^{-3}$ (left to right panels), and the respective line-of-sight depths are $A_{\rm V,los} = 3, 10, 10$.

6.3.4 FIR versus distance

Figure 6.7 shows the dependence of the FIR intensity on distance from the respective central star in M42, M43 and NGC 1977. The FIR intensity scales with the incident FUV radiation field. However, geometry and line-of-sight effects are important. While, in principle, the incident radiation field can be estimated from the stellar luminosity and the (true) distance from the illuminating source, oftentimes only the projected distance is known.

We find that both in the limb-brightened edge of the Veil Shell and in OMC4 at $d < 1$ pc the FIR intensity scales with d^{-2} approximately. The incident radiation field at a distance of 1 pc is $G_0 \sim 500$, derived from the presumed face-on geometry of the ISF in the OMC4 region using $G_0 \simeq I_{\rm FIR}/2/1.3\times10^{-4}\,{\rm erg\,s^{-1}\,cm^{-2}\,sr^{-1}}$ (Hollenbach & Tielens 1999). This is a third of the value derived from the total FIR luminosity from the Orion Nebula (cf. Paper I) and reflects the geometry of the region. In fact, this discrepancy corresponds to an angle of 70° between the incident radiation and the surface normal. At $d > 1$ pc, the FIR intensity in OMC4 scales with an exponent somewhat smaller than 2. This region is characterized by large columns of cold dust that produce a FIR excess (cf. Paper I).

In M43 and NGC 1977, we do not find a strong dependence of the FIR intensity on distance. We attribute this to the geometry of these regions. M43 is a half-spherical shell situated in front of a dense background cloud close to the ISF. NGC 1977 is an expanding H II region (Pabst et al. 2020), whose limb-brightened shell is readily observed in surface tracers. Considering only points in the NGC 1977 shell with

Table 6.1: Summary of FIR-distance correlation in Fig. 6.7.

Region	a	b	ρ	rms [dex]
Veil Shell	0.32 ± 0.07	-2.08 ± 0.31	-0.94	0.19
OMC4	0.17 ± 0.04	-1.65 ± 0.27	-0.88	0.19
M43	–	–	-0.41	0.27
NGC 1977	0.07 ± 0.05	-2.04 ± 1.3	-0.68	0.13

Notes. $I_{\rm FIR} = a(d/1\,{\rm pc})^b$. In NGC 1977 fit only for $d > 1.5\,$pc. ρ is the Pearson correlation coefficient, rms is the root-mean-square of the residual of the least-squares fit.

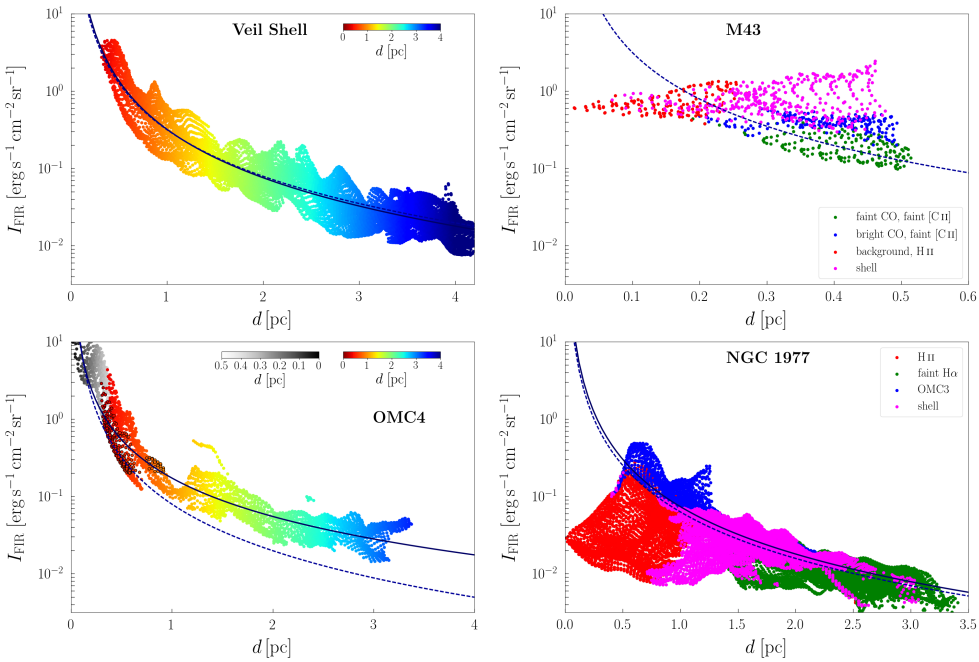

Figure 6.7: FIR intensity versus (projected) distance from respective central stars in M42 (top left: Veil Shell, bottom left: OMC4), M43 (top right) and NGC 1977 (bottom right). The division of M43 and NGC 1977 into the regions given in the legend is described in Section 6.3.2. The blue solid lines are the fits summarized in Table 6.1. The blue dashed lines indicate a FIR intensity scaling with d^{-2}.

$d > 1.5$ pc, the FIR intensity drops with d^{-2} approximately. However, this fit also describes points with $d < 1.5$ pc to a certain extent.

In summary, we observe geometric dilution of the radiation field in M42, but not in M43 and in NGC 1977 only partly. Table 6.1 summarizes the FIR-distance correlations discussed above. The Veil Shell and OMC4 exhibit a strong correlation, measured by the correlation coefficient ρ, while this is less pronounced in M43 and NGC 1977. The spread in the correlations is non-negligible, with 0.19 dex in the Orion Nebula being the smallest ($\rho = -0.69$, $rms = 0.44$ dex for the entire of NGC 1977). The scatter around the fits can be due to geometry effects and the deviation of the real distance from the projected distance.

The intensity of the incident radiation field, G_0 in Habing units, can be expressed as

$$G_0 \simeq 200\chi \frac{L_\star}{1 \times 10^4\, L_\odot} \left(\frac{1\,\mathrm{pc}}{d}\right)^2, \tag{6.2}$$

where $\chi = L_{\mathrm{FUV}}/L_\star$. For early B stars and late O stars ($T_{\mathrm{eff}} \simeq 2.5\text{-}4.0 \times 10^4$ K), $\chi \simeq 0.5$. We estimate the central star's luminosity assuming it is re-radiated in dust continuum emission. In M42, we have $L_{\mathrm{FIR}} \simeq 1.5 \times 10^5\, L_\odot$, hence theory predicts $G_0 \simeq 1.5 \times 10^3 (1\,\mathrm{pc}/d)^2$. From the decline of the FIR intensity in OMC4, we estimate $G_0 \simeq 500 (1\,\mathrm{pc}/d)^2$. As we have shown in Paper I, also from the edge-on PDR in the Eastern Rim we estimate $G_0 \simeq 500 (1\,\mathrm{pc}/d)^2$. This discrepancy is likely caused by the geometry of the Orion Nebula.

In M43, we obtain $L_{\mathrm{FIR}} \simeq 1.4 \times 10^4\, L_\odot$, hence we expect $G_0 \simeq 1.0\text{-}1.5 \times 10^3$ in the shell at $d \simeq 0.3\text{-}0.4$ pc from NU Ori. In NCG 1977, $L_{\mathrm{FIR}} \simeq 1.8 \times 10^4\, L_\odot$. For OMC3 at a distance of $d \simeq 0.4$ pc from 42 Orionis, we compute $G_0 \simeq 1.1 \times 10^3$. In the shell at a distance of $d \simeq 1.0\text{-}1.5$ pc, we estimate $G_0 \simeq 100\text{-}300$.

6.3.5 [C II] versus 70 μm

In all four regions, the [C II] intensity is tightly correlated with the intensity of the 70 μm dust continuum emission. Table 6.2 summarizes the [C II]-70 μm correlations in the four regions shown in Fig. 6.8. As observed in Paper I, the correlations exhibit two regimes, with decreasing slope from low to high 70 μm intensity. We fit and discuss only the regime with $I_{70\,\mu\mathrm{m}} > 5 \times 10^2\,\mathrm{MJy\,sr^{-1}}$, since the low-intensity regime is problematic because of calibration uncertainties in the PACS bands.

The [C II] intensity scales with the 70 μm intensity with a power of 0.57-0.60 (for $I_{70\,\mu\mathrm{m}} > 5 \times 10^2\,\mathrm{MJy\,sr^{-1}}$). Largest scatter about the regression curve (and the lowest correlation coefficient) is observed in NGC1977. Also, the spread is higher in OMC4 as compared to the Veil Shell. The [C II] intensity tends to turn off the regression curve towards lower values at the high-intensity end. As bright-emission regions tend to be optically thick in the [C II] line (while cooling mainly through the front side viewed edge-on), and [O I] 63 μm and 145 μm line cooling becomes significant, we expect less [C II] emission as compared to the intensity in the 70 μm band. In M43, the [C II]-70 μm correlation is very tight, but high-intensity points (towards the shell and the H II region/background cloud) again tend to follow a slightly shallower slope. The slopes of the low-intensity regimes ($I_{70\,\mu\mathrm{m}} < 5 \times 10^2\,\mathrm{MJy\,sr^{-1}}$) are very similar and agree within the error margins (1.12-1.33), but the standard errors of the fit parameters are very large and the correlation coefficients low ($\rho = 0.6\text{-}0.7$).

Table 6.2: Summary of [C II]-70 μm correlation in Fig. 6.8.

Region	a	b	ρ	rms [dex]
Veil Shell	0.57 ± 0.23	-5.07 ± 0.76	0.94	0.10
OMC4	0.60 ± 0.17	-5.27 ± 0.61	0.91	0.13
M43	0.60 ± 0.19	-5.24 ± 0.77	0.94	0.06
NGC 1977	0.60 ± 0.62	-5.10 ± 1.86	0.77	0.10

Notes. $\log_{10} I_{[\mathrm{C\,II}]} = a \log_{10} I_{70\,\mu\mathrm{m}} + b$. Fit for $I_{70\,\mu\mathrm{m}} > 5 \times 10^2\,\mathrm{MJy\,sr^{-1}}$. ρ is the Pearson correlation coefficient, rms is the root-mean-square of the residual of the least-squares fit.

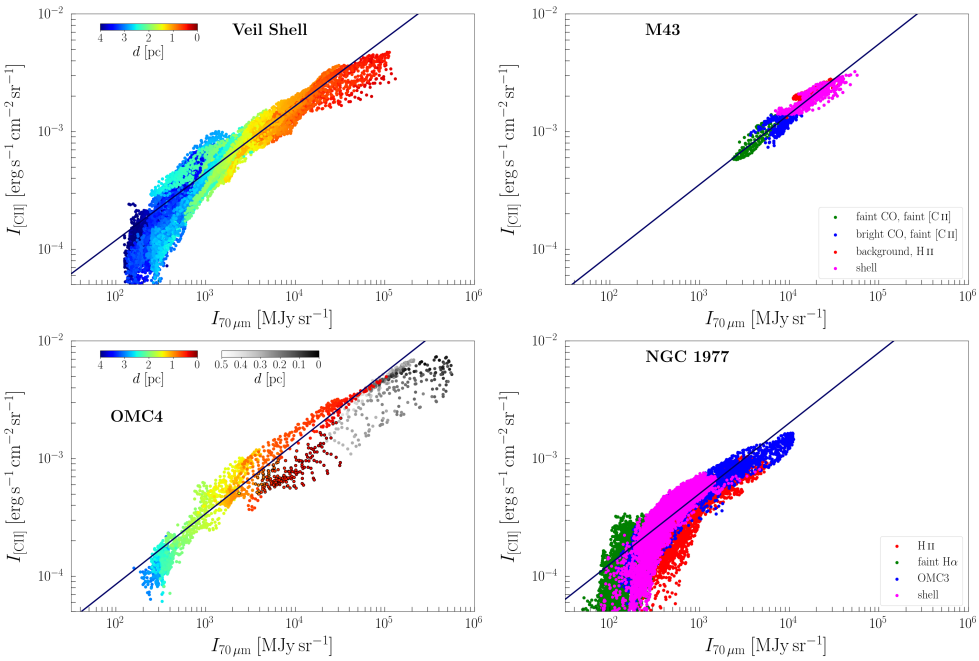

Figure 6.8: [C II] intensity versus PACS 70 μm intensity in M42 (top left: Veil Shell, bottom left: OMC4 with OMC1 (in grey scale; black-edged red points lie to the west of Orion S)), M43 (top right) and NGC 1977 (bottom right). The color scale in M42 indicates the distance from θ^1 Ori C. The division of M43 and NGC 1977 into the regions given in the legend is described in Section 6.3.2. The blue solid lines are the fits summarized in Table 6.2.

6.3.6 [C II] versus FIR

In all four regions, the [C II] intensity is tightly correlated with the FIR intensity[2]. Table 6.3 summarizes the [C II]-FIR correlation in the four regions shown in Fig. 6.9. Like the [C II]-70 μm correlation, the [C II]-FIR correlation exhibits two regimes, but we fit only the regime with $I_{\rm FIR} > 3 \times 10^{-2}\,{\rm erg\,s^{-1}\,cm^{-2}\,sr^{-1}}$.

The [C II] intensity depends less than linear on the FIR intensity, the exponent lying in the range 0.53-0.88 (for $I_{\rm FIR} > 3 \times 10^{-2}\,{\rm erg\,s^{-1}\,cm^{-2}\,sr^{-1}}$). The correlation coefficient in M42 and M43 is larger than 0.9, in NGC 1977 it is significantly lower (0.79). Most scatter about the regression curve is observed in OMC4, which also possesses a larger slope. Also the bright-CO and faint-[C II] regions in M43, lying close to the spine of the ISF, deviate from the regression curve, which might be due to the FIR emission stemming from the colder molecular background. The same is true for OMC3, as part of the ISF. As the FIR intensity is dominated by the PACS 70 μm band, the [C II]-FIR correlation is very similar to the [C II]-70 μm correlation. The low-intensity regime ($I_{\rm FIR} < 3 \times 10^{-2}\,{\rm erg\,s^{-1}\,cm^{-2}\,sr^{-1}}$) is again fitted with exponents larger than unity, but with large standard errors of the fit parameters and lower correlation coefficients ($\rho \simeq 0.8$).

The points in the cavity to the west of the molecular ridge of Orion S/BN-KL, that is in OMC1w, lie below the average regression of the OMC4 correlation. This region is just to the north of the extension of the Orion Bar and is characterized by a higher [C II] centroid velocity as compared to the average molecular background velocity. This region is subject to large-scale shocks identified by Henney et al. (2007). The dust temperature in OMC1w is somewhat lower than in the region to the southeast of the Orion Bar. The dust optical depth at 160 μm lies between 8×10^{-3} and 1×10^{-2}. Thus, although this region is associated with OMC1, it is included in our OMC4 correlation. Points in the region south of OMC1 and north of OMC4, OMC1s, are also included in the OMC4 correlation. Those points have higher [C II] intensity at the same FIR intensity as points in OMC1w.

[2]Again, we exclude the very bright (in FIR emission) regions of the BN/KL and Orion S cores, that are saturated in our SEDs.

Table 6.3: Summary of [C II]-FIR correlation in Fig. 6.9.

Region	a	b	ρ	rms [dex]
Veil Shell	0.60 ± 0.27	-2.56 ± 0.26	0.94	0.09
OMC4	0.88 ± 0.33	-2.59 ± 0.29	0.92	0.17
M43	0.61 ± 0.21	-2.63 ± 0.06	0.92	0.07
NGC 1977	0.53 ± 0.39	-2.62 ± 0.48	0.79	0.08

Notes. $\log_{10} I_{[\mathrm{C\,II}]} = a \log_{10} I_{\mathrm{FIR}} + b$. Fit for $I_{\mathrm{FIR}} > 3 \times 10^{-2}\,\mathrm{erg\,s^{-1}\,cm^{-2}\,sr^{-1}}$. ρ is the Pearson correlation coefficient, rms is the root-mean-square of the residual of the least-squares fit.

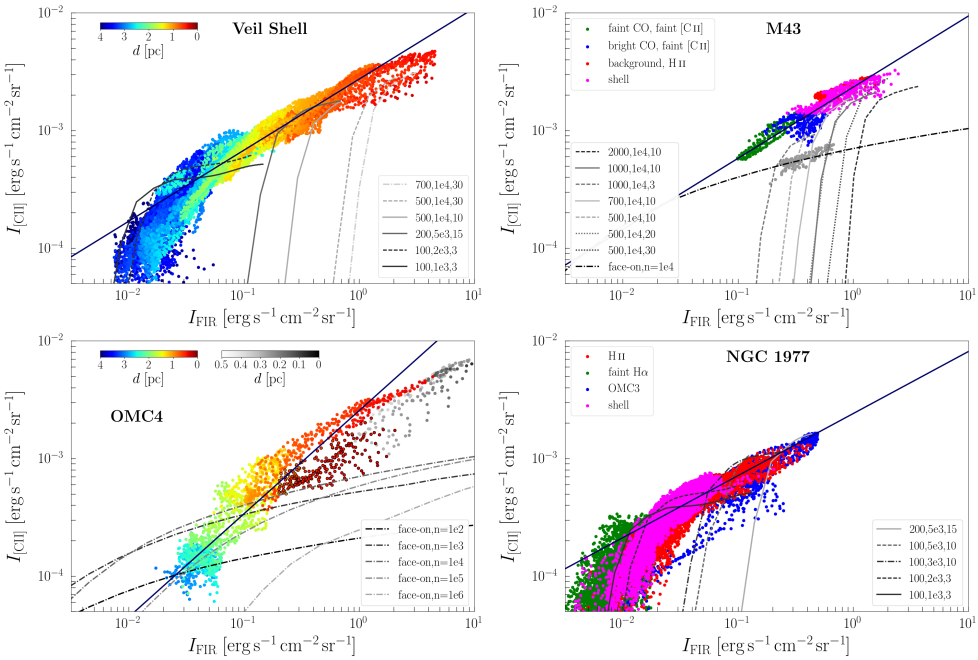

Figure 6.9: [C II] intensity versus FIR intensity in M42 (top left: Veil Shell, bottom left: OMC4 with OMC1 (in grey scale; black-edged red points lie to the west of Orion S)), M43 (top right) and NGC 1977 (bottom right). The color scale in M42 indicates the distance from θ^1 Ori C. The division of M43 and NGC 1977 into the regions given in the legend is described in Section 6.3.2. The blue solid lines are the fits summarized in Table 6.3. Dashed lines are edge-on model outputs with the parameters (G_0, n, $A_{\mathrm{V,los}}$) given in the legend. Dashed dotted lines in the OMC4 and the M43 panels are face-on model outputs for the densities given in the legend. Grey points in M43 correspond to the estimated intensities of the background PDR towards the center of M43 (cf. Section 6.4.1).

6.3.7 [C II] versus 8 μm

The [C II] intensity is tightly correlated with the intensity in the IRAC 8 μm band. Table 6.4 summarizes the [C II]-8 μm correlation in the four regions shown in Fig. 6.10.

The overall [C II]-8 μm relation is similar in all four regions. The [C II] intensity depends less than linear on the 8 μm intensity, with an exponent of 0.56-0.87. The correlation coefficient for each region is larger than 0.9, and the scatter around the regression is usually small ($rms < 0.11$ dex). The [C II] intensity tends to turn off the regression curve towards lower values at the high-intensity end. In the correlation plot of OMC4, points in OMC1w have lower [C II] intensity at the same 8 μm intensity compared to points in OMC1s. Points within OMC1 continue the general [C II]-8 μm trend.

One difficulty in the interpretation of the correlation is the unknown additive offset in the IRAC 8 μm band. We estimated it at $2 \times 10^{-3}\,\mathrm{erg\,s^{-1}\,cm^{-2}\,sr^{-1}}$, but it might also be half as large. This does not affect the regression greatly if restrict ourselves to the high-intensity end. It will affect, however, the estimate of the [C II] intensity from the 8 μm intensity at low intensities.

The correlation of the [C II]/FIR ratio versus the 8 μm/FIR ratio is less tight, $\rho \simeq 0.7$. The [C II]/FIR ratio varies by two orders of magnitude, whereas the 8 μm/FIR ratio is less variable and varies only from 0.05 to 0.2 in the mapped regions. Higher values seem to be achieved with lower radiation field, but this relation is not very pronounced in OMC4 and M43. In both these regions, there is a significant contribution to the FIR emission form the somewhat colder dust in background molecular cloud. In general, the [C II]/FIR measures the heating efficiency, while the 8 μm/FIR ratio is a measure for the charge of the PAH molecules.

Table 6.4: Summary of [C II]-8 μm correlation in Fig. 6.10.

Region	a	b	ρ	rms [dex]
Veil Shell	0.67 ± 0.27	-1.74 ± 0.42	0.97	0.09
OMC4	0.56 ± 0.10	-1.96 ± 0.29	0.98	0.09
M43	0.68 ± 0.20	-1.85 ± 0.28	0.93	0.06
NGC 1977	0.87 ± 0.45	-1.31 ± 1.18	0.92	0.11

Notes. $\log_{10} I_{[\mathrm{C\,II}]} = a \log_{10} I_{8\,\mu\mathrm{m}} + b$. Fit for $I_{8\,\mu\mathrm{m}} > 3 \times 10^{-4}\,\mathrm{erg\,s^{-1}\,cm^{-2}\,sr^{-1}}$. ρ is the Pearson correlation coefficient, rms is the root-mean-square of the residual of the least-squares fit.

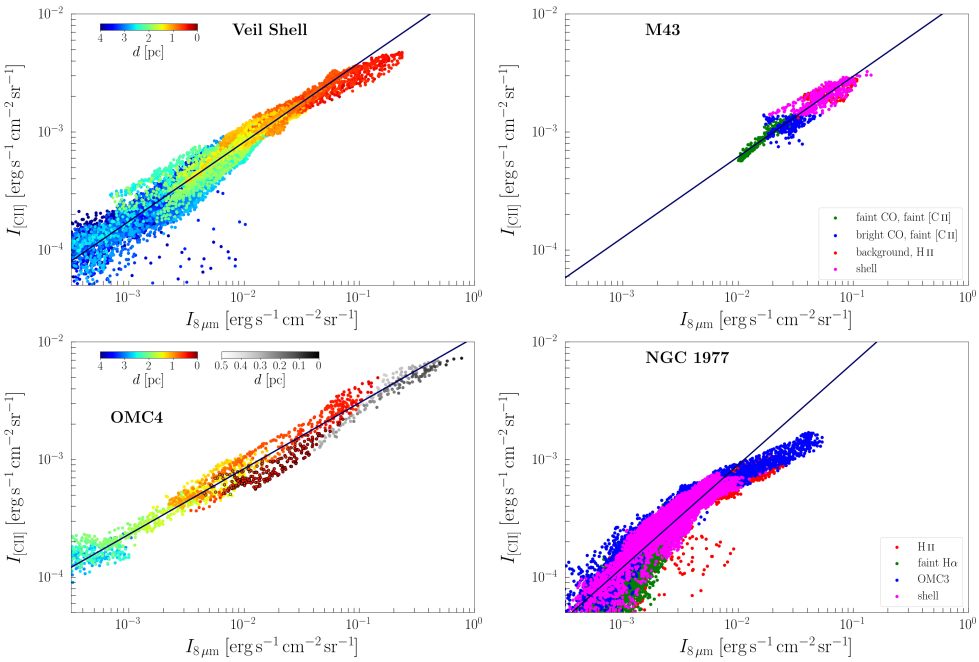

Figure 6.10: [C II] intensity versus IRAC 8 μm intensity in M42 (top left: Veil Shell, bottom left: OMC4 with OMC1 (in grey scale; black-edged red points lie to the west of Orion S)), M43 (top right) and NGC 1977 (bottom right). The color scale in M42 indicates the distance from θ^1 Ori C. The division of M43 and NGC 1977 into the regions given in the legend is described in Section 6.3.2. The blue solid lines are the fits summarized in Table 6.4.

6.3.8 FIR versus 8 μm

The FIR and 8 μm intensities are tightly correlated. Table 6.5 summarizes the FIR-8 μm correlations in the four regions shown in Fig. 6.11. We fit only the high-intensity regime ($I_{\rm FIR} > 3 \times 10^{-2}\,{\rm erg\,s^{-1}\,cm^{-2}\,sr^{-1}}$).

While both the [C II]-FIR and the [C II]-8 μm relations are far from linear, the 8 μm-FIR relation is approximately linear. The correlation coefficient is larger than 0.9 in M42 and M43, and 0.83 in NGC 1977. Scatter about the regression curve is significant, though, with 0.11-0.15 dex. In OMC4, the FIR-8 μm relation differs slightly from the relations found in the other regions, with a power-law exponent smaller than unity. Points in OMC1w have higher FIR intensity than others with the same 8 μm intensity. Points inside OMC1 continue the trend of those high-FIR points.

As the FIR measures the incident (FUV) radiation field, the good correlation between the 8 μm and FIR intensities implies that the PAH flux is proportional to the incident FUV field. Given that the IRAC 8 μm band measures the emission by PAH cations (Peeters et al. 2002), this implies that there is little variation in the PAH ionization balance within each of these regions and between the regions. Conversely, this implies that the observed 8 μm intensity is a good measure of the incident FUV field. Overall, we find that $I_{\rm FIR}/I_{8\,\mu{\rm m}} \simeq 10$. Towards higher radiation field ($G_0 \sim 10^3$) the ratio is somewhat increased $I_{\rm FIR}/I_{8\,\mu{\rm m}} \simeq 20$, decreasing down to $I_{\rm FIR}/I_{8\,\mu{\rm m}} \simeq 5$ at $G_0 \sim 100$ (in the southern Veil Shell). However, this behavior is less clear in regions where FIR emission from colder background dust is mixed within the line of sight, as in OMC4 and the center of M43.

Table 6.5: Summary of FIR-8 μm correlation in Fig. 6.11.

Region	a	b	ρ	rms [dex]
Veil Shell	1.06 ± 0.44	1.26 ± 0.92	0.95	0.14
OMC4	0.70 ± 0.24	0.84 ± 0.56	0.95	0.15
M43	1.08 ± 0.36	1.25 ± 0.51	0.92	0.11
NGC 1977	1.00 ± 0.50	1.00 ± 1.12	0.83	0.15

Notes. $\log_{10} I_{\rm FIR} = a \log_{10} I_{8\,\mu\rm m} + b$. Fit for $I_{\rm FIR} > 3 \times 10^{-2}\,{\rm erg\,s^{-1}\,cm^{-2}\,sr^{-1}}$. ρ is the Pearson correlation coefficient, rms is the root-mean-square of the residual of the least-squares fit.

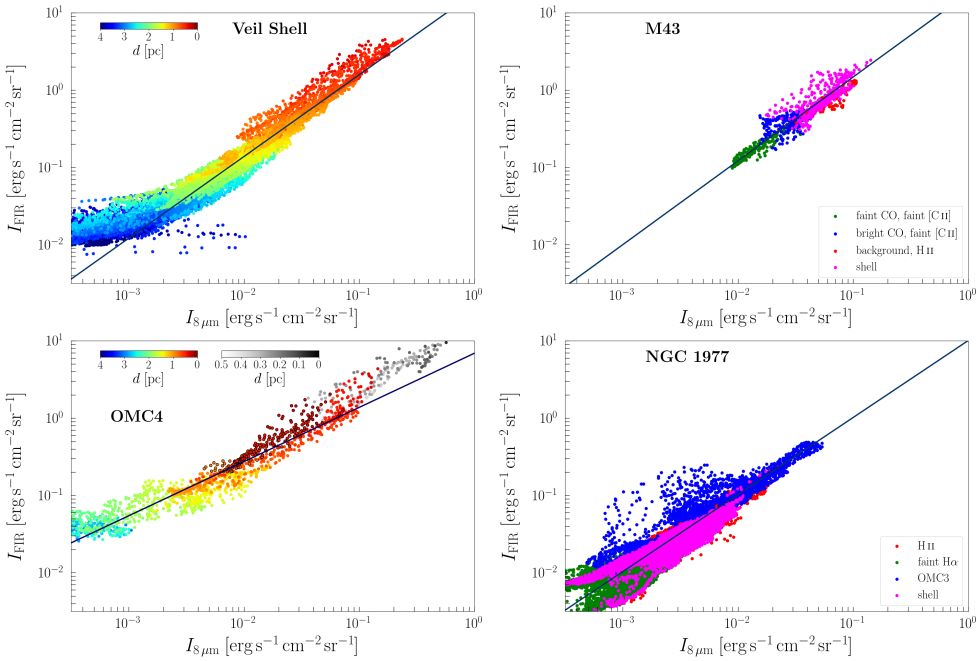

Figure 6.11: FIR intensity versus IRAC 8 μm in M42 (top left: Veil Shell, bottom left: OMC4 with OMC1 (in grey scale; black-edged red points lie to the west of Orion S)), M43 (top right) and NGC 1977 (bottom right). The color scale in M42 indicates the distance from θ^1 Ori C. The division of M43 and NGC 1977 into the regions given in the legend is described in Section 6.3.2. The blue solid lines are the fits summarized in Table 6.5.

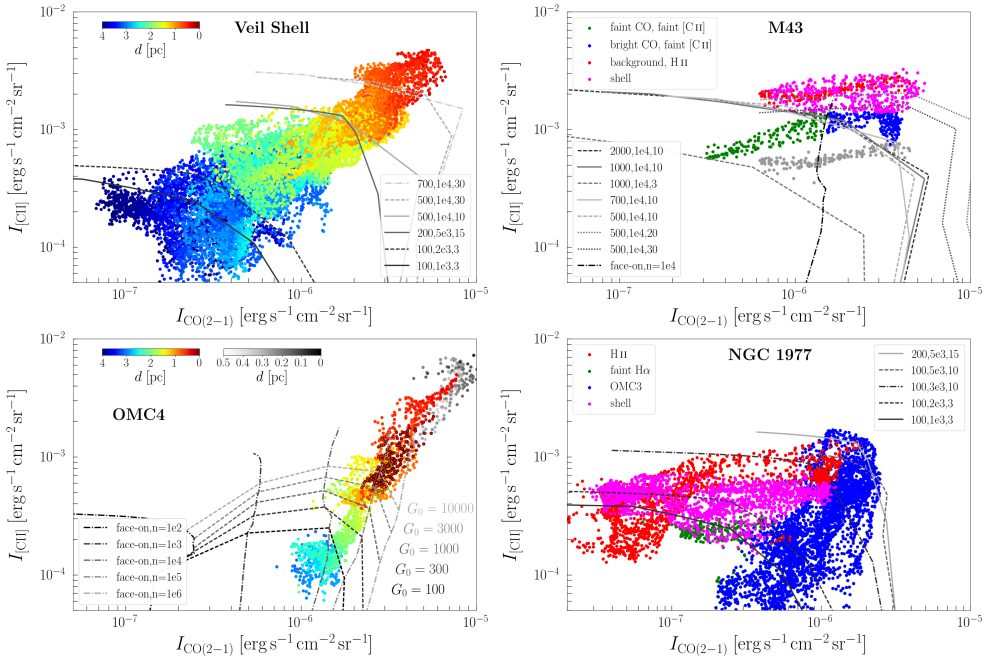

Figure 6.12: [C II] versus CO(2-1) intensity in M42 (top left: Veil Shell, bottom left: OMC4 with OMC1 (in grey scale; black-edged red points lie to the west of Orion S)), M43 (top right) and NGC 1977 (bottom right). The color scale in M42 indicates the distance from θ^1 Ori C. The division of M43 and NGC 1977 into the regions given in the legend is described in Section 6.3.2. Dashed lines are edge-on model outputs with the parameters (G_0, n, $A_{V,los}$) given in the legend. Dashed dotted lines in the OMC4 and the M43 panels are face-on model outputs for the densities given in the legend. Grey points in M43 correspond to the estimated intensities of the background PDR towards the center of M43.

6.3.9 [C II] versus CO(2-1)

Collectively, the [C II]-CO(2-1) correlations in Fig. 6.12 do not follow a clear trend. The correlation coefficient ρ is about 0.37 in M43 and 0.01 in NGC 1977. Only in OMC3, $\rho = 0.67$. Despite the fact that the Veil Shell is a PDR viewed edge-on and we expect a spatial offset between the [C II]- and the CO-emitting gas layers, [C II] and CO(2-1) intensities show a correlation, albeit with large scatter ($\rho = 0.79$). The Veil Shell itself is mostly CO-dark, however containing several CO-emitting globules (Goicoechea et al. 2020). CO emission is mostly stemming from the background molecular cloud and not the shell itself. Only in the Eastern Rim there is corresponding CO(2-1) emission at a slight spatial offset. Towards OMC4, [C II] and CO(2-1) intensities also exhibit a correlation, with less scatter than in the Veil shell ($\rho = 0.93$).

In the center of M43, CO(2-1) emission stems mainly from the molecular cloud behind the H II region, but has an additional broad, weak component of yet undetermined origin (Pabst et al. 2020). The [C II]-bright edge is also bright in CO(2-1), albeit with a slight spatial separation. The shell of NGC 1977 has nearly constant [C II] intensity, but the CO(2-1) varies by a factor of about 30. In contrast, the CO(2-1) intensity is towards the OMC3 region varies little, while [C II] varies by two orders of magnitude.

The [C II]/FIR-CO(2-1)/FIR correlations, shown in Fig. 6.13, exhibit somewhat different behavior than the [C II]-CO(2-1) correlations. The normalized intensities

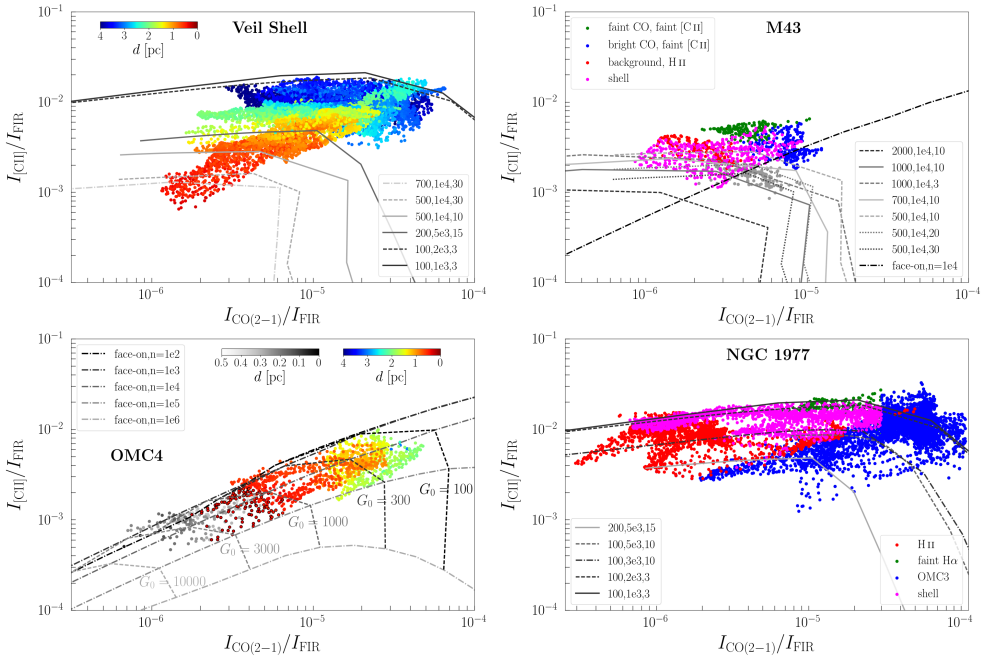

Figure 6.13: [C II]/FIR versus CO(2-1)/FIR in M42 (top left: Veil Shell, bottom left: OMC4 with OMC1 (in grey scale; black-edged red points lie to the west of Orion S)), M43 (top right) and NGC 1977 (bottom right). The color scale in M42 indicates the distance from θ^1 Ori C. The division of M43 and NGC 1977 into the regions given in the legend is described in Section 6.3.2. Dashed lines are edge-on model outputs with the parameters (G_0, n, $A_{\mathrm{V,los}}$) given in the legend. Dashed dotted lines in the OMC4 and the M43 panels are face-on model outputs for the densities given in the legend. Grey points in M43 correspond to the estimated intensities of the background PDR towards the center of M43.

are generally less correlated than the absolute intensities ($\rho = 0.53$ in the Veil Shell, $\rho = 0.77$ in OMC4, $\rho = 0.22$ in M43, but $\rho = 0.17$ in NGC 1977 and $\rho = 0.67$ in OMC3 only). If one were to fit regression curves to the data (both absolute and normalized intensities), no consistent picture would emerge, the exponents of the power laws differing widely. This is reflected in the global correlations discussed in Paper I.

6.3.10 Summary of the correlation studies

In summary, the correlations of the [C II] intensity with the 70 μm, FIR, and 8 μm intensity, respectively, are tight. The four regions, the M42 Veil Shell, OMC4, M43, and NGC 1977, behave in a similar manner, and the spread we observe is minor. The spread may be due to the dependency of the gas heating efficiency on the physical conditions and possibly subtle variations of the abundance of PAHs and VSGs through the regions. Most important to note is that the correlation of the [C II] intensity with each of the 70 μm, FIR, and 8 μm intensity is not linear, but scales with those intensities to a power of less than unity. The FIR-8 μm correlation deviates only slightly from linearity, whereas the correlation of the [C II] intensity with the CO(2-1) intensity requires a more in-depth study, which we will pursue in Section 4.

6.4 Discussion

6.4.1 Comparison of PDR models with observations

We estimated the input parameters of our PDR models, the gas density n, the incident radiation field G_0, and the line-of-sight depth $A_{\rm V,los}$, from the SED results and the [C II] and CO data. For the Eastern Rim of the Orion Nebula, Pabst et al. (2020) report a gas density, as estimated from the spatial separation of peak [C II] and CO(2-1) emission, of $n \simeq 1 \times 10^4\,{\rm cm}^{-3}$, while the density drops to $n \simeq 2 \times 10^3\,{\rm cm}^{-3}$ in the southern Veil Shell, estimated from the dust optical depth. In the rim of M43, Pabst et al. (2020) find $n \simeq 1 \times 10^4\,{\rm cm}^{-3}$ from the [C II] and CO peak separation, as well. In NGC 1977, the dust optical depth indicates a density of $n \simeq$ 2-5 $\times 10^3\,{\rm cm}^{-3}$. The radiation field in the Orion Nebula is estimated from the FIR-distance relation, that is $G_0 \simeq 500(1\,{\rm pc}/d)^2$ (cf. Fig 6.7). The FIR emission towards the molecular background of M43 suggests $G_0 \simeq 2000$. In case of NGC 1977 we used the stellar parameters of 42 Orionis to estimate the radiation field. In most of the shell, $G_0 \simeq$ 100-200, in concordance with Kim et al. (2016). The radiation field in OMC3 may be slightly higher, $G_0 \sim$ 400-1000; Howe et al. (1991) estimate $G_0 \simeq 360$.

The depth of the edge-on PDR along the line of sight was estimated from the dust optical depth. In the Eastern Rim, $\tau_{160} \simeq 1 \times 10^{-2}$, which corresponds to $A_{\rm V,los} \simeq 30$. In the southern part of the Eastern Rim, $\tau_{160} \simeq 5 \times 10^{-3}$, hence $A_{\rm V,los} \simeq 15$. In the Southern Shell, we find $\tau_{160} \simeq 1 \times 10^{-3}$, that is $A_{\rm V,los} \simeq 3$. In the east of the M43 shell, $\tau_{160} \simeq 1 \times 10^{-2}$, and in the western NGC 1977 shell $\tau_{160} \simeq 3 \times 10^{-3}$, that is $A_{\rm V,los} \simeq 10$. We produce PDR models for the parameters estimated here, but let them vary around those values. This way we are able to reject some combinations of input parameters. In the correlation plots, we plot the edge-on model outputs only for $x > 0.07\,{\rm pc}$, which corresponds to the spatial resolution ($36''$) of the data.

We observe that the edge-on PDR models with the estimated parameters generally match the observations very well. As suggested by the geometry of an edge-on shell, the models require a larger column density than face-on models would provide. Regions in the Veil Shell with $d < 1.0\,{\rm pc}$ tend to emit stronger in [C II] than accounted for by the models with $G_0 =$ 500-700, $n = 1 \times 10^4\,{\rm cm}^{-3}$, and $A_{\rm V,los} = 30$. In the region of OMC4 and the ISF in the background of the Orion Nebula, the deviation of the expected [C II] emission from face-on models from the observations is even larger. While the face-on PDR models do not exceed an intensity of $1 \times 10^{-3}\,{\rm erg\,s^{-1}\,cm^{-2}\,sr^{-1}}$, the observations emit as much as $4 \times 10^{-3}\,{\rm erg\,s^{-1}\,cm^{-2}\,sr^{-1}}$ outside the Huygens Region/OMC1 and up to $6 \times 10^{-3}\,{\rm erg\,s^{-1}\,cm^{-2}\,sr^{-1}}$ towards the background PDR in OMC1. Perhaps in OMC1 and OMC4, edge-on models would be more appropriate. In summary, the edge-on models agree well with the observations if we allow the edge-on column to vary between 3 and 30 times that of the face-on column.

The [C II] emission towards the center of M43 consists of three components: the blue-shifted expanding shell, the H II region, and the PDR on the surface of the background molecular cloud. According to the velocity profile in (Pabst et al. 2020, Fig. 21), only 30% of [C II] emission towards the center of M43 stem from the background cloud, with 65% arising in the H II region and 5% from the foreground shell. The grey points in Fig. 6.9c show to the emission from the background PDR, where we have assumed 50% of the FIR emission to stem from the background PDR. This emission from the M43 PDR background can be fitted by a face-on PDR model with $n \simeq 1 \times 10^4\,{\rm cm}^{-3}$.

The shell of M43 emits slightly more [C II] intensity than predicted by the edge-on

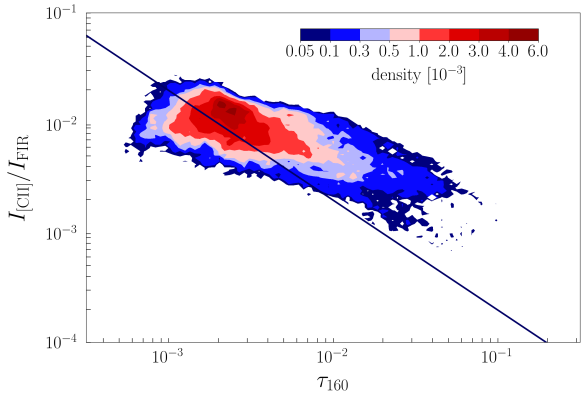

Figure 6.14: Correlation plot of [C II]/FIR with dust optical depth τ_{160}. The line indicates the inversely linear relation expected for a cloud slab of constant dust temperature (Goicoechea et al. 2015b), running through the median values of [C II]/FIR and τ_{160}.

models with $G_0 = 1000$, $n = 1 \times 10^4\,\mathrm{cm}^{-3}$, and $A_{\mathrm{V,los}} = 10$. A larger column, that is higher $A_{\mathrm{V,los}}$, mainly increases the FIR intensity, as the [C II] line is already optically thick. The [C II] may be matched by models with lower radiation field, but larger column, that is $G_0 = 500$ and $A_{\mathrm{V,los}} = 20$-30. The lower-G_0 models with higher $A_{\mathrm{V,los}}$ reproduce the [C II] versus CO(2-1) correlation in the shell more accurately.

The NGC 1977 shell seems to be characterized by $A_{\mathrm{V,los}} = 3$-10, while the PDR model output is less sensitive to the exact density and radiation field. Also the correlations of the [C II] intensity with CO(2-1) intensity in the shell can be described by edge-on models with $G_0 = 100$-200 and $n = 1$-$5 \times 10^3\,\mathrm{cm}^{-3}$. The PDR associated with OMC3 will be analyzed in more detail by Kabanovic et al. (in prep.).

The edge-on PDR models with the same parameter as in the [C II]-FIR correlation seem to be able to explain the [C II]/FIR-CO(2-1)/FIR correlation (Fig. 6.13) in the Veil Shell. However, the behavior of the [C II]-CO(2-1) correlation (Fig. 6.12) reflects the presence of uncorrelated emission, as we will discuss below. The points in OMC4 lie close to the face-on model with $n = 1 \times 10^4\,\mathrm{cm}^{-3}$ and varying radiation field ($G_0 \simeq 200$-2000). Points in OMC1 continue the trend towards lower CO(2-1)/FIR ratio, but seem to deviate towards lower-density models. The neutral gas density in OMC1 is expected to be higher, however, $n \simeq 1 \times 10^5\,\mathrm{cm}^{-3}$. Compared to uniform face-on models with adequate incident radiation field ($G_0 \simeq 2 \times 10^4$), OMC1 emits too much [C II] intensity. Invoking a clumpy PDR structure generally increases the amount of [C II] emission from the models (e.g., Cubick et al. 2008). For M43, all edge-on models produce similar [C II]/FIR ratios at similar CO(2-1)/FIR ratios, while the background PDR intensities scatter around the face-on model prediction, indicating either varying density or varying geometry. Points in NGC 1977 neatly follow the edge-on model predictions.

Figure 6.14 shows the global dependence of the [C II]/FIR ratio on the dust optical depth τ_{160}. As opposed to points lying in OMC1, studied in (Goicoechea et al. 2015b, Fig. 15), we do not observe a linear reciprocal trend in the [C II]/FIR ratio with τ_{160} on larger scales. Goicoechea et al. (2015b) expect $\log_{10} I_{[\mathrm{C\,II}]}/I_{\mathrm{FIR}} \simeq -\log_{10} \tau_{160} + C$ for a cloud slab of constant dust temperature viewed in face-on geometry. The fact that we do not observe this behavior globally indicates that, unlike for OMC1, the temperature varies on large scales. However, there seems to be a decreasing trend of [C II]/FIR with

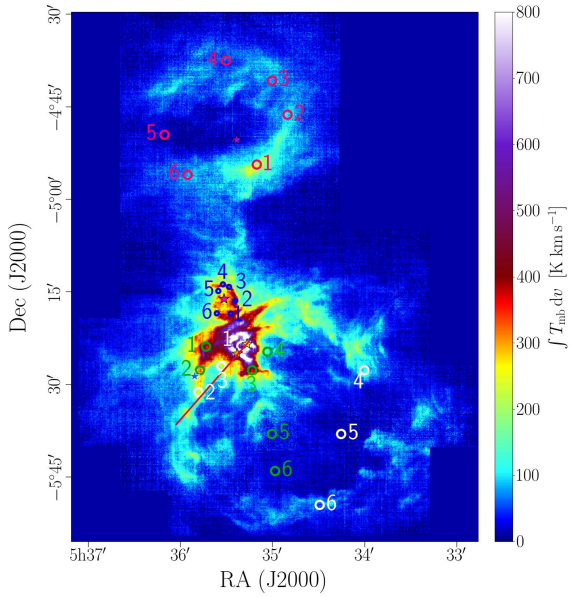

Figure 6.15: Positions of spectra (green and white circles: spectra in M42, blue: M43, red: NGC 1977) and line cut in Fig. 6.23 (red line) on [C II] line-integrated emission at its native resolution.

increasing τ_{160}. Low [C II]/FIR ratios are found towards the OMC4/ISF region, where τ_{160} is large due to a large column of cooler dust. This cool dust likely emanates from deeper layers in the cloud that are not exposed to FUV radiation.

We will follow up this discussion with a closer look at the spectra in these high-[C II] intensity regions (cf. Fig. 6.15). The [C II] spectra along with CO(2-1) spectra are shown in Fig. 6.16. We conclude that all but one spectra exhibit multiple components, which may explain the enhanced [C II] emission from these regions. Towards OMC1w, that has relatively less [C II] intensity, we observe a single line component. A detailed discussion of these spectra can be found in Appendix 6.D. We remark here that the analysis of the [^{13}C II] $F = 2$-1 line, where possible, indicates that only about 20-35% of the gas column estimated from the dust optical depth is traced by [C II] (a more thorough analysis of the [^{13}C II] emission from Orion A will be done by Kabanovic et al., in prep.) and that the power-law behavior of the [C II]-FIR and [C II]-8 μm correlations does not seem to be caused by increasing optical depth with increasing intensity. In addition, in some regions we see the effects of local sources on the gas kinematics.

Figure 6.17 shows [C II] and CO(2-1) spectra towards regions of different geometry. In OMC1, [C II] and CO(2-1) are slightly shifted from each other. Spectra 3, 4 and 6 show the velocity shift between [C II] and CO(2-1) emission towards regions where [C II] emission is arising in an edge-on geometry. This indicates that the [C II] and CO(2-1) emission arise in different regions of the cloud. In contrast, spectra taken towards the molecular background in face-on geometry, such as spectra 2 and 5, exhibit little systematic velocity shift. However, even spectra 2 and 5 show substructure that deviates from a Gaussian spectral form. Comparing the line widths of the [C II] and CO spectra would yield insight into the turbulent motions of the respective gas layers, but this is outside the scope of this study and will be subject of a follow-up study.

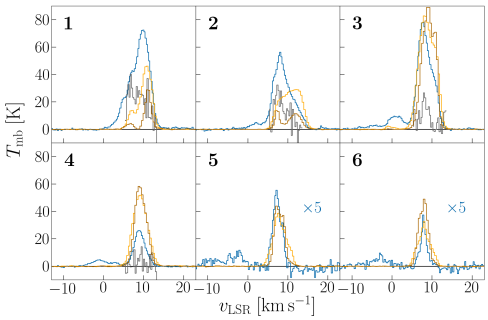

Figure 6.16: Spectra towards high-intensity regions in M42, indicated by green circles with radius 40″ in Fig. 6.15. Blue: [C II], yellow: ^{12}CO(2-1), brown: ^{13}CO(2-1) (multiplied by 3). Additionally, the [^{13}C II] F = 2-1 hyperfine component is plotted (grey) in its systemic velocity (multiplied by 20) in spectra 1-4.

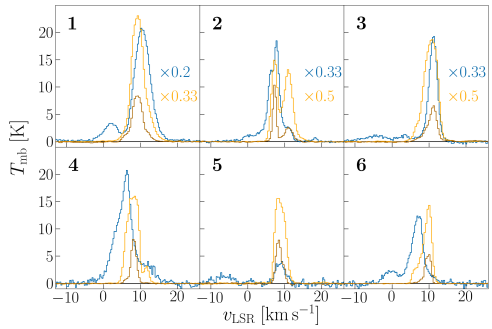

Figure 6.17: Spectra towards six regions of different geometry, indicated by white circles with radius 40″ in Fig. 6.15 (OMC1, behind the Orion Bar, Eastern Rim, Western Edge, M42 cloud background, southern Veil Shell). Blue: [C II], Yellow: ^{12}CO(2-1), Brown: ^{13}CO(2-1) (not multiplied by 3).

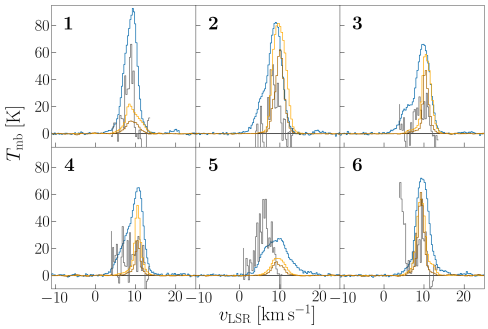

Figure 6.18: Spectra towards the M43 shell, indicated by blue circles with radius 20″ in Fig. 6.15. Blue: [C II], yellow: ^{12}CO(2-1), brown: ^{13}CO(2-1) (multiplied by 3). Additionally, the [^{13}C II] F = 2-1 hyperfine component is plotted (grey) in its systemic velocity (multiplied by 20).

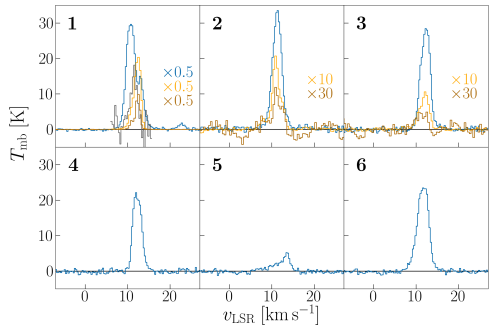

Figure 6.19: Spectra towards the NGC 1977 shell, indicated by red circles with radius 40″ in Fig. 6.15. Blue: [C II], yellow: ^{12}CO(2-1), brown: ^{13}CO(2-1) (multiplied by 3).

In general, the PDR models also reproduce the [C II]-CO relationship, but the scatter in those correlations is generally large. From examination of the spectra, the relation of [C II] with CO(2-1) emission is not immediately clear. In most cases we find a velocity offset between the [C II] and the CO(2-1) lines. Also the global morphology is very different. While [C II] emission traces the edge-on shells and illuminated face-on PDR surfaces, CO(2-1) emission traces the deeper molecular layers of a PDR and the background molecular cloud, that might not be co-located with the shell. In case of face-on PDRs, low-J CO emission arises predominantly in deeper layers of the PDR, and the velocity difference is generally less than towards edge-on structures.

In M43, models with $G_0 = 2000$, $n = 1 \times 10^4\,\mathrm{cm}^{-3}$, and $A_{\mathrm{V,los}} = 10$ clearly produce too much FIR emission. The observations agree better with models with $G_0 = 700$-1000, however [C II] emission is somewhat enhanced compared to the model predictions. As in the shell of M42, spectra towards the edge of M43 consists of at least two components, shown in Fig. 6.18. Again, a detailed description and discussion of the spectra is provided in Appendix 6.D. The [C II] column, computed from the [^{13}C II] $F = 2$-1 line, where possible, traces only a fraction (30-60%) of the total gas column estimated from the dust optical depth. It is evident, however, that the C^+ column (with $A_{\mathrm{V}} \simeq 15$) is substantially larger than expected for a face-on PDR in this conditions. The edge-on geometry of the M43 rim becomes very pronounced. The face-on model with $n = 1 \times 10^4\,\mathrm{cm}^{-3}$ also reproduces the [C II] and FIR emission from the background molecular cloud, that is after subtraction of the contribution from the foreground shell (grey points).

[C II] and CO(2-1) spectra towards OMC3 and the NGC 1977 shell are shown in Fig. 6.19. FIR line emission towards OMC3 at the edge of NGC 1977 has been subject to modelling efforts previously. Howe et al. (1991) conclude that the spatial distribution of [C II] emission can be explained by a clumpy medium. Spectrum 1 towards OMC3 can be fitted better by an emitting and a (strong) absorbing component than by two emitting components. The [^{13}C II] line is slightly asymmetric, as well, but this is hard to quantify due to noise. Yet it is significantly shifted from the [^{12}C II] component, which signifies self-absorption (Kabanovic et al. in prep.). In a clumpy medium, the strong emission and absorption may be easily explained by temperature gradients between the clump and inter-clump medium. While the [C II] spectrum may be fitted by one emitting and one absorbing component, both the ^{12}CO and the ^{13}CO spectrum comprise two emitting components. It is unclear how the CO components are related to the [C II] components. As in other spectra, we find a significant velocity offset.

While CO emission in OMC3 is strong, in the rest of the shell that is covered by the CO observations it is very weak. ^{13}CO is detected, but at low temperatures the ^{12}CO line in FUV-illuminated gas can still be optically thin with enhanced ^{13}CO emission due to chemical fractionation (e.g., Goicoechea et al. 2020). In the case of optically thick ^{12}CO emission, the excitation temperature is very low ($T_{\mathrm{ex}} \simeq 4$-5 K). Possibly CO emission stems from a molecular background, that is not associated with the [C II]-emitting shell, and that is only faintly illuminated. Another possibility is that the CO-emitting gas originates from two slightly velocity-shifted parts of the expanding gas around the NGC 1977 H II region.

Summarizing, the spectra shed light on why [C II] emission may be underestimated by the standard PDR models we employ. First of all, virtually all spectra consist of more than one component. One needs geometrically more accurate and multi-component models to understand the precise emission characteristics of both edge-on and face-on geometries. Edge-on models should incorporate temperature gradients,

that can lead to self-absorption (Kabanovic et al. in prep.). In some cases, clumpy PDR models might be a good choice. Also dynamics of the gas should be taken into account. Those can lead to pressure variations within the gas by shear or compression. Furthermore, as we see velocity shifts in the [C II] and CO(2-1) line emission, photo-evaporation may be important and this can alter the emission from a PDR (Bertoldi 1989; Störzer & Hollenbach 1998; Bron et al. 2018). Most of our discussed lines can be fitted by Gaussians, but the spatial relationship of the emission components is often unclear. We notice that in regions where we attribute the emission to edge-on PDRs, the velocity of the CO-emitting gas is generally offset from the velocity of the [C II]-emitting gas. Either, this means that the gas is subject to shear, or that [C II] and CO trace different, possibly unrelated, layers of gas. In edge-on (half-)shells such as the Veil Shell, CO(2-1) emission arises in the molecular background, while [C II] emission stems from the edge-on shell. Compared to M42 and M43, NGC 1977 is evolving rather slowly at its advanced age and tends to emit narrower lines. This might reflect the mild stellar feedback it is experiencing at this stage. At the same time, M42 and M43 are still heavily affected by driving stellar feedback and lines tend to be broader, hinting at increased turbulence.

6.4.2 The G_0-$p_{\rm th}$ relationship

Our data show a clear trend of increasing thermal pressure with increasing strength of the radiation field. A similar trend is apparent in studies of fine-structure line emission from the PDRs (Young Owl et al. 2002) as well as in studies of the CO ladder in PDRs (Joblin et al. 2018), albeit that those relations are displaced somewhat (cf. Fig. 6.20). For the study of Young Owl et al. (2002), this displacement reflects an overestimate of the incident FUV field in several of the sources. Specifically, they adopted a G0 of 5000 for NGC 1977S (the bright region in the south-west of NGC 1977), while we derive a value of 1100. After correction, the data for this particular source agrees, not surprisingly as both analysis are based upon fine-structure line studies. Likewise, the G_0 value adopted for the Orion Bar by Young Owl et al. (2002) is somewhat higher than current estimates (Salgado et al. 2016; Joblin et al. 2018). The results of the studies by Joblin et al. (2018) and Wu et al. (2018) are displaced towards higher pressures. Both these studies rely on high-J CO transitions with high critical densities. Consequently, clumps or gas density enhancements dominate the emission in these lines, whereas the fine-structure lines measure the interclump gas. The offset of these studies might be due to the importance of self-gravity in the clumps, which will dominate the pressure distribution. Hence, the high-J CO lines may not be good measures of the pressure in the [C II]-emitting PDR layers. As a corollary, we do not expect that constant-pressure PDR models will be applicable to these environments. Joblin et al. (2018) note that specifically the [C II] emission in their sources predominantly comes from lower-density interclump gas, that fills the beam.

Using the model of an H II region bordering on a PDR in pressure equilibrium, Seo et al. (2019) derive an analytic expression for the correlation between $p_{\rm th}$ and G_0 in the PDR:

$$p_{\rm th} \simeq 4.6 \times 10^4 f^{-1/2} (\frac{\Phi_{\rm FUV}}{10^{51}\,{\rm s}^{-1}})^{-1/4} G_0^{3/4}\,{\rm K\,cm^{-3}}, \tag{6.3}$$

where $f = \Phi_{\rm FUV}/\Phi_{\rm EUV}$ is the ratio of the FUV flux to the H-ionizing flux. For relevant spectral types, this ratio is constant to within a factor 1.5 (Young Owl et al. 2002). This relation is also shown in Fig. 6.20. The theoretical relation is well above

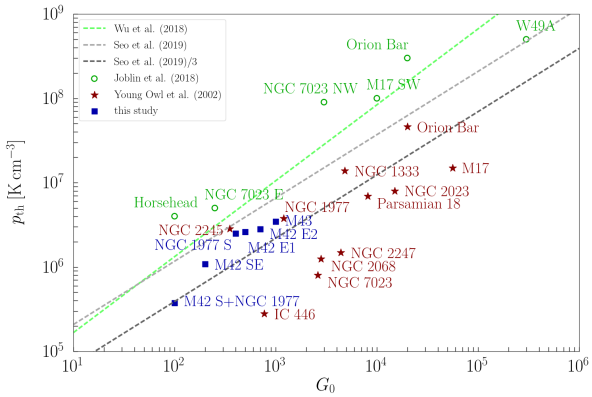

Figure 6.20: Thermal pressure versus incident radiation field in several PDRs. Red points are from Young Owl et al. (2002) (based on FIR line analysis), green points are from Joblin et al. (2018) (based on high-J CO line analysis), dark blue points are from this study. The green dashed line is the fit by Wu et al. (2018) (based on high-J CO line analysis). The dashed grey line is the analytic solution of Seo et al. (2019), once divided by 3 to account for pressure equipartition.

the empirical relation derived from the fine-structure lines but below the data derived from the CO analysis.

We note that all our analysis and that of Young Owl et al. (2002) only measures the thermal pressure in the PDR. The total pressure includes contributions from turbulence and magnetic fields and should be balanced by the thermal pressure from the ionized gas and radiation pressure. For the three sources in Orion, we have compared these and concluded that there is equipartition between thermal, turbulent and magnetic pressure in the PDR and that radiation pressure is typically not very important (Pabst et al. 2020). Moreover, while there is approximate pressure equilibrium between the plasma and the ionized gas within the Veil Shell, there is a strong pressure gradient from the background molecular cloud towards us, which drives the rapid expansion of the shell. In the PDRs of M43 and NGC 1977, the pressure of the ionized gas exceeds the PDR pressure. This pressure drives the expansion of the bubbles in those two regions.

In a linear fit, we find $p_{\rm th}/G_0 \simeq 5 \times 10^3\,{\rm K\,cm^{-3}}$ for our data points. The data points of Joblin et al. (2018) agree well with the empirical relation of Wu et al. (2018). We note that the error bars of the data points are usually large, which is mostly due to the uncertainty in the estimated gas density ($\sigma \sim 0.5\,{\rm dex}$). As discussed before, the detailed physics of the models used to infer physical conditions strongly affect the resulting estimates. This applies to our data points, as well, since we rely on the standard PDR structure and dust properties to estimate the gas density in M42, M43, and NGC 1977. Besides the pressure of the H II region acting on the PDR, the correlation between thermal pressure or gas density and the incident radiation field may also reflect the star-formation history of a region, as Young Owl et al. (2002) comment.

Howe et al. (1991) demonstrated that [C II] emission from OMC3 can be modelled successfully employing a clumpy PDR model. Considering the geometry of a source is certainly important in modelling efforts. A slight deviation from pure edge-on or face-on geometry results in differing estimates of the physical conditions. Considering

the detailed line shape of the observed lines is equally important. Often emission lines reveal several line components mixed within the line of sight or foreground components by self-absorption. Complex velocity profiles may also hint at the presence of a clumpy medium, hydrodynamic instabilities and/or colliding filaments and gas flows. These processes imply a less homogeneous ISM than usually accounted for in PDR models.

While we recognize that real PDRs might contains clumps and gas-density enhancements (Joblin et al. 2018; Goicoechea et al. 2016) and that this may influence the analysis, we want to emphasize that the characteristics of PDRs derived from the analysis of fine-structure lines are in good agreement with the simple theoretical model based upon the Strömgren relation in combination with pressure equilibrium between the ionized and PDR gas and taking equipartition of thermal, turbulent, and magnetic pressures into account.

6.4.3 The origin of [C II] emission and CO-dark gas

In this section, we will discuss the morphology of the emission and the implications thereof. This was done briefly in Paper I, but we continue with a more detailed discussion in this paper. Table 6.6 compiles the luminosities and masses towards the regions we have defined in our analysis.

As we have stated in Paper I, most of the [C II] emission (70%) comes from the limb-brightened shell edges in M42, M43, and NGC 1977, that is moderately irradiated PDR surfaces, but a significant contribution (20%) also comes from the more diffuse emission from weakly irradiated surfaces. Although the heavily irradiated PDRs close to the central stars emit very bright [C II] emission, their contribution to the total [C II] emission is minor (10-20%) compared to the large shells.

The massive shells comprise a significant amount of CO-dark gas, with only a few solar masses contained in dense CO-emitting globules found in the Veil Shell (Goicoechea et al. 2020). If we rely on the gas mass estimated from the dust opacity, we find that 25% of the gas mass in the Orion Nebula is contained in the expanding shell. However, the shell mass estimate might be contaminated by the molecular background. In a conservative estimate, we attribute only 10% of the total gas mass (i.e. $1000\,M_{\odot}$) to the shell. The mass in the dense molecular core, OMC1 with BN/KL and Orion S, is also 15% of the total gas mass within the mapped area. Another 20% are comprised in the dense filament, the ISF. Both fractions agree with the mass fractions traced by CO emission (8% and 14%, respectively). The CO emission in the line of sight towards the expanding shell likely stems from the background gas rather than the shell itself (as judged from the velocity structure of the spectra). While most of the CO emission in the region of the Orion Nebula originates from the extended background cloud, Hα emission is concentrated around OMC1, almost 50% stemming from the small OMC1 region.

Also 30% of the FIR emission stem from the OMC1 region, including the FIR emission of the Bright Ridge comprising BN/KL and Orion S in the three PACS bands, that accounts for 15% (see Paper I for a discussion of the "[C II] deficit" or "FIR excess"). About 25% stem from the much larger shell. About 10% stem from the region of the OMC4, that is not bright in surface tracers, but contributes by its large area. The same amount arises from the bright Eastern Rim, that has half the area of the OMC4 region. While FIR emission from the OMC1 region contributes significantly to the total FIR emission from the Orion Nebula, only 10% of the total [C II] emission originate in OMC1. About 30% of the [C II] emission stem from the shell. Also OMC4 is a minor contributor with 10%, where we note that most of the emission associated

Table 6.6: Luminosities and masses of M42, M43 and NGC 1977 per subregion.

Region		A [pc^2]	$L_{\rm FIR}$ [L$_\odot$]	$L_{\rm [C\,II]}$ [L$_\odot$]	$L_{\rm [C\,II]}/L_{\rm FIR}$	$M_{\rm gas}$ [a] [M$_\odot$]	$L_{\rm CO(2\text{-}1)}$ [b] [L$_\odot$]	$M_{\rm CO}$ [c] [M$_\odot$]	$L_{24\mu\rm m}$ [d] [L$_\odot$]	$L_{\rm H\alpha}$ [e] [L$_\odot$]
M42	all	45	1.8×10^5	510	2.8×10^{-3}	10900	1.1	8800	4700	3500
	OMC1[f]	0.31	8.2×10^4	53	6.5×10^{-4}	1500	8.9×10^{-2}	720	–	1500
	Bright Ridge[f]	0.07	3.7×10^4	11	2.9×10^{-4}	870	2.8×10^{-2}	220	–	470
	Eastern Rim	1.3	1.7×10^4	59	3.5×10^{-3}	510	9.2×10^{-2}	740	810	260
	OMC4	2.5	1.6×10^4	45	2.8×10^{-3}	2100	1.5×10^{-1}	1200	640	470
	Veil Shell	8.7	3.5×10^4	150	4.3×10^{-3}	2500	2.3×10^{-1}	1800	1200	590
M43	all	0.74	1.4×10^4	38	2.7×10^{-3}	530	3.0×10^{-2}	240	740	190
	background, H II	0.13	3.1×10^3	8.9[g]	2.8×10^{-3}	53	4.6×10^{-3}	37	100	99
	faint CO, faint [C II]	0.14	8.8×10^2	4.1	4.7×10^{-3}	29	2.5×10^{-3}	20	49	12
	bright CO, faint [C II]	0.16	2.0×10^3	6.0	3.0×10^{-3}	200	9.2×10^{-3}	74	87	18
	shell	0.31	8.2×10^3	19	2.3×10^{-3}	250	1.4×10^{-2}	110	410	63
NGC	all	17	1.8×10^4	160	8.9×10^{-3}	2600	1.2×10^{-1}	950	1000	63
1977	H II	2.9	4.7×10^3	37[h]	7.9×10^{-3}	310	1.1×10^{-2}	87	300	17
	OMC3	2.6	5.8×10^3	34	5.9×10^{-3}	1200	8.9×10^{-2}	720	190	8.6
	faint Hα	6.9	3.2×10^3	33	9.7×10^{-3}	730	3.0×10^{-2}	240	280	19
	shell	6.2	5.4×10^3	69	1.3×10^{-2}	670	1.6×10^{-2}	130	100	7.9

Notes. [a] Gas mass derived from dust mass, using $N_H \simeq 6 \times 10^{24}\,\rm cm^{-2}\,\tau_{160}$ (Weingartner & Draine 2001). [b] The CO(2-1) map does not cover the entire NGC 1977 region (cf. Fig. 2 in Paper I). [c] Gas mass from CO(2-1) intensity, using $X(\rm CO) \simeq 2 \times 10^{20}\,\rm cm^{-2}\,(K\,km\,s^{-1})^{-1}$ (Bolatto et al. 2013). [d] The MIPS 24 μm image is saturated towards the Huygens/OMC1 region. [e] The Hα surface brightness in the EON is largely due to scattered light from the bright Huygens Region (O'Dell & Harris 2010). Also Hα emission in M43 has to be corrected for a contribution of scattered light from the Huygens Region (Simón-Díaz et al. 2011). [f] The Bright Ridge contains the BN/KL region and Orion S and is part of OMC1. Values for OMC1 include the Bright Ridge, where we have estimated the FIR luminosity from an SED fit to the three PACS bands, that are only saturated at the core of BN/KL. [g] 2.4 $L_\odot$ from background PDR, 6.0 $L_\odot$ from ionized gas, 0.5 $L_\odot$ from foreground neutral shell. [h] 6.2 $L_\odot$ from ionized gas, 31 $L_\odot$ from neutral shell.

with OMC4 actually stems from the regions close to OMC1, which can therefore be attributed to relatively warm, heavily irradiated gas. The bright Eastern Rim, with its four times larger area compared to OMC1, contributes with 10% as well. Adding the contributions from the defined areas, leaves 40% of [C II] emission that stems from less pronounced features, that is the extended background and structures lying outside the shell, which may be excited by local sources or bubbles spawning off the large bubble blown by θ^1 Ori C.

We now turn to the other two regions within the Orion Nebula complex. In M43, 50% of [C II] emission arise in the region we have defined as the shell. However, this emission is likely contributed to by a significant emitting background. About 25% stem from the inner region. Of this emission, a spectral analysis shows that only 25% arise from the background, while 5% stem from the expanding shell and 70% from the H II gas filling the bubble. Faint [C II] emission can be observed outwards of the shell, accounting for 25% of the total emission. The percentages in the FIR emission are similar, slightly more (60%) stemming from the shell region. Hα emission is concentrated in the inner H II region, while 24 μm emission is observed mainly towards the shell. Also CO emission is dominated by the shell region and follows its morphology. The face-on shell seen towards the H II region does not exhibit CO emission, hence we conclude that the expanding shell is not very massive and that the edge-on shell structures are sculpted within the molecular background. In Pabst et al. (2020) we estimated an expanding shell mass of only 8 $M_\odot$, which amounts to 1.5% of the total gas mass in M43. This compares to 5% of [C II] emission stemming from the face-on shell. If we adopt a shell mass of 1000 $M_\odot$ in M42, 10% of the gas mass account for 25% of the [C II] emission, which is an equal relative mass to luminosity ratio.

In NGC 1977, the total [C II]/FIR ratio is significantly increased compared to M42 and M43, at almost 1%. Most of the gas mass as traced by the dust opacity, almost 50%, is concentrated in OMC3, a dense region where the ISF bends westward. 25% of the gas mass are situated in the shell surrounding the H II region. However, we cannot exclude the possibility that not all the mass is part of the expanding shell. As the expansion velocity is rather low, 1.5 km s^{-1} (Pabst et al. 2020), the expansion may have stalled in denser parts of the NGC 1977 region. Also we find significant dust emission outside of the shell, accounting for 25% of the total mass. In the inner part of the shell, the enclosed H II region, we find about 10% of the mass, amounting to a similar mass per area ratio as in the outward regions. Hα and 24 μm are distributed in a similar fashion, predominantly arising from the H II region. The total CO emission originates almost entirely from OMC3, but this is due to the fact that the CO observations have insufficient coverage in the less CO-bright areas. We can draw the preliminary conclusion, however, that we find a significant amount of CO emission besides OMC3, which may stem from a more extended molecular background or is associated with the shell structure.

The rather extended shell in NGC 1977 dominates the total [C II] emission in this region, contributing 43%. The dense and bright OMC3 contributes only about 20%. 25% originate in the [C II]-emitting shell towards the H II region, with a minor contribution from the ionzed gas (cf. Pabst et al. 2020). As before, a significant amount of [C II] emission stems from weakly emitting surfaces, in NGC 1977 this is about 20% within the map coverage. Only 30% of the total FIR emission stem from the shell, only slightly more from OMC3.

A recent study by Lebouteiller et al. (2019) concerning the origin of the [C II] line emission and pertaining to its utility as a star-formation tracer, concludes that

in the giant H II region N11 in the LMC more than 90% of the [C II] emission arises in CO-dark H_2 gas and that most of the molecular gas is CO-dark (above 40%). Dwarf galaxies generally have lower metallicity and penetration of FUV photons, and therefore photodissociation of CO is enhanced. The GOT C+ survey has shown that 20% of the Galactic [C II] emission arise from ionized gas (Pineda et al. 2014), while 30% stem from PDRs, and only 25% from CO-dark H_2 gas. Pineda et al. (2013) note that most of the [C II] emission in the Milky Way arises in moderately FUV-illuminated regions ($G_0 \simeq$ 2-50), that is large faint surfaces rather than small dense and bright PDRs. Our observations towards the Orion Nebula are in good agreement with this conclusion, the bright inner OMC1 region being a minor contributor to the total [C II] luminosity. The [C II] observations towards L1630, comprising the Horsehead Nebula, predominantly highlight the PDR surfaces illuminated by σ Ori, where 95% of the total [C II] emission in the mapped area arise. Yet, regions that are bright in [C II] trace only 8% of the gas mass, while 85% of the mass is associated with strong CO emission (Pabst et al. 2017). In the Orion Nebula complex, we find that 70% of the [C II] emission arises in PDR surfaces. The [C II]-emitting regions we have defined contain 64% of the gas mass (traced by dust). A portion of that gas mass, about 30-50%, is likely associated with the molecular background rather than the PDR surface. Hence, bright [C II] emission, that traces the H/H_2 transition in a PDR, traces about 30% of the total gas mass in the Orion Nebula complex. In the Orion-Eridanus region, an area of $\sim 400\,\mathrm{pc} \times 400\,\mathrm{pc}$, [C II] emission (observed with COBE) is dominated by the emission from extended low-density, low-UV field molecular cloud surfaces associated with the active regions of massive star formation (Abdullah & Tielens 2020).

As concluded in Paper I, [C II] from PDRs is the main origin of [C II] from the Orion Nebula complex, with about 70%. The [C II] emission from ionized gas is a minor contributor, less than 5% in M42 and NGC 1977, but 15% in M43. From the remainder, we estimate that CO-dark H_2 gas, that is not captured in bright PDR surfaces, contributes with about 20%. These percentages elucidate the importance of observations towards fainter extended regions, as we have seen that those can carry a significant amount of [C II] luminosity.

6.4.4 Photoelectric heating efficiency

In Paper I we have discussed the observed [C II] deficit, that is the decrease in the [C II]/FIR intensity with increasing FIR intensity, and related it to a decreased photoelectric heating efficiency in dense PDRs, in addition to the importance of [O I] cooling. Here, we will examine the heating efficiency of PDR material in more detail. We estimate the photoelectric heating efficiency by the observed cooling efficiency of the gas, which we will approximate by the observed [C II]/FIR ratio. At intermediate temperatures and densities, the cooling is dominated by cooling through the [C II] line. At higher temperatures and densities, like those in the Huygens Region, the [O I] 63 μm line becomes important (Hollenbach & Tielens 1999). However, in the shell surrounding the Extended Orion Nebula, gas cooling is most likely dominated by [C II], as the temperatures and densities are rather moderate. In M43 and the densest part of NGC 1977 (in OMC3), [O I] emission will contribute significantly (Herrmann et al. 1997; Young Owl et al. 2002).

Theoretically, the photoelectric heating efficiency depends on the ionization parameter $\gamma = G_0 T_{\mathrm{gas}}^{1/2}/n_{\mathrm{e}}$ (Bakes & Tielens 1994, Eq. 43). In Paper I, we estimated γ in each pixel of the map. Here, we set the gas density in OMC4 so that it varies equally with distance from OMC1 as in the Veil Shell. The gas density in the shell of M43

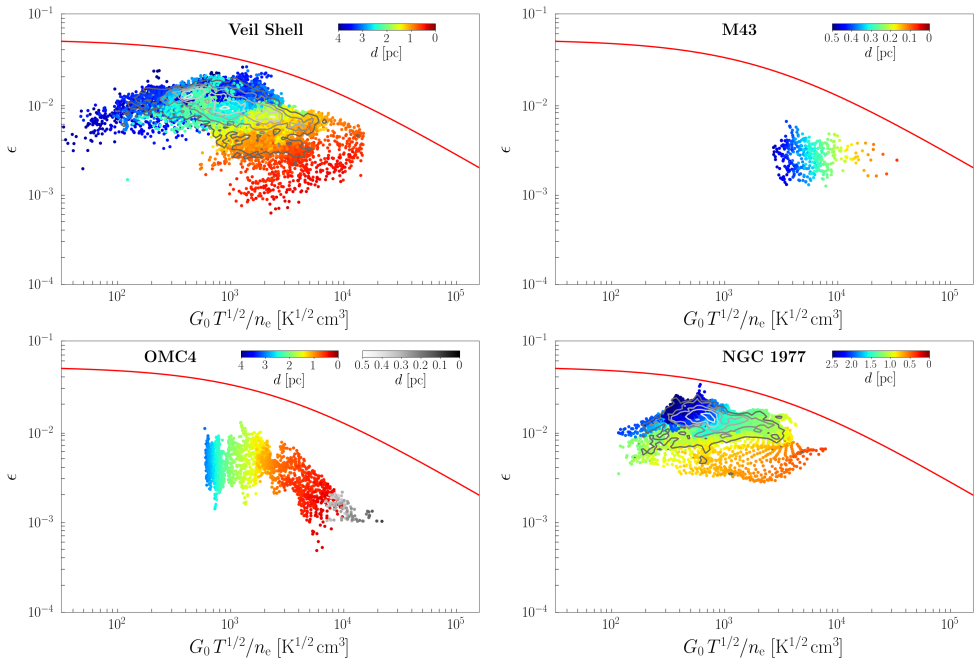

Figure 6.21: The photoelectric heating efficiency ϵ, equated as cooling efficiency [C II]/FIR, in M42 (top left: Veil Shell, bottom left: OMC4 with OMC1 (in grey scale)), the shell of M43 (top right), and the shell of NGC 1977 (bottom right) as function of the ionization parameter $\gamma = G_0 T^{1/2}/n_e$. Colors indicate the distance from θ^1 Ori C in the Orion Nebula, from NU Ori in M43, and from 42 Orionis in NGC 1977, respectively. Contours in the upper-left and lower-right panel indicate the density levels above which 90, 70, 50, 30, and 10% of the points lie. The red curve is the theoretical prediction of Eq. 43 by Bakes & Tielens (1994).

is set to $n \simeq 1 \times 10^4\,\mathrm{cm}^{-3}$ (cf. Pabst et al. 2020). We use $G_0 \simeq 150(1\,\mathrm{pc}/d)^2$ in M43 and $G_0 \simeq 200(1\,\mathrm{pc}/d)^2$ in NGC 1977, approximated from the total FIR luminosity of M43 and NGC 1977, respectively. The correlations between the photoelectric heating efficiency ϵ and the ionization parameter γ in the Orion Nebula (the Veil Shell and OMC4), the shell of M43, and the shell of NGC 1977 are shown in Fig. 6.21. For M42, the data reveals a similar trend with a decreased efficiency with increased ionization parameter as the theoretical predictions of Bakes & Tielens (1994). The cooling efficiency is generally lower in OMC4, due to a "FIR excess" from dense gas behind the [C II]-emitting layers (cf. Fig. 2 in Paper 1). M43 comprises to few data points to reveal a clear trend. For NGC 1977, the observations reveal a heating efficiency that is largely independent of the ionization parameter, but this is complying with the near-constant theoretical heating efficiency for low γ. However, virtually all points lie below the theoretical heating curve. As a caveat, we note that it is hard to constrain γ observationally, which is mainly due to the difficulty of obtaining a robust gas density estimate, but we deem it unlikely that we overestimate the density systematically by an order of magnitude. We observe this same behavior when averaging over the regions and employing average values of γ.

Figure 6.22 shows the average cooling rate as a function of γ averaged over the regions defined in M42, M43, and NGC 1977, together with data from the literature. The estimated parameters for M42, M43, and NGC 1977 employed in this figure are

Table 6.7: Cooling efficiency and estimated physical parameters to compute γ in Fig. 6.22.

Region		$L_{[\mathrm{C\,II}]}/L_{\mathrm{FIR}}$	G_0 [a]	n [b] [cm^{-3}]	T [c] [K]
M42	all	3.6×10^{-3}	1×10^3	1×10^4	200
	OMC1 [d]	6.5×10^{-4}	2×10^4	1×10^5	300
	Eastern Rim	3.5×10^{-3}	500	1×10^4	100
	OMC4	2.8×10^{-3}	500	1×10^4	100
	Veil Shell	4.3×10^{-3}	200	3×10^3	100
M43	all	2.7×10^{-3}	1×10^3	1×10^4	120
	background, H II	2.8×10^{-3}	1.5×10^3	1×10^4	120
	faint CO, faint [C II]	4.7×10^{-3}	300	1×10^3	100
	bright CO, faint [C II]	3.0×10^{-3}	300	1×10^4	100
	shell	2.3×10^{-3}	1×10^3	1×10^4	120
NGC	all	8.9×10^{-3}	100	5×10^3	90
1977	H II	7.9×10^{-3}	200	5×10^3	90
	OMC3	5.9×10^{-3}	200	2×10^4	100
	faint Hα	9.7×10^{-3}	100	1×10^3	50
	shell	1.3×10^{-2}	100	5×10^3	70

Notes. [a] Estimated from average distance to respective central star with systematic uncertainty of $\pm 50\%$. [b] Estimated from [C II]-CO separation in Eastern Rim and M43 shell, otherwise τ_{160}, with systematic uncertainty of $\pm 50\%$. [c] Estimated from [C II] excitation temperature (cf. Appendix A in Paper I). PDR models predict up to twice as large temperature for the [C II]-emitting layers. [d] [O I] 63 μm cooling contributes significantly in OMC1. We find $L_{[\mathrm{O\,I}]} \simeq 320\,L_\odot$ (Higgins et al. in prep.), hence $(L_{[\mathrm{C\,II}]} + L_{[\mathrm{O\,I}]})/L_{\mathrm{FIR}} \simeq 4.5 \times 10^{-3}$. The Bright Ridge with BN/KL and Orion S accounts for $L_{[\mathrm{O\,I}]} \simeq 90\,L_\odot$, hence including this area yields a cooling efficiency of $(L_{[\mathrm{C\,II}]} + L_{[\mathrm{O\,I}]})/L_{\mathrm{FIR}} \simeq 5.1 \times 10^{-3}$ for the PDR.

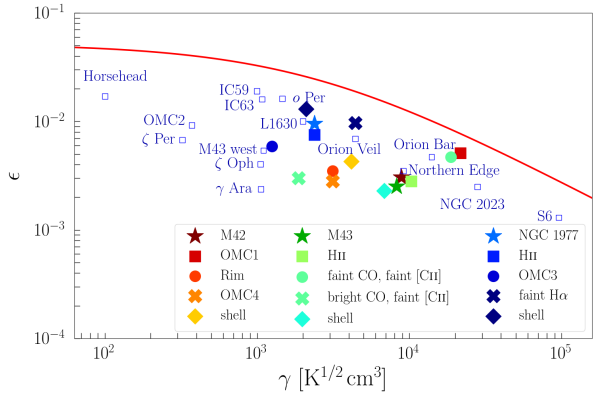

Figure 6.22: The average photoelectric heating efficiency ϵ, equated as cooling efficiency [C II]/FIR, in M42, M43, and NGC 1977, divided into the previously defined subregions, as function of the ionization parameter $\gamma = G_0 T^{1/2}/n_e$. OMC1 includes [O I] cooling, but excludes the BN/KL region and Orion S. Parameters for Orion A are given in Table 6.7. The photoelectric heating efficiency in PDRs and diffuse sight lines from the literature is plotted as open blue squares (cf. Fig. 9 in Paper I). Data for the diffuse ISM are taken from Gry et al. (1992) and van Dishoeck & Black (1986), data of NGC 2023 are from Hollenbach & Tielens (1999), data for the Horsehead and L1630 are from Pabst et al. (2017), data for IC 59 and IC 63 are from Andrews et al. (2018), data for the Orion Bar, S6, M43 west, and OMC2 are from Herrmann et al. (1997), and data for the Orion Veil are from Salas et al. (2019). The red curve is the theoretical prediction of Eq. 43 by Bakes & Tielens (1994).

given in Table 6.7. We include [O I] 63 μm cooling from Higgins et al. (in prep.) in OMC1. The [O I] 63 μm line is expected to be important in the Eastern Rim and M43, as well, with $I_{[\mathrm{O\,I}]}/I_{[\mathrm{C\,II}]} \sim 3$ (Pound & Wolfire 2008; Kaufman et al. 2006), but will be of little significance in the extended shell of NGC 1977. Observations of [O I] 63 μm and 145 μm line emission in the Orion Nebula would provide the means to establish better estimates of the gas temperature and gas density, besides the fact that it substantially contributes to the gas cooling.

These average heating efficiencies show the same trend as the overall data in Fig. 6.21 with a decrease with increasing ionization parameter but the spread is rather large. The Orion data also agrees well with previous studies, both for bright PDRs using fine-structure line measurements as also for diffuse clouds from UV absorption line studies. This earlier data set also shows a large spread. Comparing the data to the theoretical results of Bakes & Tielens (1994), we see a similar behavior of decreasing heating efficiency with increasing γ, consistently in Orion and earlier studies, but displaced by a factor of ~ 5 to lower ϵ. There seems to be an additional factor, besides the ionization parameter, that affects the coupling of FUV photons to the neutral atomic gas. This factor could be a variable abundance of PAHs and VSGs in different regions within Orion (and other lines of sight). A lower abundance of PAHs and VSGs diminishes the heating efficiency systematically, while a variable composition of the PAH family or a varying ratio of PAHs to VSGs can cause variation in the heating efficiency. As shown by Berné et al. (2015) and Croiset et al. (2016) in the case of NGC 7023, the population of PAHs is very sensitive to the physical conditions (G_0 and n). Furthermore, the recombination rates of PAHs, employed in the theoretical model, are not well-constrained experimentally.

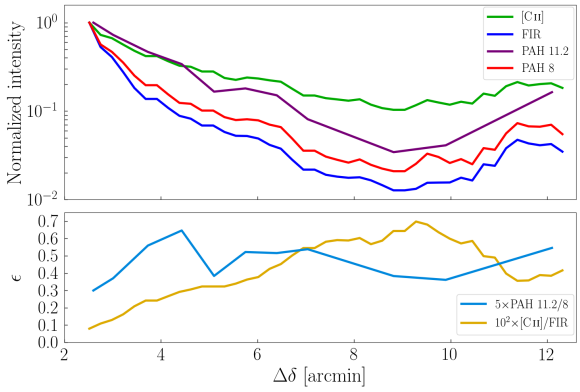

Figure 6.23: Line cut from the Orion Bar to the southwest, reaching the Eastern Rim at 12′, indicated in Fig. 6.15. The offset is given with respect to θ^1 Ori C. The 11.2 μm intensities are taken from Table 1 in Boersma et al. (2012).

The heating efficiency describes the energy input per FUV photon. When equating the cooling efficiency [C II]/FIR with the heating efficiency, we assume that only FUV photons are re-radiated in FIR energy. While this may be a good approximation for hot stars, cooler stars emit a significant amount of their energy in the spectrum below 6 eV. Those lower-energy photons contribute to the heating of the large dust grains and increase the FIR intensity emitted by those. For early-type B stars the FIR intensity is therefore increased by 1.4 (Young Owl et al. 2002). Also the energy spectrum changes with spectral type, which induces changes in the heating efficiency as derived by Bakes & Tielens (1994) for the radiation field at 3×10^4 K. For early B stars ($T_{\rm eff} \simeq 2.5\times10^4$ K), Spaans et al. (1994) derive a ∼15% lower heating efficiency. While those two corrections might bridge the gap between the observations and predictions in NGC 1977 (except OMC3), cooling efficiencies in regions in M42 and M43 are about 5 times smaller than predicted by theory at the estimated γ. Another complication in the interpretation of the observed [C II]/FIR ratio is the fact that most structures are observed in edge-on geometry. In the M42 and M43 edges, the [C II] line tends to be optically thick towards the observer. The real cooling efficiency might be higher (by a factor of $\sim$ 2) than observed if the shell structures cool mainly through the (unobservable) face-on surfaces. Only OMC1 lies close to the theoretical curve, but we note that the cooling is dominated by the [O I] 63 μm line[3].

The Orion [C II] survey also provides a way to link the observed heating efficiency directly to the characteristics of the local PAH family. Rubin et al. (2011) and Boersma et al. (2012) have analyzed a set of Spitzer/IRS spectra that systematically explored the behavior with distance of PAHs in the PDR associated with the Veil. As Fig. 6.23 shows, the intensity of the [C II], FIR, and PAH bands all smoothly decrease with distance from the Orion Bar (and hence the illuminating star). The gas heating efficiency, however, shows a clear peak at about 10′ from the Bar. In contrast, the ratio of the 8 to 11.2 um bands is largely constant over the full distance range probed. This band ratio is generally thought to probe the degree of ionization of the emitting PAHs as the former band traces emission by ionized PAHs while the latter is dominated by neutral PAHs (Peeters et al. 2002; Boersma et al. 2012). Given the general relation

[3]The observed [C II] intensity in OMC1 is higher than predicted by standard face-on PDR models (Pound & Wolfire 2008; Kaufman et al. 2006), but the [O I] 63 μm intensity is predicted accurately.

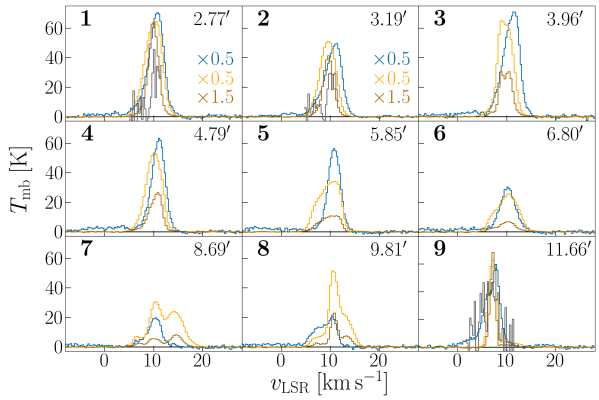

Figure 6.24: [C II] (blue), ^{12}CO(2-1) (yellow), and ^{13}CO (brown) spectra along the line cut behind the Orion Bar in Fig. 6.23. The offset with respect to θ^1 Ori C is given in arcminutes. In addition, the [^{13}C II] F = 2-1 component is plotted (grey) in its systemic velocity and multiplied by 20 in spectra 1, 2, and 9.

between G_0 and n discussed in section 4.2, we expect little variation in the ionization parameter with distance and that is borne out by the constant $8\,\mu$m/$11.2\,\mu$m band ratio. As a corollary, this again suggests that there is another factor that affects the gas heating efficiency besides ionization. That could be abundance of PAHs and VSGs. However, the intensity ratio ($8\,\mu$m+$11.2\,\mu$m)/FIR is constant along the line cut, which hints that VSGs play an important role.

Most of the observed [C II] and FIR emission will stem from the background PDR. The [C II]/FIR increases with distance from the origin of the line cut, until it hits the Eastern Rim, where it gradually decreases as the Rim piles up along the line of sight. The decrease of the cooling efficiency in the Rim may be due to increased G_0 (as a result of the geometry). Alternatively, the edge-on geometry of the Rim increases the optical depth of the [C II] line compared to the FIR intensity, which leads to a diminished observed [C II]/FIR ratio. As we expect the [C II] line to be optically thick in the Rim, the latter will certainly be an important effect. Yet, we cannot exclude that G_0 in the Rim is higher than in the molecular background, as reflected in the higher dust temperature in the Rim (cf. Fig. 6.1).

Spectra along the line cut reveal complex dynamics of the gas, and potentially foreground or self-absorption of the [C II] line, that can effect the cooling and heating efficiency in this region. The CO(2-1) intensity peaks strongly between 8 and 10 arcmin. Those are the points (positions V1 and V2) that show deviating characteristics in the study of Boersma et al. (2012), that is a shift in peak position and line width. Positions V1 and V2 positions also exhibit a higher fullerene-to-PAH ratio than other positions. CO pv diagrams reveal dynamic structures in this region. While those structures are more manifest in CO, spectra towards selected regions reveal weaker corresponding [C II] components (cf. Fig. 6.24, spectra 7 and 8). FIR emission seems to be dominated by re-radiation of FUV photons from θ^1 Ori C and/or θ^2 Ori A, as concluded from the persistent decline in FIR intensity.

6.5 Conclusion

In Paper I, we have studied the correlations of the [C II] intensity with the dust continuum intensity at 70 μm, the FIR intensity (40-500 μm), PAH 8 μm intensity, and CO(2-1) intensity in the Orion Nebula complex. Here, we have focused on these same correlations divided into several subregions (Veil Shell, OMC4, M43, and NGC 1977, further divided up into more subregions). Typically, the observed correlations show only minor variations between these regions. However, the [C II]-CO(2-1) correlations are very different between the regions as they are very sensitive to the geometry. The geometric complexity of these regions is quite apparent when examining individual spectra towards several representative regions. We have compared the observations with constant-density PDR models and concluded that, in general, the edge-on PDR models are able to reproduce the observed intensities, while face-on PDR models cannot explain the observations. The estimated physical parameters, that serve as model inputs, correspond to a constant $p_{\rm th}/G_0$ ratio, which has been observed towards several other PDRs, as well. We have explicated the origin of the [C II] emission within the mapped area in greater detail than in Paper I, focusing on the detailed PDR processes and source properties. Furthermore, we have compared the properties of PAHs in the southeast of the Orion Bar (as measured by *Spitzer*) to the [C II] cooling efficiency, but do not find a correlation between the two: While the [C II] cooling efficiency varies with distance from the Orion Bar, the PAH properties (e.g., size and charge) do not do so. Future studies may include the [O I] 63 μm and 145 μm cooling lines and alter the picture obtained by the study of the [C II] 158 μm line alone. Moreover, the James Webb Space Telescope (JWST) will be able to measure ISM/PAH properties with higher accuracy, and these results may shine further light on the observed variations in the cooling efficiency.

Acknowledgements

This work is based on observations made with the NASA/DLR Stratospheric Observatory for Infrared Astronomy (SOFIA). SOFIA is jointly operated by the Universities Space Research Association, Inc. (USRA), under NASA contract NNA17BF53C, and the Deutsches SOFIA Institut (DSI) under DLR contract 50 OK 0901 to the University of Stuttgart. JRG thanks the Spanish MCIU for funding support under grant AYA2017-85111-P and PID2019-106110GB-I00. This project has received funding from the European Research Council (ERC) under the European Union's Horizon 2020 research and innovation programme (Grant agreement No. 851435). Research on the interstellar medium at Leiden Observatory is supported through a Spinoza award of the Dutch Science Organisation (NWO). We thank C. R. O'Dell for constructive discussions and S. T. Megeath for helpful advice. This work made use of the TOPCAT software (Taylor 2005).

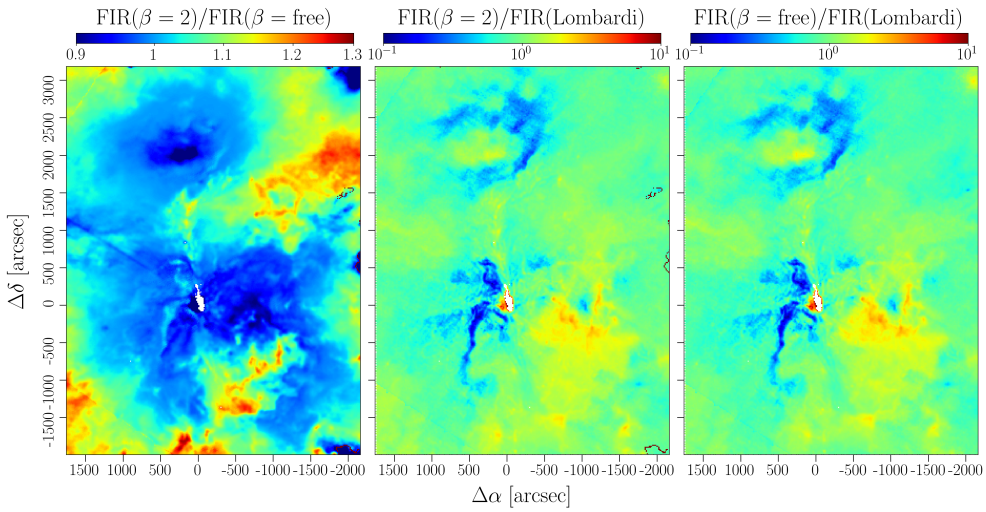

Figure 6.25: Ratios of FIR intensity from different SED fits ($\beta = 2$, β free and the Lombardi et al. (2014) result).

6.A Comparison with Lombardi SED fits

As opposed to Lombardi et al. (2014), we include the shorter-wavelength PACS 70 μm and 100 μm bands, since we do not expect them to be opaque in the extended structures we are mainly interested in. In fact, the extended shell of the Orion Nebula has $\tau_{160} < 10^{-2}$, which translates into $\tau_{70} < 3 \times 10^{-2}$; even the densest cores along the ISF are described by $\tau_{160} \lesssim 10^{-1}$. Comparing our derived FIR intensity, we note that it agrees with the FIR intensity computed from the SED maps of Lombardi et al. (2014), except in the bright eastern arm, the Rim, and the bubble edge of NGC 1973, 1975, and 1977. Here, we obtain significantly lower FIR intensity than Lombardi et al. (2014) (cf. Fig. 6.25). These filaments contain warmer dust that is only captured by the shorter-wavelength bands, leading Lombardi et al. (2014) to derive too high a dust temperature and too low a dust optical depth. Lombardi et al. (2014) obtain higher dust temperatures in the Eastern Rim, yet significantly lower dust optical depth.

Figs. 6.25 and 6.26 show the ratios of the results of different SED fits performed on the region of the EON. Fig. 6.25 shows the ratios of the FIR intensity of our $\beta = 1.5$ SED fit, an SED fit where we let β a free parameter, and the Lombardi et al. (2014) result. Fig. 6.26 shows the ratios of the dust temperatures from these same fits. From the right-hand panel it becomes obvious that the fit of Lombardi et al. (2014) yields significantly higher FIR intensity and dust temperature in the brightest parts of the EON, especially the eastern Rim, the OMC1 region and M43. This might be due to the fact that Lombardi et al. (2014) uses only the longer wavelength bands, that do not capture the peak of the SED of the warmer dust in these bright regions. This apparently results in an overestimation of the dust temperature and consequentially of the FIR intensity.

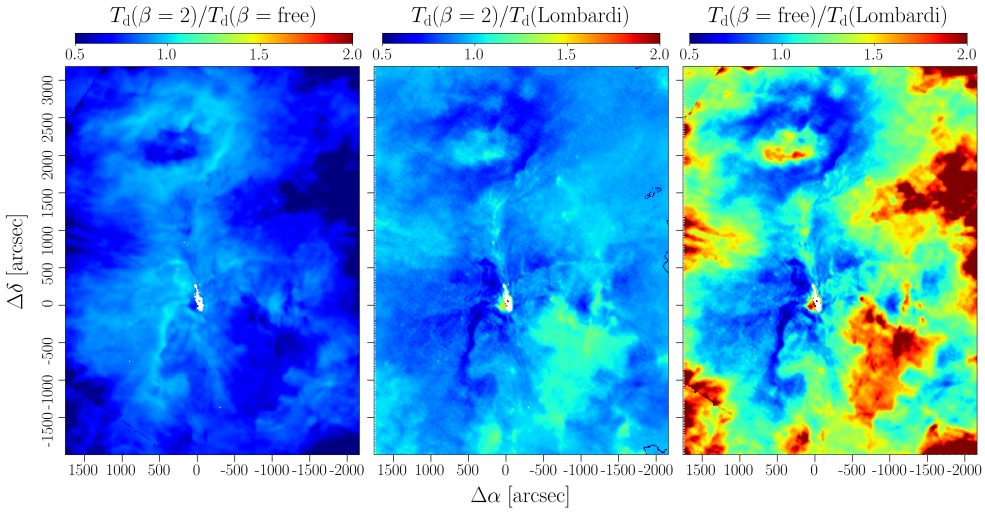

Figure 6.26: Ratios of the dust temperature T_d from different SED fits ($\beta = 2$, β free and the Lombardi et al. (2014) result).

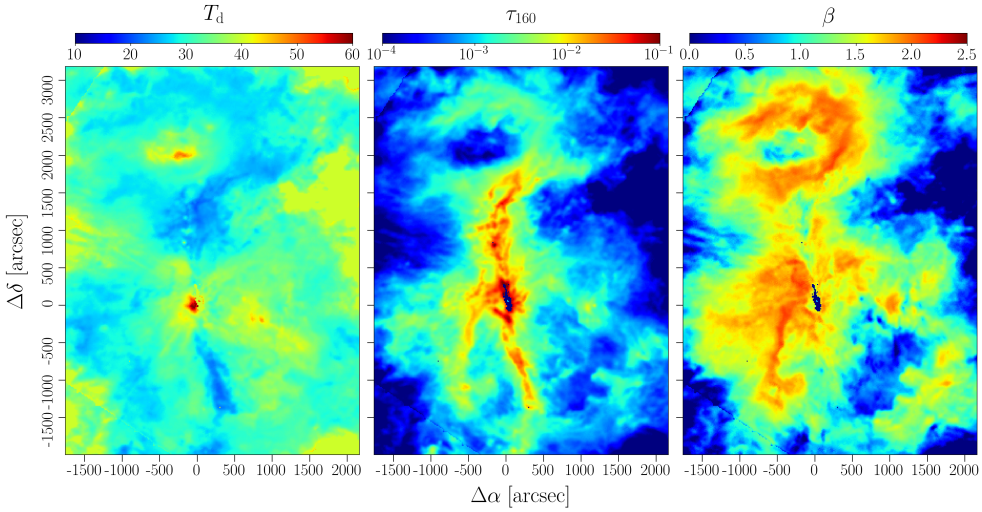

Figure 6.27: Maps of the three SED fit output parameters T_d, τ_{160} and β.

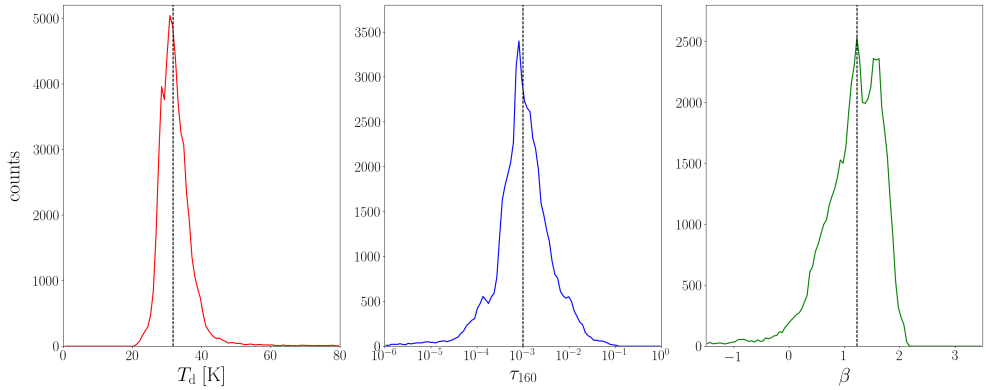

Figure 6.28: Histograms of the three SED fit output parameters T_d, τ_{160} and β. Dashed black lines indicate the median values ($\hat{T}_\mathrm{d} \simeq 31.7\,\mathrm{K}$, $\hat{\tau}_{160} \simeq 1.0 \times 10^{-3}$, $\hat{\beta} \simeq 1.23$).

6.B Correlation plots from free-β SED fit

In this section, we present the correlation plots of results of an SED fit where we let the grain emissivity index β be a free parameter. Fig. 6.27 shows the resulting maps of the three SED output parameters T_d, τ_{160} and β. From this figure, we notice that there seems to be a rather tight correlation between the resulting β and τ_{160}, which we quantify in Fig. 6.32.

Most of the pixels seem to be consistent with a β of $\simeq 1.5$, as suggested by Lombardi et al. (2014). The latter use low-resolution *Planck* images to constrain β, which amounts to $\beta \simeq 1.6$ in the Orion Nebula complex. The median of all pixels in our SED fit is β of $\simeq 1.2$, but when including only pixels with $\tau_{160} > 5 \times 10^{-4}$, which comprise most of the visible structure, the median shifts to β of $\simeq 1.4$. The peak values, around which the β values are clustered, is $\beta \simeq 1.6$. Standard models, however, suggest $\beta \simeq 2$ (Weingartner & Draine 2001). The study of Extaluze et al. (2013) suggests varying β according to the environment (radiation field). We note that β can be affected by the presence of an additional warm dust population in the hot gas and we determine low β in the EON cavity.

In ratio plots of the dust temperature from the three different SED fits, shown in Fig. 6.26, shell structures and interior show distinct deviations from unity, seemingly confirming the assumption that dust properties and, hence, β indeed vary with environment (cf. Extaluze et al. 2013). Denser, warmer structures close to the Trapezium stars seem to be characterized by $\beta \gtrsim 2$, while the extended shell has $\beta \simeq$ 1-2 and the dilute shell interior $\beta \simeq$ 0-1.

In histograms of the SED output parameters (Fig. 6.28), the dust temperature lies mostly in the range of $T_\mathrm{d} \simeq$ 20-50 K, dust opacity can be mostly found in $\tau_{160} \simeq 10^{-4}$-$10^{-2}$, and the grain emissivity index varies mostly between $\beta \simeq$ 0-2, yet with a significant tail of negative values. The latter correspond to areas with little FIR emission and thus poor fit results.

In Fig. 6.29, we clearly see that the dust temperature decreases with increasing distance from the presumably dominant heating source θ^1 Ori C. Points corresponding to lower τ_{160} tend to be more distant and scatter around the mean dust temperature.

From Fig. 6.30, we conclude that also in a free-β SED fit there is no correlation between the resulting dust temperature and optical depth. Independent of τ_{160}, most

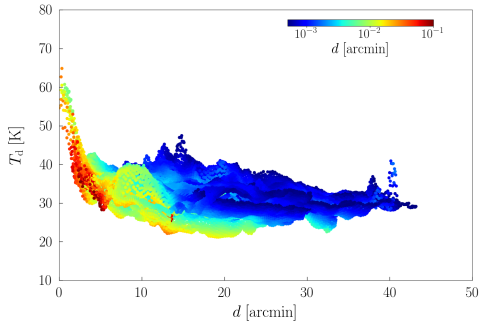

Figure 6.29: Dust temperature T_d from an SED fit with β a free parameter versus distance from θ^1 Ori C. Colors code the dust optical depth for $\tau_{160} > 5 \times 10^{-4}$.

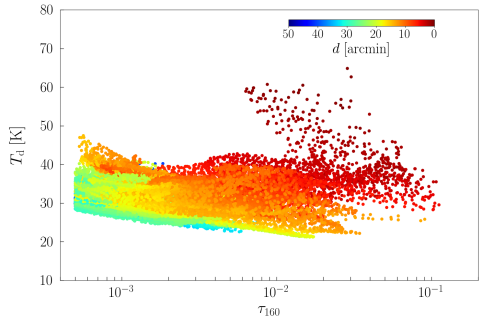

Figure 6.30: Dust temperature T_d versus dust optical depth $\tau_{160}(> 5 \times 10^{-4})$ in a SED fit with β a free parameter ($\rho \simeq 0.11$). Colors code the distance from θ^1 Ori C.

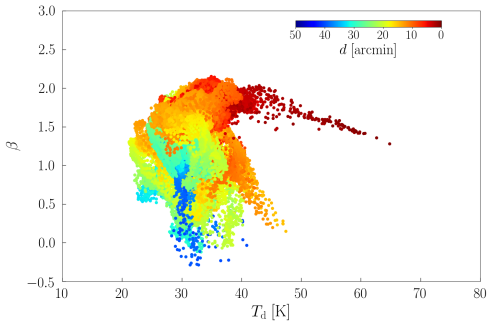

Figure 6.31: Dust temperature T_d versus grain emissivity index β for $\tau_{160} > 5 \times 10^{-4}$ ($\rho \simeq 0.00$). Colors code the distance from θ^1 Ori C.

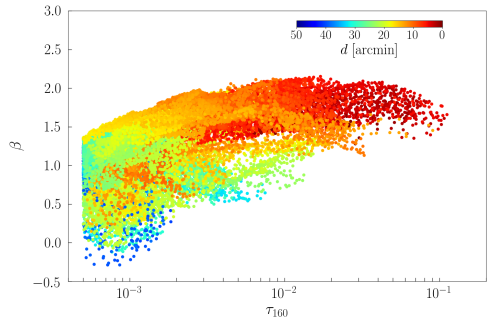

Figure 6.32: Dust optical depth $\tau_{160}(> 5 \times 10^{-4})$ versus grain emissivity index β ($\rho \simeq 0.32$). Colors code the distance from θ^1 Ori C.

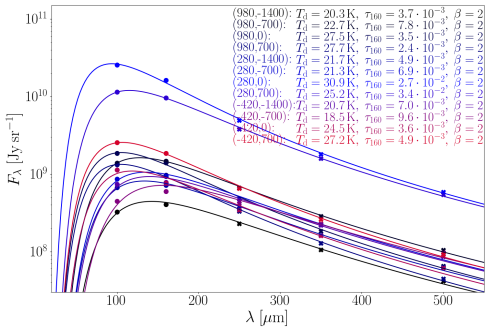

Figure 6.33: SED fits to single pixels with $\beta = 2$.

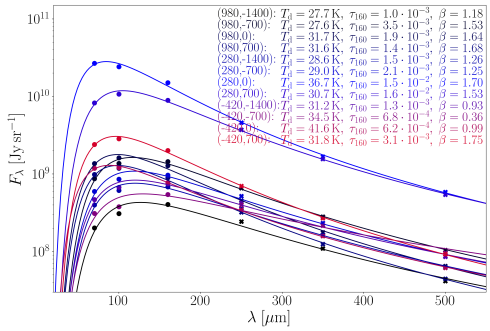

Figure 6.34: SED fits to single pixels with free β.

of the data points scatter around the mean dust temperature $T_\mathrm{d} \simeq 31.4\,\mathrm{K}$ with a standard deviation of $\sigma_{T_\mathrm{d}} \simeq 4.0\,\mathrm{K}$.

There is no correlation between T_d and β, as can be seen from Fig. 6.31. The mean grain emissivity index is $\beta \simeq 1.33$, but with significant scatter around this value.

The correlation between τ_{160} and β has a significant slope (Fig. 6.32), even though there is substantial scatter, which amounts to a correlation index of only $\rho \simeq 0.32$. Deeper structures tend to have higher β, but this is not reflected in dust temperature, as discussed above. This might be due to the fact that deeper structures also contain colder gas along with warmer (surface) gas, which leads to a relative suppression of the long-wavelength tail, resulting in a higher β.

6.C SED fits to single points

Figure 6.33 shows SED fits with $\beta = 2$ towards representative points. Fig. 6.34 shows SED fits where we let β vary freely for the same selection of points.

6.D Spectral line fits

6.D.1 M42

Spectrum 1 (Eastern Rim, north) exhibits two [C II] main components. Both can be observed in [^{13}C II], as well. From the fit results, we obtain two rather different results: The $7.3\,\mathrm{km\,s^{-1}}$ yields a moderate excitation temperature, while the $10.5\,\mathrm{km\,s^{-1}}$ component seems to arise in very warm gas. The latter than traces only a very small column, while the former traces one third of the dust-traced column. Despite the high temperature, the second component displays a very narrow emission line, where the line broadening appears to be almost thermal. The origin of this component is unclear. In channel maps, it seems to be connected to the OMC1 core, that has a bright eastern extension at that velocity.

The bright [C II] emission in spectrum 2 (Eastern Rim, south) requires an incident radiation field of $G_0 \simeq 10^4$ (from models). The excitation temperatures we derive from the [^{13}C II] line (two components) are not extreme. Both components trace about 15% of the dust column. While the [C II] components are relatively narrow, the high-velocity ^{12}CO and ^{13}CO components emit rather broad lines. We do not observe

Table 6.8: Line fits to [C II]-bright spectra 1-6 in M42.

spectrum	line	comp. #	$T_{\rm P}$ [K]	$v_{\rm P}$ [km s^{-1}]	$\Delta v_{\rm FWHM}$ [km s^{-1}]
1	[C II]	1	35.1	7.4	2.3
		2	56.0	10.4	1.4
	[^{13}C II]	1	1.3	7.1	5.2
		2	0.7	10.6	3.0
	^{12}CO	1	12.8	7.3	2.5
		2	47.1	11.0	3.0
	^{13}CO	1	4.2	6.7	2.3
		2	28.9	11.2	1.8
2	[C II]	1	4.3	2.1	1.6
		2	50.7	7.9	1.5
		3	19.0	11.7	1.7
	[^{13}C II]	2	1.4	7.7	2.3
		3	0.6	10.6	2.0
	^{12}CO	1	23.4	8.8	3.9
		2	28.2	12.5	3.6
	^{13}CO	1	4.5	7.5	1.4
		2	3.7	11.9	3.7
3	[C II]	1	2.6	-0.6	14.0
		2	7.5	1.2	3.5
		3	76.3	7.8	3.0
		4	32.9	10.6	2.5
	[^{13}C II]	2	1.0	8.3	2.5
	^{12}CO	1	2.2	-0.3	2.4
		2	83.5	8.4	3.7
		3	41.8	11.3	2.1
	^{13}CO	1	29.4	9.1	3.5
		2	12.0	11.1	1.1
4	[C II]	1	4.5	-1.0	4.4
		2	2.2	3.2	2.4
		3	25.7	9.1	3.3
	^{12}CO	1	52.5	9.3	4.2
	^{13}CO	1	19.5	9.4	3.4
5	[C II]	1	10.7	7.3	2.2
		2	3.4	8.9	0.8
	^{12}CO	1	36.7	7.8	3.3
		2	9.5	10.6	2.0
	^{13}CO	1	15.0	8.0	2.9
6	[C II]	1	1.2	-2.9	4.6
		2	6.3	8.0	1.8
	^{12}CO	1	27.4	8.2	3.8
	^{13}CO	1	15.8	8.0	2.8

Notes. Line fit uncertainties are of the order $\sigma_{T_{\rm P}} \simeq 0.5\,{\rm K}$, $\sigma_{v_{\rm P}} \simeq 0.1\,{\rm km\,s^{-1}}$, and $\sigma_{v_{\rm FWHM}} \simeq 0.1\,{\rm km\,s^{-1}}$.

Table 6.9: Parameters and results of [^{13}C II] analysis in M42.

spectrum, comp.	$T_{\rm P}([^{12}{\rm C\,II}])$ [K]	$T_{\rm P}([^{13}{\rm C\,II}])$ [K]	Δv [km s^{-1}]	$T_{\rm d}$ [K]	τ_{160}	$\tau_{[{\rm C\,II}]}$	$T_{\rm ex}$ [K]	$N_{\rm C^+}$ [cm^{-2}]	$N_{\rm C^+}/\mathcal{A}_{\rm C}/N_{\rm H}$
1, 1	35	1.3	2.3	37	1×10^{-2}	3.9	81	3.0×10^{18}	0.32 ($A_{\rm V,los}\simeq10$)
1, 2	56	0.7	1.4	37	1×10^{-2}	0.6	171	6.3×10^{17}	0.07 ($A_{\rm V,los}\simeq2$)
2, 2	51	1.4	1.5	34	1×10^{-2}	2.8	100	1.7×10^{18}	0.18 ($A_{\rm V,los}\simeq5$)
2, 3	19	0.6	1.7	34	1×10^{-2}	3.3	61	1.4×10^{18}	0.15 ($A_{\rm V,los}\simeq4$)
3	76	1.0	3.0	29	5×10^{-2}	0.7	192	1.8×10^{18}	0.04 ($A_{\rm V,los}\simeq6$)

Notes. Line fit uncertainties are of the order $\sigma_{T_{\rm P}}\simeq0.5$ K. $T_{\rm P}([^{13}{\rm C\,II}])$ is barely above the noise level and is uncertain by $\sigma_{T_{\rm P}}\simeq0.3$ K.

a significant broad [C II] component that might stem from the ionized gas, that is seen in Hα towards this region. It is not certain how additional possible sources (e.g. T Ori) affect the excitation and dynamics in this region.

The bright [C II] emission of spectrum 3 (south of OMC1, north of OMC4) consists of two components. Despite the strong main [C II] line, the [^{13}C II] line is very weak. This indicates rather low optical depth, but high temperature. Because of the relatively weak [^{13}C II] line, it is unlikely that the main [C II] line is self- or foreground absorbed. Rather, we fit two emission components. We can only detect the brighter component in [^{13}C II]. This [C II] component traces only a small fraction of the total dust column. The high temperature is reflected in the associated very bright CO emission (with a broad ^{13}CO line), that traces a 4 times larger gas column than [C II] ($A_{\rm V,los}\simeq40$). The other CO component, associated with the fainter [C II] main component, seems to arise in relatively more moderate conditions (narrow ^{13}CO line) and seems to trace only a thin ($A_{\rm V,los}\simeq3$) layer of gas. In addition to the strong main line, we observe a very broad component in the [C II] spectrum at negative velocities, that possibly stems from ionized gas expanding towards the observer.

The brighter [C II] components require very extreme conditions, according to the standard models of the PDR Toolbox (Kaufman et al. 2006; Pound & Wolfire 2008). Also in the central regions of the Orion Nebula, the [C II] intensity is higher than expected from standard PDR models. Constant pressure models, as opposed to constant density models, might hold clues to the reason for this behavior.

In spectrum 4 (west of Orion S), we observe a single bright [C II] main component, well separated from two weak low-velocity components. Also the CO spectra reveal only one component. In the region of spectrum 4, we observe the lower branch of the [C II]-FIR correlation in the ISF (although this region lies adjacent to the main spine). Despite the face-on geometry in this area, the [C II] emission lies above the model predictions. We cannot exclude a tilted surface, however. If we assume optically thick [C II] emission, we compute an excitation temperature of $T_{\rm ex}=64$ K. The CO excitation temperature is only slightly lower and both emissions need rather high radiation field and density (from the models). The ^{13}CO line is rather broad, which hints at elevated turbulence. The CO emission traces a large column of gas, $A_{\rm V,los}\simeq20$, which is 1/5 of the dust-traced column. The dust temperature is rather moderate ($T_{\rm d}=27$ K), the background consisting of a large column of cold dust. From the FIR intensity we estimate a radiation field of $G_0\simeq4\times10^3$, which is 2-3 times lower than required for the [C II] and CO intensity according to the models.

In spectra 5 and 6 (south of OMC4 in the ISF), we notice that the CO excitation temperature is further decreasing with distance from the Trapezium. The CO column

density remains constant, CO tracing a column of $A_{\rm V,los} \simeq 10$. From comparison with the [C II] emission, we see that G_0 is dropping, but n remains approximately constant, $n \simeq$ 1-5 $\times 10^4\,{\rm cm}^{-3}$.

6.D.2 M43

All spectra have too strong [C II] emission as to be consistent with face-on geometry. The column traced by [C II] corresponds to $A_{\rm V,los} \simeq 15$ in most cases. This clearly indicates an edge-on illuminated gas column, given the rather moderate radiation field in M43. Most spectra, both [C II] and CO, consist of at least two components. Spectrum 5 is the most enigmatic. The [C II] spectrum can be fitted only with four components plus one component that we attribute to [^{13}C II] emission (it could be a red-shifted [^{12}C II] component, as well). However, the [^{13}C II] component appears to be rather strong compared to the [^{12}C II] component, which yields a very high [C II] optical depth. The ^{12}CO spectrum clearly comprises two components, but cannot be fitted satisfactorily with Gaussian profiles, while the ^{13}CO spectrum can. We note that spectrum 5 lies in a region where the shell surrounding the M43 H II region seems to be interrupted, possibly allowing for ionized gas flowing out of the cavity. Outflows may lead to irregular line shapes in the surface layers of a molecular cloud. However, we do not observe a broad component in the [C II] spectrum, that might stem from the ionized gas itself. The fact that most spectra comprise more than one emission component may indicate that the gas layers along the line of sight experience shear due to stellar feedback. We judge that the spectra in M43 can be explained by emitting components only, rather than invoking additional absorbing layers.

6.D.3 NGC 1977

The CO component at 8 km s^{-1} in spectrum 2 corresponds to a weak [C II] component, that cannot be fitted properly because it is just above the noise level. Again, it is unlikely that ^{13}CO is self-absorbed, hence we conclude that there are two emitting CO components within the line of sight.

The [C II] line in spectrum 3 is almost Gaussian, but slightly asymmetric. In a two-component fit the [C II] components line up with the CO components. This might indicate that the shell around NGC 1977 is indeed moving at differential velocities and that CO emission arises within the shell at low density. The cloud depth derived from the ^{13}CO line is about $A_{\rm V,los} \simeq$ 0.1-0.4.

The [C II] line in spectrum 4 is slightly asymmetric. The line widths in a two-component fit are close to the thermal line width, as in spectrum 3. We do not find a good fit with an absorbing component instead of a second emitting component. Since we expect the region to be in dynamic expansion, we may expect line asymmetries, and the Gaussian two-component fit may be misleading.

Also the [C II] line in spectrum 5 has a relatively (close to thermal) line width, but an additional broad wing. Spectrum 5 is taken towards the [C II]-faint region, where the shell may be breaking open. The broad wing might be a signature of an ionized outflow or increased turbulence in the neutral gas due to the rupture (as in M43). The narrow line in spectrum 5 is blue-shifted with respect to the lines in other [C II] spectra towards NGC 1977, possibly reflecting an increased backward pressure in this region.

The [C II] line in spectrum 6 is slightly asymmetric, as well, and can be fitted with two Gaussian components.

Table 6.10: Line fits to spectra 1-6 in M43.

spectrum	line	comp. #	$T_{\rm P}$ [K]	$v_{\rm P}$ [km s^{-1}]	$\Delta v_{\rm FWHM}$ [km s^{-1}]
1	[C II]	1	73.9	8.7	3.9
		2	29.5	9.8	1.5
	[^{13}C II]	1	2.7	8.7	2.0
	^{12}CO	1	19.9	8.7	2.6
		2	9.4	11.2	2.8
	^{13}CO	1	3.1	9.2	3.4
		2	0.4	11.1	2.1
2	[C II]	1	21.8	5.5	3.5
		2	82.7	9.1	3.6
	[^{13}C II]	2	2.1	8.5	2.3
	^{12}CO	1	85.4	10.0	3.7
	^{13}CO	1	19.6	10.1	2.6
3	[C II]	1	17.5	5.6	3.6
		2	67.3	10.0	3.7
	[^{13}C II]	2	1.0	9.5	3.4
	^{12}CO	1	3.1	6.8	1.9
		2	59.4	10.8	2.5
	^{13}CO	1	0.8	7.8	1.7
		2	15.2	10.6	1.6
4	[C II]	1	32.4	8.7	5.5
		2	45.2	11.0	2.6
	^{12}CO	1	9.0	10.6	4.3
		2	42.9	10.7	1.4
	^{13}CO	1	1.8	10.5	3.6
		2	6.8	10.7	1.1
5	[C II]	1	20.9	6.9	4.1
		2	22.9	10.3	3.0
	[^{13}C II]	1	2.1	6.2	1.7
	^{12}CO	1	13.1	9.7	3.9
		2	0.97	11.4	1.3
	^{13}CO	1	3.2	9.3	2.6
		2	1.2	11.2	1.4
6	[C II]	1	3.7	5.4	1.6
		2	72.1	9.7	3.5
		3	5.3	12.6	5.6
	[^{13}C II]	2	1.7	9.6	2.3
	^{12}CO	1	2.4	6.2	1.8
		2	57.9	9.4	2.5
		3	7.2	12.4	1.5
	^{13}CO	1	1.0	7.3	2.0
		2	18.8	9.4	1.5
		3	2.0	10.2	3.4

Notes. Line fit uncertainties are of the order $\sigma_{T_{\rm P}} \simeq 0.5\,{\rm K}$, $\sigma_{v_{\rm P}} \simeq 0.1\,{\rm km\,s^{-1}}$, and $\sigma_{v_{\rm FWHM}} \simeq 0.1\,{\rm km\,s^{-1}}$.

Table 6.11: Parameters and results of [^{13}C II] analysis in M43.

spectrum	$T_{\rm P}$([^{12}C II]) [K]	$T_{\rm P}$([^{13}C II]) [K]	Δv [km s^{-1}]	$T_{\rm d}$ [K]	τ_{160}	$\tau_{\rm [C\,II]}$	$T_{\rm ex}$ [K]	$N_{\rm C^+}$ [cm^{-2}]	$N_{\rm C^+}/\mathcal{A}_{\rm C}/N_{\rm H}$
1	74	2.7	3.9	37	1×10^{-2}	3.8	124	7.7×10^{18}	0.61 ($A_{\rm V,los}\simeq25$)
2	83	2.1	3.6	36	2×10^{-2}	2.5	139	5.2×10^{18}	0.36 ($A_{\rm V,los}\simeq15$)
3	67	1.0	3.7	38	9×10^{-3}	1.1	149	2.6×10^{18}	0.30 ($A_{\rm V,los}\simeq10$)
5	21	2.1	1.7	37	5×10^{-3}	11	64	5.0×10^{18}	1.03 ($A_{\rm V,los}\simeq15$)
6	72	1.7	3.5	34	1×10^{-2}	2.2	127	4.2×10^{18}	0.36 ($A_{\rm V,los}\simeq15$)

Notes. Line fit uncertainties are of the order $\sigma_{T_{\rm P}}\simeq0.5$ K.

Table 6.12: Line fits to spectra 1-6 in NGC 1977.

spectrum	line	comp. #	$T_{\rm P}$ [K]	$v_{\rm P}$ [km s^{-1}]	$\Delta v_{\rm FWHM}$ [km s^{-1}]
1	[C II]	1	141.2	11.7	2.9
		2	-101.1	12.0	2.2
	[^{13}C II]	1	3.0	11.6	2.0
	^{12}CO	1	15.6	11.7	2.1
		2	33.2	12.7	1.4
	^{13}CO	1	5.0	11.1	1.0
		2	20.2	12.6	1.1
2	[C II]	1	(1.0)	(8.0)	(2.0)
		2	32.8	11.4	2.6
	^{12}CO	1	0.3	8.0	1.5
		2	1.0	11.0	1.1
		3	1.1	11.5	3.0
	^{13}CO	1	0.09	8.7	2.6
		2	0.38	11.1	1.2
		3	0.22	12.7	1.2
3	[C II]	1	12.7	11.2	1.6
		2	27.4	12.7	1.9
	^{12}CO	1	0.61	11.7	3.1
		2	0.52	12.6	1.5
	^{13}CO	1	0.14	11.1	2.4
		2	0.12	12.7	0.7
4	[C II]	1	11.1	11.6	1.3
		2	19.0	12.7	2.0
5	[C II]	1	2.1	11.6	5.1
		2	3.8	13.7	1.5
6	[C II]	1	22.8	11.6	3.1
		2	5.2	12.7	1.0

Notes. Line fit uncertainties are of the order $\sigma_{T_{\rm P}}\simeq0.5$ K, $\sigma_{v_{\rm P}}\simeq0.1$ km s^{-1}, and $\sigma_{v_{\rm FWHM}}\simeq0.1$ km s^{-1}.

Table 6.13: Parameters and results of [^{13}C II] analysis in NGC 1977.

spectrum	$T_{\rm P}$([^{12}C II]) [K]	$T_{\rm P}$([^{13}C II]) [K]	Δv [km s^{-1}]	$T_{\rm d}$ [K]	τ_{160}	$\tau_{\rm [C\,II]}$	$T_{\rm ex}$ [K]	$N_{\rm C^+}$ [cm^{-2}]	$N_{\rm C^+}/\mathcal{A}_{\rm C}/N_{\rm H}$
1	141	3.0	2.9	31	1×10^{-2}	2.0	211	5.2×10^{18}	0.42 ($A_{\rm V,los}\simeq15$)

Notes. Line fit uncertainties are of the order $\sigma_{T_{\rm P}}\simeq0.5$ K.

Table 6.14: Line fits to spectra 1-10 in the southeast of the Orion Bar.

spectrum	line	comp. #	T_P [K]	v_P [km s^{-1}]	Δv_{FWHM} [km s^{-1}]
1	[C II]	1	35.3	9.1	5.1
		2	117.8	10.9	3.0
	[^{13}C II]	2	3.4	11.0	2.5
	^{12}CO	1	115.6	9.9	4.0
		2	35.3	11.3	1.9
	^{13}CO	1	7.6	9.9	4.2
		2	35.3	10.1	2.1
2	[C II]	1	52.1	9.9	4.4
		2	62.3	11.5	2.6
	[^{13}C II]	2?	3.0	10.6	1.9
	^{12}CO	1	93.5	9.5	3.7
		2	23.0	10.9	2.2
	^{13}CO	1	1.4	7.0	1.2
		2	27.4	9.8	2.4
3	[C II]	1	54.0	10.6	4.0
		2	30.4	12.0	2.0
	^{12}CO	1	55.3	9.0	2.1
		2	49.0	10.9	2.3
	^{13}CO	1	8.0	8.9	1.2
		2	10.1	10.6	2.0
4	[C II]	1	3.1	2.2	15.9
		2	61.7	11.1	3.1
	^{12}CO	1	50.6	10.0	3.6
		2	12.0	11.6	1.8
	^{13}CO	1	6.4	10.2	3.2
		2	4.2	11.3	1.5
5	[C II]	1	2.3	-0.9	16.2
		2	56.4	10.9	2.9
	^{12}CO	1	27.7	8.9	4.3
		2	24.5	11.5	2.5
	^{13}CO	1	3.2	9.4	4.3
		2	2.2	11.7	2.0
6	[C II]	1	1.8	-0.6	19.6
		2	28.7	10.3	3.7
	^{12}CO	1	7.1	7.2	2.3
		2	25.8	10.6	4.5
	^{13}CO	1	0.6	6.9	2.1
		2	2.3	10.4	3.7
7	[C II]	1	4.4	7.5	3.2
		2	19.7	10.5	2.7
		3	2.3	14.3	1.1
	^{12}CO	1	7.0	6.9	2.1
		2	28.6	10.4	2.6
		3	24.2	14.4	4.3
	^{13}CO	1	0.8	7.0	1.9
		2	2.0	10.3	2.9
		3	2.7	14.8	2.9
8	[C II]	1	14.1	8.3	4.8
		2	13.1	10.7	1.8
		3	(1.0)	(13.0)	(4.0)
	^{12}CO	1	7.3	7.7	3.0
		2	45.8	10.8	1.9
		3	21.4	13.1	3.5
	^{13}CO	1	0.8	7.8	2.9
		2	7.7	10.9	1.5
		3	2.5	13.5	2.6
9	[C II]	1	9.5	5.9	7.8
		2	26.7	6.1	1.8
		3	49.6	8.0	1.7
	[^{13}C II]	2/3	2.3	6.8	4.1
	^{12}CO	1	30.6	7.2	1.6
		2	4.8	10.6	4.8
	^{13}CO	1	6.9	7.3	1.1
		2	0.5	9.7	6.0
10	[C II]	1	20.2	7.0	4.5
		2	26.4	8.0	1.8
	[^{13}C II]	2	3.0	7.9	1.6
	^{12}CO	1	66.0	7.3	1.8
		2	4.2	11.1	3.0
		1	23.1	7.4	1.3
	^{13}CO	2	0.6	10.9	2.6

Notes. Line fit uncertainties are of the order $\sigma_{T_P} \simeq 0.5\,\mathrm{K}$, $\sigma_{v_P} \simeq 0.1\,\mathrm{km\,s^{-1}}$, and $\sigma_{v_{FWHM}} \simeq 0.1\,\mathrm{km\,s^{-1}}$.

6.D.4 Spectra behind the Bar

Spectra with bright [C II] emission, where we can detect the [^{13}C II] $F = 2$-1 line, can be interpreted as exhibiting a significant absorbing component. However, invoking an absorbing component gives rise to rather extreme derived excitation condition, which we do not expect behind the Orion Bar and in the Eastern Rim. As the [^{13}C II] line is often only marginally detected, fit uncertainties are large. Deeper observations are needed to investigate this matter further (Kabanovic et al. in prep.). All spectra along the line cut behind the Orion Bar show multiple features, that are enigmatic in origin. A more detailed study, comparing with velocity-resolved data sets like CO rotational lines, optical and dust emission, would be needed to understand the structure of the background PDR and the Eastern Rim. We report here that the relation between [C II] and CO(2-1) emission is complex, as components in the respective spectra are not easy to match with each other.

Table 6.15: Parameters and results of [^{13}C II] analysis of spectra to the southeast of the Orion Bar.

spectrum	$T_{\rm P}([^{12}{\rm C\,II}])$ [K]	$T_{\rm P}([^{13}{\rm C\,II}])$ [K]	Δv [km s^{-1}]	$T_{\rm d}$ [K]	τ_{160}	$\tau_{[{\rm C\,II}]}$	$T_{\rm ex}$ [K]	$N_{\rm C^+}$ [cm^{-2}]	$N_{\rm C^+}/\mathcal{A}_{\rm C}/N_{\rm H}$
1	118	3.4	2.5	38	3.0×10^{-2}	2.9	175	5.4×10^{18}	0.32 ($A_{\rm V,los} \simeq 15$)
2	62	1.9	2.9	37	1.8×10^{-2}	3.1	113	4.3×10^{18}	0.25 ($A_{\rm V,los} \simeq 15$)
9	50	1.8	1.7	33	0.9×10^{-2}	3.8	95	2.6×10^{18}	0.30 ($A_{\rm V,los} \simeq 10$)
10	26	1.1	1.8	30	1.0×10^{-2}	4.4	67	2.2×10^{18}	0.23 ($A_{\rm V,los} \simeq 10$)

Notes. Line fit uncertainties are of the order $\sigma_{T_{\rm P}} \simeq 0.5$ K.

Bibliography

Abdullah, A. & Tielens, A. G. G. M. 2020, A&A, 639, A110

Abel, N. P., Brogan, C. L., Ferland, G. J., et al. 2004, ApJ, 609, 247

Abel, N. P., Dudley, C., Fischer, J., Satyapal, S., & van Hoof, P. A. M. 2009, ApJ, 701, 1147

Abel, N. P., Ferland, G. J., & O'Dell, C. R. 2019, ApJ, 881, 130

Abel, N. P., Ferland, G. J., O'Dell, C. R., & Troland, T. H. 2016, ApJ, 819, 136

Abel, N. P., Ferland, G. J., Shaw, G., & van Hoof, P. A. M. 2005, ApJS, 161, 65

Abergel, A., Teyssier, D., Bernard, J. P., et al. 2003, A&A, 410, 577

Allen, C., Costero, R., Ruelas-Mayorga, A., & Sánchez, L. J. 2017, MNRAS, 466, 4937

Allers, K. N., Jaffe, D. T., Lacy, J. H., Draine, B. T., & Richter, M. J. 2005, ApJ, 630, 368

Andrews, H., Peeters, E., Tielens, A. G. G. M., & Okada, Y. 2018, A&A, 619, A170

Arab, H., Abergel, A., Habart, E., et al. 2012, A&A, 541, A19

Arthur, S. J. 2012, MNRAS, 421, 1283

Bakes, E. L. O. & Tielens, A. G. G. M. 1994, ApJ, 427, 822

Balega, Y. Y., Chentsov, E. L., Rzaev, A. K., & Weigelt, G. 2015, in Astronomical Society of the Pacific Conference Series, Vol. 494, Physics and Evolution of Magnetic and Related Stars, ed. Y. Y. Balega, I. I. Romanyuk, & D. O. Kudryavtsev, 57

Balick, B., Gammon, R. H., & Hjellming, R. M. 1974, PASP, 86, 616

Bally, J. 2008, Overview of the Orion Complex, ed. B. Reipurth, Vol. 4, 459

Bally, J., Chambers, E., Guzman, V., et al. 2018, AJ, 155, 80

Bally, J., Langer, W. D., Stark, A. A., & Wilson, R. W. 1987, ApJ, 312, L45

Balog, Z., Müller, T., Nielbock, M., et al. 2014, Experimental Astronomy, 37, 129

Barinovs, G., van Hemert, M., Krems, R., & Dalgarno, A. 2005, ApJ, 620, 537

Bedijn, P. J. & Tenorio-Tagle, G. 1981, A&A, 98, 85

Bennett, C. L., Fixsen, D. J., Hinshaw, G., et al. 1994, ApJ, 434, 587

Bernard-Salas, J., Habart, E., Arab, H., et al. 2012, A&A, 538, A37

Berné, O., Joblin, C., Deville, Y., et al. 2007, A&A, 469, 575

Berné, O., Marcelino, N., & Cernicharo, J. 2010, Nature, 466, 947

Berné, O., Marcelino, N., & Cernicharo, N. 2014, ApJ, 795, 13

Berné, O. & Matsumoto, Y. 2012, ApJ, 761, L4

Berné, O., Montillaud, J., & Joblin, C. 2015, A&A, 577, A133

Bertoldi, F. 1989, ApJ, 346, 735

Bischetti, M., Piconcelli, E., Feruglio, C., et al. 2018, A&A, 617, A82

Bock, J. J., Hristov, V. V., Kawada, M., et al. 1993, ApJ, 410, L115

Boersma, C., Rubin, R. H., & Allamandola, L. J. 2012, ApJ, 753, 168

Bohlin, R. C., Savage, B. D., & Drake, J. F. 1978, ApJ, 224, 132

Bolatto, A. D., Wolfire, M., & Leroy, A. K. 2013, ARA&A, 51, 207

Boreiko, R. T. & Betz, A. L. 1996, ApJ, 467, L113

Brisbin, D., Ferkinhoff, C., Nikola, T., et al. 2015, ApJ, 799, 13

Bron, E., Agúndez, M., Goicoechea, J. R., & Cernicharo, J. 2018, arXiv e-prints, arXiv:1801.01547

Buckle, J. V., Davis, C. J., di Francesco, J., et al. 2012, MNRAS, 422, 521

Calzetti, D., Kennicutt, R. C., Engelbracht, C. W., et al. 2007, ApJ, 666, 870

Capak, P. L., Carilli, C., Jones, G., et al. 2015, Nature, 522, 455

Carlyle, J. & Hillier, A. 2017, A&A, 605, A101

Castor, J., McCray, R., & Weaver, R. 1975, ApJ, 200, L107

Chevalier, R. A., Blondín, J. M., & Emmering, R. T. 1992, ApJ, 392, 118

Chevance, M., Madden, S. C., Lebouteiller, V., et al. 2016, A&A, 590, A36

Churchwell, E., Povich, M. S., Allen, D., et al. 2006, ApJ, 649, 759

Chuss, D. T., Andersson, B.-G., Bally, J., et al. 2019, ApJ, 872, 187

Crawford, M. K., Genzel, R., Townes, C. H., & Watson, D. M. 1985, ApJ, 291, 755

Croiset, B. A., Candian, A., Berné, O., & Tielens, A. G. G. M. 2016, A&A, 590, A26

Croxall, K. V., Smith, J. D., Wolfire, M. G., et al. 2012, ApJ, 747, 81

Cuadrado, S., Salas, P., Goicoechea, J. R., et al. 2019, A&A, 625, L3

Cubick, M., Stutzki, J., Ossenkopf, V., Kramer, C., & Röllig, M. 2008, A&A, 488, 623

Da Rio, N., Robberto, M., Soderblom, D. R., et al. 2009, ApJ SS, 183, 261

Da Rio, N., Tan, J. C., & Jaehing, K. 2014, ApJ, 795, 55

Dagdigian, P. J. 2019, J. Chem. Phys., 151, 054306

Dale, J. E., Ngoumou, J., Ercolano, B., & Bonnell, I. 2013, MNRAS, 436, 3430

Dale, J. E., Ngoumou, J., Ercolano, B., & Bonnell, I. A. 2014, MNRAS, 442, 694

Dalgarno, A. & McCray, R. A. 1972, ARA&A, 10, 375

De Looze, I., Baes, M., Bendo, G. J., Cortese, L., & Fritz, J. 2011, MNRAS, 416, 2712

Diaz-Miller, I. R., Franco, J., & Shore, S. N. 1998, ApJ, 501, 192

Díaz-Santos, T., Armus, L., Charmandaris, V., et al. 2013, ApJ, 774, 68

Draine, B. T. 2011, Physics of the Interstellar and Intergalactic Medium (Princeton University Press)

Duffell, P. C. 2016, ApJ, 821, 76

Dwek, E. & Arendt, R. G. 1992, ARA&A, 30, 11

Elmegreen, B. G. & Lada, C. J. 1977, ApJ, 214, 725

Evans, Neal J., I., Dunham, M. M., Jørgensen, J. K., et al. 2009, ApJS, 181, 321

Extaluze, M., Goicoechea, J. R., Cernicharo, J., et al. 2013, A&A, 556, A137

Federrath, C. & Klessen, R. S. 2012, ApJ, 761, 156

Field, D., Lemaire, J. L., Pineau des Forets, G., et al. 1998, A&A, 333, 280

Flower, D. R. & Pineau Des Forêts, G. 2010, MNRAS, 406, 1745

Freyer, T., Hensler, G., & Yorke, H. 2006, ApJ, 638, 262

Fuente, A., Rodrıguez-Franco, A., Garcıa-Burillo, S., Martın-Pintado, J., & Black, J. H. 2003, A&A, 406, 899

García-Díaz, M. T. & Henney, W. J. 2007, AJ, 133, 952

García-Díaz, M. T., Henney, W. J., López, J. A., & Doi, T. 2008, Rev. Mexicana Astron. Astrofis., 44, 181

Gatto, A., Walch, S., Naab, T., et al. 2017, MNRAS, 466, 1903

Geen, S., Pellegrini, E., Bieri, R., & Klessen, R. 2020, MNRAS, 492, 915

Genzel, R. & Stutzki, J. 1989a, ARA&A, 27, 41

Genzel, R. & Stutzki, J. 1989b, ARA&A, 27, 41

Genzel, R., Tacconi, L. J., Gracia-Carpio, J., et al. 2010, MNRAS, 407, 2091

Gerin, M., Ruaud, M., Goicoechea, J. R., Gusdorf, A., & Godard, B. 2015, A&A, 573, A30

Goicoechea, J. R., Chavarría, L., Cernicharo, J., et al. 2015a, ApJ, 799, 102

Goicoechea, J. R., Compiègne, M., Habart, E., & Goldsmith, P. 2009, ApJ, 699, L165

Goicoechea, J. R., Cuadrado, S., Pety, J., et al. 2017, A&A, 601, L9

Goicoechea, J. R., Pabst, C. H. M., Kabanovic, S., et al. 2020, A&A, 639, A1

Goicoechea, J. R., Pety, J., Cuadrado, S., et al. 2016, Nature, 537, 207

Goicoechea, J. R., Santa-Maria, M. G., Bron, E., et al. 2019, A&A, 622, A91

Goicoechea, J. R., Teyssier, D., Etxaluze, M., Goldsmith, P. F., & Ossenkopf, V. 2015b, ApJ, 812, 75

Goldsmith, P. F., Langer, W. D., Pineda, J. L., & Velusamy, T. 2012, ApJ Supplement Series, 203, 13

Graciá-Carpio, J., Sturm, E., Hailey-Dunsheath, S., et al. 2011, ApJ, 728, L7

Graf, U. U., Simon, R., Stutzki, J., et al. 2012, A&A, 542, L16

Grellmann, R., Preibisch, T., Ratzka, T., et al. 2013, A&A, 550, A82

Grenier, I. A., Casandjian, J.-M., & Terrier, R. 2005, Science, 307, 1292

Griffin, M. J., Abergel, A., Abreu, A., et al. 2010, A&A, 518, L3

Großschedl, J. E., Alves, J., Meingast, S., et al. 2018, A&A, 619, A106

Großschedl, J. E., Alves, J., Teixeira, P. S., et al. 2019, A&A, 622, A149

Gry, C., Lequeux, J., & Boulanger, F. 1992, A&A, 266, 457

Guan, X., Stutzki, J., Graf, U. U., et al. 2012, A&A, 542, L4

Güdel, M., Briggs, K. R., Montmerle, T., et al. 2008, Science, 319, 309

Habart, E., Abergel, A., Boulanger, F., et al. 2011, A&A, 527, A122

Habart, E., Abergel, A., Walmsley, C., Teyssier, D., & Pety, J. 2005, A&A, 437, 177

Hacar, A., Alves, J., Tafalla, M., & Goicoechea, J. R. 2017, A&A, 602, L2

Haid, S., Walch, S., Seifried, D., et al. 2018, MNRAS, 478, 4799

Heays, A. N., Bosman, A. D., & van Dishoeck, E. F. 2017, A&A, 602, A105

Heiles, C. 1994, ApJ, 436, 720

Henney, W. J. & O'Dell, C. R. 1999, AJ, 118, 2350

Henney, W. J., O'Dell, C. R., Zapata, L. A., et al. 2007, AJ, 133, 2192

Herrera-Camus, R., Bolatto, A. D., Wolfire, M. G., et al. 2015, ApJ, 800, 1

Herrera-Camus, R., Sturm, E., Graciá-Carpio, J., et al. 2018, ApJ, 861, 95

Herrmann, F., Madden, S. C., Nikola, T., et al. 1997, ApJ, 481, 343

Higgins, D. R. 2011, PhD thesis, -

Hillenbrand, L. A. 1997, ApJ, 113, 1733

Hohle, M. M., Neuhauser, R., & Schutz, B. F. 2010, Astron. Nach., 331, 349

Hollenbach, D., Kaufman, M. J., Neufeld, D., Wolfire, M., & Goicoechea, J. R. 2012, ApJ, 754, 105

Hollenbach, D. J., Takahashi, T., & Tielens, A. G. G. M. 1991, ApJ, 377, 192

Hollenbach, D. J. & Tielens, A. G. G. M. 1999, RvMP, 71, No. 1

Hopkins, P. F., Quataert, E., & Murray, N. 2012, MNRAS, 421, 3488

Howarth, I. D. & Prinja, R. K. 1989, ApJS, 69, 527

Howe, J. E., Jaffe, D. T., Genzel, R., & Stacey, G. J. 1991, ApJ, 373, 158

Hummer, D. G. & Storey, P. J. 1987, MNRAS, 224, 801

Isobe, T., Feigelson, E. D., Akritas, M. G., & Babu, G. J. 1990, ApJ, 364, 104

Jaffe, D., Zhou, S., Howe, J., Herrmann, F., & Madden, S. 1994, ApJ, 436, 203

Jenkins, E. B. & Tripp, T. M. 2011, ApJ, 734, 65

Joblin, C., Bron, E., Pinto, C., et al. 2018, A&A, 615, A129

Johnstone, D. & Bally, J. 1999, ApJ, 510, L49

Kaplan, K. F., Dinerstein, H. L., Oh, H., et al. 2017, ApJ, 838, 152

Kaufman, M. J., Wolfire, M. G., & Hollenbach, D. J. 2006, ApJ, 644, 283

Kennicutt, Robert C., J. 1998, ApJ, 498, 541

Kennicutt, Robert C., J., Hao, C.-N., Calzetti, D., et al. 2009, ApJ, 703, 1672

Kennicutt, R. & Evans, N. 2012, ARA&A, 50, 531

Kester, D., Avruch, I., & Teyssier, D. 2014, in American Institute of Physics Conference Series, Vol. 1636, Bayesian Inference and Maximum Entropy Methods in Science and Engineering, 62–67

Khusanova, Y., Béthermin, M., Le Fèvre, O., et al. 2020, arXiv e-prints, arXiv:2007.08384

Kim, C.-G., Ostriker, E. C., & Kim, W.-T. 2013, ApJ, 776, 1

Kim, J. S., Clarke, C. J., Fang, M., & Facchini, S. 2016, ApJL, 826, L15

Kirk, H., Di Francesco, J., Johnstone, D., et al. 2016, ApJ, 817, 167

Knudsen, K. K., Richard, J., Kneib, J.-P., et al. 2016, MNRAS, 462, L6

Knyazeva, L. N. & Kharitonov, A. V. 1998, ARep, 42, 60

Kounkel, M., Hartmann, L., Loinard, L., et al. 2017, ApJ, 834, 142

Kovalenko, A., Dung Tran, T., Rednyk, S., et al. 2018, ApJ, 856, 100

Kramer, C., Abreu-Vicente, J., García-Burillo, S., et al. 2013, A&A, 553, A114

Kraus, S., Weigelt, G., Balega, Y. Y., et al. 2009, A&A, 497, 195

Krumholz, M. R. & Matzner, C. D. 2009, ApJ, 703, 1352

Lada, C. J., Forbrich, J., Lombardi, M., & Alves, J. F. 2012, ApJ, 745, 190

Langer, W. D. & Penzias, A. A. 1990, ApJ, 357, 477

Langer, W. D., Velusamy, T., Pineda, J. L., et al. 2010, A&A, 521, L17

Lebouteiller, V., Cormier, D., Madden, S. C., et al. 2019, A&A, 632, A106

Lehmann, H., Vitrichenko, E., Bychkov, V., Bychkova, L., & Klochkova, V. 2010, A&A, 514, A34

Leitherer, C. 1988, ApJ, 334, 626

Li, A. & Draine, B. T. 2001, ApJ, 544, 778

Lique, F., Kłos, J., Alexander, M. H., Le Picard, S. D., & Dagdigian, P. J. 2018, MNRAS, 474, 2313

Lombardi, M., Bouy, H., Alves, J., & Lada, C. J. 2014, A&A, 566, A45

Luhman, M. L., Satyapal, S., Fischer, J., et al. 2003, ApJ, 594, 758

Mac Low, M.-M. & McCray, R. 1988, ApJ, 324, 776

Magdis, G. E., Rigopoulou, D., Hopwood, R., et al. 2014, ApJ, 796, 63

Malhotra, S., Kaufman, M. J., Hollenbach, D., et al. 2001, ApJ, 561, 766

Mangum, J. G., Emerson, D. T., & Greisen, E. W. 2007, A&A, 474, 679

Marconi, A., Testi, L., Natta, A., & Walmsley, C. M. 1998, A&A, 330, 696

McCray, R. & Kafatos, M. 1987, ApJ, 317, 190

McKee, C. F. & Ostriker, J. P. 1977, ApJ, 218, 148

Megeath, S. T., Gutermuth, R., Muzerolle, J., et al. 2012, AJ, 144, 192

Megeath, S. T., Gutermuth, R., Muzerolle, J., et al. 2016, AJ, 151, 5

Megier, A., Strobel, A., Bondar, A., et al. 2005, ApJ, 634, 451

Meixner, M., Haas, M. R., Tielens, A. G. G. M., Erickson, E. F., & Werner, M. 1992, ApJ, 390, 499

Menten, K. M., Reid, M. J., Forbrich, J., & Brunthaler, A. 2007, A&A, 474, 515

Meyer, M., Flaherty, K., Levine, J., et al. 2008, Handbook of Star Forming Regions, 1, 662

Milam, S. N., Savage, C., Brewster, M. A., Ziurys, L., & Wyckoff, S. 2005, ApJ, 634, 1126

Mookerjea, B., Sandell, G., Jarrett, H., & McMullin, J. 2009, A&A, 507, 1485

Muench, A., Getman, K., Hillenbrand, L., & Preibisch, T. 2008, Star Formation in the Orion Nebula I: Stellar Content, ed. B. Reipurth, Vol. 4, 483

Naab, T. & Ostriker, J. P. 2017, ARA&A, 55, 59

Nagy, Z., Van der Tak, F. F. S., Ossenkopf, V., et al. 2013, A&A, 550, A96

Naiman, J. P., Ramirez-Ruiz, E., & Lin, D. N. C. 2018, MNRAS, 478, 2794

Nakamura, F., McKee, C. F., Klein, R. I., & Fisher, R. T. 2006, ApJS, 164, 477

Neufeld, D. A. & Wolfire, M. G. 2016, ApJ, 826, 183

Norman, C. A. & Ikeuchi, S. 1989, ApJ, 345, 372

Ochsendorf, B. B., Brown, A. G. A., Bally, J., & Tielens, A. G. G. M. 2015, ApJ, 808, 111

Ochsendorf, B. B., Cox, N. L. J., Krijt, S., et al. 2014, A&A, 563, A65

O'Dell, C. R. 2001, ARAA, 39, 99

O'Dell, C. R. 2018, MNRAS, 478, 1017

O'Dell, C. R., Ferland, G. J., Porter, R. L., & van Hoof, P. A. M. 2011, ApJ, 733, 9

O'Dell, C. R. & Goss, W. M. 2009, AJ, 138, 1235

O'Dell, C. R. & Harris, J. A. 2010, ApJ, 140, 985

O'Dell, C. R., Henney, W. J., Abel, N. P., Ferland, G. J., & Arthur, S. J. 2009, ApJ, 137, 367

O'Dell, C. R., Kollatschny, W., & Ferland, G. J. 2017, ApJ, 837, 151

O'Dell, C. R., Walter, D. K., & Dufour, R. J. 1992, ApJ, 399, L67

O'Dell, C. R. & Yusef-Zadeh, F. 2000, ApJ, 120, 382

Okada, Y., Higgins, R., Ossenkopf-Okada, V., et al. 2019, A&A, 631, L12

Okada, Y., Pilleri, P., Berné, O., et al. 2013, A&A, 553, A2

Orkisz, J. H., Pety, J., Gerin, M., et al. 2017, A&A, 599, A99

Oskinova, L. M., Todt, H., Ignace, R., et al. 2011, Mon. Not. R. Astron. Soc., 416, 1456

Ossenkopf, V., Röllig, M., Neufeld, D. A., et al. 2013, A&A, 550, A57

Osterbrock, D. E. 1989, Astrophysics of gaseous nebulae and active galactic nuclei (University Science Books)

Ostriker, J. P. & McKee, C. F. 1988, Reviews of Modern Physics, 60, 1

Pabst, C., Higgins, R., Goicoechea, J. R., et al. 2019, Nature, 565, 618

Pabst, C. H. M., Goicoechea, J. R., Teyssier, D., et al. 2020, A&A, 639, A2

Pabst, C. H. M., Goicoechea, J. R., Teyssier, D., et al. 2017, A&A, 606, A29

Pauldrach, A. W. A., Hoffmann, T. L., & Lennon, M. 2001, A&A, 375, 161

Peeters, E., Hony, S., Van Kerckhoven, C., et al. 2002, A&A, 390, 1089

Pellegrini, E. W., Baldwin, J. A., Ferland, G. J., Shaw, G., & Heathcote, S. 2009, ApJ, 693, 285

Pentericci, L., Carniani, S., Castellano, M., et al. 2016, ApJL, 829, L11

Penzias, A. A., Jefferts, K. B., Wilson, R. W., Liszt, H. S., & Soloman, P. M. 1972, ApJ, 178, L35

Peters, T., Naab, T., Walch, S., et al. 2017, MNRAS, 466, 3293

Peterson, D. E. & Megeath, S. T. 2008, Handbook of Star Forming Regions Vol. I

Petit, V., Owocki, S. P., Oksala, M. E., & the MiMeS Collaboration. 2012, ASP Conference Series, 465, 48

Pety, J. 2005, in SF2A-2005: Semaine de l'Astrophysique Francaise, ed. F. Casoli, T. Contini, J. M. Hameury, & L. Pagani, 721–722

Pety, J., Guzmán, V. V., Orkisz, J. H., et al. 2017, A&A, 599, A98

Pety, J., Teyssier, D., Fossé, D., et al. 2005, A&A, 435, 885

Pineda, J. L., Fischer, C., Kapala, M., et al. 2018, ApJ, 869, L30

Pineda, J. L., Langer, W. D., & Goldsmith, P. F. 2014, A&A, 570, A121

Pineda, J. L., Langer, W. D., Velusamy, T., & Goldsmith, P. F. 2013, A&A, 554, A103

Poglitsch, A., Waelkens, C., Geis, N., et al. 2010, A&A, 518, L2

Pound, M. W. & Wolfire, M. G. 2008, Astronomical Society of the Pacific Conference Series, Vol. 394, The Photo Dissociation Region Toolbox, ed. R. W. Argyle, P. S. Bunclark, & J. R. Lewis, 654

Prosser, C. F., Stauffer, J. R., Hartmann, L., et al. 1994, ApJ, 421, 517

Reipurth, B., Bally, J., Fesen, R., & Devine, D. 1998, Nature, 396, 343

Risacher, C., Güsten, R., Stutzki, J., et al. 2016, A&A, 595, A34

Rubin, R. H., Simpson, J. P., O'Dell, C. R., et al. 2011, MNRAS, 410, 1320

Rybak, M., Hodge, J. A., Vegetti, S., et al. 2020a, MNRAS, 494, 5542

Rybak, M., Zavala, J. A., Hodge, J. A., Casey, C. M., & Werf, P. v. d. 2020b, ApJ, 889, L11

Salas, P., Oonk, J. B. R., Emig, K. L., et al. 2019, A&A, 626, A70

Salgado, F., Berné, O., Adams, J. D., et al. 2016, ApJ, 830, 118

Sandell, G., Mookerjea, B., Güsten, R., et al. 2015, A&A, 578, A41

Schaye, J., Crain, R. A., Bower, R. G., et al. 2015, MNRAS, 446, 521

Schneider, N., Simon, R., Guevara, C., et al. 2020, PASP, 132, 104301

Schulz, N. S., Testa, P., Huenemoerder, D. P., Ishibashi, K., & Canizares, C. 2006, ApJ, 653, 636

Sellgren, K. 1986, ApJ, 305, 399

Seo, Y. M., Goldsmith, P. F., Walker, C. K., et al. 2019, ApJ, 878, 120

Sheffer, Y. & Wolfire, M. G. 2013, ApJ, 774, L14

Shibai, H., Okuda, H., Nakagawa, T., et al. 1991, ApJ, 374, 522

Silich, S. & Tenorio-Tagle, G. 2013, ApJ, 765, 43

Simón-Díaz, S., García-Rojas, J., Esteban, C., et al. 2011, A&A, 530, A57

Simón-Díaz, S., Herrero, A., Esteban, C., & Najarro, F. 2006, A&A, 448, 351

Smith, J. D. T., Croxall, K., Draine, B., et al. 2017, ApJ, 834, 5

Sofia, U. J., Lauroesch, J. T., Meyer, D. M., & Cartledge, S. I. B. 2004, ApJ, 605, 272

Sofia, U. J. & Parvathi, V. S. 2009, ASP Conference Series, 414, 236

Sofia, U. J., Parvathi, V. S., Babu, B. R. S., & Murthy, J. 2011, AJ, 141, 22

Soler, J. D., Beuther, H., Rugel, M., et al. 2019, A&A, 622, A166

Spaans, M., Tielens, A. G. G. M., van Dishoeck, E. F., & Bakes, E. L. O. 1994, ApJ, 437, 270

Spitzer, L. 1978, Physical Processes in the Interstellar Medium (New York: Wiley-Interscience)

Stacey, G., Townes, C., Geis, N., et al. 1989, BAAS, 21, 1180

Stacey, G. J., Geis, N., Genzel, R., et al. 1991, ApJ, 373, 423

Stacey, G. J., Hailey-Dunsheath, S., Ferkinhoff, C., et al. 2010, ApJ, 724, 957

Stahl, O., Kaufer, A., Rivinius, T., et al. 1996, A&A, 312, 539

Stahl, O., Wade, G., Petit, V., Stober, B., & Schanne, L. 2008, A&A, 487, 323

Sternberg, A., Hoffmann, T. L., & Pauldrach, A. W. A. 2003, ApJ, 599, 1333

Stone, J. M. & Gardiner, T. 2007, ApJ, 671, 1726

Storey, P. J. & Hummer, D. G. 1995, MNRAS, 272, 41

Störzer, H. & Hollenbach, D. 1998, ApJ, 495, 853

Störzer, H. & Hollenbach, D. 1999, ApJ, 515, 669

Subrahmanyan, R., Goss, W. M., & Malin, D. F. 2001, AJ, 121, 399

Taylor, M. B. 2005, in Astronomical Society of the Pacific Conference Series, Vol. 347, Astronomical Data Analysis Software and Systems XIV, ed. P. Shopbell, M. Britton, & R. Ebert, 29

Tielens, A. G. G. M. 2008, ARA&A, 46, 289

Tielens, A. G. G. M. 2010, The Physics and Chemistry of the Interstellar Medium (New York: Cambridge University Press)

Tielens, A. G. G. M. & Hollenbach, D. J. 1985, ApJ, 291, 722

Tielens, A. G. G. M., Meixner, M. M., van der Werf, P. P., et al. 1993, Science, 262, 86

Townsley, L. K., Broos, P. S., Garmire, G. P., et al. 2014, ApJS, 213, 1

Tran, T. D., Rednyk, S., Kovalenko, A., et al. 2018, ApJ, 854, 25

Troland, T. H., Goss, W. M., Brogan, C. L., Crutcher, R. M., & Roberts, D. A. 2016, ApJ, 825, 2

Vallini, L., Gallerani, S., Ferrara, A., Pallottini, A., & Yue, B. 2015, ApJ, 813, 36

van der Werf, P. P. & Goss, W. M. 1989, A&A, 224, 209

van der Werf, P. P., Goss, W. M., & O'Dell, C. R. 2013, ApJ, 762, 101

van Dishoeck, E. F. & Black, J. H. 1986, ApJS, 62, 109

Venemans, B. P., McMahon, R. G., Walter, F., et al. 2012, ApJ, 751, L25

Vitrichenko, E. A. 2002, AstL, 28, 324

Walch, S., Whitworth, A. P., Bisbas, T. G., Hubber, D. A., & Wünsch, R. 2015, MNRAS, 452, 2794

Walch, S., Whitworth, A. P., Bisbas, T. G., Wünsch, R., & Hubber, D. 2013, MNRAS, 435, 917

Walch, S. K., Whitworth, A. P., Bisbas, T., Wünsch, R., & Hubber, D. 2012, MNRAS, 427, 625

Walter, F., Decarli, R., Carilli, C., et al. 2012, ApJ, 752, 93

Wareing, C. J., Pittard, J. M., Wright, N. J., & Falle, S. A. E. G. 2018, MNRAS, 475, 3598

Watkins, E. J., Peretto, N., Marsh, K., & Fuller, G. A. 2019, A&A, 628, A21

Weaver, R., McCray, R., Castor, J., Shapiro, P., & Moore, R. 1977, ApJ, 218, 377

Weilbacher, P. M., Monreal-Ibero, A., Kollatschny, W., et al. 2015, A&A, 582, A114

Weingartner, J. C. & Draine, B. T. 2001, ApJ, 548, 296

Welty, D. E., Xue, R., & Wong, T. 2012, ApJ, 745, 173

Wiesenfeld, L. & Goldsmith, P. 2014, ApJ, 780, 183

Williams, J. P. & McKee, C. F. 1997, ApJ, 476, 166

Wilson, T. L., Filges, L., Codella, C., Reich, W., & Reich, P. 1997, A&A, 327, 1177

Wolfire, M., McKee, C., Hollenbach, D., & Tielens, A. 2003, ApJ, 587, 278

Wolfire, M. G., Hollenbach, D., & McKee, C. F. 2010, ApJ, 716, 1191

Wolfire, M. G., Hollenbach, D., McKee, C. F., Tielens, A. G. G. M., & Bakes, E. L. O. 1995, ApJ, 443, 152

Wolfire, M. G., Hollenbach, D., & Tielens, A. G. G. M. 1989, ApJ, 344, 770

Wu, R., Bron, E., Onaka, T., et al. 2018, A&A, 618, A53

Young, E. T., Becklin, E. E., Marcum, P. M., et al. 2012, ApJ, 749, L17

Young Owl, R. C., Meixner, M. M., Fong, D., et al. 2002, ApJ, 578, 885

Zari, E., Brown, A. G. A., de Bruijne, J., Manara, C. F., & de Zeeuw, P. T. 2017, A&A, 608, A148

Zuckerman, B. 1973, ApJ, 183, 863

Samenvatting

Het interstellaire medium

Behalve de met het oog zichtbare sterren bevindt zich ook ijl gas tussen de sterren, het zogenaamde interstellaire medium (ISM). Voor het grootste deel (90%) is dit interstellaire gas waterstof, ongeveer 10% is helium, en er zijn kleine hoeveelheden sporenelementen zoals koolstof, zuurstof, stikstof en zwavel. Het ISM neemt verschillende vormen aan (naar de toestand waarin waterstof zich bevindt): Ten eerste zijn er moleculaire wolken (waterstof is moleculair en koud), die door samen te klonteren nieuwe sterren kunnen vormen. Ten tweede is er gas dat door de ultraviolet (uv) straling van zware sterren geïoniseerd (en warm) is. Ten derde is er neutraal atomair gas dat zich vaak aan de overgang van die twee eerste fases bevindt. Dit laatste kan warm of koud zijn, afhankelijk van de mate waarin het aan straling blootgesteld is en zijn dichtheid. Behalve waterstof spelen de overige elementen een belangrijke rol bij het koelen van het ISM, daarover later meer. En behalve gas bevindt zich ook stof in het ISM (ongeveer 1% van de gasmassa in de Melkweg), kleine grafiet- of silicaatkorreltjes, en grote moleculen uit voornamelijk koolstof en waterstof, zogenaamde polycyclische aromatische koolwaterstoffen (PAKs). Die twee zijn belangrijk voor het verhitten van het gas.

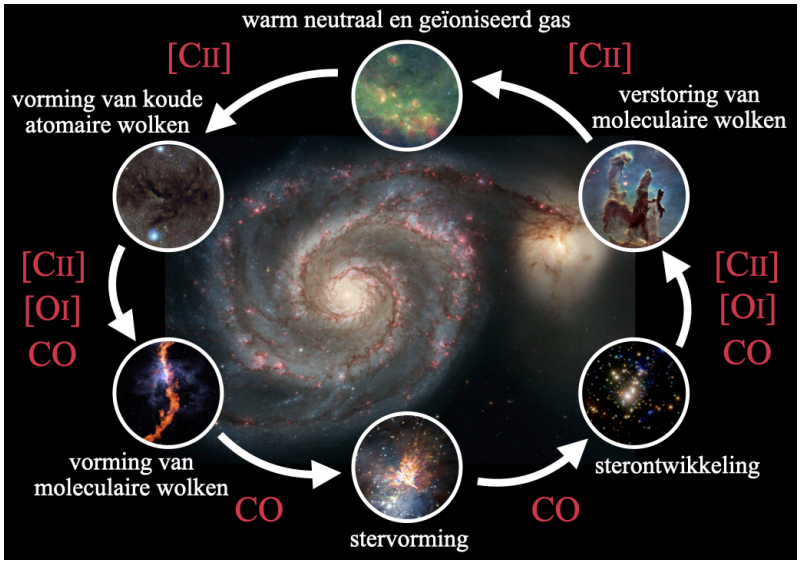

Figuur 6.1: De levenscyclus van het interstellaire medium. Rode letters benoemen de belangrijkste emissielijnen die in een bepaalde fase waargenomen kunnen worden.

Het materiaal in het interstellaire medium (gas en stof) bevindt zich een kringloop en wordt telkens herbruikt (zie figuur 6.1). Beginnend met de vorming van een ster, wordt tijdens de stellaire evolutie materiaal van de ster naar de omgeving afgevoerd, hoe zwaarder de ster hoe meer massa dat is. Het grootste massaverlies lijdt een ster aan het einde van zijn leven, wanneer hij zijn envelop afstoot en verschrompelt tot een witte dwerg of in een supernova ontploft. Vooral supernovae verspreiden grote

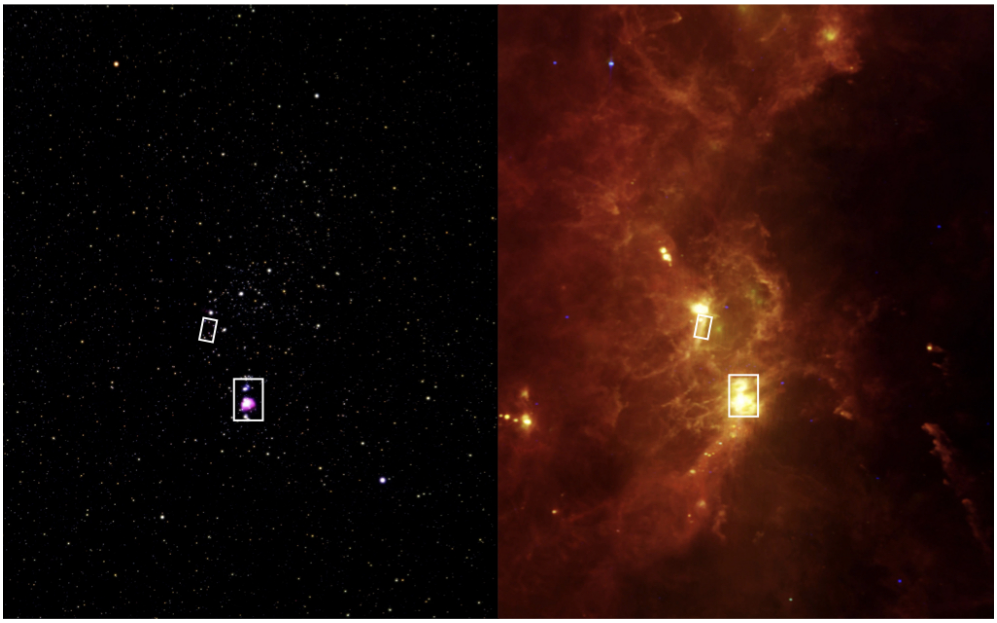

Figuur 6.2: De constellatie van Orion in zichtbaar licht (*links*) en infraroodstraling (*rechts*) (beeld: NASA, JPL-Caltech, IRAS/H. McCallon). De witte rechthoeken omlijsten de gebieden die in dit proefschrift bestudeerd zijn, de Paardekopnevel boven en de Orionnevel eronder.

hoeveelheden gas (met nieuwe, zware elementen) en stof in een wijde omtrek van de oorspronkelijke ster. Een gedeelte van de energie die vrij komt (ook tijdens het leven van een ster), verstoort en verscheurt de moleculaire wolk waarin de ster geboren werd. Dat materiaal wordt samen met de stellaire uitvloeisels verhit en vormt een uitgedijde ijle fase van het ISM, al dan niet geïoniseerd, het zogenaamde warme neutrale of geïoniseerde medium. Dat ijle gas koelt af in de loop der tijd en zal uiteindelijke koude neutrale wolken vormen. Door verder af te koelen en onder de invloed van de zwaartekracht samen te trekken, ontstaat eruit een nieuwe moleculaire wolk. Klonten met hogere dichtheid trekken sneller samen en kunnen dicht genoeg worden om nieuwe stervorming in gang te zetten. Zo is de cirkel rond.

Een favoriet studieobject van sterrenkundigen is de Orionnevel en de Orion moleculaire wolk. Behalve de sterren die de constellatie van Orion vormen bevindt zich in die richting een gigantische moleculaire wolk in de ruimte. De moleculaire wolk zendt voornamelijk infraroodstraling en radiogolven uit die met speciale telescopen waargenomen kunnen worden (zie figuur 6.2). De Orionnevel (zie figuur 6.3) is een stervormingsgebied, een gebied waarin nieuwe sterren gevormd worden. In zijn midden bevinden zich vier grote en zware sterren, de zogenaamde Trapeziumsterren, die ervoor zorgen dat het omliggende gas geïoniseerd is (in een zogenoemd H II gebied) en ook in optische en uv golflengtes straalt (zie figuur 6.4). Doordat de Orionnevel dichtbij is, op een afstand van ongeveer 400 parsec (een parsec is 3,26 lichtjaar of $3{,}09\times10^{16}$ m), en buiten de schijf van de Melkweg valt, is hij makkelijk te bestuderen en kunnen zelfs eenvoudige telescopen zijn structuur oplossen (de eerste die een tekening maakte van de structuur van de Orionnevel was Christiaan Huygens in 1659). De Orion moleculaire wolk wordt in twee delen opgesplitst, Orion A in het zuiden en

Figuur 6.3: De Orionnevel, waargenomen door de *Hubble Space Telescope* (beeld: NASA, ESA/M. Robberto).

Figuur 6.4: De Trapeziumsterren in het H II gebied van de Orionnevel, ook Huygensgebied genoemd (beeld: NASA/C. R. O'Dell and S. K. Wong).

Orion B in het noorden. De Orionnevel bevindt zich aan het oppervlak van de Orion A moleculaire wolk. Ook in de Orion B moleculaire wolk zijn stervormingsgebieden te vinden, de heldersten zijn de reflectienevels NGC 2023 en NGC 2024. In de Orion B moleculaire wolk bevindt zich ook de iconische Paardekopnevel (zie figuur 6.5).

De interacties tussen sterren en het interstellaire medium

Sterren, en dan met name massarijke sterren, zenden uv straling uit. Die uv fotonen ioniseren waterstof en andere elementen, afhankelijk van de golflengte, en verhitten het gas door het fotoelektrische effect op stofkorrels en PAKs (het fotoelektrische effect is het fenomeen dat fotonen elektronen uit een materiaal kunnen slaan, die vervolgens een overschot aan energie hebben die ze met het overige gas kunnen delen). Hele zware sterren zenden bovendien ook materiedeeltjes uit, een zogenaamde wind. Die winden kunnen door hun grote snelheid het ISM op miljoenen graden verhitten. Er ontstaat een heet plasma dat Röntgen straling emitteert. Dat plasma zorgt voor een schokgolf die het omliggende gas opveegt en in een dunne schil van neutraal gas comprimeert (zie figuur 6.6). Meestal is zo'n schil niet helemaal symmetrisch en ontstaat er na verloop van tijd een breuk, waardoor het plasma naar buiten kan stromen. Op die manier kunnen door veel sterren samen veel grotere structuren gevormd worden, zoals de Orion-Eridanusbel die geheel de constellatie van Orion omvat. Zoals boven beschreven, zorgen massarijke sterren ervoor dat de moleculaire wolk die hun geboorteplaats was, verstoord en verscheurd wordt. Dit heet negatieve terugkoppeling, omdat verdere stervorming in die moleculaire wolk voorkomen wordt. Er is echter ook de mogelijkheid van positieve terugkoppeling, wanneer de schokgolf, die zich in de moleculaire wolk (of de uitdijende schil) verplaatst, tot compressie van het gas en daardoor nieuwe stervorming leidt. Dit laatste is waargenomen in een aantal stervormingsgebieden, maar

Figuur 6.5: De moleculaire wolk L1630 in de omstreken van de Paardekopnevel in infraroodlicht (blauw: 3,4 μm (voornamelijk sterren), blauwgroen: 4.6 μm, groen: 12 μm (emissie van PAKs), rood: 22 μm (emissie van stofdeeltjes)) (beeld: NASA, JPL-Caltech). Links boven de Paardekopnevel bevinden zich de (veel helderde) reflectienevels NGC 2023 en NGC 2024. Rechts van de Paardekopnevel nadert de ster σ Ori de moleculaire wolk. De rode boog voor de ster is een boeggolf van stofdeeltjes, die de ster voor zich uit schuift.

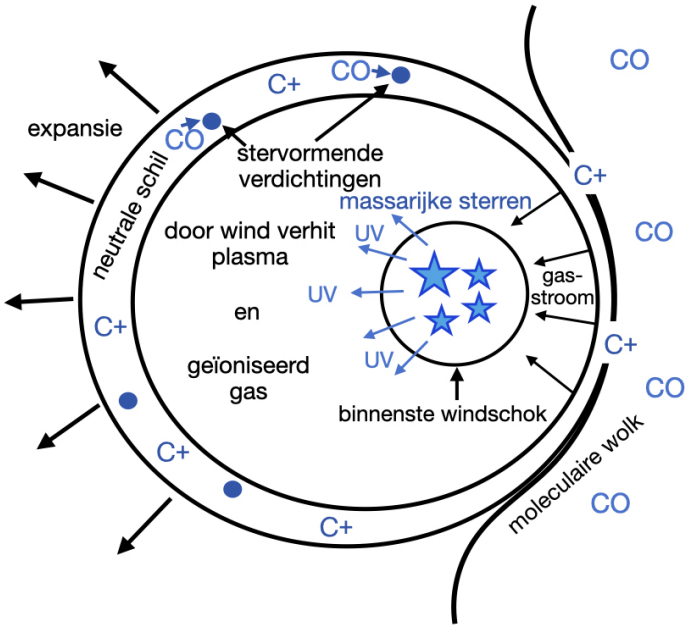

Figuur 6.6: Schema van een interactie tussen massarijke sterren en een moleculaire wolk.

de precieze omstandigheden waarin of negatieve of positieve terugkoppeling overweegt zijn op dit moment niet voldoende opgehelderd.

Minder massarijke sterren vormen het omliggende gas alleen door middel van hun uv straling. Ook deze straling, of beter gezegd de overdruk die in het geïoniseerde gas ontstaat, kan ervoor zorgen dat een dunne schil van neutraal gas opgeveegd wordt. Deze expanderen doorgaans minder snel dan de door een stellaire wind opgeveegde schillen, maar kunnen ook behoorlijk groot worden. We zullen twee voorbeelden van deze type van expansie zien.

Infraroodstraling en fijnstructuurlijnen

Gas dat verhit is koelt ook af. Hierbij helpen fijnstructuurovergangen van sporenelementen (alles behalve waterstof). De fijnstructuur van een atoom (al dan niet geïoniseerd) is de splitsing van energieniveau's door de koppeling van de elektronenbaanmomentum met de elektronenspin en relativistische effecten. Tussen die gesplitste energieniveau's vinden overgangen met lage energie plaats. De meeste van die overgangen zijn "verboden" overgangen, die dus een hele kleine waarschijnlijkheid hebben. Omdat de tijdschalen waarop het ISM evolueert zo groot zijn en de dichtheid van het ISM zo laag, spelen zij echter de hoofdrol. Verschillende atomen en ionen hebben verschillende fijnstructuurovergangen die in verschillende fases van het ISM aangeslagen worden. Ik beperk me hier tot het bespreken van de fijnstructuurlijn van geïoniseerd koolstof (in spectroscopische notatie [C II]) met een golflengte van 158 μm, omdat ik die in dit proefschrift gebruikt heb om twee gebieden in Orion te bestuderen.

Het warme neutrale ISM (met een temperatuur van ongeveer 100 K en een dichtheid van 10^3-10^5 deeltjes per kubieke centimeter) koelt voornamelijk door middel van de [C II] lijn af. Hier is waterstof atomair of moleculair, maar koolstof is nog steeds geïoniseerd door de invallende uv straling. Geïoniseerd waterstofgas bevat ook koolstofionen, maar de [C II] emissie is daar minder prominent omdat andere overgangen een grotere bijdrage leveren aan de koeling. Behalve de lijnemissie is er ook continuumemissie van de stofkorreltjes en de emissie van de PAKs. Figuur 6.7 laat zien hoe een typisch infraroodspectrum van het ISM eruit ziet, namelijk een combinatie van continuumemissie en lijnemissie.

Dit proefschrift

In dit proefschrift heb ik gebruik gemaakt van infraroodwaarnemingen gedaan met het upGREAT instrument op SOFIA. SOFIA ("Stratospheric Observatory for Infrared Astronomy") is een gemodificeerde Boeing 747-SP uitgerust met een spiegel van 2,5 m doorsnede. In de stratosfeer wordt infraroodstraling (golflengtes tussen 3 en 500 micrometer) veel minder geabsorbeerd door waterdamp in de atmosfeer (zie figuur 6.7), waardoor waarnemingen mogelijk zijn. Het instrument upGREAT ("upgraded German Receiver for Astronomy at Terahertz Frequencies") is een heterodyne ontvanger, wat betekent dat het signal van een lokale oscillator in het astronomische signal gemengd wordt door middel van een mixer. Het resulterende elektronische signal kan door elektronische bouwstenen versterkt worden en levert spectra met hoge spectrale resolutie. De spectraallijn die we gebruiken is de fijnstructuurlijn van geïoniseerde koolstof, [C II]. Met behulp van hoge-resolutie spectra met hoge ruimtelijke resolutie (voor de [C II] lijn gemeten door SOFIA/upGREAT is dit een spectrale resolutie van

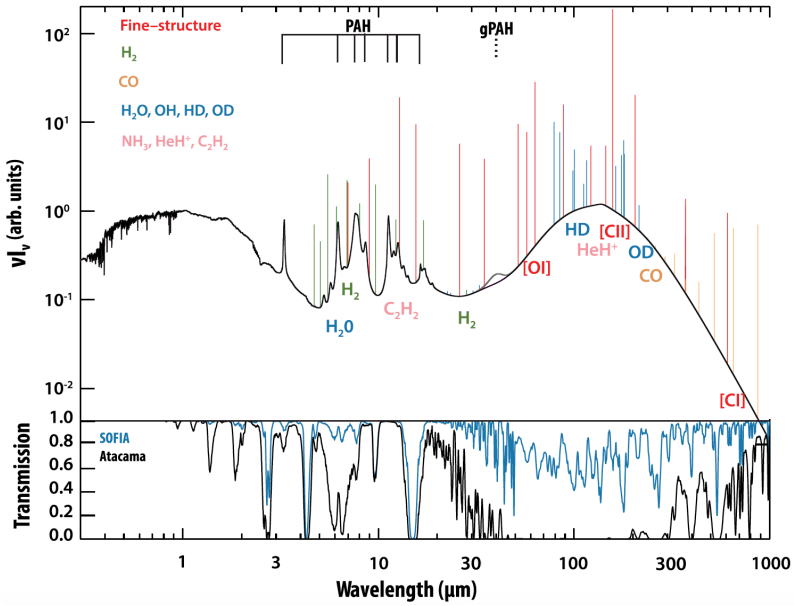

Figuur 6.7: *Boven*: Een model van interstellaire emissie (continuum en lijnen). *Onder*: Atmosferische transmissie voor infraroodstraling vanaf de grond (Atacama) en SOFIA (afbeelding: K. Ennico et al., JAI 7,4, 2018).

0,2 km/s en een ruimtelijke resolutie van 15,9 boogseconden) kan men een nauwkeurig beeld schetsen van de bewegingen van het interstellaire gas. Emissie van geïoniseerde koolstof, de [C II] lijn, kan in een aantal fases van het ISM waargenomen worden: oppervlakken van moleculaire wolken in de buurt van een ster, het warme neutrale of geïoniseerde ISM, en koude atomaire wolken. Op galactische schaal leveren al deze fases een bijdrage aan de totale [C II] emissie, maar onze waarnemingen beperken zich tot gebieden dichtbij massarijke sterren.

In hoofdstuk 2 kijken we naar de Paardekopnevel. Deze nevel is een uitstulping van de L1630 moleculaire wolk die deel uitmaakt van de Orion B moleculaire wolk. De Paardekopnevel en L1630 eromheen worden verhit door de O9.5V ster σ Ori, die de wolk nadert en verdampt. Aan het oppervlak van de wolk ontstaat zo een photodissociatiegebied (PDR, "photodissociation region") met de typische gelaagde structuur: Aansluitend aan het H II gebied, het gebied waarin waterstof geïoniseerd is, bestaat de bovenste laag van de wolk uit atomair waterstofgas waarin koolstof nog geïoniseerd is. Wat dieper in de wolk combineert waterstof tot waterstofmoleculen, maar koolstof is nog steeds geïoniseerd. Pas nog dieper wordt koolstof neutral en vormt zich ook snel koolstofmonoxide (CO), het na waterstof meest abundante molecuul in het ISM. Waar koolstof geïoniseerd is, koelt het gas af door emissie van de verboden [C II] lijn en andere verboden lijnen van sporenelementen (zuurstof, stikstof, zwavel). Het CO-bevattende gas koelt af door emissie van rotationele lijnen van CO en andere moleculen. Deze lijnen kunnen gemeten worden radiotelescopen zoals de IRAM 30m telescoop. Voor de studie van de Paardekopnevel gebruiken wij de laagste rotationele overgang van CO, de CO(1-0) lijn met een golflengte van 2,6 mm. Verder vergelijken wij de [C II] emissie met de continuum ver-infrarood emissie (λ = 40-500 μm), die door stofdeeltjes geëmitteerd wordt, en de emissie van PAKs in de *Spitzer*/IRAC

8 μm band. De *Herschel*/PACS en SPIRE banden op 70 μm, 160 μm, 250 μm, 350 μm en 500 μm leveren bovendien schattingen voor de optische diepte van het stof en de stoftemperatuur. We vinden goede correlaties tussen de [C II] emissie en de PAH 8 μm emissie zoals ook de geïntegreerde ver-infrarood (FIR, "far-infrared") emissie, wat laat zien dat de [C II] emissie van het oppervlak van de wolk komt. De CO(1-0) emissie is complementair aan de [C II] emissie, wat aantoont dat wij de wolk in een "edge-on" configuratie waarnemen, van de zijkant dus. Dat compliceert de vergelijking van de waarnemingen met PDR modellen enigszins, maar we slagen erin om de waarnemingen goed te reproduceren met edge-on PDR modellen. Het merendeel van de [C II] emissie rondom de Paardekopnevel stamt van de PDR oppervlakken, en maar 5% kunnen aan het H II gas toegeschreven worden.

In hoofdstuk 3 maken wij wederom gebruik van de [C II] lijn, maar deze keer waargenomen over een veel groter gebied (ruim een vierkante graad), namelijk de Orionnevel (M42) in de Orion A moleculaire wolk. Hier zien we de kracht van hoge spectrale en ruimtelijke resolutie. Door middel van positie-snelheidsdiagrammen kunnen wij de expansie van de Orionnevel zichtbaar maken en voor het eerst kwantificeren. De hete sterren in de Orionnevel, en met name de zwaarste van de Trapezium sterren, de O7V ster θ^1 Ori C, verhitten het ISM tot heet plasma dat Röntgen straling uitzendt. Het hete plasma expandeert en veegt daardoor een schil van koeler neutraal gas op. Die schil, met een straal van 2,5 parsec, straalt in [C II] emissie. We bepalen de massa van de schil uit de optische diepte van het stof verkregen uit de *Herschel*/PACS en SPIRE banden op 70 μm, 100 μm, 160 μm, 250 μm, 350 μm en 500 μm. Met een massa van 1.500 zonsmassa's en een snelheid van 13 km/s wordt een groot gedeelte van gasmassa behorend bij het stervormingsgebied, de moleculaire kern OMC1 ("Orion molecular core 1"), uit het gebied uitgestoten. De expansiekarakteristieken kunnen goed beschreven worden door een eenvoudig analytisch model voor wind-gedreven gasbellen. Dat geeft een schatting voor de leeftijd van de schil, namelijk 200.000 jaar. De schil zal uiteindelijk openbreken en het hete plasma zal uitvloeien in het omliggende medium en de grotere gasstructuren van de Orion-Eridanusbel aanvullen.

Hoofdstuk 4 bespreekt de expanderende schillen van de nevels M43 en NGC 1973, 1975 en 1977 (kort NGC 1977). Beiden liggen in de buurt van de Orionnevel en zijn onderdeel van dezelfde [C II] kaart. In tegenstelling met de Orionnevel bevatten M43 en NGC 1977 minder zware sterren (de B0.5V ster NU Ori en de B1V ster 42 Orionis, respectievelijk) die geen noemenswaardige stellaire wind produceren. Deze twee nevels zijn H II gebieden met een omgevende neutrale schil. De schil van M43 met een straal van 0,3 parsec heeft een massa van 8 zonsmassa's en expandeert met een snelheid van 6 km/s. De schil van NGC 1977 met een straal van 1,0 parsec heeft een massa van 700 zonsmassa's en expandeert met 1,5 km/s. Beiden kunnen goed beschreven worden door een analytisch model van expanderende H II gebieden. Deze geven een leeftijd van 20.000 jaar voor M43 en een leeftijd van 400.000 jaar voor NGC 1977. De leeftijd van de schil kan niet meteen vertaald worden in de leeftijd van de ster, want jonge sterren kunnen lang ingebed zijn in de moleculaire wolk voor ze in het ijle medium terecht komen waar ze een expansie op gang kunnen zetten.

In hoofdstuk 5 onderzoeken wij in hoeverre de [C II] emissie van de Orionnevel een verklaring geeft voor [C II] waarnemingen van extragalactische bronnen. Omdat de [C II] lijn de helderste FIR lijn is, kan zij in bronnen op grote afstand waargenomen worden, en het is aangetoond dat er een correlatie is tussen de [C II] luminositeit en het ster-vormingspotentiaal van een sterrenstelsel. Wij onderzoeken eerst de correlaties tussen de [C II] intensiteit in de Orionnevel en de stof-70 μm, PAK-8 μm, geïntegreerde

FIR en CO(2-1) intensiteit ($\lambda = 1,3\,\mathrm{mm}$). We zien goede correlaties tussen [C II] en de eerste drie, hoewel deze niet lineair schalen maar met een macht kleiner dan 1. De relatie tussen [C II] en CO(2-1) toont een trend, maar ook grote spreiding. In extragalactische bronnen van hoge FIR luminositeit wordt een verminderde [C II] luminositeit waargenomen. Wij zien dit ook in onze data: De [C II] intensiteit in verhouding met de FIR intensiteit neemt af met stijgende FIR intensiteit in de buurt van de Trapezium sterren. Wij wijten dit aan het belang van gaskoeling door de zuurstof fijnstructuurlijn [O I] op $63\,\mu$m. Een klein effect kan ook een minder efficient verwarmingsmechanisme zijn door toenemende ionisatie van PAKs en stofkorrels in de buurt van de hete sterren. We zien echter ook een verminderde [C II]/FIR verhouding in gezichtslijnen met grote kolommen van stof, warm of koud. Een mogelijke interpretatie van de [C II]/FIR deficiëntie zou dan ook een in termen van een FIR overschot zijn. Als we de [C II] luminositeit met het stervormingspotentiaal van de Orionnevel vergelijken, zoals dat bekend is uit tellingen van jonge stellaire objecten, zien we dat de formules die op extragalactische waarnemingen geijkt zijn de daadwerkelijke stellaire inhoud onderschatten, ongeveer met één à twee ordes van grote. Dit zou erop kunnen wijzen dat grote oppervlakken die minder intensieve straling uitzenden wezenlijk bijdragen aan galactische [C II] emissie. Wij zien een trend in die richting ook in onze data.

Hoofdstuk 6 is een uitwerking van het PDR aspect, dat in hoofdstuk 5 ten behoeve van overzichtelijkheid en begrijpelijkheid onderbelicht bleef. Allereerst splitsen wij het gebied van de hele [C II] kaart in Orion A in vier gebieden: de schil van de Orionnevel, het moleculaire filament rondom de moleculaire kern OMC4 in het midden van die schil, M43 en NGC 1977. De laatste twee gebieden worden wederom onderverdeeld in het H II gebied, dichte moleculaire gebieden en de [C II]-emitterende schil. We zien eigenlijk dat de correlaties die we in het voorafgaande hoofdstuk globaal hebben onderzocht ([C II] intensiteit versus stof-70 μm, PAK-8 μm en FIR intensiteit), weinig variaties tonen in die vier gebieden apart. Alleen de correlatie tussen de [C II] intensiteit en de CO(2-1) intensiteit is ingewikkelder. Deze onderzoeken we nader door spectra in representatieve gebieden te bestuderen. Dat laat zien dat er in elke emissielijn meerdere componenten zijn die niet altijd met elkaar in verband te brengen zijn. Mogelijk dat de dynamiek van de gebieden, onder invloed van de sterren, ons hier parten speelt. Dit laat ook zien dat stervormingsgebieden heel complex zijn en dat het eigenlijk niet mogelijk is om fysische eigenschappen uit het meten van een gemiddelde lijn (zoals in extragalactische studies gebeurt) te achterhalen. We zien ook dat het door die veelheid aan componenten moeilijk is om de emissie weer te geven in PDR modellen. Desondanks komen onze edge-on PDR modellen bij het voorspellen van de [C II] intensiteit aardig in de buurt, maar we merken wel op dat er afwijkingen zijn. Tot slot relateren wij de [C II] koelingsefficiëntie, zoals gemeten door de [C II]/FIR intensiteitsverhouding, aan de karakteristieken van de PAKs afgeleid uit PAK spectra. We zien echter niet dat de PAK ionisatie of molecuulafmetingen significant varieëren, maar de [C II]/FIR efficiëntie doet dat wel. Mogelijk betekent dat dat kleine stofkorrels ook belangrijk zijn voor de verhitting van het gas. Hier zouden toekomstige missies, zoals de *James Webb Space Telescope*, licht in het donker kunnen brengen.

Kortom, de waarnemingen die ik in dit proefschrift bestudeerd heb, laten de rijkdom van stervormingsgebieden zien. Niet alleen is er een rijkdom aan verschillende emissielijnen (de belangrijksten zijn [C II], [O I] en de CO lijnen), maar ook een rijkdom aan emissiecomponenten, die in elke lijn weer schijnen te verschillen. Dit laat onverlet dat de expansiebewegingen op grote schaal zeer nauwkeurig bepaald kunnen worden. Opvolgend op dit proefschrift zal de SOFIA FEEDBACK C^+ Legacy Survey

11 stervormingsgebieden in de Melkweg waarnemen en de mate waarin sterren hun omgeving beïnvloeden met grotere nauwkeurigheid dan gekend kunnen kwantificeren. Dit zal ons in staat stellen om beter te begrijpen hoe ook veel grotere structuren in ons heelal, die wezenlijk door stellaire terugkoppelingen bepaald worden, ontstaan en vergaan.

Zusammenfassung

Das interstellare Medium

Neben den mit bloßem Auge sichtbaren Sternen befindet sich auch dünnes Gas zwischen den Sternen, das sogenannte interstellare Medium (ISM). Zum größten Teil (90%) ist dieses interstellare Gas Wasserstoff, ungefähr 10% ist Helium, und es enthält kleine Mengen Spurenelemente sowie Kohlenstoff, Sauerstoff und Schwefel. Das ISM nimmt verschiedene Formen an (nach dem Zustand, in dem Wasserstoff sich befindet): Zum Ersten sind da die Molekülwolken (Wasserstoff ist molekular und kalt), die, indem sie zusammenfallen, neue Sterne bilden können. Zum Zweiten gibt es Gas, das durch die Ultraviolettstrahlung (UV) von schweren Sternen ionisiert (und warm) ist. Zum Dritten gibt es neutrales atomares Gas, das sich oftmals am Übergang zwischen den beiden erstgenannten Phasen befindet. Diese letzte Phase kann warm oder kalt sein, je nach dem Maß, in dem es Strahlung ausgesetzt ist, und seiner Dichte. Außer Wasserstoff spielen die übrigen Elemente eine wichtige Rolle beim Kühlen des ISM, darüber später mehr. Und außer Gas befindet sich auch Staub im ISM (ungefähr 1% von der Gasmasse in der Milchstraße), kleine Grafit- oder Silikatkörnchen, und große Moleküle aus hauptsächlich Kohlenstoff und Wasserstoff, sogenannte polyzyklische aromatische Kohlenwasserstoffe (PAKs). Diese beiden sind wichtig für das Heizen des Gases.

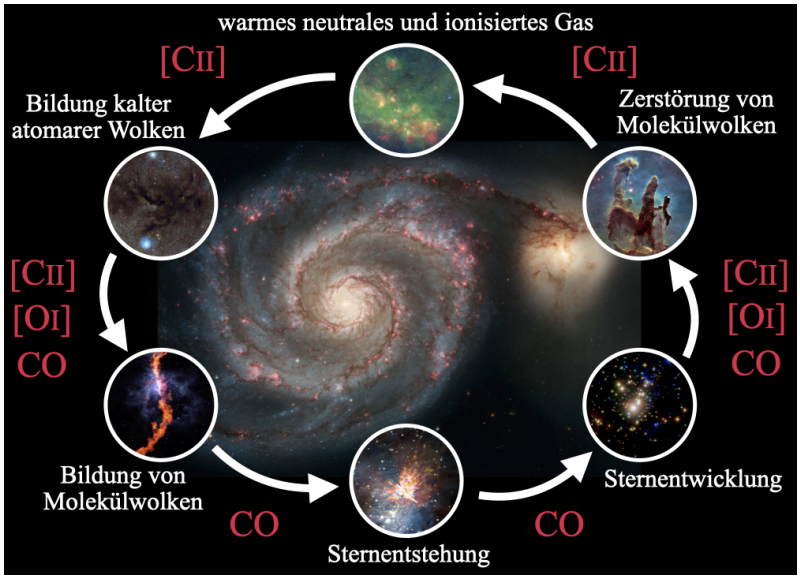

Abbildung 6.1: Der Lebenszyklus des interstellaren Mediums. Rote Buchstaben benennen die wichtigsten Emissionslinien, die in einer bestimmten Phase beobachtet werden können.

Das Material im interstellaren Medium (Gas und Staub) befindet sich in einem Kreislauf und wird stets wiederverwendet (siehe Abbildung 6.1). Beginnend bei der Entstehung eines Sternes, wird während der stellaren Evolution Material vom Stern in die Umgebung abgeführt, je schwerer der Stern, desto mehr Masse ist das. Den größten Masseverlust erleidet ein Stern am Ende seines Lebens, wenn er seine Hülle abstößt und zu einem weißen Zwerg schrumpft oder als Supernova explodiert. Vor

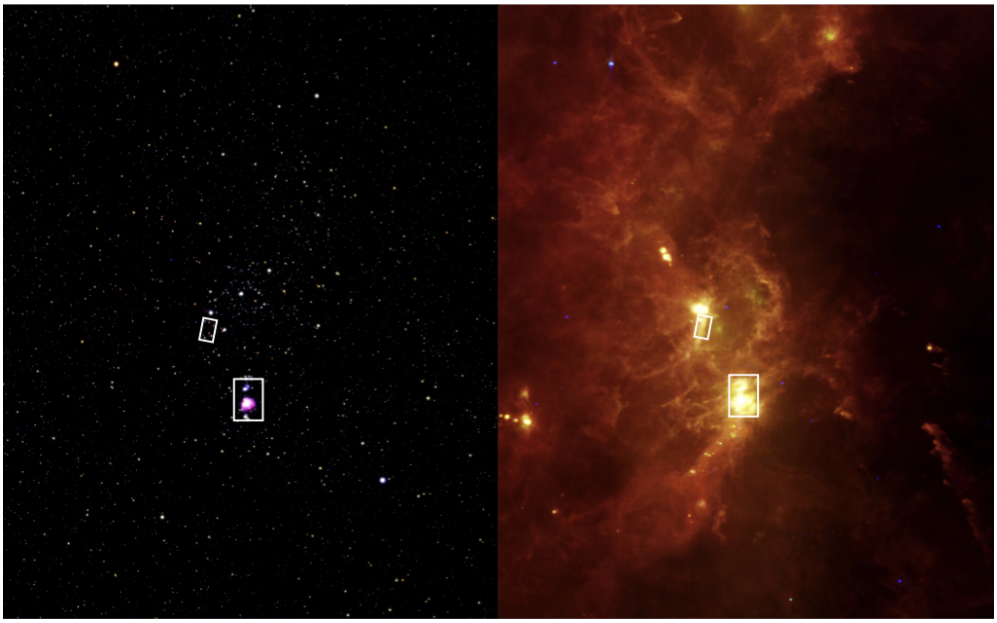

Abbildung 6.2: Das Sternbild von Orion in sichtbarem Licht (*links*) und Infrarotstrahlung (*rechts*) (Bild: NASA, JPL-Caltech, IRAS/H. McCallon). Die weißen Rechtecke umrahmen die Gebiete, die in dieser Arbeit studiert werden, den Pferdekopfnebel oben und den Orionnebel darunter.

allem Supernovae verteilen große Mengen Gas (mit neuen, schweren Elementen) und Staub in einer weiten Umgebung des ursprünglichen Sterns. Ein Teil der Energie, die frei wird (auch zu Lebzeiten des Sterns), zerstört und zerreißt die Molekülwolke, in der der Stern geboren wurde. Dieses Material wird zusammen mit den stellaren Ausflüssen aufgeheizt und bildet eine sich ausdehnende dünne Phase des ISM, entweder ionisiert oder neutral, das sogenannte warme neutrale oder ionisierte Medium. Dieses dünne Gas kühlt im Laufe der Zeit ab und bildet schließlich kalte neutrale Wolken. Indem es weiter abkühlt und sich unter Einfluss der Schwerkraft zusammenzieht, entsteht aus diesem eine neue Molekülwolke. Klumpen mit höherer Dichte ziehen sich schneller zusammen und können dicht genug werden, sodass neue Sternentstehung in Gang gesetzt wird. So schließt sich der Kreis.

Ein beliebtes Forschungsobjekt von Astronomen ist der Orionnebel und die Orion-Molekülwolke. Neben den Sternen, die das Sternbild von Orion bilden, befindet sich in dieser Richtung auch eine gigantische Molekülwolke im Raum. Die Molekülwolke sendet vornehmlich Infrarotstrahlung und Radiowellen aus, die mit speziellen Teleskopen beobachtet werden können (siehe Abbildung 6.2). Der Orionnebel (siehe Abbildung 6.3) ist ein Sternentstehungsgebiet, ein Gebiet, in dem neue Sternen entstehen. In seiner Mitte befinden sich vier große und schwere Sterne, die sogenannten Trapeziumsterne, die dafür sorgen, dass das umgebende Gas ionisiert ist (in einem sogenannten H II-Gebiet) und auch in optischer und UV-Strahlung strahlt (siehe Abbildung 6.4). Dadurch dass der Orionnebel nicht weit entfernt ist, mit einem Abstand von ungefähr 400 Parsec (ein Parsec sind 3,26 Lichtjahre oder $3{,}09\times10^{16}$ m), und außerhalb der Scheibe der Milchstraße liegt, ist er leicht zu untersuchen und selbst einfache Teleskope können seine Struktur auflösen (der Erste, der eine Zeichnung von der Struktur des

Abbildung 6.3: Der Orionnebel, beobachtet vom *Hubble Space Telescope* (Bild: NASA, ESA/M. Robberto).

Abbildung 6.4: Die Trapeziumsterne im H II-Gebiet des Orionnebels, auch Huygensgebiet genannt (Bild: NASA/C. R. O'Dell and S. K. Wong).

Orionnebels machte, war Christiaan Huygens im Jahr 1659). Die Orion-Molekülwolke wird in zwei Teile aufgeteilt, Orion A im Süden und Orion B im Norden. Der Orionnebel befindet sich an der Oberfläche der Orion-A-Molekülwolke. Auch in der Orion-B-Molekülwolke sind Sternentstehungsgebiete zu finden, die hellsten sind die Reflektionsnebel NGC 2023 und NGC 2024. In der Orion-B-Molekülwolke befindet sich auch der ikonische Pferdekopfnebel (siehe Abbildung 6.5).

Die Interaktionen zwischen Sternen und dem interstellaren Medium

Sterne, und vor allem massereiche Sterne, senden UV-Strahlung aus. Diese UV-Photonen ionisieren Wasserstoff und andere Elemente, je nach Wellenlänge, und erhitzen das Gas durch den photoelektrischen Effekt auf Staubkörnern und PAKs (der photoelektrische Effekt ist das Phänomen, dass Photonen Elektronen aus einem Material schlagen können, die dann einen Energieüberschuss haben, den sie auf das übrige Gas verteilen können). Sehr schwere Sterne senden außerdem Materieteilchen aus, einen sogenannten Wind. Diese Winde können aufgrund ihrer großen Geschwindigkeit das ISM auf Millionen Grad erhitzen. Es entsteht ein heißes Plasma, das Röntgenstrahlung emittiert. Dieses Plasma sorgt für eine Schockwelle, die das umgebende Gas aufkehrt und in einer dünnen Schale von neutralem Gas komprimiert (siehe Abbildung 6.6). Meistens ist solch eine Schale nicht ganz symmetrisch und es entsteht nach einiger Zeit eine Bruchstelle, wodurch das Plasma herausströmen kann. Auf diese Weise können durch viele Sterne zusammen viel größere Strukturen gebildet werden, sowie die Orion-Eridanus-Blase, die das gesamte Sternbild von Orion umgibt. Wie oben beschrieben, sorgen massereiche Sterne dafür, dass die Molekülwolke, die ihr Geburtsort war, auseinandergerissen wird. Dies heißt negative Rückkopplung, da weitere Stern-

Abbildung 6.5: Die Molekülwolke L1630 in der Umgebung des Pferdekopfnebels in Infrarotlicht (blau: 3,4 μm (hauptsächlich Sterne), blaugrün: 4.6 μm, grün: 12 μm (Emission von PAKs), rot: 22 μm (Emission von Staubteilchen)) (Bild: NASA, JPL-Caltech). Links über dem Pferdekopfnebel befinden sich die (viel helleren) Reflektionsnebel NGC 2023 und NGC 2024. Rechts vom Pferdekopfnebel nähert sich der Stern σ Ori der Molekülwolke. Der rote Bogen vor dem Stern ist eine Bugwelle von Staubteilchen, die der Stern vor sich her schiebt.

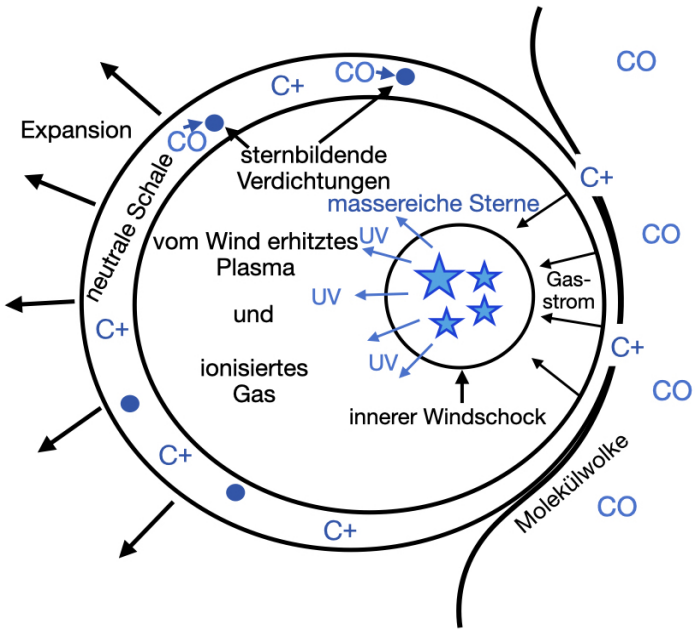

Abbildung 6.6: Schema einer Interaktion zwischen massereichen Sternen und einer Molekülwolke.

entstehung in der Molekülwolke verhindert wird. Es gibt jedoch auch die Möglichkeit der positiven Rückkopplung, wenn die Schockwelle, die sich in die Molekülwolke (oder in die sich ausdehnenden Schale) bewegt, zur Kompression des Gases und dadurch zu neuer Sternentstehung führt. Dieses letzte wurde in einigen Sternentstehungsgebieten beobachtet, aber die genauen Umstände, unter denen negative oder positive Rückkopplung vorherrschend ist, sind im Moment nicht ausreichend bekannt.

Weniger massereiche Sterne formen das umgebende Gas nur mittels ihrer UV-Strahlung. Auch diese Strahlung, oder besser der Überdruck, der im ionisierten Gas entsteht, kann dafür sorgen, dass eine dünne Schale von neutralem Gas zusammengekehrt wird. Diese expandieren meistens weniger schnell als die durch einen stellaren Wind gebildeten Schalen, aber auch sie können ansehnlich groß werden. Wir werden zwei Beispiele dieses Typs von Expansion sehen.

Infrarotstrahlung und Feinstrukturlinien

Gas, das erhitzt ist, kühlt auch ab. Hierbei helfen Feinstrukturübergänge von Spurenelementen (alles außer Wasserstoff). Die Feinstruktur eines Atoms (oder Ions) ist die Aufspaltung von Energieniveaus durch die Kopplung des Elektron-Bahn-Impulses mit dem Elektronenspin und relativistische Effekte. Zwischen den aufgespaltenen Energieniveaus finden Übergänge mit niedriger Energie statt. Die meisten dieser Übergänge sind „verbotene“ Übergänge, die also eine sehr kleine Wahrscheinlichkeit haben. Da die Zeitskalen, in denen das ISM evoluiert, so groß sind, und die Dichte des ISM so gering, spielen sie jedoch die Hauptrolle. Verschiedene Atome und Ionen haben verschiedene Feinstrukturübergänge, die in verschiedenen Phasen des ISM angeregt werden. Ich beschränke mich hier auf die Besprechung der Feinstrukturlinie von ionisiertem Kohlenstoff (in spektroskopischer Notation [C II]) mit einer Wellenlänge von 158 μm, da ich diese in dieser Doktorarbeit benutzt habe, um zwei Gebiete in Orion zu studieren.

Das warme neutrale ISM (mit einer Termperatur von ungefähr 100 K und einer Dichte von 10^3-10^5 Teilchen per Kubikzentimeter) kühlt hauptsächlich mittels der [C II]-Linie ab. Hier ist Wasserstoff atomar oder molekular, aber Kohlenstoff ist noch immer ionisiert durch die einfallende UV-Strahlung. Ionisiertes Wasserstoffgas enthält auch Kohlenstoffionen, aber die [C II]-Emission ist dort weniger prominent, da andere Übergänge einen größeren Beitrag zur Kühlung liefern. Neben der Linienemission gibt es auch Kontinuumsemission der Staubkörnchen und Emission der PAKs. Abbildung 6.7 zeigt ein typisches Infrarotspektrum des ISM, eine Kombination von Kontinuumsemission und Linienemission.

Diese Doktorarbeit

In dieser Arbeit habe ich von Infrarotbeobachtungen, ausgeführt durch das upGREAT-Instrument auf SOFIA, Gebrauch gemacht. SOFIA („Stratospheric Observatory for Infrared Astronomy“) ist eine modifizierte Boeing 747-SP, ausgerüstet mit einem Spiegel von 2,5 m Durchmesser. In der Stratosphäre wird Infrarotstrahlung (Wellenlängen zwischen 3 und 500 Mikrometern) viel weniger durch Wasserdampf in der Atmosphäre absorbiert (siehe Abbildung 6.7), wodurch Beobachtungen möglich sind. Das Instrument upGREAT („upgraded German Receiver for Astronomy at Terahertz Frequencies “) ist ein heterodyner Empfänger, was bedeutet, dass das Signal eines lokalen Oszillators in das astronomische Signal gemischt wird mittels eines Mixers. Das resultie-

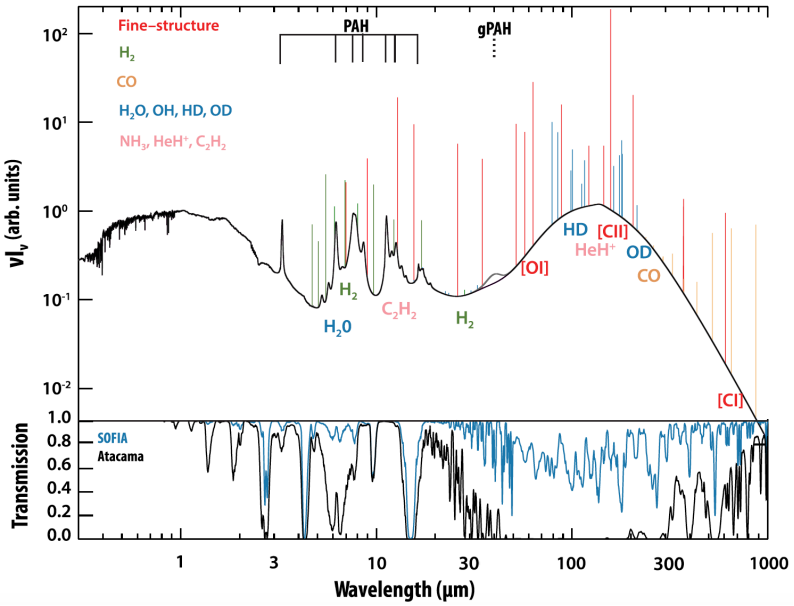

Abbildung 6.7: *Oben*: Ein Modell interstellarer Emission (Kontinuum und Linien). *Unten*: Atmosphärische Transmission für Infrarotstrahlung von der Erde (Atacama) und SOFIA aus (Abbildung: K. Ennico et al., JAI 7,4, 2018).

rende elektronische Signal kann durch elektronische Bausteine verstärkt werden und liefert Spektren mit hoher spektraler Auflösung. Die Spektrallinie, die wir benutzen, ist die Feinstrukturlinie von ionisiertem Kohlenstoff, [C II]. Mit Hilfe von hochaufgelösten Spektren mit hoher räumlicher Auflösung (für die [C II]-Linie, gemessen von SOFIA/upGREAT, ist das eine spektrale Auflösung von 0,2 km/s und eine räumliche Auflösung von 15,9 Bogensekunden) kann man ein detailliertes Bild skizzieren von den Bewegungen des interstellaren Gases. Emission von ionisertem Kohlenstoff, die [C II]-Linie, kann in verschiedenen Phasen des ISM beobachtet werden: Oberflächen von Molekülwolken in der Nähe eines Sterns, das warme neutrale oder ioniserte ISM, und kalte atomare Wolken. Auf galaktischen Skalen liefern all diese Phasen einen Beitrag zur totale [C II]-Emission, aber unsere Beobachtungen beschränken sich auf Gebiete in der Nähe von massereichen Sternen.

In Kapitel 2 schauen wir uns den Pferdekopfnebel an. Dieser Nebel ist eine Ausstülpung der L1630-Molekülwolke, die ein Teil der Orion-B-Molekülwolke ist. Der Pferdekopfnebel und L1630 darum herum werden erhitzt durch den O9.5V-Stern σ Ori, der sich der Wolke nähert und sie verdampft. An der Oberfläche der Wolke ensteht so ein Photodissoziationsgebiet (PDR, „photodissociation region“) mit der typischen geschichteten Struktur: Anschließend an das H II-Gebiet, das Gebiet, worin Wasserstoff ionisiert ist, besteht die oberste Schicht der Wolke aus atomarem Wasserstoff, worin Kohlenstoff noch ionisiert ist. Etwas tiefer in der Wolke kombiniert Wasserstoff zu Wasserstoffmolekülen, aber Kohlenstoff ist noch immer ionisiert. Erst noch etwas tiefer in der Wolke wird Kohlenstoff neutral und es bildet sich auch schnell Kohlenstoffmonoxid (CO), das nach Wasserstoff meist abundante Molekül im ISM. Wo Kohlenstoff ionisiert ist, kühlt sich das Gas durch Emission der verbotenen [C II]-Linie und andere verbotenen Linien von Spurenelementen (Sauerstoff, Stickstoff, Schwefel).

Das CO-enthaltende Gas kühlt sich durch Emission von Rotationslinien von CO und anderen Molekülen. Diese Linien können durch Radioteleskope wie das IRAM-30m-Teleskop gemessen werden. Für die Studie des Pferdekopfnebels benutzen wir den niedrigsten Rotationsübergang von CO, die CO(1-0)-Linie mit einer Wellenlänge von 2,6 mm. Weiterhin vergleichen wir die [C II]-Emission mit der Kontinuumsferninfrarotemission (λ = 40-500 μm), die von Staubteilchen emittiert wird, und der Emission von PAKs im *Spitzer*/IRAC-8 μm-Band. Die *Herschel*/PACS- und SPIRE-Bänder bei 70 μm, 160 μm, 250 μm, 350 μm und 500 μm liefern außerdem Schätzungen für die optische Tiefe des Staubs und die Staubtemperatur. Wir finden gute Korrelationen zwischen der [C II]-Emission und der PAK-8 μm-Emission sowie der integrierten Ferninfrarotemission (FIR, „far-infrared“), was zeigt, dass die [C II]-Emission von der Oberfläche der Wolke stammt. Die CO(1-0)-Emission ist komplementär zu der [C II]-Emission, was zeigt, dass wir die Wolke in einer „edge-on“-Konfiguration beobachten, von der Seite also. Das verkompliziert den Vergleich der Beobachtungen mit PDR-Modellen, aber wir können die Beobachtungen trotzdem gut reproduzieren mit edge-on-PDR-Modellen. Der Großteil der [C II]-Emission rund um den Pferdekopfnebel stammt von den PDR-Oberflächen und nur 5% können dem H II-Gebiet zugeschrieben werden.

In Kapitel 3 machen wir wiederum Gebrauch von der [C II]-Linie, aber dieses Mal über ein viel größeres Gebiet (gut ein Quadratgrad) beobachtet, nämlich den Orionnebel (M42) in der Orion-A-Molekülwolke. Hier sehen wir die Kraft hoher spektraler und räumlicher Auflösung. Mittels Positionsgeschwindigkeitsdiagrammen können wir die Expansion des Orionnebels sichtbar machen und zum ersten Mal quantifizieren. Die heißen Sterne im Orionnebel, und vor allem der schwerste der Trapeziumsterne, der O7V-Stern θ^1 Ori C, erhitzen das ISM zu einem heißen Plasma, das Röntgenstrahlung aussendet. Das heiße Plasma expandiert und kehrt dadurch eine Schale von kühlerem neutralem Gas auf. Die Schale, mit einem Radius von 2,5 Parsec, strahlt in [C II]-Emission. Wir bestimmen die Masse der Schale aus der optischen Tiefe des Staubs, gewonnen aus den *Herschel*/PACS- und SPIRE-Bändern bei 70 μm, 100 μm, 160 μm, 250 μm, 350 μm und 500 μm. Mit einer Masse von 1.500 Sonnenmassen und einer Geschwindigkeit von 13 km/s wird ein großer Teil der Gasmasse, die zu dem Sternentstehungsgebiet, dem Molekülkern OMC1 („Orion molecular core 1“), gehört, aus dem Gebiet ausgestoßen. Die Expansionscharakteristiken werden gut beschrieben durch ein einfaches analytisches Modell für windgetriebene Gasblasen. Das gibt eine Schätzung des Alters der Schale, nämlich 200.000 Jahre. Die Schale wird schließlich aufbrechen und das heiße Plasma wird in das umliegende Medium ausfließen und die größeren Gasstrukturen der Orion-Eridanus-Blase auffüllen.

Kapitel 4 bespricht die expandierenden Schalen der Nebel M43 sowie NGC 1973, 1975 und 1977 (kurz NGC 1977). Beide liegen in der Nähe des Orionnebels und sind Teil derselben [C II]-Karte. Im Gegenteil zum Orionnebel enthalten M43 und NGC 1977 weniger schwere Sterne (den B0.5V-Stern NU Ori sowie den B1V-Stern 42 Orionis), die keinen nennenswerten stellaren Wind produzieren. Diese zwei Nebel sind H II-Gebiete mit einer umgebenden neutralen Schale. Die Schale von M43 mit einem Radius von 0,3 Parsec hat eine Masse von 8 Sonnenmassen und expandiert mit einer Geschwindigkeit von 6 km/s. Die Schale von NGC 1977 mit einem Radius von 1,0 km/s hat eine Masse von 700 Sonnenmassen und expandiert mit 1,5 km/s. Beide werden gut durch ein analytisches Modell von expandierenden H II-Gebieten beschrieben. Diese ergeben ein Alter von 20.000 Jahren für M43 und ein Alter von 400.000 Jahren für NGC 1977. Das Alter der Schale kann nicht unmittelbar in das Alter des Sterns übersetzt werden, denn junge Sterne können lange in der Molekülwolke eingebettet sein, bevor sie ins

dünne Medium gelangen, wo sie eine Expansion in Gang bringen können.

In Kapitel 5 untersuchen wir, in wie weit die [C II]-Emission des Orionnebels eine Erklärung liefert für [C II]-Beobachtungen von extragalaktischen Quellen. Da die [C II]-Linie die stärkste FIR-Linie ist, kann sie auch in Quellen mit großem Abstand beobachtet werden, und es wurde gezeigt, dass es eine Korrelation zwischen der [C II]-Luminosität und dem Sternentstehungspotential einer Galaxie gibt. Wir untersuchen zunächt die Korrelationen zwischen der [C II]-Intensität und der Staub-70 μm-, PAK-8 μm-, integrierter FIR- sowie CO(2-1)-Intensität ($\lambda = 1,3$ mm). Wir sehen gute Korrelationen zwischen der [C II]-Intensität und den ersten drei, wobei diese nicht linear proportional sind, sondern mit einem Exponenten kleiner als 1 gehen. Das Verhältnis zwischen [C II] und CO(2-1) zeigt auch einen Trend, aber auch große Streuung. In extragalaktische Quellen von hoher FIR-Luminosität wird eine verminderte [C II]-Luminosität beobachtet. Wir sehen das auch in unseren Daten: Die [C II]-Intensität nimmt im Verhältnis zur FIR-Intensität mit steigender FIR-Intensität in der Nähe der Trapeziumsterne ab. Wir schreiben dies der Bedeutung von Gaskühlung durch die Sauerstofffeinstrukturlinie [O I] bei 63 μm zu. Ein kleiner Effekt kann auch ein weniger effizienter Heizmechanismus durch zunehmende Ionisation von PAKs und Staubkörnern in der Nähe heißer Sterne sein. Wir sehen jedoch auch ein vermindertes [C II]/FIR-Verhältnis in Sichtlinien mit großen Säulen von Staub, warm oder kalt. Eine mögliche Interpretation der [C II]-FIR-Defizienz wäre dann auch eine Beschreibung als FIR-Überschuss. Wenn wir die [C II]-Luminosität mit dem Sternentstehungspotential des Orionnebels, wie es bekannt ist aus Zählungen von jungen stellaren Objekten, vergleichen, sehen wir, dass die Gleichungen, die auf extragalaktische Beobachtungen geeicht sind, den tatsächlichen stellaren Inhalt unterschätzen, ungefähr um ein bis zwei Grössenordnungen. Dies kann anzeigen, dass große Oberflächen, die weniger intensive Strahlung aussenden, wesentlich zur galaktische [C II]-Emission beitragen. Wir sehen einen Trend in dieser Richtung auch in unseren Daten.

Kapitel 6 ist eine Ausführung des PDR-Aspekts, der in Kapitel 5 zugunsten der Übersichtlichkeit und Verständlichkeit unterbelichtet blieb. Zuallererst teilen wir das Gebiet der ganzen [C II]-Karte in vier Gebiete auf: Die Schale des Orionnebels, das molekulare Filament um den Molekülkern OMC4 in der Mitte der Schale, M43 und NGC 1977. Die letzten zwei Gebiete werden wiederum aufgeteilt in das H II-Gebiet, dichte molekulare Gebiete und die [C II]-emittierende Schale. Wir sehen eigentlich, dass die Korrelationen, die wir im vorhergehenden Kapitel global untersucht haben ([C II]-Intensität versus Staub-70 μm-, PAK-8 μm- und FIR-Intensität), wenig Variationen in den vier getrennten Gebieten zeigen. Nur die Korrelation zwischen der [C II]-Intensität und der CO(2-1)-Intensität ist komplizierter. Diese untersuchen wir näher, indem wir Spektren in repräsentativen Gebieten studieren. Das zeigt, dass in jeder Emissionslinie mehrere Komponenten vorhanden sind, die nicht immer mit einander in Beziehung zu setzen sind. Möglicherweise werden wir genarrt von der Dynamik, induziert durch die Sterne, der Gebiete. Dies zeigt auch, dass Sternentstehungsgebiete sehr komplex sind, und dass es eigentlich nicht möglich ist, physikalische Eigenschaften aus der Messung einer gemittelten Linie (wie das in extragalaktische Studien der Fall ist) zu bestimmen. Wir sehen auch, dass es durch die Vielheit an Komponenten schwierig ist, die Emission wiederzugeben in PDR-Modellen. Nichtsdestotrotz nähern unsere edge-on-PDR-Modelle die [C II]-Intensität ganz ordentlich, aber wir bemerken, dass es Abweichungen gibt. Zum Schluss relatieren wir die [C II]-Kühlungseffizienz, gemessen als [C II]/FIR-Intensitätsverhältnis, an die aus PAK-Spektren abgeleiteten Charakteristiken der PAKs. Wir sehen jedoch nicht, dass die PAK-Ionisation oder die

Molekülgröße signifikant variiert, wohl aber das [C II]-FIR-Verhältnis. Möglicherweise bedeutet das, dass kleine Staubkörner auch wichtig sind für die Erwärmung des Gases. Hier könnten zukünftige Missionen, wie das *James Webb Space Telescope*, Licht ins Dunkel bringen.

Kurzum, die Beobachtungen, die ich in dieser Arbeit studiert habe, zeigen den Reichtum von Sternentstehungsgebieten. Nicht nur gibt es einen Reichtum an verschiedenen Emissionslinien (die wichtigsten sind [C II], [O I] und die CO-Linien), sondern auch einen Reichtum an Emissionskomponenten, die in jeder Linie wieder verschieden zu sein scheinen. Nichtsdestotrotz können die Expansionsbewegungen auf großer Skala sehr genau bestimmt werden. Dieser Arbeit nachfolgend wird der SOFIA FEEDBACK C^+ Legacy Survey 11 Sternentstehungsgebiete in der Milchstraße beobachten und das Maß, in dem Sterne ihre Umgebung beeinflussen, mit größerer Genauigkeit als bisher quantifizieren können. Dies wird uns in die Lage versetzen, besser zu verstehen, wie auch viel größere Strukturen in unserem Universum, die wesentlich durch stellare Rückkopplung bestimmt werden, entstehen und vergehen.

Publications

1st author:

[1] Pabst, C. H. M., Goicoechea, J. R., Teyssier, D., Berné, O., Higgins, R. D., Chambers, E. T., Kabanovic, S., Güsten, R., Stutzki, J., Tielens, A. G. G. M.
Expanding bubbles in Orion A: [C II] observations of M42, M43, and NGC 1977
A&A, 639, A2 (2020)

[2] Pabst, C., Higgins, R., Goicoechea, J. R., Teyssier, D., Berné, O., Chambers, E., Wolfire, M., Suri, S. T., Guesten, R., Stutzki, J., Graf, U. U., Risacher, C., Tielens, A. G. G. M.
Disruption of the Orion molecular core 1 by wind from the massive star θ^1 Orionis C
Nature, 565, 618 (2019)

[3] Pabst, C. H. M., Goicoechea, J. R., Teyssier, D., Berné, O., Ochsendorf, B. B., Wolfire, M. G., Higgins, R. D., Riquelme, D., Risacher, C., Pety, J., Le Petit, F., Roueff, E., Bron, E., Tielens, A. G. G. M.
[C II] emission from L1630 in the Orion B molecular cloud
A&A, 606, A29 (2017)

2nd author:

[4] Schneider, N., Simon, R., Guevara, C., Buchbender, C., Higgins, R. D., Okada, Y., Stutzki, J., Güsten, R., Anderson, L. D., Bally, J., Beuther, H., Bonne, L., Bontemps, S., Chambers, E., Csengeri, T., Graf, U. U., Gusdorf, A., Jacobs, K., Justen, M., Kabanovic, S., Luisi, M., Menten, K., Mertens, M., Mookerjea, B., Ossenkopf-Okada, V., Pabst, C., Pound, M. W., Ramsey, K., Richter, H., Reyes, N., Ricken, O., Röllig, M., Russeil, D., Sánchez-Monge, Á., Sandell, G., Tiwari, M., Wiesemeyer, H., Wolfire, M., Wyrowski, F., Zavagno, A., Tielens, A. G. G. M.
FEEDBACK: a SOFIA Legacy Program to Study Stellar Feedback in Regions of Massive Star Formation
PASP, 132,1016 (2020)

[5] Goicoechea, J. R., Pabst, C. H. M., Kabanovic, S., Santa-Maria, M. G., Marcelino, N., Tielens, A. G. G. M., Hacar, A., Berné, O., Buchbender, C., Cuadrado, S., Higgins, R., Kramer, C., Stutzki, J., Suri, S., Teyssier, D., Wolfire, M.
Molecular globules in the Veil bubble of Orion. IRAM 30 m ^{12}CO, ^{13}CO, and $C^{18}O$ (2-1) expanded maps of Orion A
A&A, 639, A1 (2020)

[6] Salas, P., Oonk, J. B. R., Emig, K. L., Pabst, C., Toribio, M. C., Röttgering, H. J. A., Tielens, A. G. G. M.
Carbon radio recombination lines from gigahertz to megahertz frequencies towards Orion A
A&A, 626, A70 (2019)

[7] Fuster, A., Pabst, C., Pfeifer, C.
Berwald spacetimes and very special relativity
PhysRevD, 98, 084062 (2018)

[8] Fuster, A., Pabst, C.
Finsler pp-waves
PhysRevD, 94, 104072 (2016)

Curriculum Vitae

I was born on September 18, 1989, in Marburg, Germany. My parents and me soon moved to Munich. I was raised alternatingly there and in Walnut Creek, California. When I was five years old, my parents settled in the municipality of Wolfenbüttel. From an early age, I was fascinated by stars and the larger universe. In high school, my passion altered slightly to atomic physics and quantum physics. This was kindled in earnest in 2007 by my participation, facilitated by my earlier physics teacher Herr Kloppe, in a 10-day workshop on Bose-Einstein condensation of the JGW-Schülerakademie under the direction of Christian Hagendorf and Steffen-Patrick Rath, at that time two PhD students at the École Normal Supérieur in Paris, France. The workshop treated both theoretical and experimental aspects, but I was mainly drawn towards theory. I spent my last high-school year deepening my knowledge of theoretical physics and math, encouraged by my maths and physics teachers Herr Wesche and Herr Genther.

In 2008, I went to Göttingen to study physics. My interests were mainly in theoretical physics and my Bachelor thesis, under the supervision of Dr. Manfred Requardt, treated typical microstates of macrosystems, also known as Canonical Typicality and Normal Typicality (the latter is a concept introduced by John von Neumann). After graduating with a Bachelor degree from the Georg-August-Universität, I moved to Leiden to pursue a Master degree in theoretical physics in 2012. I graduated from the Master program at Leiden University in 2015 with a thesis on pp-waves in General Very Special Relativity, a modification of general relativity on a Finsler-type geometry, under the supervision of Prof. Dr. Ana Achúcarro and Dr. Andrea Fuster. However, I was becoming increasingly dissatisfied with the hypotheticality of theoretical research and longed for something more tangible. I applied for a PhD position at the Sterrewacht and was lucky enough to get hired by Prof. Dr. Xander Tielens. He offered me the freedom to choose whatever topic would fascinate me, but due to my inability to choose, he set me to work on the topic on which he just had submitted a SOFIA proposal: the [CII] emission from the Orion Nebula. I began studying the [C II] emission from the Horsehead Nebula and adjacent molecular cloud as preparation. Xander made sure that I would be onboard SOFIA when the observations of the large Orion Nebula map were taken, which was in November 2016 and February 2017. After learning a lot about data reduction, the scientific analysis could begin, which to this date has lead to the four papers that constitute this thesis.

While the large data set of the [C II] emission from the Orion Nebula invites for more and more detailed studies, SOFIA has also obtained [C II] observations of the Tarantula Nebula in the Large Magellanic Cloud (a satellite galaxy of our Milky Way). During the next year, I will study this data set in combination with SOFIA/HAWC+ measurements of the polarization of interstellar dust grains. This will teach us something on the importance of magnetic fields in regulating stellar feedback.

Acknowledgements

There are too many people that have helped pave my way and I am bound to forget at least some of them. I hope that I will be forgiven.

First of all, I wish to thank Xander Tielens for offering me the opportunity to develop into a real astronomer (although I try to keep true to my inclinations towards theoretical physics and mathematics). The path has been very muddy and I am very much indebted to his patience and confidence in me.

Javier Goicoechea has been a great co-supervisor, always keen on offering feedback and bearing new insights. Of course, I am also indebted to the other members of the C+SQUAD, without whom this thesis would not exist; it has been a great honor to be admitted as the only sailor on a ship full of captains.

I am grateful to all who operate SOFIA and who have allowed me a glimpse of its intricacies. I am particularly grateful to the GREAT team, who explained the working of the instrument and the data pipeline to me and assisted in the data reduction and the ensuing data analysis. In particular, Ronan Higgins did a wonderful job and we would have been lost in the thickets of the wilderness without him.

During the past year, Bob O'Dell shared his lifelong passion and his expertise on the Orion Nebula with me. I thank him for many fruitful discussions, not only on the Orion Nebula, but on Nietzsche, Heidegger, and Camus, as well.

I would not have been able to write this thesis without the constant support of Tjerk Oosterkamp. He helped me to navigate the deep seas of writing a PhD thesis. He never tired of throwing a life buoy when I was about to drown. His wife Jannette Prins, and pastors Pieter Kleingeld and Bram Dijkstra provided food on the journey untiringly.

After the disastrous event in December 2017, and during the journey through hell that followed, the community of the NGK Oegstgeest never wavered in their sympathy and care. I thank all of them with all my heart. In particular, I am grateful for many shared meals to Carin, Jan, Janneke, Wouter, and Annemarie. Our kerngroep also shared many meals together and many a gezellige evening: I thank Femmy, Aline, Jelle, Hester, Kees, Anna, Simon, Coriëtte, Marijke, Anne-Marije, and Gertjan.

My debts to Alexandra Schouten-Voskamp and Caroline de Bruin have grown immense. I will not be able to pay them back in bakery. I thank both for their unerringly wise advise and undiminishing patience. Kimberly Emig has been a loyal sister-in-arms at the Sterrewacht. I thank her for her friendship and support, especially in the form of baked goods and other food and recipes.

Gesa, Steffi, and Britta have been loyal companions for shorter or longer periods of my life. All of them have helped me to battle the monsters and thorny bushes that blocked the way occasionally. We have shared many sweet moments (with pie and cookies) and I am very thankful for their friendship. Also much valued were the infamous Christmas dinners and the friendship of Matthijs, Lennart, Tom, Mark, and Henk, all of whom have known the sorrows of a PhD student. I thank Frank for sharing his enthusiasm about all things in nature, in particular the starry sky, and his profound reflections. Anne and Micha have been steadfast friends, as well. Esther Heizmann-Linder continued to offer advice and new perspectives. Ana Achúcarro and Andrea Fuster never lost confidence in my abilities. I am grateful to know them and for their friendship.

I also thank my family, who went through the ups and downs with me. Of course,

I would not be here without my parents. I thank them for their unrelenting love and support. They and their spouses did the most humanly possible to get me to the end of this trajectory.